The University of Reading

Measurements and Interpretations of the Water Vapour Continuum at Near Infrared Wavelengths

Thesis submitted in fulfilment of requirements for the degree of PhD

APRIL 2008

David Paynter

Department of Meteorology

Declaration

I confirm that this is my own work and the use of all material from other sources has been properly and fully acknowledged.

David Paynter

Acknowledgements

I would like to thank my supervisors Keith Shine and Kevin Smith for providing excellent support and encouragement throughout the PHD. I also wish to thank Garry Williams who made this PhD possible by spending many hours sorting out the experimental setup at RAL. I am also indebted to Igor Ptashnik whose expert advice and guidance I have found invaluable. A special thank you to Shweta Wahi and Helen Greatrex for their help, support and friendship. Thank you to NERC for funding me and more importantly funding the measurements at the MSF facility. Thanks to all of my friends and colleagues in the Meteorology Department at the University of Reading, who have kept me sane during my hunt for water dimers. Finally, I wish to thank my family, who have always provided love and stability.

Abstract

The self and foreign water vapour continuum have been derived using high spectral resolution laboratory-based Fourier transform spectrometer measurements of pure water vapour and water vapour mixed with air between 1200 and 8000 cm^{-1}. These measurements were conducted over a temperature range of 296-351 K and a vapour pressure range of 12-274 mb. Over this pressure range it was found that the optical depth of the self continuum had a pressure squared dependence and a strong negative temperature dependence. The foreign continuum optical depth scaled with the product of the vapour and air pressure and had a weak negative temperature dependence.

The derived self continuum in numerous regions showed reasonable agreement with the semi-empirical MT_CKD and CKD models. However, features were detected in the continuum around 3200 cm^{-1}, 3600 cm^{-1} and 3700 cm^{-1} that are not predicted by either model, but are consistent with theoretically predicted water dimer transitions. It was also apparent that the MT_CKD continuum overestimates the size of the continuum in 3950 – 4150 cm^{-1}, 5500-5700 cm^{-1} and 7400-7600 cm^{-1} regions.

The foreign continuum was found to agree well with MT_CKD and CKD in 1200-2000 cm^{-1} region. However, in some areas of the 3400-4000 cm^{-1} region, there was evidence of the CKD model overestimating the continuum by up to 50%.

Seasonal clear-sky zonal-mean atmospheric shortwave absorption and heating rates by the continuum derived in this work were compared to those calculated for CKD and MT_CKD. In the 1200-8000 cm^{-1} region the CKD continuum predicted a clear sky globally averaged shortwave absorption of 1 Wm^{-2}, the MT_CKD continuum 0.79 Wm^{-2} and this work 1.14 Wm^{-2} out of total shortwave absorption of 36.5 Wm^{-2}.

Table of Contents

1. Motivation

Water vapour is the most important absorber of both longwave and shortwave radiation. In clear skies it accounts for an estimated 57% of the total long wave atmospheric absorption and 72% of the total shortwave absorption (Kiehl and Trenberth 1997). Because of this substantial amount of absorption water vapour acts as an important greenhouse gas. When investigating climate change, due to the increased amount of water vapour a warmer atmosphere can hold, water vapour acts as a positive feedback that increases the Earth's sensitivity to carbon dioxide and other radiative forcing gases by almost a factor of two (Held and Soden 2000). For this reason, accurate quantification of both longwave and shortwave absorption due to water vapour in the atmosphere is vital for the understanding of climate processes.

It has been well documented that during the 1990's at the time most general circulation models (GCMs) appeared to underestimate the amount of absorbed shortwave radiation by between 25-30 Wm^{-2} (Ramanathan and Vogelmann 1997). Numerous authors have attempted to explain this discrepancy with respect to lack of knowledge of cloud physics (Cess et al. 1995; Ramanathan et al. 1995) and propose that it is necessary to increase the radiative forcing due to clouds. However, others claimed that this excess absorption is still seen in clear sky cases and thus the problem is the result of extra absorption due to water vapour and aqueous aerosol not being taken into account by models (Arking 1996; Li et al. 1997; Arking 1999).

A recent study of 20 GCMs (Wild 2005) summarised in Figure 1.1 showed that on average they predicted 74 Wm^{-2} annual global mean absorption of shortwave radiation in atmosphere. There was considerable variation from model to model, with a standard deviation of 7.3 Wm^{-2} and a range of 30 Wm^{-2}. Analysis from the GEBA field site data showed that on average these models overestimate the surface flux by 9 Wm^{-2}. This suggests that, whilst models are becoming better at explaining observations, there is still a considerable uncertainty in how to parameterise shortwave absorption.

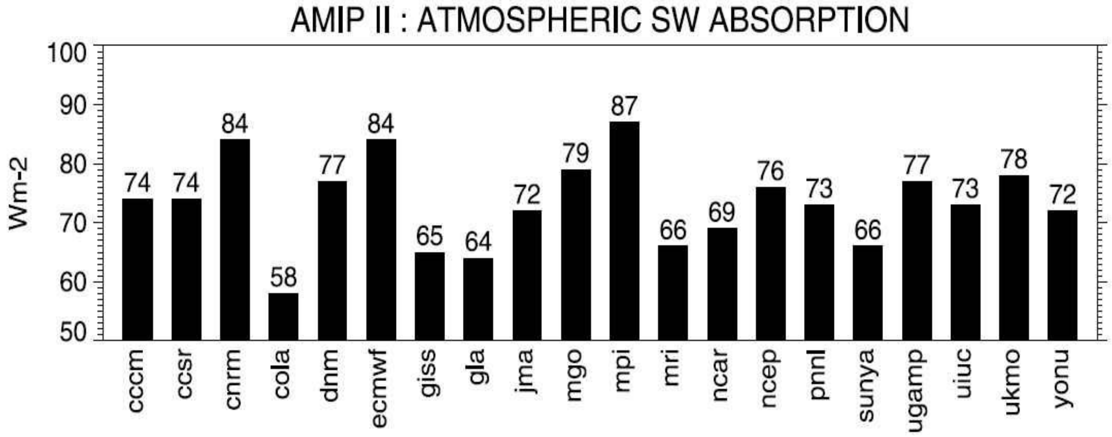

Figure 1.1 Comparison of the estimates of global annual mean averaged shortwave radiation from 20 GCMs. From Wild (2005).

It is quite likely that a combination of numerous physical mechanisms could explain the lack of agreement between GCMs and observations. Uncertainty in absorption due to water vapour could be one of the possible causes that would explain both the clear and cloudy sky discrepancy. Water vapour absorption can be seen to consist of a highly variable line absorption and a less structured background continuum absorption. The line absorption results from rotational and vibrational transitions of the water molecules. This absorption is usually estimated using data about the individual spectral lines from a database like HITRAN (e.g. Rothman et al. 2005) or GEISA (Jacquinet-Husson et al. 2005).

The physical mechanisms behind the continuum are still not well understood. Indeed, it has been described as the major source of uncertainty in gaseous radiative transfer (Held and Soden 2000). Most GCMs account for the continuum using the semi-empirical Clough-Kneiyz-Davies (CKD) model (Clough et al. 1989). In simple terms, this model defines the continuum as the difference between the actual measured water vapour absorption and the contribution from line absorption. It then attempts to fit the continuum to line absorption parameters. This allows the continuum to be predicted even where no measurements have been conducted, providing one knows the line parameters.

In the shortwave, roughly 95 % of the solar absorption by water vapour occurs between 2000 and 14,000 cm^{-1} (Collins et al. 2006). Despite this fact, the CKD continuum is only fitted to laboratory measurements by Burch (1985) and Tobin (1996) between 1200 and 2500 cm^{-1}. At longer wavenumbers the continuum is estimated using the line absorption parameters. This is mainly because there are very few measurements of the continuum above 2500 cm^{-1}. The only two other sets known to exist prior to the work reported in this thesis, but not made use of by the CKD continuum, are those of Burch (1985) between 3200 and 4200 cm^{-1} and Ptashnik et al. (2004) between 5000 and 5600 cm^{-1}.

Despite this lack of knowledge about the behaviour of the continuum in the shortwave, it has been shown that the CKD model suggests the continuum contributes about 4% of the total absorbed shortwave (Collins et al. 2006).

The continuum can be split into a self and foreign component. The self component scales with the square of the partial pressure of water vapour, whilst the foreign continuum scales with the product of the partial pressure of water vapour and the partial pressure of the foreign broadening gas. Table 1.1 shows how the contribution of each continuum to the atmospheric absorption of solar radiation varies for different standard atmospheres (taken from the work of Collins et al (2006)). The value of the total shortwave absorption including continuum is also shown for reference. It can be seen that the self continuum contribution varies far more than that of the foreign. This is because of the pressure squared dependence causes its contribution to increase greatly in the humid tropical atmosphere.

Absorption	**HLS**	**HLW**	**MLS**	**MLW**	**TRO**
All Continuum	4.39	2.98	4.78	3.46	5.32
Self continuum	0.42	0.1	0.84	0.1	1.42
Total absorption	109.0	67.4	121.1	84.1	133.0

Table 1.1 The calculated atmospheric shortwave absorption (Wm^{-2}) by the continuum for different standard atmospheres assuming a solar zenith angle of 60 degrees. Values from Collins et al 2006. HLS = high latitude summer, HLW = high latitude winter, MLS = Mid latitude winter, TRO= tropical.

There are presently three mechanisms which have been put forward as an explanation of the continuum. The first mechanism considers changing the line shape associated with the water molecule, the second that the continuum is the result of an additional absorption mechanism called collision induced absorption, while the third proposes that the water dimer could contribute. The first mechanism was initially proposed by the CKD model (Clough et al. 1989). The line shape for water vapour is changed so to match the observed continuum in 1200-2000 cm^{-1} region. The same change is then applied to all lines in regions where no continuum measurements have been conducted. However, the current level of understanding about the line shape suggests that the change in line shape should not be significant enough to explain the whole continuum (Ma and Tipping 1999; Ma and Tipping 2002).

A later version of CKD known as MT_CKD (Mlawer et al. Personal communication; Mlawer et al. 1999) suggests that collisions between water molecules cause greater line absorption than is currently predicted by the presently used parameters. This mechanism is known as collision induced absorption. As with the adjustment to the line shape, the amount of absorption is fitted to match up with continuum measurements between 1200 and 2200 cm^{-1}. There has been very little theoretical work about collision induced absorption in water vapour, although that which has been done points to it only being able to explain a small amount of the continuum absorption (Brown and Tipping, 1999).

Another mechanism proposed as a contributor to the continuum is the water dimer (two hydrogen bonded water molecules). There is a great deal of disagreement about the magnitude of the contribution of the water dimer to the self continuum. Chylek et al. (1999), using theoretical predictions by Tso et al. (1998) suggested that for overhead sun in a tropical atmosphere the water dimer could contribute up to 6 Wm^{-2} to shortwave absorption. However, atmospheric measurements by Daniel et al. (1999) between 14,500cm and 16,000 cm^{-1} did not detect any noticeable dimer features where Tso et al. predicted they should be clearly observable. Likewise Hill and Jones (2000), measuring atmospheric absorption between 10,000 cm^{-1} and 18,000 cm^{-1}, did not detect any of the features predicted by Tso et al. and concluded that water dimer features must be at least 20 times less than that predicted. While these results do not rule out the possibility of dimer absorption elsewhere, they do suggest that the predictions of Tso et al. are too strong and should be scaled down.

Vaida et al. (2001) make use of different theoretical predictions by Low and Kjaergaard (1999) and suggest a value for overhead sun in the tropics between 1.6 Wm^{-2} and 3.3 Wm^{-2}. Ptashnik et al. (2004) claimed to detect dimer features between 5000 and 5600 cm^{-1} in the pure water vapour continuum measured in near-atmospheric laboratory conditions. Using the abundance of atmospheric dimer predicted by these features, along with the predictions of Schofield and Kjaergaard (2003), they estimate dimer absorption for overhead sun in tropical conditions between 2 Wm^{-2} and 7.2 Wm^{-2}.

Even though the Collins et al. (2006) calculations shown in Table 1.1 are for a different solar zenith angle, it is clear that if the dimer contribution to the continuum is towards the upper end of that suggested by Ptashnik et al. then this would result in considerably more continuum absorption than is suggested by CKD. The uncertainty in the contribution to shortwave absorption by water dimers is mainly because there is limited theoretical understanding of the dimer band shape.

There have also been some attempts to suggest that water complexes such as H_2O-N_2 and H_2O-O_2 could contribute to the foreign continuum (Kjaergaard et al. 2003; Daniel et al. 2004). However, the few calculations performed so far predict that these should only explain a fraction of the foreign continuum.

This work presents measurements of the self and foreign continua between 1200 and 8000 cm^{-1} within the major water absorption bands. The main aim is to quantify the amount of absorption from the continuum in this spectral region. The second aim is to use the properties of the observed continuum to try to distinguish which of the afore-mentioned physical mechanisms provides the best explanation of the continuum.

To achieve this, numerous Fourier Transform Spectrometer measurements of both pure water vapour and water vapour mixed with air were conducted in laboratory conditions. The line absorption of water vapour for the measurement conditions is then calculated using information from the HITRAN database. The continuum is then defined by taking the difference between the measured and calculated absorption. In order to categorise the properties of the continuum under different conditions, the water vapour spectrum was measured at different vapour pressures (20 mb -275 mb) and temperatures (296K -351 K).

1.1. Plan

Chapter 2 gives the background and context of this thesis. It contains a basic overview of the physics behind molecular absorption used in this work. The principles behind the different versions of CKD are then discussed. This is followed by a description of the properties of the water dimer, explaining why it is a possible candidate for describing the self continuum. The basic workings of a Fourier transform spectrometer are also described

Chapter 3 discuses the methods used for deriving the self continuum. It describes the experimental setup and introduces the techniques by which the self continuum is derived in this work. The HITRAN database, which is used for calculating the line absorption, is discussed. This includes investigating the accuracy of the various parameters used. Various experimental errors which could affect the values of the derived continuum are discussed.

Chapter 4 is the main self continuum results chapter. It presents the self continuum measurements and compares the values obtained to other measurements and models. The possibility of the water dimer contributing to the self continuum is also investigated.

Chapter 5 focuses on the temperature dependence of the self continuum. Here the temperature dependence of the self continuum is derived and then compared to that predicted by both CKD and water dimer theory.

Chapter 6 describes the foreign continuum results. It explains the methods behind deriving the foreign continuum and discusses the various errors that could contribute to the continuum. It presents the foreign continuum measurements and compares the values obtained to other measurements and models.

Chapter 7 is the atmospheric effects chapter. Here estimates of the clear sky shortwave absorption and heating rates are calculated using the continuum derived in the earlier chapters. This is compared to the estimates of other continuum models and the work of other authors.

Chapter 8 presents the conclusions of this thesis and suggests future work.

2. Background

This chapter aims to explain some of the theories and literature used and referred to in this thesis. It starts by introducing the Beer Lambert law upon which many of the results derived in later chapters are based. It will then summarise the basic principles behind molecular absorption. Attention is then given to defining the continuum and explaining the principles behind some of the models. The possibility of the water dimer contributing to the continuum is then discussed. Finally the chapter closes with a brief overview of the workings of the Fourier Transform Spectrometer used to perform the measurements presented in this thesis.

2.1. The Beer Lambert Law

The Beer Lambert law (e.g. Petty 2004) can be derived by considering an amount of electro-magnetic radiation travelling through a homogeneous layer of absorbing gas of thickness L, as shown in Figure 2.1. At some arbitrary point s in this layer the intensity of the radiation at a particular wavenumber ν, is I_ν(s). After then travelling through an infinitesimally thin layer of absorbing gas of thickness ds the intensity is given by $I_\nu(s+ds)$.

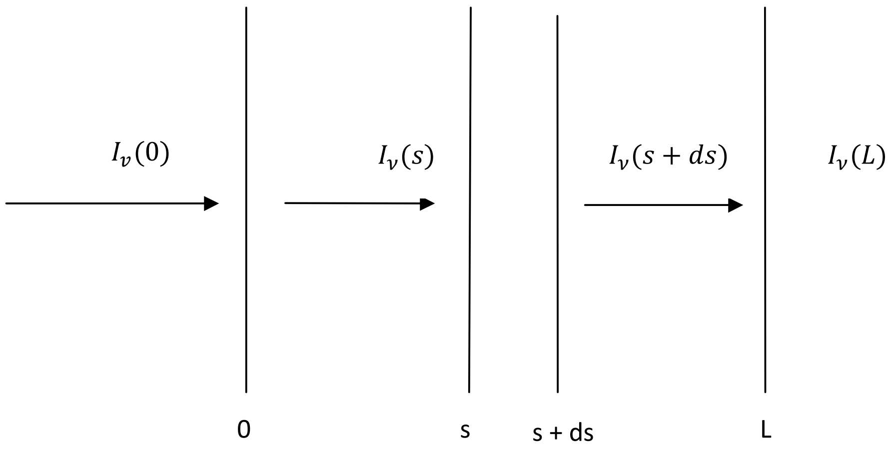

Figure 2.1

The change in radiation over this thin layer can be seen as being very small compared to I_ν(s), so that it can be said,

$$dI_\nu \equiv I_\nu(s+ds) - I_\nu(s). \tag{2.1}$$

If scattering is ignored, the radiation absorbed by this thin layer will be the product of the number of molecules in the path of the radiation and the absorption per molecule. Thus, (2.1) can be written as a product of these quantities and the radiation entering the ds layer,

$$dI_\nu \equiv I_\nu(s+ds) - I_\nu(s) \approx -I_\nu(s) N_V \sigma_\nu ds, \tag{2.2}$$

where N_V is the number of molecules per cm^3 and σ_ν is the absorption cross section, which gives the absorption per molecule at a particular wavenumber in units of cm^2.

A more convenient expression for N_V written in terms of pressures and temperature can be obtained from the ideal gas law, which states that,

$$PV = NkT, \tag{2.3}$$

where P is the pressure of the gas, V is the volume, N is the number of molecules, k is Boltzmann's constant and T is temperature. From this the number of molecules per unit volume is simply,

$$N_V = \frac{P}{\mathrm{k}T}. \tag{2.4}$$

By substituting (2.4) into the RHS of (2.2) we obtain the expression,

$$dI_\nu = -I_\nu(s) \frac{P\sigma_\nu}{kT} ds. \tag{2.5}$$

Rearranging this becomes,

$$\frac{dI_\nu}{I_\nu} = -\frac{P\sigma_\nu}{kT} ds. \tag{2.6}$$

By integrating over the total path length L, as shown in figure 2.1,

$$\int_{I_\nu(0)}^{I_\nu(L)} \frac{dI_\nu}{I_\nu} = -\int_0^L \frac{P\sigma_\nu}{kT} ds. \tag{2.7}$$

Solving this equation allows us to define the optical depth τ_ν of layer L as the natural logarithm of the outgoing divided by the incoming radiation. This is also equal to the number of molecules multiplied by the absorption cross section along that path,

$$\tau_\nu(L,P,T) = \frac{P\sigma_\nu}{kT} L = -\ln\left(\frac{I_\nu(L)}{I_\nu(0)}\right). \tag{2.8}$$

Another useful quantity to define is transmittance $T(0,L)$, which is the ratio of outgoing to incoming radiation from the layer. Thus for a layer of thickness L,

$$T(0,L) = \frac{I_\nu(L)}{I_\nu(0)} = \exp(-\tau_\nu). \tag{2.9}$$

2.2. Molecular transitions

In simple terms, molecular absorption can be seen as the process of transferring energy from a photon into the motion of a molecule. In a classical sense one would expect molecules to absorb all energies of photons. However, as the physics of the atom are subject to the laws of quantum mechanics this is not the case. The Schrödinger equation tells us that molecules will only absorb photons with very specific amounts of energy. These levels are defined by both the solutions of the Schrödinger equation and by selection rules which govern which solutions are allowed. A more detailed discussion of molecular absorption can be found in numerous textbooks such as, Goody and Yung (1989) and Atkins (2005).

There are three sorts of transitions that can occur when a photon interacts with a molecule; electronic, vibrational and rotational. Electronic transitions happen when the absorption of the photon causes an electron to change its orbit. These transitions require the most energy to occur and are normally associated with absorption of visible and UV photons beyond 20,000 cm^{-1}.

The bonds between molecules are such that the constituent atoms are always in motion relative to each other. Vibrational transitions occur when the absorption causes this motion to change and is associated with the mid-infrared up to the UV region (~1000 cm^{-1} to ~20,000 cm^{-1}).

Finally, molecules also rotate about their axes. Photons can cause this motion to change. These transitions require the lowest energy of the three and normally associated with the mid and far infrared region (~<1000 cm^{-1}).

To get an exact solution to the Schrödinger equation, the motion of every electron and atom making up a molecule has to be taken into to account. To solve the Schrödinger equation for all but the simplest of atoms would be too complicated. For this reason the assumption is made that the wave function of each sort of motion can be treated independently (e.g. Atkins 2005). That is to say that the wave function can be written as a product of each of these components as,

$$\Psi_{total} = \psi_{rotational}\psi_{vibrational}\psi_{electronic}. \tag{2.10}$$

This allows each component to be solved separately, resulting in a solution to the Schrödinger equation,

$$E_{total} = E_{rotational} + E_{vibrational} + E_{electronic}. \tag{2.11}$$

As this work is concerned with the spectral region between 1200 and

8000 cm^{-1} the electronic component of the wave function can be neglected. However, the rotational energies are still important, because the observed transitions are the sum of changes in both the vibrational and rotational energies. The solution to the Schrödinger equation for both vibrational and rotational transitions will now be considered in more detail and related to the water molecule.

2.2.1. Vibrational transitions

Each bond in a molecule can be approximately modelled as a simple harmonic oscillator (SHO). It is a well known result from quantum mechanics that the solution to the Schrödinger equation for a one dimensional SHO is (e.g. Phillips 2003)

$$E = \frac{h\nu_k}{c}\left(n + \frac{1}{2}\right), \tag{2.12}$$

where n is the vibrational quantum number c is the speed of light and ν_k, expressed in unit of cm^{-1}, is determined by the strength of the bond between the two atoms. An important concept for dealing with molecular vibrations is degrees of freedom. For a molecule consisting of N atoms there are a total of 3N degrees of freedom. Three degrees of freedom relate to the translational motion of the molecule and another three relate to the rotation of the molecule (2 in the case of a linear molecule). The remaining 3N – 6 (3N-5 for a linear molecule) degrees of freedom left are vibrational modes. For a water molecule this means there are 3 vibrational degrees of freedom. Each degree of freedom will have its own SHO motion. Hence, the total vibrational energy is the sum of SHO relating to each degree of freedom,

$$E_{vibrational} = \sum_{k}^{3N-6} \frac{h\nu_k}{c}\left(n_k + \frac{1}{2}\right). \tag{2.13}$$

The transitions from one energy level to another are governed by the selection rule,

$$\Delta n_k = \pm 1. \tag{2.14}$$

This means that each SHO solution is only allowed to change by a single quanta, such that,

$$\Delta E_{vibrational,k} = hw_k. \tag{2.15}$$

In reality the assumption that the vibrational structure of a molecule can be modelled using a SHO is not a very good approximation for a lot of molecules. The Morse potential (Morse 1929) is used to define the bonds between the atoms more realistically. This potential accounts for the fact that real bonds have an anharmonic component and a dissociation energy. Solving the Schrödinger equation using the Morse Potential gives energy levels of,

$$E_{vibrational} = \sum_{k}^{3N-6} \frac{h\nu_k}{c}\left(n_k + \frac{1}{2}\right) - \frac{h\nu_k}{c}\left(n_k + \frac{1}{2}\right)^2 x, \tag{2.16}$$

where x is,

$$x = \frac{h\nu_k}{4D_e c}, \tag{2.17}$$

and D_e is the dissociation energy of the bond.

There are no selection rules for the Morse potential, unlike for the SHO. This allows what are known as vibrational overtone spectra to occur, which are spectral lines resulting from transitions of greater than one quantum. So the energy change can be written as,

$$\Delta E_k = \frac{\mathrm{h}}{\mathrm{c}}(\Delta n_k \nu_k - \Delta n_k x \nu_k) \tag{2.18}$$

For a water molecule each k can be seen as referring to a mode of vibration of the whole molecule. These three motions are bending, asymmetric stretching and the symmetric stretching and are shown in Figure 2.2.

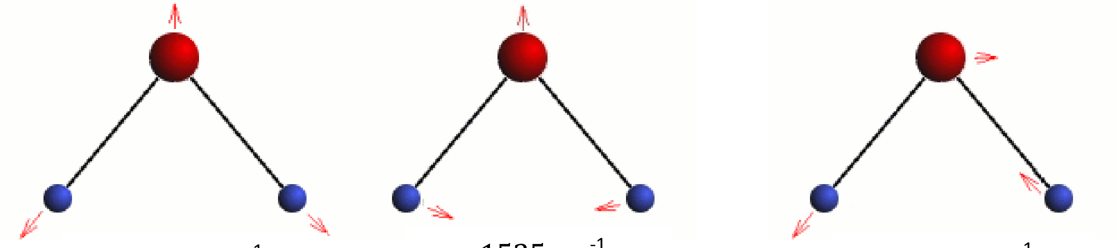

ν_1 = 3657 cm^{-1}
Symmetric stretch

ν_2 = 1525 cm^{-1}
Bending

ν_3 = 3736 cm^{-1}
Asymmetric

Figure 2.2 The three different motions of the water molecule associated with each vibrational mode. From Tennyson et al. (1998).

2.2.2. Rotational transitions

The rotational spectrum exists due to a change in the angular momentum of a molecule. Consider that a molecule can be seen to have moments of inertia I_a , I_b and I_c about three independent axes. Values of these depend upon the structure of the molecule. For a single atom then, practically its entire mass is centred on the nucleus, which on a molecular level can be considered a point mass. Thus, we can say that $I_a = I_b = I_c \approx 0$. For, a simple diatomic molecule, like CO, the distance between the atoms is enough for the moment of inertia to be significant. An axis of rotation is defined through the two atoms (I_c). Two other axis can be defined perpendicular to this, and can be seen as having an equal moments of inertia ($I_a = I_b$). I_c has a similar moment of inertia as there would be through the nucleus of an atom and therefore can be approximated to zero. However, the moments of inertia through the other two axes are clearly significant on a molecule scale.

The energy level at which absorption occurs is determined by the magnitude of the angular momentum (L) of the molecule. Classically this is defined as,

$$L = Iw, \tag{2.19}$$

where the amount of energy absorbed is,

$$E = \frac{L^2}{2I}. \tag{2.20}$$

In quantum mechanics (e.g. Phillips, 2003) this has the discrete form of,

$$L = \frac{h}{2\pi}\sqrt{J(J+1)}, \tag{2.21}$$

and,

$$E = \frac{J(J+1)h^2}{8\pi^2 I}. \tag{2.22}$$

Where

$$J = \pm 1$$

Quantum mechanics selection rules tell us that J can only change by ±1. Thus, if we are looking at a change in energy from one J value to the next it can be seen that,

$$\Delta E = 2B(J+1), \tag{2.23}$$

where,

$$B = \frac{h^2}{8\pi^2 I}. \tag{2.24}$$

This tells us that for a simple diatomic molecule, the spectra should consist of equally spaced lines. The result also applies for any linear molecule, as its moment of inertia has similar properties to a diatomic molecule.

So far this analysis has assumed that a molecule is a rigid rotor and hence its shape is not affected by its rotation. In reality this is not the case, as the bonds between the molecules are affected by the rotation of the molecule. From the frame of reference of the molecule, centrifugal force can be seen as pulling the bonds apart due to the speed of rotation. For this a correction is applied such that (e.g. Goody and Yung 1989),

$$\Delta E = 2B(J+1) - DJ^2(J+1)^2, \tag{2.25}$$

where

$$D = \frac{h^4}{32\pi^4 I^2 r^2 k}. \tag{2.26}$$

Here r is the inter-atomic bond length and k is the force constant of the inter-atomic bond. In these examples for a linear molecule we can assume that we are interested effectively in the moment of inertia about one axis only. For this reason only one rotational quantum number J is required in to describe its change in energy. A more complex molecule, like water, has 3 unique moments of inertia. A molecule which has three unique moments of inertia is called an asymmetric top. The moment of intertia about each axis will have its own set of quantum numbers.

For these molecules there are simultaneous changes in more than one quantum number at a time. This results in very complex and irregular spectrum, like that seen for water vapour. In fact if the total value of angular momentum is J there are 2J+1 different sorts of motion (e.g Goody and Yung, 1989) relating to that state. Each of these sub-states are designated using the pseudo quantum numbers κ_a and κ_c which represent the projection of the total angular moment about the a and c axis respectively. Each state is labelled as J_{κ_a,κ_c}. Figure 2.3 shows the positions and intensities of the water molecule transitions for the spectral region studied in this thesis. Distinct bands resulting from different vibrational transitions can be observed, along with the highly structured and irregular component caused by the rotational transitions.

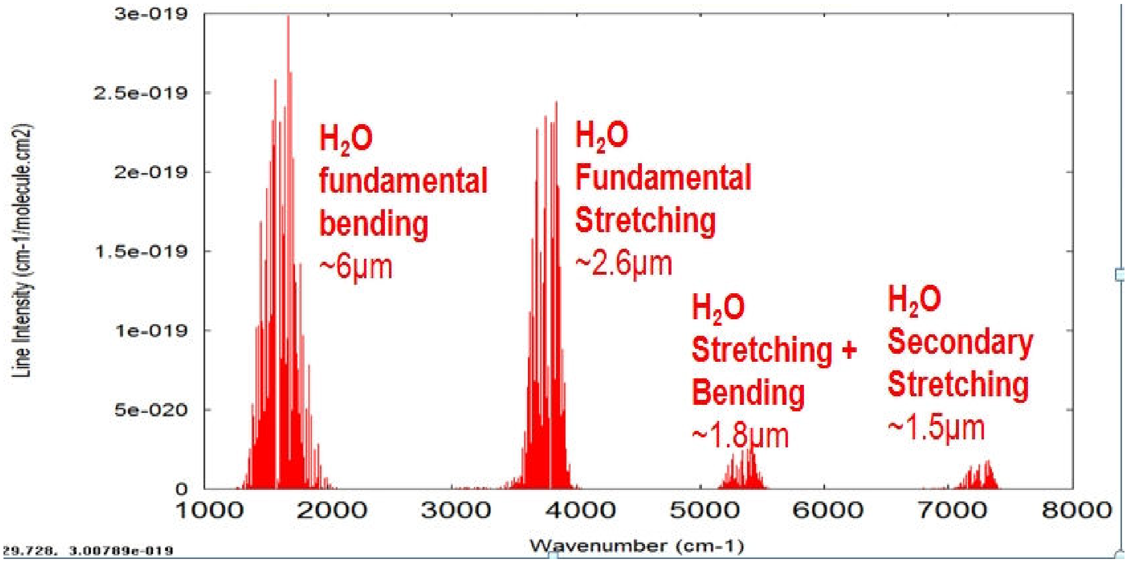

Figure 2.3 The position and strengths of water molecule transitions for the region investigated in this work as obtained from the HITRAN 2004 database (Rothman et al., 2005). Each band of lines is the result of different vibrational motions. The structure within each band is due to rotational transitions. The wavelength of each band is also indicated.

2.2.3. Population of states

Absorption line intensity is determined by the number of molecules in the lower energy state of that transition and the change of the dipole moment associated with that transition. Obviously the first parameter is important as it tells us how many molecules are in a ready state for a particular transition to occur. This can be dealt with statistically by considering there are N molecules, and we want to know how many of those molecules (N_i) have an energy E_i above the ground state of the molecule. It can be shown that (e.g. Liou, 2002)

$$\frac{N_i}{N} = \frac{g_i exp\left(-\frac{c_2 E_i}{T}\right)}{\sum_i^N g_i exp\left(-\frac{c_2 E_i}{T}\right)} = \frac{g_i exp\left(-\frac{c_2 E_i}{T}\right)}{Q(T)}. \tag{2.27}$$

Here g(i) is the degeneracy of state, $c_2 = \frac{hc}{k}$ = 1.438 cm K, and Q(T) is the partition function which is defined by,

$$Q(T) = \sum_i^N g_i exp\left(-\frac{c_2 E_i}{T}\right). \tag{2.28}$$

It can be split into three components, each relating to different sorts of transitions:

$$Q(T) = Q(T)_{(e)lectronic}\, Q(T)_{(v)ibrational} Q(T)_{(r)otational}. \tag{2.29}$$

However, at the temperatures at which this study has been conducted (296 K to 351 K) it has been shown (Marcus and Tennyson 2000) that for water only $Q_r(T)$ has a value significantly above unity. The rotational partition function is the sum of all of the rotational states:

$$Q_r = \sum_i^N g_{n_i}(2J+1)\exp\left(-\frac{c_2 E_i}{T}\right). \tag{2.30}$$

where g_n is determined by spin state statistics and takes a value of either 0.25 or 0.75 depending on the transition.

2.3. The dipole moment

Whilst the population of states determines how many molecules are in a state to accept a photon, the dipole moment determines how much energy a particular transition will absorb. The dipole moment for a molecule is given by (e.g. Atkins 2005),

$$\boldsymbol{\mu} = \sum q_i r_i. \tag{2.31}$$

It is a measure of the distribution of charge about the axis of rotation. It is this charge that a photon will interact with. In simple terms the greater the dipole moment the more photons that can interact with a single molecule. Some molecules, like N_2 have no net dipole moment and thus do not absorb any electromagnetic radiation by this mechanism. Others, like CO_2 also have no net dipole moment, but the motion resulting from vibrational transitions produces a temporary dipole moment. For this reason CO_2 has a ro-vibrational, but no pure rotational spectra. Water vapour has a permanent dipole moment and thus exhibits both a rotational and ro-vibrational structure.

As different states will have different sorts of motion associated with them the dipole moment will vary dramatically for different transitions. An arbitrary transition i which involves the molecule changing from a state described by wave function Ψ_m to that described by Ψ_n has an associated dipole moment called a transition moment (R^i), which can be obtained from (e.g. Thorne et al. 1999),

$$R^i = \int \Psi_m \boldsymbol{\mu} \, \Psi_n dv. \tag{2.32}$$

We are now in a position to define the strength of a spectral line at a temperature T as the product of the number of molecules in the lower energy state of the transition being observed, as given in equation (2.27), and the strength of dipole transition moment as,

$$S_i(T) = A_i \frac{g_i exp\left(-\frac{c_2 E_i}{T}\right)}{Q(T)} R^i, \tag{2.33}$$

where Q(T) is the partition function, E_i the lower state energy of the transition and A is given by,

$$A_i = \frac{8\pi^3}{3hc} v_i \left[1 - \exp\left(-\frac{c_2 v_i}{T}\right)\right] \approx \frac{8\pi^3}{3hc} v_i. \tag{2.34}$$

The exponential term corrects for stimulated emission which occurs in the far infrared. However, for the spectral regions studied in this work this can be regarded to have a value of one. The other constants convert S into unit of absorption of $cm^{-1}/(molecule.cm^{-2})$.

2.4. Line shape

Whilst the Schrödinger equation predicts that absorption from a spectral line should occur at an exact wavenumber in reality the absorption resulting from any transition is spread out over wavenumber space. The absorption cross section at any point in the spectrum v, is a product of the line strength S centred at v_i multiplied by a normalised line shape function f such that,

$$\sigma(v) = S(v_i) f(v - v_i). \tag{2.35}$$

There are three main mechanisms which cause this broadening; natural, Doppler and collisional broadening. Each will now be discussed.

2.4.1. Natural broadening

When absorption occurs, a molecule only remains in an energetically excited state for a finite time before spontaneous emission occurs. According to the Heisenberg Uncertainty Principle, this finite amount of time relates to an uncertainty in the energy of that state given by,

$$\Delta t \Delta E \approx \frac{h}{2\pi}. \qquad (2.36)$$

It can shown (e.g. Thorne et al. 1999) that this results in a Lorentzian line shape of the form,

$$f(\nu - \nu_{\mathrm{i}}) = \frac{\alpha_N}{\pi((\nu - \nu_{\mathrm{i}})^2 + \alpha_N^2)}, \qquad (2.37)$$

where ν_i is line centre, α_N line and the natural broadening half-width i given by,

$$\alpha_N = \frac{h}{4\pi\Delta t}. \qquad (2.38)$$

2.4.2. Doppler Broadening

Doppler broadening occurs because an absorbing molecule has motion relative to the radiation source. Hence, consider that the wavenumber (ν) 'seen' by a molecule at speed V is shifted compared to that observed by a stationary observer (ν_i) such that,

$$\nu = \nu_i \left[1 + \frac{V}{c}\right]. \qquad (2.39)$$

The velocities of molecules in equilibrium obey the Maxwell Boltzmann distribution. This states that the probability of a molecule of mass m, having a particular velocity V at temperature T is given by,

$$p(V)dV = \sqrt{\left(\frac{m}{2\pi KT}\right)} \exp\left(-\frac{mV^2}{2kT}\right) dV. \qquad (2.40)$$

By substituting (2.39) into (2.40) an expression for the distribution of line centres can be obtained:

$$f(\nu - \nu_i) = \sqrt{\left(\frac{m}{2\pi kT}\right)} \exp\left(-\frac{mc^2}{kT}\left(\frac{\nu - \nu_i}{\nu_i}\right)^2\right). \qquad (2.41)$$

Where the half width half maximum is,

$$\alpha_D = \nu_i \sqrt{\left(\frac{2kT}{mc^2}\right)}. \qquad (2.42)$$

Due to the temperature and wavenumber dependence, the value for α_D varies over the region in which this thesis is interested from a minimum of 0.002 cm^{-1} at 1200 cm^{-1} and 296 K to a maximum of 0.012 cm^{-1} at 8000 cm^{-1} and 351

K.

2.4.3. Collisional Broadening

Collisional broadening occurs because a molecule in the process of absorbing or emitting a photon collides with another molecule before spontaneous emission occurs. This leads to a reduction in the lifetime of a transition and thus a corresponding uncertainty. The probability of a molecule undergoing a collision obeys Poisson's law, such that the number of molecules that have experienced a collision after time t is (e.g. Thorne et al. 1999),

$$N(t) = NExp\left(-\frac{t}{t_0}\right), \tag{2.43}$$

where t_0 is the average time between collisions and N is the number of molecules.

Collisions are normally modelled using what is known as the impact approximation. This assumes that the duration of a collision is far less than the average time between collisions ($t_c \ll t_0$). The collision can therefore be modelled as happening at sometime t after the molecule absorbs a photon and causing an instantaneous shift in the absorbing frequency. If this collision is Fourier transformed from time space into wavenumber space, it leads to the form,

$$f_L(\nu - \nu_i) = \frac{\alpha_L}{\pi((\nu - \nu_i + \delta)^2 + \alpha_L^2)}, \tag{2.44}$$

where it can be shown that,

$$\alpha_L = \frac{1}{2\pi c t_0}. \tag{2.45}$$

And where δ is a shift in line centre caused by the collision.

The half width is inversely proportional to the time between collisions. The sooner a collision occurs after a photon is absorbed the greater uncertainty. Hence, because of an increased likelihood of a collision, α scales linearly with vapour pressure.

The self broadened half-width is normally written as the half-width at 1 atmosphere (1013 mb) and 296 K ($\alpha_{L\,i}^{0}(P_0T_0)$) multiplied by the partial pressure of the broadening gas and a product of the temperature governed by a exponent n_i.

$$\alpha_i(P,T) = \alpha_{L\,i}^{0}(P_0T_0)\left(\frac{P}{P_0}\right)\left(\frac{T_0}{T}\right)^{n_i}. \tag{2.46}$$

while,

$$\delta_i(P) = \left(\frac{P}{P_0}\right)\delta^0(P_0). \tag{2.47}$$

$\delta_i(P)$ is the shift in the line centre which is caused by collisions. The theoretical factors which determine of value of $\alpha_L^0(P_0T_0)$ and $\delta_i(P)$ are complex and beyond the scope of this work, but are discussed in more detail in Goody and Yung (1989). They are strongly affected by both the transition which is occurring at the time of the collision (i.e its value will vary from transition to transition) and the state of the colliding molecule. Indeed, for water vapour it has been found that there is strong J dependence affecting the half-width of lines. It is well known that lines with a low J value can be over an order of magnitude broader than those with a high J value. There is also theoretical evidence (Gamache and Hartmann 2004) and experimental evidence (Zou and Varanasi 2003) for there being a dependence of half width upon vibrational quantum number, although this effect is far smaller than that observed for rotational lines and is normally around 5-10%.

The nature of the molecules interacting with water makes also large difference to the broadening value. In general the half-widths for the same transition are five times larger for water-water collisions compared to water-nitrogen collisions (Rothman et al., 1996). This is due to the stronger dipole-dipole interaction present when two water molecules collide compared to when a water molecule collides with nitrogen or an oxygen molecules (See section 3.3 for more discussion). For this reason for each line the Lorentzian half-width can be considered to consist of two parts, a self broadened component and foreign broadened component such that,

$$\alpha_i(P,T) = \left(\alpha_{S\,i}^{0}\left(\frac{P_S}{P_0}\right) + \alpha_{F\,i}^{0}\left(\frac{P_F}{P_0}\right)\right)\left(\frac{T_0}{T}\right)^{n_i}. \tag{2.48}$$

2.4.4. Voigt Profile

If the degree of one broadening mechanism is substantially greater than the others, one can safely ignore the other mechanisms. For instance, one can ignore the natural broadening process in the atmosphere, as the Doppler and Lorentzian half-widths will always be greater. However, quite often there exists a situation where both Doppler broadening and collisional broadening half-widths are comparable. In this case near the line centre the line will exhibit a Gaussian like shape associated with Doppler broadening, whilst away from the line centre it will exhibit a Lorentzian like shape. This is because the Lorentzian line shape falls off far slower with wavenumber and thus will always dominate away from the line centre.

To accurately predict the line shape a convolution between the two sorts of line shape has to be calculated. This convolution is known as the Voigt line shape. However, as there exists no exact solution to this convolution, numerical approximations have been developed (Herbert 1974; Drayson 1976; Pierluissi et al. 1977).

2.5. Line by Line calculations

Using the expressions derived in the last three sections it is now possible to derive an expression for the optical depth of a molecule along a homogenous path. As will be seen for this work most of the time it is safe to assume a Lorentzian line shape. In this case the optical depth (τ_H) of an absorber at pressure P_s, Temperature T and path length L will be given by,

$$\tau_{\mathrm{H}}(\mathrm{P_s},\mathrm{T},\mathrm{L}) = \frac{P_S L}{kT}\frac{\mathrm{Q_r(T_0)}}{\mathrm{Q_r(T)}}\sum_{i=1}^{N}\frac{\exp\left(-\frac{c_2 E_i}{T}\right)}{\exp\left(-\frac{c_2 E_i}{T_0}\right)} S_i(T_0,\nu_i)\frac{\alpha_{L_i}}{\pi\left((\nu-\nu_i+\delta_i)^2+\alpha_{L_i}^2\right)} \tag{2.49}$$

where,

$$\alpha_{L_i}(P,T) = \left(\alpha_{S\,i}^0\left(\frac{P_S}{P_0}\right) + \alpha_{F\,i}^0\left(\frac{P_F}{P_0}\right)\right)\left(\frac{T_0}{T}\right)^{n_i}, \tag{2.50}$$

Where P_0 = 1.0 atm (1013 mb) and T_0 = 296 K. N refers to the number of spectral lines which are present. There are numerous line-by-line (LBL) codes which exist that calculate optical depth. For this work the Reference Forward Model (RFM (Dudhia 2005)) line-by-line code was used, along with a basic line by code based on (2.49). It is general convention to calculate the contribution for each line out to 25 cm^{-1} away from the line centre. These line-by-line calculations require the input of spectral lines catalogues which provide S_i , α_S^0 , α_F^0 etc. This work uses the HITRAN 2004 database (Rothman et al., 2005) which is discussed in more detail in section 3.3.

2.6. The water vapour continuum

If the optical depth of water vapour is calculated using a line-by-line code as described above, it is found that there are substantial differences between the calculated optical depth and that observed, which cannot be explained by experimental errors. This difference is known as the water vapour continuum. Its history and properties will now be discussed. A more detailed discussion can be found in, for example, Ptasnhik et al. (2008) and Ma and Tipping (1999).

The water vapour continuum was first mentioned by Hettner (1918) as absorption observed between 700 and 1200 cm^{-1} attributed to water vapour, but occurring away from the band centres. It was not until 20 years later that Elsasser (1938) suggested that this absorption could be the result of a contribution far from the line centres of strong water vapour lines. Since then there have been numerous measurements which have identified continuum like absorption. Most have focused on the atmospheric window between 700 and

1200 cm^{-1} (Bignell 1970; Roberts et al. 1976; Montgomery 1978; Dianovklokov et al. 1981; Cormier et al. 2005), some have also detected continuum like absorption in various near infrared regions between 1200 cm^{-1} and 5600 cm^{-1} (Burch 1982; Burch 1984; Burch 1985; Tobin et al. 1996; Ptashnik et al. 2004)

All measurements of the continuum in the atmospheric windows show it to be smooth and gradually decreasing away from the band centres. Nearer the band centre the measured absorption is greater than that predicted using a Lorentzian line shape extending to infinity. However, at greater distances away from the band centre the measured absorption is less than that predicted using a Lorentzian line shape. The measurements in the bands have shown the continuum to have more structure. Here, the continuum is derived in the narrow windows between the lines, which are referred to as micro-windows. This is because even at very low pressures the line centres in most of the water bands are saturated. In the bands the continuum can vary quite significantly from one micro-window to the next, but is always greater than that predicted using the Lorentzian line shape. In general the continuum absorption is greatest where the monomer absorption is strongest. An example of the continuum derived in the micro-windows is shown in Figure 2.4. Here the large difference between the measured and calculated spectra can be observed.

As measurements of the continuum have demonstrated, it can be broken down into two components; the self and the foreign. Only the self continuum is observed when there is just pure water vapour present, whilst both the foreign and self is observed when water vapour is mixed with other atmospheric gases. In all of the aforementioned studies the optical depth of the foreign continuum has been observed to scale with the product of the vapour pressure added to the sum of the pressures of the foreign broadening gases. The optical depth of the self continuum has always been observed to scale with the square of the vapour pressure.

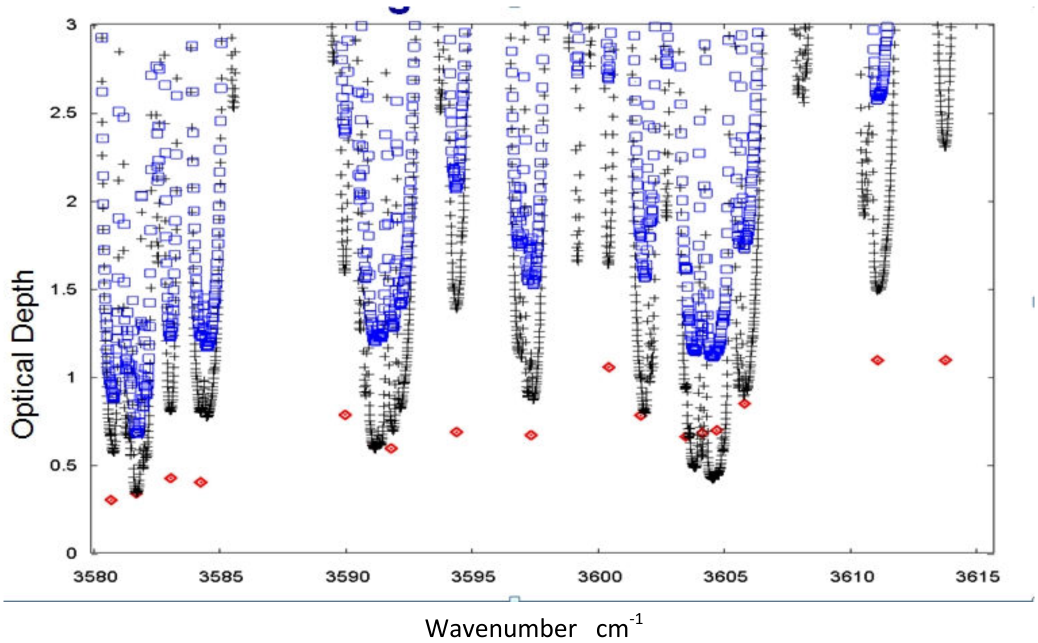

Figure 2.4 An example of the optical depth predicted by a line by-line code (black crosses) compared to that measured (blue squares). The continuum (red diamonds), derived in the micro-windows between the line centres, is defined simply as the difference between the two.

The optical depth of the self continuum is greater than the foreign given the same amount of absorbing gas. For example the optical depth of the self continuum observed with 5 mb of pure water vapour, will be greater than that from the foreign continuum of 5 mb of water vapour mixed with 5 mb of atmospheric gas. The amount by which the self continuum has been measured to be greater than the foreign varies from as little as 5 times more in the band centres to than 500 times more between the major absorbing bands (Burch 1982; Burch 1984; Burch 1985; Tobin et al. 1996; Cormier et al. 2005).

Another key difference is the temperature dependence. Measurements have revealed the that the self continuum has a strong negative exponential temperature dependence (Roberts et al. 1976; Montgomery 1978; Burch 1984; Ptashnik et al. 2004; Cormier et al. 2005). The exact strength of this dependence is observed to vary throughout the spectrum and is greater between the bands than in the band centres. The foreign continuum has been observed to have a much weaker temperature dependence, which does not appear to vary spectrally (Burch 1984; Cormier et al. 2005).

So far there have been three separate theories put forward to explain the continuum. These are far wings theories, collision induced absorption and water complex theories. Each of these will now be discussed in turn.

2.7. Lorentzian correction theories

These theories consider that modelling the interaction between water molecules using the Lorentzian line shape is not adequate.

2.7.1. CKD model

The work of Clough Kneizys and Davis (1989) represents the first attempt, to develop a method which explains continuum absorption by changing the Lorentzian line shape. The CKD continuum has been superseded by the MT_CKD continuum, which, as will be discussed, explains the continuum using collision induced absorption. However, it is still instructive to outline the CKD theory as it introduces numerous concepts used when defining the continuum.

The CKD model changes the Lorentzian line shape using what is known as the χ function. It considers that continuum absorption results from an adjustment to the Lorentzian line shape at a distance away from the line centre, where it can be said,

$$(v - v_i)^2 \gg \left({\alpha^0_S}_i \left(\frac{P_s}{P_0} \right) + {\alpha^0_F}_i \left(\frac{P_F}{P_0} \right) \right)^2 . \tag{2.51}$$

It also assumes that a LBL code will only calculate the line absorption out to 25 cm^{-1} away from the line centre and therefore any absorption beyond this resulting from a line also have to be explained by the continuum. Away from the line centre where equation (2.51) holds, the Lorentzian line shape used in a LBL code can be split into self $f_{L_s}(v - v_i)$ and foreign broadened $f_{L_F}(v - v_i)$ components. We can define the Lorentzian line shape used in a LBL code as,

$$\begin{aligned} f_L(v - v_i) &= \underbrace{\frac{\alpha^0_{Si}\left(\frac{P_S}{P_0}\right)\left(\frac{T_0}{T}\right)^{n_i}}{\pi(v - v_0)^2}}_{f_{L_S}(v - v_i)} + \underbrace{\frac{\alpha^0_{Fi}\left(\frac{P_F}{P_0}\right)\left(\frac{T_0}{T}\right)^{n_i}}{\pi(v - v_0)^2}}_{f_{L_F}(v - v_i)} \qquad |(v - v_i)| < 25 \text{ cm}^{-1} \\ f_L(v - v_i) &= 0. \qquad |(v - v_i)| \geq 25 \text{ cm}^{-1} \end{aligned} \tag{2.52}$$

The correction which CKD makes to the line shape inside of 25 cm^{-1} can be seen as adding extra absorption to the line. Beyond 25 cm^{-1}, where no absorption is defined before, it predicts the absorption as a Lorentzian function multiplied by the χ function. To account for the fact that the self and foreign continua are different, there is a χ_s function which alters the $f_{L_s}(v - v_i)$ component and χ_f function that alters the $f_{L_f}(v - v_i)$ component. Hence, when performing LBL calculations CKD suggested that instead of $f_{L_s}(v - v_i)$ line shape the $f_{CKD_s}(v - v_i)$ line shape should be used, which is defined as,

$$f_{CKD_s}(v-v_i) = f_{L_s}(v-v_i) + \underbrace{\frac{\alpha^0_{S_i}\chi_S\left(\frac{P_S}{P_0}\right)\left(\frac{T_0}{T}\right)^{n_i}}{\pi 25^2}}_{f_{\chi_S}(v-v_i)} - \underbrace{\frac{\alpha^0_{S_i}\left(\frac{P_S}{P_0}\right)\left(\frac{T_0}{T}\right)^{n_i}}{\pi 25^2}}_{f_{BASE_S}(v-v_i)} \qquad |(v-v_i)| < 25 \text{ cm}^{-1}$$

$$f_{CKD_S}(v-v_i) = \frac{\alpha^0_{S_i}\chi_S\left(\frac{P_S}{P_0}\right)\left(\frac{T_0}{T}\right)^{n_i}}{\pi(v-v_i)^2} \qquad |(v-v_i)| \geq 25 \text{ cm}^{-1} \tag{2.53}$$

Likewise $f_{CKD_F}(v-v_i)$

$$f_{CKD_F}(v-v_i) = f_{L_F}(v-v_i) + \underbrace{\frac{\alpha^0_{F_i}\chi_F\left(\frac{P_F}{P_0}\right)\left(\frac{T_0}{T}\right)^{n_i}}{\pi 25^2}}_{f_{\chi_F}(v-v_i)} - \underbrace{\frac{\alpha^0_{F_i}\left(\frac{P_F}{P_0}\right)\left(\frac{T_0}{T}\right)^{n_i}}{\pi 25^2}}_{f_{BASE_F}(v-v_i)} \qquad |(v-v_i)| < 25 \text{ cm}^{-1} \tag{2.54}$$

$$f_{CKD_F}(v-v_i) = \frac{\alpha^0_{F_i}\chi_F\left(\frac{P_F}{P_0}\right)\left(\frac{T_0}{T}\right)^{n_i}}{\pi(v-v_i)^2} \qquad |(v-v_i)| \geq 25 \text{ cm}^{-1}$$

where

$$\chi_S = 8.63\exp(-z_1^2) + (0.83z_2^2 + 0.33z_2^4)\exp(-|z_2|), \tag{2.55}$$

and

$$\chi_F = 6.65\exp(-z_3^2), \tag{2.56}$$

and at 296 K,

$$z_1 = \left|\frac{v-v_i}{400}\right| \quad z_2 = \left|\frac{v-v_i}{250}\right|, \quad z_3 = \left|\frac{v-v_i}{75}\right|. \tag{2.57}$$

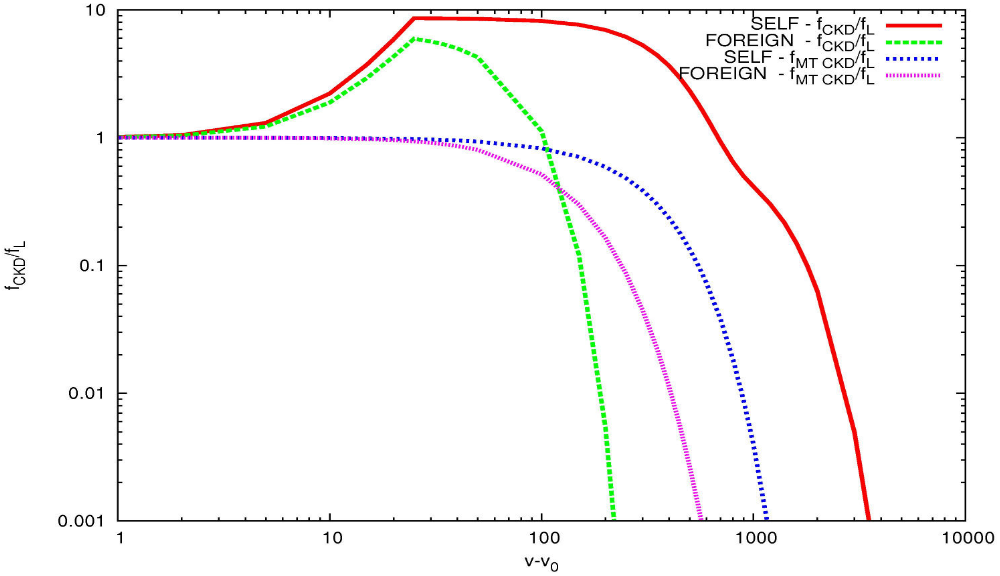

Figure 2.5 The ratio of the corrected line shapes to the Lorentzian for both CKD and MT_CKD (described in section 2.7). $\frac{f_{ckd_S}}{F_{L_S}}$ *(red),* $\frac{f_{ckd_F}}{F_{L_F}}$*(green) from CKD and* $\frac{f_{\theta_S}}{F_{L_S}}$ *(blue) and* $\frac{f_{\theta_F}}{F_{L_F}}$ *(purple) from MT_CKD.*

CKD defines the self continuum optical depth as,

$$\tau_{c_S} = \tau(f_{CKD_S}) + \tau(f_{BASE_S}) - \tau(f_{L_S}). \tag{2.58}$$

Likewise the foreign continuum is,

$$\tau_{c_F} = \tau(f_{CKD_F}) + \tau(f_{BASE_F}) - \tau(f_{L_F}). \tag{2.59}$$

In CKD, the continuum is not simply the difference between the optical depth calculated using f_{CKD} and f_{L_F}. It also includes the optical depth calculated using f_{BASE}. This term as defined in (2.53) and (2.54), is the value of the Lorentzian line shape calculated at 25 cm^{-1} from the line centre. It is called the base term, as it defines a base under each spectral line. The reason for including this term is not physical, as it is adding to the continuum something which is already explained by the Lorentzian line shape. However, the continuum is often defined as including this base term. In this thesis, unless it is explicitly specified, at no time is this base term included in the continuum.

The form of the χ function, as well as the various parameters used to fit it, have no underlying physical basis. One of the properties of the Lorentzian line shape (and indeed the Doppler line shape) is that it integrates to unity between plus and minus infinity. Physically this means that collisions cause a change in the ro-vibrational wave function, but not the in the dipole moment of the water molecule. That is to say, collisions do not result in any extra absorption occurring, but just a change in the wavenumbers over which absorption occurs. The CKD model by adding on the χ function causes the area under the line shape to be greater than unity. Hence, to have a physical basis requires that the χ function arises from a change in the dipole moment. However, there appears to be no justification for why a change in the dipole moment would result in the change in the line shape predicted by the χ function. Another possibility is that it 'borrows' some of the absorption from nearer the line centre and redistributes it further away from the line centre. This seems unlikely, as it is well known that the Lorentzian describes the line centres for water vapour accurately.

In fact the coefficients in CKD have been fitted to various measurements of Burch (1985;1984;1981) and Roberts et al. (1976). In some regions (for instance 700 -1200 cm^{-1}) this semi empirical form as defined above has been ignored completely and the continuum has been defined empirically based on measurements. The CKD continuum and the measurements to which it is fitted are summarised in Figure 2.6.

The z coefficients are fitted at 296 K and 260 K. From the continuum derived at these two temperatures the optical depth at any other temperature is defined using the empirical formula,

$$\tau_S(v,T) = \tau_S(v,296)\left(\frac{296}{T}\right)\left(\frac{\tau_S(v,260)}{\tau_S(v,296)}\right)^{\frac{296-\mathrm{T}}{36}}. \tag{2.60}$$

As the foreign continuum has a far weaker temperature dependence, it is assumed in the CKD model to be linear,

$$\tau_F(v,T) = \tau_F(v,296)\left(\frac{296}{T}\right). \tag{2.61}$$

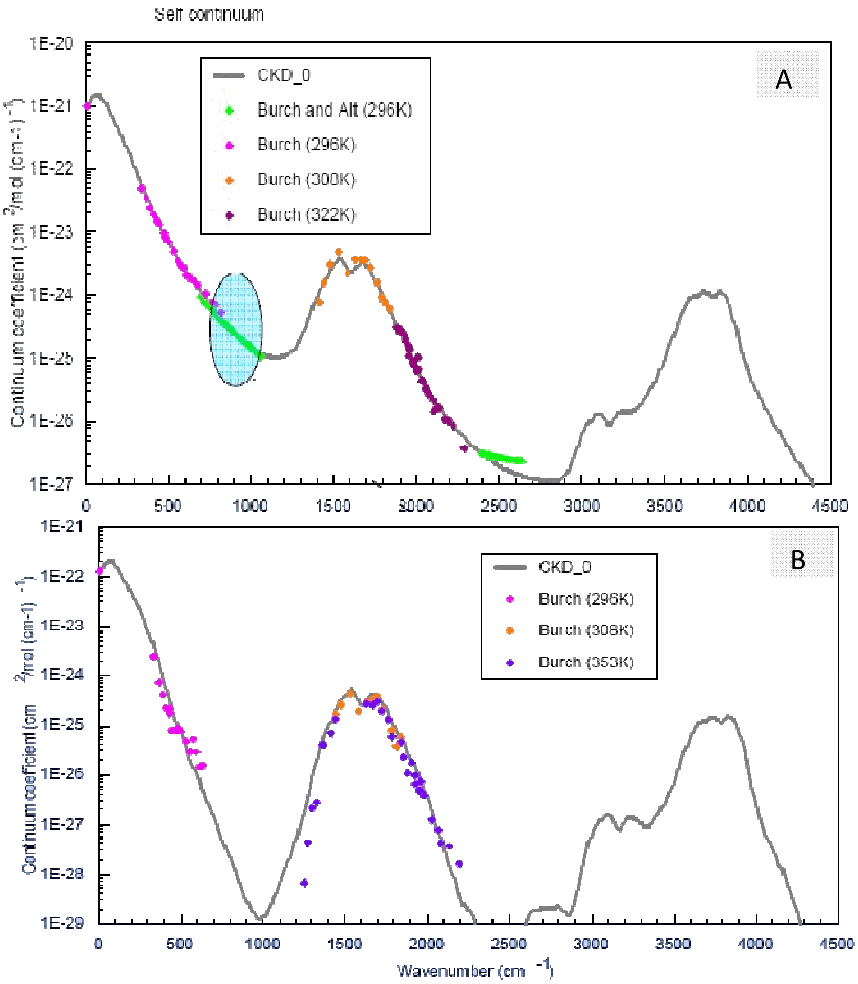

Figure 2.6 The different continuum measurement sets to which the self (panel A) and foreign (panel B) CKD model is fitted. Courtesy of Eli Mlawer.

2.7.2. Ma and Tipping

The work of Ma and Tipping (1999; 2002), attempts to formulate a more accurate line shape for the water molecule based upon physical principles. Their work attempted to model the collisions between water molecules in the far wings. The reader will recall that the Lorentzian line shape assumes that the time between collisions is far greater than the collision time itself. However, for the collisions which cause the contribution further away from the line centre this is not the case. In these regions a different formulism, the Quasi-static approximation is used(e.g. Thorne et al. 1999). This approximation assumes that a collision can be regarded as a constant perturbation throughout a transition. This causes a change in the potential of the absorbing molecule and thus the wavenumber at which the transition occurs to be constantly shifted for the lifetime of the transition. It relies on the assumption that a collision lasts long enough that each molecule is allowed to radiate at this shifted wavenumber, i.e. that the collision life time is greater than the natural lifetime.

The exact details of the Ma and Tipping approach to modelling the continuum are too detailed to deal with here. In essence, though, their model aims to explain how these collisions alter the potential of the water molecule. They show that in the far-wings the absorption must go to zero exponentially with the displacement in frequency from the line centre. Thus, if one uses a Lorentzian or Voigt profile, one would obtain too much absorption a long way from the line centre. As the quasi-static approximation is only valid in the far wings their work is of more importance explaining the sub Lorentzian nature of absorption observed far from the band centres and not the super Lorentzian absorption observed in and near the band centres. In fact in the band centres, the extra absorption predicted by Ma and Tipping is very similar to that expected by extending the Lorentzian line shape from 25 cm^{-1} out to infinity.

2.8. Collision induced absorption

Recently the CKD formulation changed to be called MT_CKD (Mlawer et al. Personal communication; Mlawer et al. 1999) This version introduced a different mechanism for explaining the continuum called collision induced absorption (CIA). CIA occurs when a collision happens at the same time as when a water molecule is absorbing a photon. This causes an additional, temporary, change in the dipole moment and thus to more absorption occurring during the collision. This phenomena is most commonly observed in molecules like N_2 (e.g. Borysow and Frommhold 1986), where due to this change in the dipole moment normally forbidden transitions are observed. However, the effect is universal. Because the lifetimes of the collisions are short, the corresponding "lines" are very broad (between 20 to 100 cm^{-1}), depending on the system.

The MT_CKD formalism still does include a correction to the Lorentzian line shape. However, unlike the CKD continuum at no point is this absorption greater than that predicted by the Lorentzian and thus is physically more realistic. In a similar fashion to the χ function a θ function is introduced. Unlike the χ function the same correction applies all of the way from the line centre to the far wings. The line shape described by MT_CKD is,

$$f_{MT\_CKD} = \underbrace{\frac{\alpha^0_{S\,i}\theta_S\left(\frac{P_S}{P_0}\right)\left(\frac{T_0}{T}\right)^{n_i}}{\pi(\nu-\nu_i)^2}}_{f_{\theta_S}(\nu-\nu_i)} + \underbrace{\frac{\alpha^0_{F\,i}\theta_F\left(\frac{P_F}{P_0}\right)\left(\frac{T_0}{T}\right)^{n_i}}{\pi(\nu-\nu_i)^2}}_{f_{\theta_F}(\nu-\nu_i)}, \tag{2.62}$$

where,

$$\theta_S = \exp\left[-\left(\frac{|\nu-\nu_i|}{310.5}\right)^{1.462}\right], \tag{2.63}$$

and

$$\theta_F = \left(1+\frac{|\nu-\nu_i|}{61.5}\right)\exp\left[-\frac{|\nu-\nu_i|}{61.5}\right]. \tag{2.64}$$

As the change in the line shape does not add extra absorption this cannot explain the continuum where there is more absorption than that predicted by the Lorenzian line shape. To explain this the CIA mechanism is introduced. The contribution from N water vapour lines to the self continuum optical depth as introduced in MT_CKD is given by,

$$\tau_{\mathrm{CIA_S}}\,(\mathrm{P_s},\mathrm{T}) = \frac{P_S L}{kT}\left(\frac{P_S}{P_0}\right)\alpha_{CIA_S}\sum_{i=1}^{N}\left(\frac{\epsilon_S(\nu-\nu_i)\varsigma_{S_i}(\nu-\nu_i)S(T_0,\nu_i)}{\alpha^2_{CIA_S}+(\nu-\nu_i)^2}\right), \tag{2.65}$$

where,

$$\epsilon(\nu-\nu_i)_S = \exp\left[-\left(\frac{(\nu-\nu_i)}{306.6}\right)^2\right], \tag{2.66}$$

and,

$$\varsigma(v-v_i)_S = 1.660exp\left(-\left(\frac{E_i}{62.77}\right)^2\right) \quad (\Delta J_i > 0)or(\,\Delta J_i = 0\ \&\ \Delta K_{a,i} > 0\,)or\ (\Delta K_{c,i} > 0\ \&\ \Delta K_{a,i}0\,) \tag{2.67}$$

$$\varsigma(\mathrm{v}-\mathrm{v_i})_{\mathrm{S}} = 1.561\exp\left(-\left(\frac{\mathrm{E_i}}{105.1}\right)^2\right). \qquad \text{all other cases}$$

E_i is the lower state energy of the transition and α_{CIA_s} = 87.72 cm^{-1}

While for the foreign continuum the CIA contribution is,

$$\tau_{\mathrm{CIA_F}}\,(\mathrm{P},\mathrm{T}) = \frac{P_S L}{kT}\left(\frac{P_F}{P_0}\right)\alpha_{CIA_F}\sum_{i=1}^{N}\left(\frac{\epsilon_F(\nu-\nu_i)\varsigma_{F_i}(\nu-\nu_i)S(T_0,\nu_i)}{\alpha^2_{CIA_F}+(\nu-\nu_i)^2}\right), \tag{2.68}$$

where

$$\epsilon(\nu-\nu_i)_F = \exp\left[-\left(\frac{(\nu-\nu_i)}{54.05}\right)^2\right], \tag{2.69}$$

and,

$$\varsigma(v-v_i)_F = 0.0658\exp\left(-\left(\frac{E_i}{255.9}\right)^2\right) \quad (\Delta J_i > 0)\ or\ (\,\Delta J_i = 0\ \&\ \Delta K_{a,i} > 0\,)\ or\ (\Delta K_{c,i} > 0\ \&\ \Delta K_{a,i} = 0\,) \tag{2.70}$$

$$\varsigma(v-v_i)_F = 0.0596\exp\left(-\left(\frac{E_i}{411.5}\right)^2\right). \qquad \text{all other cases}$$

Here α_{CIA_F} = 70.09 cm^{-1}. The philosophy behind MT_CKD is to introduce a CIA term for each water line. This additional term is calculated by assuming that each transition has an associated Lorentzian line shape with half-width defined by α_{CIA}. To make the CIA far weaker than the line absorption resulting from a transition, a scaling factor $\varsigma(\nu - \nu_i)$ is introduced which reduces the line strength by a certain factor. To obtain agreement with the observed continuum it was necessary to introduce different scaling factors for different transitions, depending on the transition's lower state energy and rotational state. It is not clear if there is any physical justification for the nature of the function. These scaling factors are also different for the self continuum and the foreign continuum to account for the difference in strength between the two. The other term $\epsilon(\nu - \nu_i)$, performs the same function as the θ function and reduces the Lorentzian contribution from CIA further away from the line centre.

For the MT_CKD the continuum is defined as,

$$\tau_{MT\ CKD_S} = (f_{\theta_S}) - \tau(f_{L_S}) + \tau_{CIA_S} + \tau(f_{base_S}). \tag{2.71}$$

$$\tau_{MT\ CKD_F} = (f_{\theta_F}) - \tau(f_{L_F}) + \tau_{CIA_F} + \tau(f_{base_F}). \tag{2.72}$$

It can be seen that unlike for the CKD continuum, the base term is not implicitly included in either formulation and is added on for the sake of convention. Figure 2.7 shows the MT_CKD foreign continuum between 0 and 2800 cm^{-1}. This demonstrates how in the band centres the CIA component dominates, whilst away from the band centre the line shape term dominates.

As with CKD, the MT_CKD continuum is fitted to measurements. Between the formulation of CKD and MT_CKD, the only new mid/near infrared measurements used were conducted by Tobin et al. (1996) between 1200 and 2000 cm^{-1}. These measurements were found to agree well with the older measurements of Burch (1981). For this reason, despite there being a change in formulation, the actual continuum predicted by MT_CKD and CKD are quite similar. In addition at wavenumbers above 2800 cm^{-1} the CKD and MT_CKD models are not fitted to any measurements and the predictions in this area are completely based upon the fitting of the parameters between 400 cm^{-1} and 2800 cm^{-1}. It should also be noted that MT_CKD has exactly the same temperature dependence as defined for CKD.

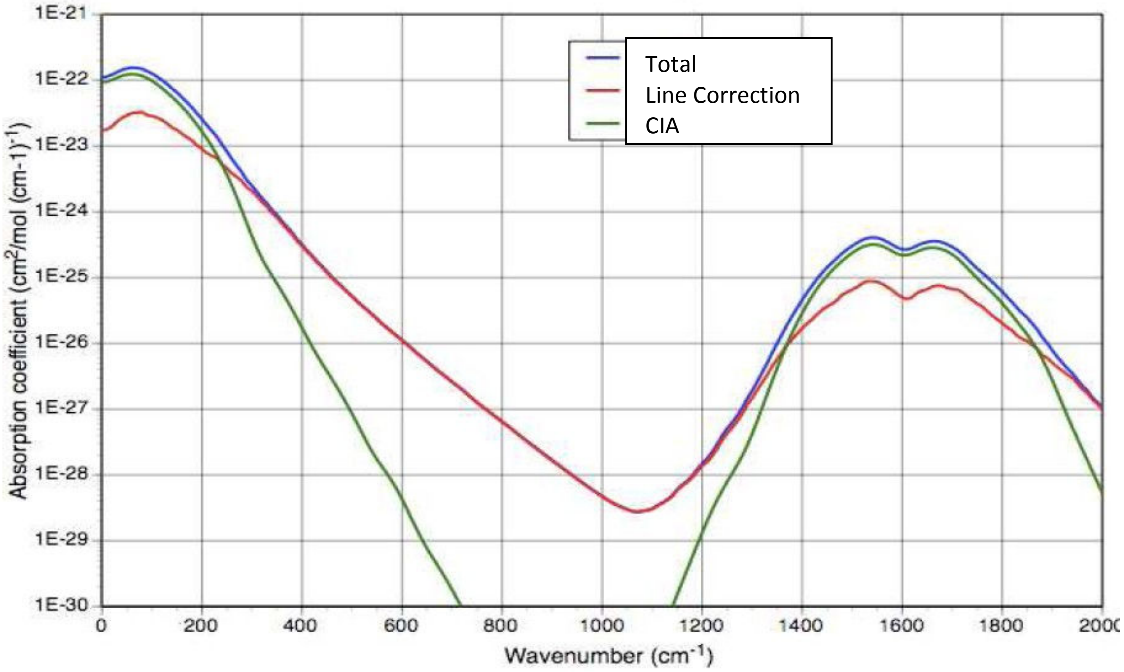

Figure 2.7 The contribution of the collision induced and line correction components to the foreign MT_CKD continuum. Courtesy of Eli Mlawer.

Whether or not CIA is a suitable mechanism to explain the continuum is still the subject of theoretical debate. Brown and Tipping (2003) have calculated the CIA contribution expected for water-nitrogen collisions in the 1200 -2000 cm^{-1} region and show it to be about an order of magnitude less than that predicted by MT_CKD. Tipping has suggested (personal communication) that a similar result would be expected for water- water collisions.

2.9. The water dimer

It was first suggested by Penner and Varanasi (1967) that the water dimer could be the major contributor to the self continuum between 700 cm^{-1} and 1200 cm^{-1}. The electronegative nature of the oxygen atom causes a water molecule to possess a permanent dipole moment, with there being a net negative charge around the oxygen atom and a net positive charge around the two hydrogen atoms. The water dimer forms when the positive charge of one of the hydrogen atoms (this water molecule is known as the donor) attracts the lone pair of electrons of the electronegative oxygen atom (this molecules is known as the acceptor) and forms a hydrogen bond. This results in the stretching of the O-H bond (OH_b) in the acceptor. A schematic of the water dimer is shown in Figure 2.8.

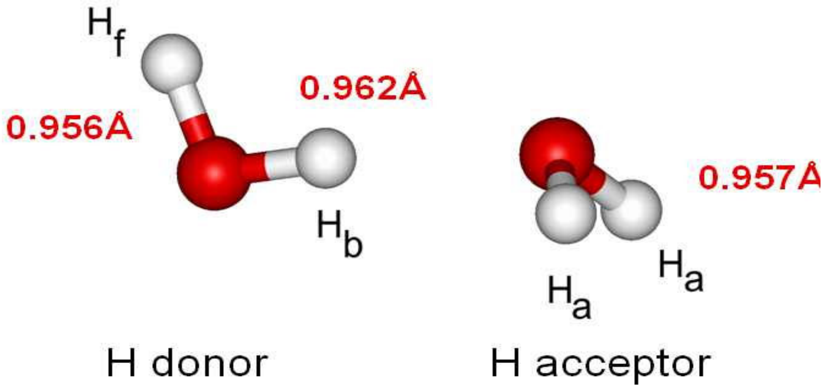

Figure 2.8 A schematic of the water dimer. The notation for the different hydrogens along with the bond lengths is shown. Note how the OH_b *bond is significantly longer than the other bonds. This results in a red shifting of the dimer spectrum compared to the water monomer. Courtesy of H. Kjaergaard.*

As only one OH bond of the acceptor is altered when a dimer is formed it is useful to consider the vibrational modes of the two OH bonds separately. The vibrational modes of the donor of the water dimer are written in the form $|x\rangle_f|y\rangle_b|z\rangle$ where b stands for hydrogen bonded bond, and f is the free bond (as shown in Figure 2.8), x is the number of vibrational quanta in the OH_f stretching mode, y the quanta in the OH_b stretching mode and z the quanta in the H_fOH_b. In the acceptor unit the hydrogens are equivalent and the notation used is $|xy\rangle_{\pm}|z\rangle$ where x and y are the number of vibrational quanta in the OH stretching mode and z is the number of bending quanta.

In typical atmospheric conditions, the water dimer concentration is less than 0.1% of the total water population and the absorption is predicted to occur in a similar area of the spectrum to that of the water molecule. For these reasons, the properties of the water dimer have largely been studied using either supersonic jets or solid matrix techniques, which create low temperature and high pressure conditions that in turn minimise the water monomer (a single water molecule) and maximise the amount of water dimer. There have been numerous studies of the water dimer in such conditions in the microwave (Fraser et al. 1989; Coudert and Hougen 1990),in the far infrared (Braly et al. 2000; Keutsch et al. 2003; Keutsch et al. 2003) and mid infrared between 1600 and 7500 cm^{-1} (Huang and Miller 1989; Huisken et al. 1996; Paul et al. 1997; Paul et al. 1999; Perchard 2001; Perchard 2001; Nizkorodov et al. 2005; Kuma et al. 2006; Kuma et al. 2007). All of these studies have shown there to be features consistent with that of water dimer.

Presently (Huang and Miller 1989; Huisken et al. 1996; Perchard 2001; Perchard 2001) have all detected features at 3600 cm^{-1} (assigned to $|0\rangle_f|1\rangle_b|0\rangle$), 3730 cm^{-1} ($|1\rangle_f|0\rangle_b|0\rangle$) and 3740 cm^{-1} ($|01\rangle_-|0\rangle$). The $|01\rangle_+|0\rangle$ transition is yet to be observed. The two fundamental bending mode transitions have also been observed by Perchard (2001) at 1593 cm^{-1} ($|00\rangle|1\rangle$) and 1610 cm^{-1} ($|0\rangle|0\rangle|1\rangle$) as well as a weaker 3190 cm^{-1} ($|0\rangle|0\rangle|2\rangle$) transition. Perchard (2001) has also measured some weaker features at 5170, 5210, 5280 and 5330 cm^{-1} that have been tentatively assigned to the $|0\rangle_f|1\rangle_b|1\rangle$, $|01\rangle_+|1\rangle$, $|01\rangle_-|1\rangle$ and $|1\rangle_f|0\rangle_b|1\rangle$ transitions respectively. Overtone spectra for some features detected by both Perchard (2001) and Nizkorodov et al. (2004) between 7000 cm^{-1} and 7300 cm^{-1}. However, there is some disagreement over the exact location and assignment of these features, but both detect features around 7200 cm^{-1} and 7240 cm^{-1}. Perhaps of greatest interest are the $|0\rangle_f|1\rangle_b|0\rangle$ and $|0\rangle_f|1\rangle_b|1\rangle$ features, as the hydrogen bond causes a considerable shift away from the main water monomer absorption and thus provides a signature by which to detect the water dimer.

Although these studies are indicators of where to expect water dimer absorption, they are not very useful for predicting the nature of dimer features in atmospheric conditions. This is firstly because they only provide information about the relative intensity of a transition, as there is no way of knowing how much water vapour is being measured. Second, because they are conducted at such low temperatures it is not known if the positions and relative intensities of the band widths detected are in any way a reflection of what would be observed in atmospheric conditions.

There have also been recent theoretical studies of the positions and band strengths in the near infrared region (Tso et al. 1998; Low and Kjaergaard 1999; Schofield and Kjaergaard 2003; Schofield et al. 2007). As the Tso et al. calculations have been largely discredited (see Vaida et al. (2000) for a discussion) we will focus on the work of Schofield and Kjaergaard (from here on referred to as S&K). The S&K dimer predictions assume that the dimer could be modelled as a harmonically coupled anharmonic oscillator. They calculate both absolute intensities and band centres of dimer transitions between 1200 and 16000 cm^{-1}. The positions and relative intensities in general were found to agree well (~30 cm^{-1}) with the measurements of Perchard (2001).

The predictions of S&K suggest that the hydrogen bond causes a red shifting which results in the $|y\rangle_b$ transitions becoming increasingly shifted away from that of the monomer at higher quanta. This prompted a study by Pfeilsticker et al (2003), which claimed to detect the $|0\rangle_f|4\rangle_b|0\rangle$ transition in atmospheric conditions, although further investigations by the same team failed to yield similar results (Lotter 2006) However, Ptashnik et al. (2004) reported measurements of the self continuum in the 5000-5600 cm^{-1} region and detected features which appear to be consistent with $|0\rangle_f|1\rangle_b|1\rangle$ and $|01\rangle_+|1\rangle$ predictions of S&K (see Figure 2.9). Ptashnik (2008) has also shown that features detected by Burch (1985) at 3600 cm^{-1} and 3730 cm^{-1} also seem to agree very well with the S&K predictions for the $|0\rangle_f|1\rangle_b|0\rangle$ and $|01\rangle_-|1\rangle$ transitions respectively. This thesis will discuss further measurement in these and additional spectral regions.

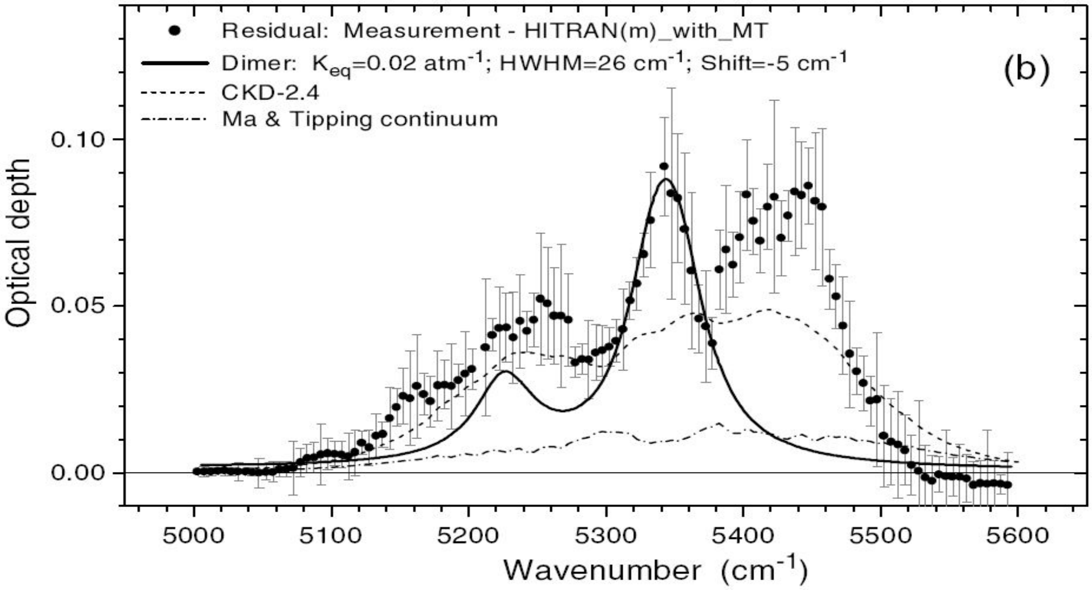

Figure 2.9 The self continuum measurements of Ptashnik et al. (2004) in the 5000-5600 cm^{-1}region compared to the predicted absorption for the water dimer, MT_CKD and Ma and Tipping continuum.

2.9.1. Optical depth of water dimer absorption

The optical depth of the water dimer can be calculated, just like that of any other absorber, as the product of the abundance and the absorption cross section:

$$\tau_d(\nu) = \frac{P_d L}{kT} \sum_{i=1}^{\mathrm{N}} f_{d_i}(T, \nu - \nu_i)\, \mathrm{S}_{\mathrm{d_i}}(T)_i, \tag{2.73}$$

where P_d is the pressure of the dimer, f_d is the line shape function, S_{d} is the line intensity and there are N absorbing dimer lines. Likewise, if the intensity ($\mathrm{S_d}$) of an arbitrary dimer line transition at a reference temperature ($\mathrm{T_0}$) is known then the intensity at a temperature (T) is,

$$S_{d_i}(T) = S_{d_i}(T_0)\frac{Q(T_0)\exp\left(-\frac{C_2E_{d_i}}{T}\right)\left[1-\exp\left(-\frac{C_2v_i}{T}\right)\right]}{Q(\mathrm{T})\exp\left(-\frac{C_2E_{d_i}}{T_0}\right)\left[1-\exp\left(-\frac{C_2v_i}{T_0}\right)\right]}, \tag{2.74}$$

where Q is the water dimer rotational partition function, C_2 is a constant with value 1.44 cm K, v_i is the position of the line centre and E_{d_i} is the lower state energy. In the near infrared region, where these measurements are made, $C_2v_i >> T$. Hence, we can state the optical depth of the dimer at a particular temperature is,

$$\tau_d(\nu,T) \approx \left(\frac{T_0}{T}\right)^{\frac{3}{2}}\frac{P_dL}{kT}\sum_{i=1}^{N} f_{d_i}(T,\nu)\,S_{d_i}(T_o)\exp\left[-c_2E_{d_i}\left(\frac{1}{T}-\frac{1}{T_0}\right)\right]. \tag{2.75}$$

Where the rotational partition function, assuming that the water dimer is a rigid rotor-harmonic can be given as,

$$\frac{Q(T_0\ )}{Q(T)} \approx (\frac{T_0}{T})^{\frac{3}{2}}. \tag{2.76}$$

2.9.2. Abundance of water dimer

In atmospheric conditions the abundance of dimers has been the subject of a great deal of theoretical debate. Before addressing this discussion it is worthwhile showing how this abundance is defined. Consider the reaction for the formation of the water dimer is,

$$H_2O + H_2O + X <=> (H_2O)_2 + \mathrm{X}, \tag{2.77}$$

where X is a molecule which takes away energy from the reaction. The equilibrium constant (K_{eq}) defines the relationship between the partial pressure of water dimer and the water monomer as (e.g. Vaida et al. 2001),

$$P_d = P_s^2K_{eq}. \tag{2.78}$$

Where K_{eq} is expressed in units of atm^{-1}.

The effect of temperature upon the value of K_{eq} can be obtained by considering the relationship between K_{eq} and the change in Gibbs free energy in standard conditions ΔG^0 (e.g. Denbigh 1981):

$$\Delta G^0 = -RTlnK_{eq}. \tag{2.79}$$

The Gibbs free energy can be defined as the difference between the change in enthalpy (ΔH^0) and entropy (ΔS^0) occurring when a water dimer is formed:

$$\Delta G^0 = \Delta H^0 - \Delta S^0T. \tag{2.80}$$

Hence, assuming that both ΔS^0 and ΔH^0 are independent of temperature, K_{eq} is

$$K_{eq} = \exp\left(\frac{\Delta S^0}{R}-\frac{\Delta H^0}{RT}\right). \tag{2.81}$$

This shows why the water dimer is attractive for explaining the self continuum; its abundance is a function of the vapour pressure squared and it has a negative temperature dependence.

Figure 2.10 compares both experimental and theoretical estimates of the equilibrium constant for atmospheric conditions. There are numerous ways to derive the equilibrium constant. Perhaps the technique most relevant to this work is that used by Ptashnik et al. (2004), who derives the equilibrium constant from measurements of the self continuum in atmospheric like conditions. Assuming that the measured continuum feature is equal to the absorption of the water dimer, by substituting equation (2.78) into (2.74) the measured optical depth can be written in terms of the equilibrium constant and water monomer pressure as,

$$\tau_{c_S}(\nu,T) = \tau_d(\nu,T) = \frac{P_s^2 L}{kT}\left(\frac{T_0}{T}\right)^{\frac{3}{2}} K_{eq} \sum_{i}^{N} f_{d_i}(T,\nu) S_{d_i}(T_o) \exp\left[-c_2 E_{d_i}\left(\frac{1}{T}-\frac{1}{T_0}\right)\right] \tag{2.82}$$

In this current form this equation is of little use for deriving the information about the water dimer from measurements of the continuum, as there are no known line lists for the water dimer and the line shape and lower state energies are not known. However, it was found that it was possible to use the band positions and strengths of S&K to fit a Lorentzian band shape to features detected in the continuum at 5240 cm^{-1} and 5230 cm^{-1} (as seen in Figure 2.9). By then making the approximation that the lower state energy is constant and assuming a value of $E_{d_{avg}}$ = 250 cm^{-1} it can shown that,

$$\tau_d(\nu,T) = \frac{P_s L}{kT} \mathrm{A(T)} \sum_{I}^{n} \frac{\alpha_{\mathrm{d,band}}}{\alpha_{\mathrm{d,band}} + (\nu - \nu_{\mathrm{i}})^2} S_{d_{band,i}} \tag{2.83}$$

where there are n dimer bands, α_{d} is the half width half maximum of the band which was fitted to be 26 cm^{-1} and,

$$A(T) = \left(\frac{T_0}{T}\right)^{\frac{3}{2}} K_{eq} \exp\left[-c_2 E_{d_{avg}}\left(\frac{1}{T}-\frac{1}{T_0}\right)\right]. \tag{2.84}$$

Hence, by obtaining a value of A(T) from fitting the S&K dimer features to agree with the measured self continuum (as seen in Figure 2.9) an estimate of equilibrium constant can be achieved. The equilibrium constant achieved using this technique was seen to agree well with values obtained by other means (see Figure 2.10).

A lower estimate of the equilibrium constant was achieved by Ptashnik et al. (2004) by using exactly the same technique, but by subtracting the MT_CKD continuum away from the measured continuum. This assumes that none of the

MT_CKD continuum is made up of the dimer absorption, which is not the option favoured by Ptashnik et al. (2004).

There have been other experimental attempts to derive the equilibrium constant. Curtiss et al. (1979) measured the thermal conductivity of steam to obtained values of ΔS^0 and ΔH^0, while Harvey and Lemmon (2004) made use of the fact that the equilibrium constant can be derived from the second virial coefficient. As most of these measurements are made at high temperatures above 360 K, there is a need to extrapolate the abundance at atmospheric temperatures. This results in a fair amount of uncertainty. Figure 2.10 shows the uncertainty in the Curtiss et al. measurements extrapolated to lower temperatures. There are also numerous theoretical estimates of the equilibrium constant (for example, Slanina and Crifo 1992; MunozCaro and Nino 1997; Scribano et al. 2006). They make use of the fact that the equilibrium constant can be written as,

$$K_{eq}(T) = \frac{VQ_{water}}{kTQ_{dimer}} \exp\left(-\frac{D_0}{KT}\right), \tag{2.85}$$

where V is the gas volume, D_0 is the dissociation energy of a complex. Q_{dimer} is the partition function of the water dimer and Q_{water} is the partition function of the water monomer. This shows that to theoretically calculate the equilibrium constant knowledge of the both the water dimer partition function and disassociation energy is required. As is discussed in Vigasin (2000), some of the theoretical uncertainty results because the temperature at which dissociation occurs is often near that of the gas temperature. Therefore, the energy states over which the partition function for the dimer is summed do not tend towards infinity and the partition function needs to be truncated. Scribano et al. (2006) have shown that including quasi bound states which exist above the disassociation energy results in a 20% increase in the value of equilibrium constant.

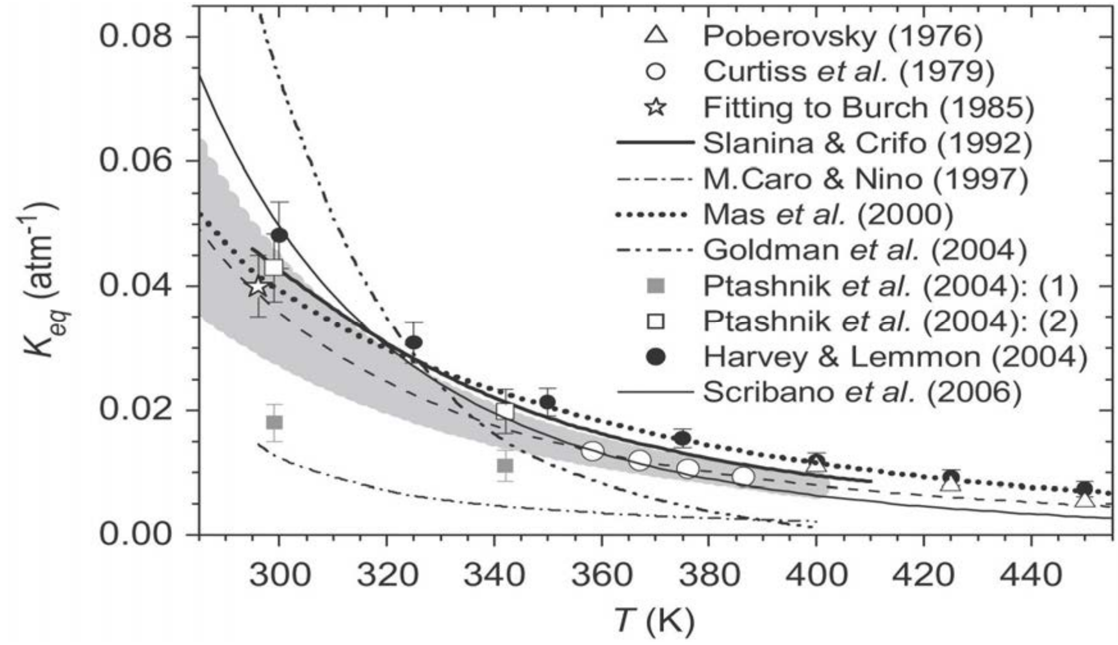

Figure 2.10 Dimerization equilibrium constant by different authors from Ptashnik et al. 2008. The symbols correspond to experimental data, while curves represent ab-initio predictions: Poberovsky spectro-photometric measurement in pressurized steam; Curtiss et al. (1979) measurement of the hot steam thermal conductivity; Fitting to the Burch continuum, performed in the current work using Water dimer band strengths from Schofield and Kjaergaard as in Ptashnik et al. (2004) ; Slanina and Crifo prediction using BGH/G pair potential; Munoz-Caro and Nino calculation ; Goldman et al. calculation, based on the rigid VRT(ASP-W)III potential; Ptashnik et al. fitting to the experimental residual obtained with and using WD band strengths from S&K; Harvey and Lemon and Mas et al. Second virial coefficients B(T), derived from experiment and from ab initio SAPT-5s pair potential respectively, are used to calculate $Keq(T)=-[B(T)-bo]/RT$*, with* $bo=38.5$ cm^3mol*; Scribano et al. calculation using flexible VRT-MCYf potential energy surface. The dashed line shows extrapolation of Curtiss et al. data as* $Keq=\exp(\Delta S/R-\Delta H/RT)$ *with the enthalpy and entropy parameters derived in* ($\Delta H^0=-3590$ cal mol^{-1}, $\Delta S^0=-18.59$ cal K^{-1} mol^{-1})*. The grey shadow represents a confidence interval for this extrapolation according to the errors in* ΔH *and* ΔS *retrieval.*

2.9.3. The dimer line shape

For the dimer to explain at least part of the water vapour continuum the broadening mechanism cannot be the result of collisional broadening. This is because it would result in a cubic dependence of optical depth upon vapour pressure in some parts of the spectra, not the squared dependence observed. Presently in atmospheric conditions individual dimer lines have not been detected. This suggests that these lines must be broad enough to merge. Indeed, Ptashnik et al. (2004) were only able to fit a band shape to the features they detected, as seen in Figure 2.9. They discovered that a Lorentzian profile with a half-width of around 30 cm^{-1} fitted well at 296 K.

There is currently no indication of the form of the dimer line shape away from the band centres. In an atmospheric sense it is most important to understand the band wings, as it is these regions where the majority of additional short wave absorption occurs (i.e. beyond what is absorbed by the monomer). It has been shown that assuming a Lorentzian band shape continues into the wings results in considerably more shortwave absorption than that currently predicted by either CKD model or Ma and Tipping (Daniel et al. 2004; Ptashnik et al. 2004).

In order to understand how the optical depth of water dimer absorption could have a partial pressure squared dependence, consider (following the terminology used in Frommhold (1993)) that when a water molecule absorbs a photon it can be classified in terms of its bound state before and after the transition. Most transitions can be classified as free-free, that is to say that the water molecule is not bound either before or after the transition. In some cases the water molecules could be in dimer state before the collision, but after the collision it is in an unbound state, these are called bound-free collisions. Some transitions are known as bound-bound, where there is a water dimer before and after the transition occurs.

Free-free transitions are those which have been dealt with so far when looking at the absorption of the water monomer and hence the dominant broadening here will be either collisional or Doppler broadening. Bound-bound collisions will be subject to both Doppler and collisional broadening. However, as noted in this case the optical depth will scale with the vapour pressure cubed and thus cannot explain the observed continuum. Bound-free transitions will have a very short life time and therefore a broad line shape. It is these which could explain the continuum, as one would expect the optical depth to scale with the square of the vapour pressure (assuming that the dissociation is caused by the absorbing of the photon rather than a collision). The exact width of the lines will be affected both by the energy of the photon being absorbed and the strength of the bond between the two water molecules. For this reason it has been suggested that higher level transitions should be very broad (many hundreds of cm^{-1}) and thus be unobservable (Suhm (2004)).

2.10. Summary of different continua

Following the example of Burch (1981), the continuum coefficient ($C(v,T)$), is used when presenting the majority of results in the next chapter. The continuum coefficient has units of $cm^2molec^{-1}atm^{-1}$. For the self continuum this is calculated from the optical depth as follows,

$$C_S(v,T) = \frac{kT\tau_{c_s}}{\mathrm{P}_s^2 L}, \tag{2.86}$$

while for the foreign continuum it can be shown that,

$$C_F(v,T) = \frac{kT\tau_{c_F}}{\mathrm{P_F} P_s L}. \tag{2.87}$$

By using the continuum coefficient the pressure dependence is removed from both continua. This is beneficial, as it allows the continuum measurements conducted at different pressures to be directly comparable (providing they are conducted at the same temperature). Figure 2.11 compares the absorption expressed in the continuum coefficient of the different continuum models discussed so far in this work between the wavenumbers of 1200 and 8000 cm^{-1}. Panel A shows the self continuum predicted by MT_CKD, CKD and the Ma and Tipping continuum along with the S&K water dimer predictions. The contribution of the Lorentzian line shape between 25 cm^{-1} and 1000 cm^{-1} from the line centre for the monomer is also shown for comparison. It can be seen that in the band centres this is very much smaller than that predicted by all of the continuum models, apart from that of Ma and Tipping. However, between the major water vapour bands the value is comparable with that predicted by the continuum models. The contribution of the base function is also shown. The reader will recall that MT_CKD and CKD continuum actually include this in the continuum. So for these continua to be directly comparable to the others this value should be subtracted. It can be seen that this only really affects the band centre and its value is generally less than 15% of the total continuum. In addition it can be seen that both versions of CKD are quite similar in the values of the continuum predicted, despite their differing mechanisms of explanation.

For the water dimer feature, a value of the equilibrium constant at 296 K of 0.04 atm^{-1} and a bandwidth of 30 cm^{-1} is assumed. This is consistent with values obtained by Ptashnik et al. (2004) when fitting to the feature at 5330 cm^{-1}. It can seen that this fitting suggests that there should be a clear difference between water dimer and the other continuum theories in the 3400-4000 cm^{-1} region (shown in Figure 2.11 panel B). This is one of the bands which is the focus of the present thesis.

Figure 2.12 shows a similar comparison for the foreign continuum. It can be seen here that the monomer Lorentzian contribution between the bands is far greater than that predicted by any continuum model. In the band centres the Ma and Tipping continuum estimate is essentially the same as that predicted by extending the Lorentzian line shape out to 1000 cm^{-1}. Once again both versions of CKD predict quite similar values for the continuum, although the CKD model does predicts consistently more absorption in all bands.

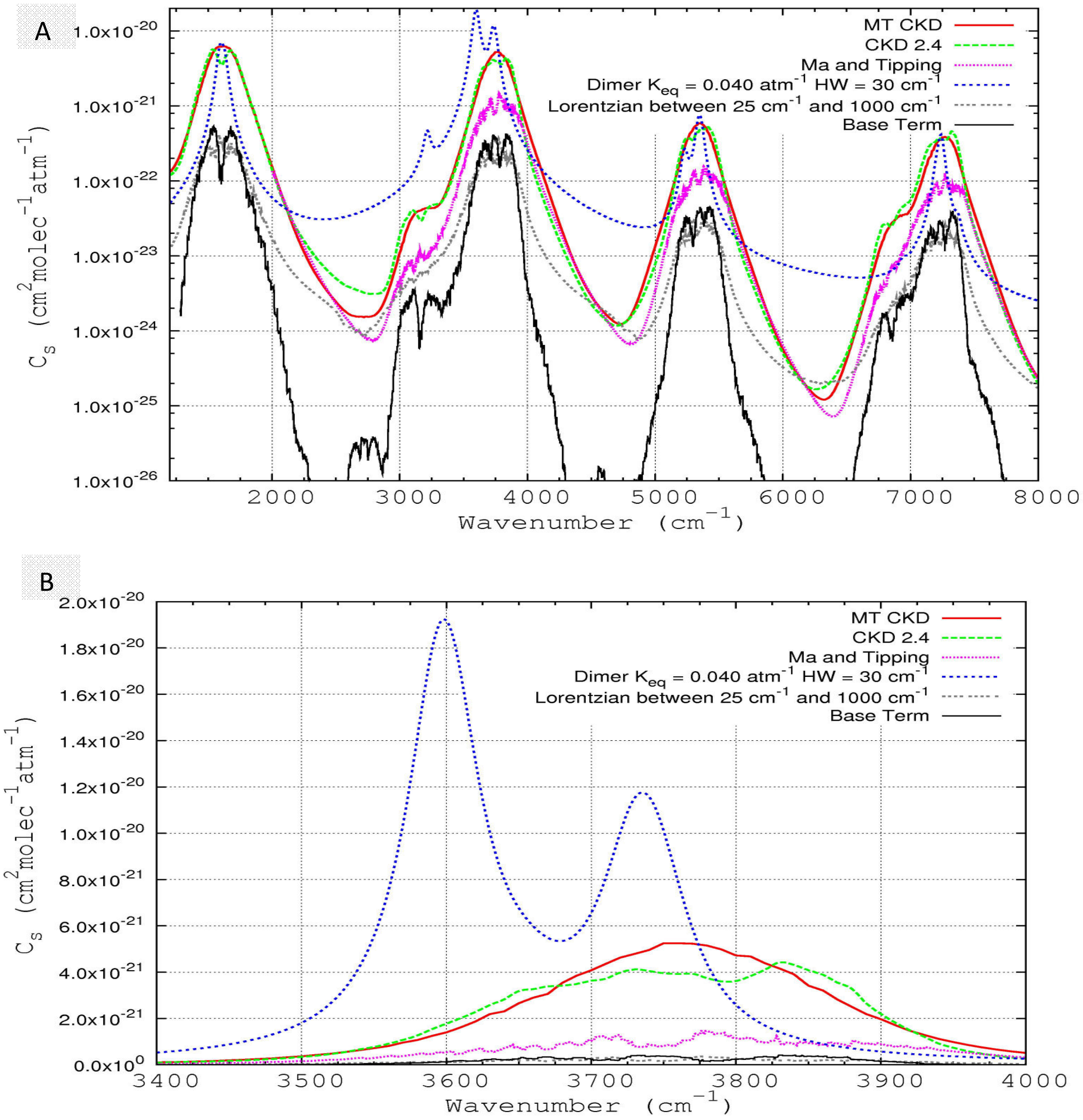

Figure 2.11 Panel A: The self continuum predicted by the various models discussed in this chapter at 296 K. The contribution of the line bases and the absorption predicted by the Lorentzian between 25cm^{-1} and 1000cm^{-1} is also shown. It should be noted that the base term is included in both the MT_CKD and CKD continuum, but not in any of the other formulations shown. Panel B: The region between 3400 and 4000 cm^{-1}, where this is a considerable difference between the predicted water dimer absorption and the other continuum models.

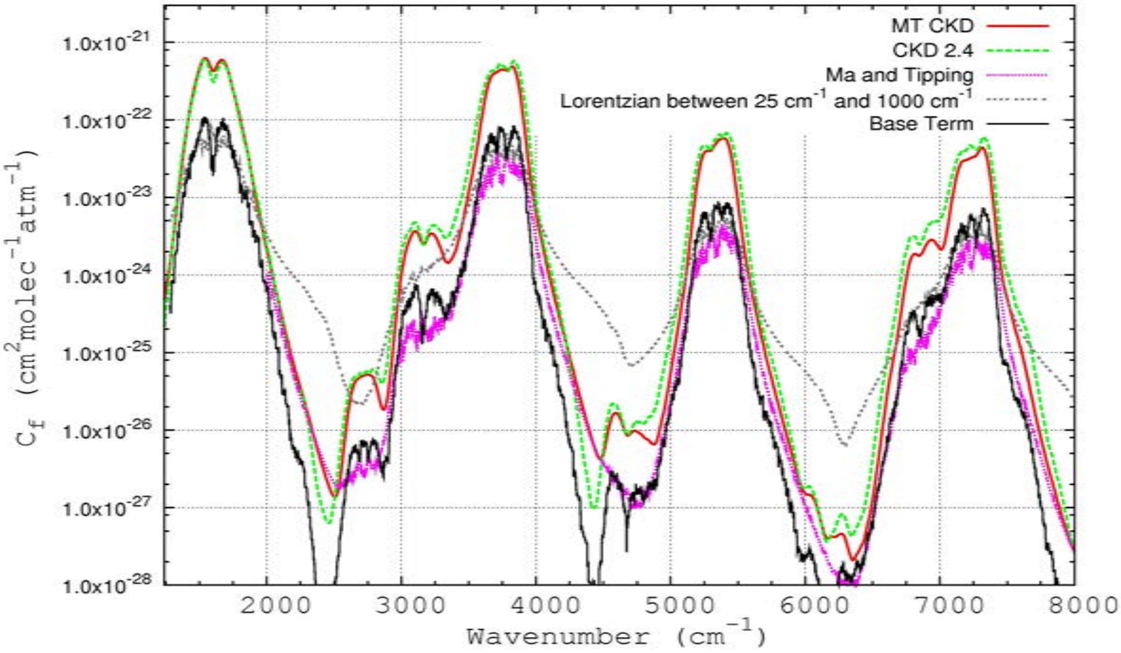

Figure 2.12 The foreign continuum predicted by the various models discussed in this chapter at 296 K. The contribution of the line bases and the absorption predicted by the Lorentzian between 25cm^{-1} and 1000cm^{-1} are also shown. It should be noted that the base is included in both the MT_CKD and CKD continuum, but not in any of the other formulations shown.

2.11. Fourier Transform Spectrometers

The measurements of water vapour spectra in this work were carried out using a Fourier Transform Spectrometer (FTS). This section aims to describe some of the salient points of how a FTS works, a more detailed discussion can be found in text books (e.g. Griffith 1986). The details of the experimental setup itself are discussed in the next chapter.

2.11.1. Basic operation

Figure 2.13 shows the schematic layout of a FTS. The FTS used during this work was based on the principle of a Michelson Interferometer. The radiation from a source is diverted down two perpendicular channels by a beam splitter. Each of these signals is reflected off a mirror and recombined at the beam splitter and then measured by a detector. Assuming a monochromatic source, an identical path length between the beam splitter and two mirrors will result in constructive interference and thus the measured amplitude at the detector is the same as originally at the source. If one of the mirrors is moved so that there is a path length difference of half a wavelength, when the two signals recombine destructive interference occurs and thus no signal is detected. For monochromatic radiation at an arbitrary wavenumber ν the intensity of detector is given by (e.g.Griffiths 1986),

$$I_D(\delta) = \left(\frac{1}{2}\right) I_S(\nu)[1 + \cos(2n\delta\nu)], \tag{2.88}$$

where δ is the shift in the mirror from zero path difference (ZPD). Figure 2.14 panel A shows an example of the interference observed for a monochromatic source of arbitrary intensity $I_S(\nu)$ at 5000 cm^{-1}. In reality the source radiation will not be monochromatic, but will have a broad wavenumber range. In this case the radiation seen at the detector will be the superposition of cosine waves of different periods and amplitudes given by,

$$I_D(\delta) = \left(\frac{1}{2}\right) \int_{\nu_1}^{\nu_2} I_S(\nu)[1 + \cos(2n\delta\nu)]d\nu. \tag{2.89}$$

This generates what is known as an interferogram. Over a broad spectral range the signal intensity is at a maximum at ZPD. There is much less signal observed either side of the ZPD, because the large wavenumber range results in destructive interference. This is demonstrated in Figure 2.14 panel B, that shows a computer generated interferogram produced for a source emitting between 4990 cm^{-1} and 5010 cm^{-1}.

The intensity measured at the detector can be Fourier transformed such it can be written as a function of wavenumber rather than of path difference,

$$I_D(\nu) = \int_{-\infty}^{\infty} I_D(\delta) \exp(i\nu\delta)\, d\delta. \tag{2.90}$$

If a sample is placed between the beam splitter and detector it is therefore possible to obtain a spectrum.

Some features of the spectra obtained using a FTS will now be discussed.

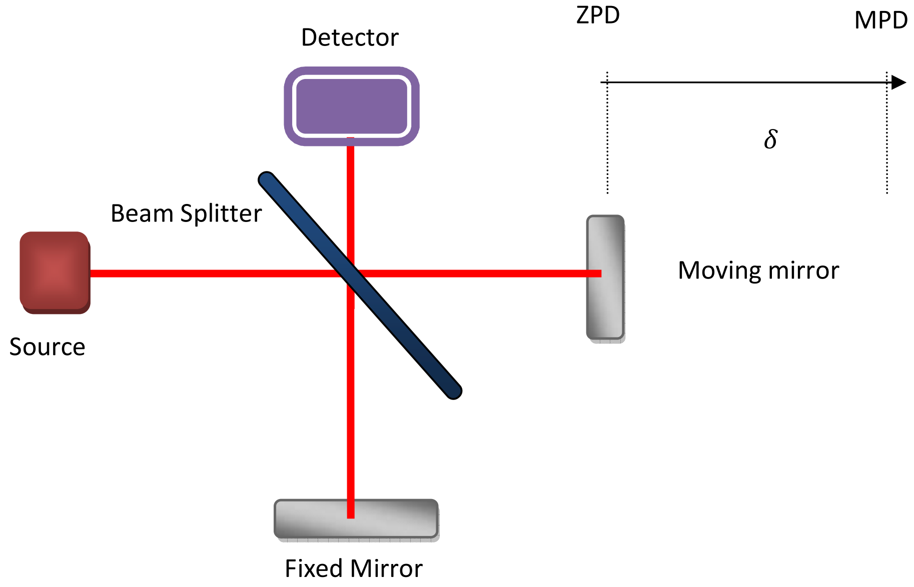

Figure 2.13 A simple schematic of a FTS.

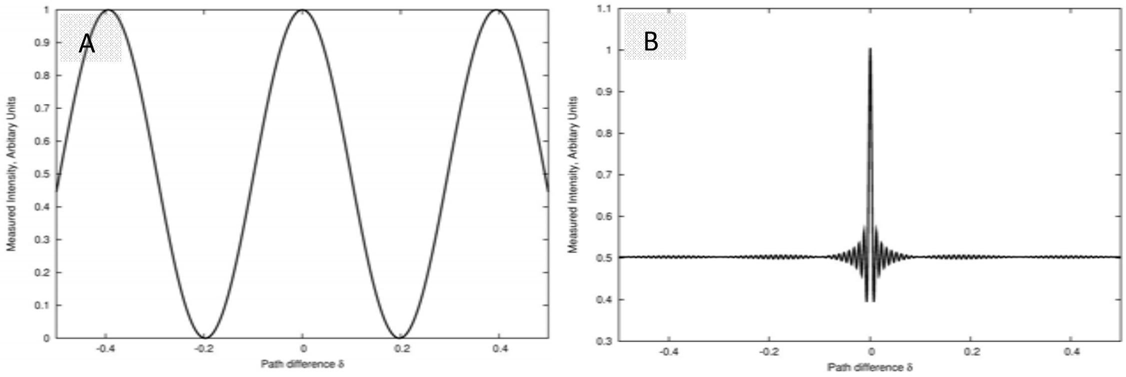

Figure 2.14 Panel A The interferogram produced by a monochromatic source at 5000 cm^{-1}. Panel B The interferogram produced by a source emitting between 4990 cm^{-1} and 5010 cm^{-1}.

2.11.2. Resolution

Resolution is defined by the Rayleigh criteron. This states that in order to resolve two lines separated by a wavenumber difference $\Delta\nu$ cm^{-1} the path difference must be at least $\frac{1}{\Delta\nu}$ cm. The reason for this definition can be explained by a simple example. Consider a spectrum consisting of a doublet of equal intensities and separated by $\Delta\nu$ cm^{-1}. The two cosine waves measured by the detector will become out of phase after the path difference is $\frac{0.5}{\Delta\nu}$ cm, but will be back in phase after $\frac{1}{\Delta\nu}$ cm. Thus, if the maximum optical path difference is not at least $\frac{1}{\Delta\nu}$ cm then it will not be possible to obtain a spectrum with enough accuracy to distinguish between the two lines.

The actual minimum separation resolved by a spectrometer is affected by the instrument and its signal processing. For the Bruker Optics 125HR used in these measurements, the resolution is defined by,

$$resolution = \frac{0.9}{\delta_m}, \tag{2.91}$$

where δ_m is the maximum optical path difference. As it takes the spectrometer more time to scan over a larger path difference, the higher the resolution the longer the measurement time. Deciding the resolution to use for a measurement is a compromise between the level of spectral information required and the time frame in which the measurements need to be made.

2.11.3. Apodization

The maximum retardation length also has an effect on the spectrum. The Fourier transform equation assumes that the interferogram is measured from ZPD to an infinite path length. Obviously, a real spectrometer will have a finite path difference so that we are effectively multiplying the interferogram through by a truncation function defined such that,

$$D(\delta) = 1 \qquad \text{if } \delta < \delta_{max}$$
$$D(\delta) = 0 \qquad \text{if } \delta > \delta_{max} \qquad (2.92)$$

The Fourier transform of $D(\delta)$, is given by,

$$f(v) = 2\delta_{max}\,\mathrm{sinc}(2\pi v\delta_{max}), \qquad (2.93)$$

where $f(v)$ is known as the instrument line shape (ILS) function. This is called Box car apodization (as one is multiplying the interferogram by a boxcar function). It needs to be taken into account when comparing measured spectra to those calculated. The effect of the instrument line shape on an ideal spectrum is obtained by convolving the idealised spectrum with the ILS function,

$$I_{D_{FTS}}(v) = \int I_{D_{ideal}}(v) \otimes f(v - v')dv'. \qquad (2.94)$$

The convolution with the sinc function causes a broadening of the line and creates lobes of negative absorption either side of the line centre. The effect of this apodization upon a monochromatic line is shown in Figure 2.15. In the case of the measurements conducted in this thesis, the broadening due to collisions and other mechanisms is more significant than that caused by ILS, this means that these lobes once convolved with the idealised spectra do not have a significant effect (see section 3.4.2).

Various functions have been developed which try to limit the effect of the lobes by cropping the FT. Norton and Beer (1976) developed numerous functions of the form,

$$D(\delta) = \sum \left[1 - \left(\frac{\delta}{\delta_{max}}\right)^2\right]^i . \qquad (2.95)$$

These functions were found to reduce the value of the negative lobes. However, they also cause the line to be artificially broadened and decrease absorption near the line centre. Figure 2.15 demonstrates the effect that these different functions upon a monochromic line.

For this work it was decided not to apply an apodization function. This was because the continuum is derived in the micro windows away from the line centres. In these regions, at the resolution at which these measurements were conducted at, the ILS is of little significance (see section 3.4.2).

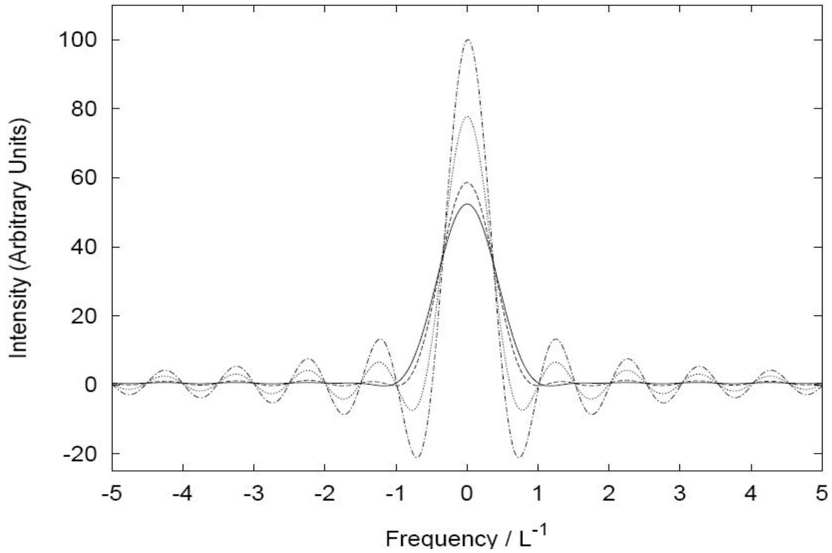

Figure 2.15 The effect of various apodization functions upon a monochromatic spectrum. In order of decreasing lobe and intensity they are Boxcar (dotted-pecked), Norton Beer Weak (dotted), Norton Beer medium (pecked) and Norton Beer Strong(solid). Courtesy of Kevin Smith.

2.11.4. Phase correction

Another possible factor leading to errors in the spectrum are phase errors. There are three common causes of phase error. The first occurs if what the spectrometer measures as the ZPD is shifted from the actual ZPD. The second is caused by the beam splitter material leading to dispersion of the source radiation, which results in the radiation taking slightly varying path lengths and therefore gives different ZPD at different wavenumbers. Finally, there are electronic filters which are designed to remove high frequency noise from the interferogram, but also have the effect of introducing a wavenumber dependent phase lag.

All of these factors cause a Sine term to be included in $I_D(\delta)$ and lead to the interferogram not being symmetrical around the ZPD position (as is the case if there are just cosine functions). To compensate for this, the moving mirror is allowed to overshoot the ZPD by a small amount. An algorithm developed by Mertz (1976) is then applied to the short double-sided interferogram to correct the asymmetry in the high resolution single sided interferogram.

2.11.5. Field of view corrections

As the source radiation in the spectrometer is not a point source this means that there will be off axis rays. These rays will have a different ZPD value than those that are on axis. This causes a circular fringe ring pattern to be produced at the detector. Only the central disc will contain information from the on axis components. The rings further out will be the result of off axis components and thus will cause a loss of resolution in the measured signal. To correct for this an aperture is used. The higher the resolution the greater the value of δ_{max} and thus the smaller the aperture should be to stop off axis rays. This results in a reduction of signal strength at the detector.

2.11.6. Sources, beam splitters and detectors

For these measurements a Bruker Optics IFS 125HR FTS was used. This has a possible spectral range from 5 cm^{-1} to 50000 cm^{-1} and a maximum resolution of 0.0015 cm^{-1}. The spectral range that it was possible to measure at any one time with this spectrometer was limited by the source, the material of the beam splitter and the type of detector used.

There are three internal sources that can be used with the IFS 125HR FTS which cover different spectral regions; a mercury lamp (<100 cm^{-1}), a Globar (300-5000 cm^{-1}) which is made of silicon carbide and a quartz halogen bulb (3000-25000 cm^{-1}). For this work that investigated between 1200 cm^{-1} and 8000 cm^{-1} only the latter two sources were used.

The beam splitter divides radiation by amplitude and works by having a material coated in a semi reflective substance. Different materials are required in different spectral regions; germanium coating on potassium bromide (400-4800 cm^{-1}), silicon on calcium fluoride (1000-10000 cm^{-1}), dielectric coating on quartz (8000-25,000 cm^{-1}) and aluminium on quartz (8000 - 45000 cm^{-1}).

The detectors work by the IR Photons causing valence band electrons to be promoted to the conduction band. The energy of IR photons is quite small, this means that the electron can be thermally excited at room temperatures, which causes thermal noise to be dominant. For this reason the detector was cooled using liquid nitrogen. Different detectors are required to measure at different wavenumbers. Two types of detectors were used during this work; mercury-cadmium telluride (800-6000 cm^{-1}) and indium antimonite (1850-9000 cm^{-1}).

2.11.7. Zero filling

The measured interferogram will be desecrate, however to FT the interferogram with complete accuracy requires it to be continuous. If the interferogram contains frequency points which are not in the desecrate interferogram information is lost. For this reason when a FT of a N point interferogram is performed it is standard practice to add N zeros to the input array. This results in an output spectra which is interpolated with twice the number of data points.

2.11.8. Baseline errors and noise

A drift of the intensity between a background and sample measurement causes what is known as a baseline error. This drift can be the result of small changes in the optical alignment or instability in the source intensity. The effect of baseline drift on this work is discussed more in the next chapter.

Background level noise results from the conversion and amplification of the measured intensity. Every time the moving mirror completes the motion from ZPD to δ_{max} it is said to complete one scan. One way of reducing noise is to increase the number of scans. It can be seen that the noise is reduced with the square root of the number of scans.

Resolution has an effect on how long it takes to achieve the same signal to noise ratio (SNR). For example, if the resolution is doubled it will take twice as long to perform the same number of scans. In addition the SNR will be halved with a doubling of resolution. This doubling also must result in a halving of the aperture used and a fourfold reduction in SNR. Thus, it can be seen that a doubling of resolution will actually result in a measurement taking sixteen times longer to achieve the same SNR. For this reason when conducting a measurement a compromise often has to be made between the resolution and the time frame for which the measurements are made over.

3. Deriving the self continuum

The self continuum is defined as the difference between an accurate measurement (τ_m) of the optical depth of pure water vapour and an accurate calculation of the optical depth (τ_H) for the measurement conditions up to 25 cm^{-1} away from the line centre. That is to say,

$$\tau_c = \tau_m - \tau_H \qquad (3.1)$$

For the calculated optical depth, by accurate it is meant that all of the spectroscopic variables (i.e line intensity and half-width etc.) are as close to reality as the constraints of the Lorentzian line shape will allow and that the pressure and temperature used are exactly those of the measurement conditions. For the measured optical depth accuracy simply means that the spectrum measured is an exact copy of reality (i.e. the act of measuring the spectrum does not cause errors). This definition is as such, because it is desired that the continuum be a representation of the absorption away from the line centres which is not accounted for using the Lorentzian line shape.

Therefore, in order to obtain the continuum the water vapour optical depth has to be measured. Then the optical depth has to be calculated for the same conditions. The aim of this chapter is to guide the reader through this process. It can be seen as being split into three key parts. The first part (sections 3.1-3.2) shows how both the measured spectra and calculated spectra are obtained. The next part then investigates the sources of data used when calculating the optical depth and investigates the errors affecting the continuum (sections 3.3- 3.4). The final part then shows how the continuum is obtained from the ensemble of measurements that were made at different pressures and temperatures. This chapters solely deals with deriving the self continuum. Where processes differ for deriving the foreign continuum is explained in chapter 6.

3.1. Obtaining a measured spectrum

This section will list details of the experimental setup and then present a step-by-step guide to how the optical depth of the spectra is obtained.

3.1.1. Experimental setup

The measured water vapour spectra were obtained using a Bruker Optics IFS 125HR Fourier transform spectrometer (FTS) at the Rutherford Appleton Laboratory Molecular Spectroscopy Facility (MSF). The water vapour sample was measured in the MSF short path absorption cell (SPAC) (Remedios 1990). The SPAC is a multi pass cell which uses mirrors at either end to reflect source radiation throughout the cell numerous times (see Figure 3.1 for layout). The longer the path length the more sensitive the reflections become to the alignment of the mirrors. Changes in vapour pressure and temperature can cause small changes in the mirror alignment, and as a result it was not possible to achieve a stable signal at path lengths greater than 19.3 m.

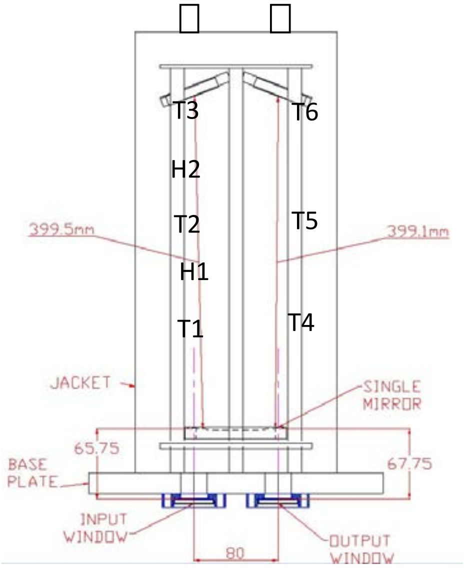

Figure 3.1 The internal layout of the SPAC. T1... T6 represent the positions of the thermistors and H1, H2 the position of the humidity sensors. Diagram courtesy of Gary Williams

In order to obtain an accurate value of the water vapour temperature there are six thermistors situated throughout the SPAC. There were also two humidity sensors (see Figure 3.1 for positions). The temperature of the SPAC was controlled using a standard household emersion heater used to heat a tank of water. A pump was then used to move this water into an outer jacket which surrounded the SPAC on all sides apart from the base. To try to reduce the possibility of any cold spots in this area, four small temperature-controlled electric heaters were inserted into the base plate below the SPAC. This setup allowed the SPAC to be heated to a maximum of 351 K and resulted in excellent temperature stability within the SPAC, with variation of less than 0.2 K during the measurement process.

A glass welded stainless-steel gas handling line was used to introduce water vapour into the SPAC. This was heated to prevent condensation of the water vapour. A turbo molecular vacuum pump connected to the line was used to evacuate the cell between measurements. A schematic of the gas line is shown in Figure 3.2. As can be seen there is one line in and out of the SPAC, which splits into three leading to the water vapour sample, pressure gauges and pumps respectively. By closing and opening various valves along these lines, it was possible to configure this setup for different parts of the measurement process. This will be discussed in the next section.

A total of four manufacturer calibrated pressure gauges were connected to the SPAC. There were three MKS-390 gauges (1000 Torr, 10 Torr and 1 Torr) and a 1000 Torr MKS 625B gauge. The MKS-390 gauges were specified to operate at temperatures up to 313 K and were not internally heated. This means that at cell temperatures above 313 K or when the vapour pressure in the cell was above SVP at the room temperature (~22 mb,~ 296 K) the MKS-390 gauges could not be used. The 625 B is heated up to 373 K and can measure up to this temperature. When possible though the 1000 Torr MKS-390 and 1000 Torr MKS 625B were used together to provide greater accuracy. The agreement was always found to be better than the instrument specification (see table 1). The 10 Torr and 1 Torr were used when the SPAC was evacuated to make sure that the pressure was low enough to perform a background measurement.

Rotary and turbo-molecular pumps were used to evacuate the SPAC and the gas lines. The rotary pump was used initially at pressures above 1 mb and then the turbo pump is used once the pressure had been reduced to 1 mb. The water vapour sample was stored in a glass Pyrex bulb which was connected by the line to both the pumps and the SPAC. The pumps were used to remove any air that may exist in the water vapour sample.

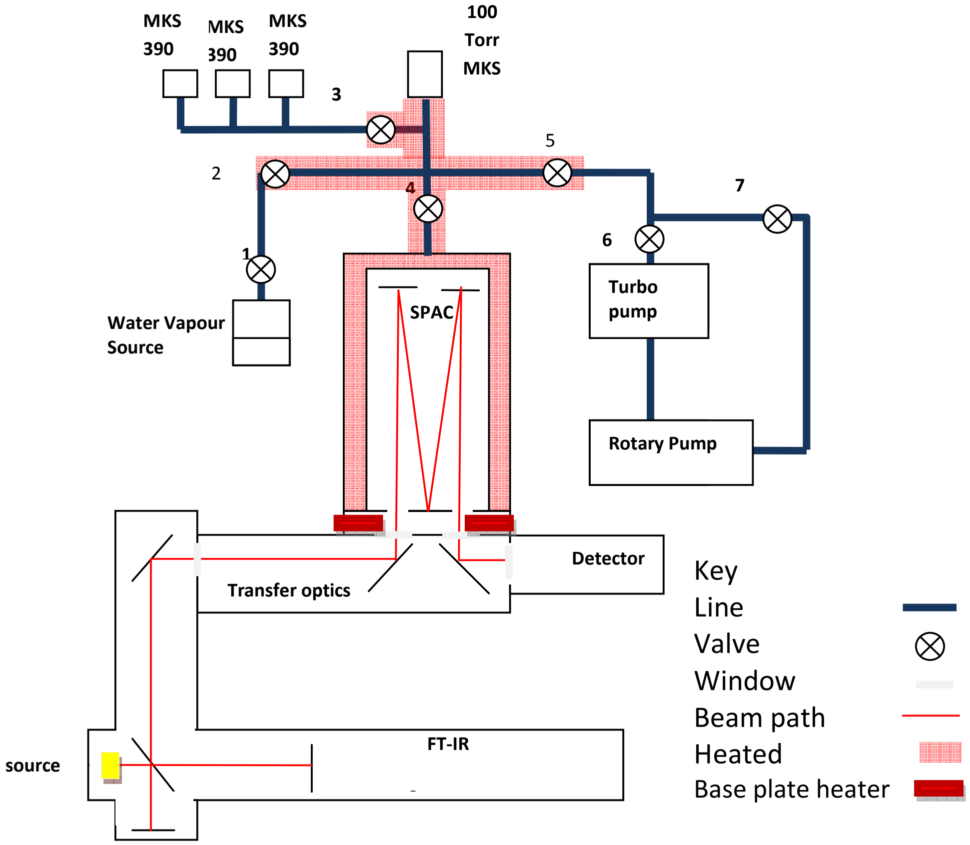

Figure 3.2 A schematic of the experimental setup

The area of line between the SPAC and the high-temperature pressure gauge was also heated with electric heater tape and surrounded with pipe insulating foam. This was done because it was very important to maintain a stable vapour pressure throughout the measurement process by not allowing water vapour to condense on any areas colder than the SPAC. As can be seen by closing valves 2, 3 and 5 it was possible to confine the water vapour to this heated area.

The radiation source, detector and various other optical components were changed to suit the spectral region of the measurement. For this work, two slightly different configurations were used, called setup A and setup B. Setup A was designed to measure near-infrared spectra between 2000 cm^{-1} and 12000 cm^{-1} and setup B the mid-infrared between 1200 cm^{-1} and 3000 cm^{-1}. The differences between these are detailed in table 3.1 and will be noted during the descriptions in this chapter.

	Setup A	**Setup B**
Possible Measureable range with setup	2000-12,000 cm^{-1}	1200-3000 cm^{-1}
Source	150 W quartz tungsten halogen source	Glow bar
Detector	Indium antimonide detector	indium antimonide detector
Path Length	17.9 m (scaled to 19.3)	16.4 m (scaled to 19.3)
Beam Splitter	Calcium fluoride	KBr
Cell windows	Calcium fluoride	Sapphire
Number of scans.	100	50
Pressure Gauges	MKS 625B - 1000 Torr Baratron absolute capacitance Temperature controlled to 373 K +/- 0.25% accuracy MKS-390 - 1 Torr Baratron (up to 313 K only), MKS-390 - 10 Torr Baratron (313 K only) MKS-390 - 1000 Torr Baratron (313 K only) +/- 0.7% accuracy	
Humidity sensor	2 Vaisala HMP234 (+/-2% accuracy)	
Thermisor	6 positions RS Components R-T curve matched ±0.2K at 296 K type UUA41J1 (-/+ 0.2 K accuracy)	
Aperture	2mm	
Apodization	Boxcar	
SPAC Mirrors	Gold coated	

Table 3.1 Details of the experimental setup

In terms of the optical layout, aside from different materials for the beam splitter and windows, the configuration is the same for both setup A and B. Figure 3.2 shows a schematic of the optical layout between the source and detector. After leaving the source it goes through the spectrometer from which it gets diverted into what is known as the transfer optics. The transfer optics reflects the signal into the SPAC. The signal then makes multiple passes through the SPAC (only four passes are shown in the diagram) before entering the transfer optics again where it is finally diverted into the detector.

Optical windows were positioned between the spectrometer and the transfer optics, between the transfer optics and the SPAC and between the transfer optics and the detector. This allowed different parts of the setup to be isolated from each other. The spectrometer, the transfer optics and the detector were pumped down to pressures below 0.2 Pa. This meant that when the SPAC was fully evacuated there should be any no absorption anywhere along the optical path of the source radiation. Therefore, the only contribution to the measured absorption was from the water vapour sample contained within the SPAC.

The spectrometer was set to a resolution of 0.03 cm^{-1}, which is not quite high enough to be able to fit individual spectral lines. However, in the micro windows, where optical depth varies far more gradually with wavenumber, this was deemed high enough by Ptashnik et al. (2004) to be able to derive the continuum accurately. Boxcar apodization was applied to the measured interferogram. The effect of the instrument line shape on the continuum when Boxcar is applied is discussed in 3.4.2. Other details of the spectrometer setup are listed in table 3.1.

3.1.2. The measurement process

In order to obtain the optical depth of a water vapour sample two measurements are required: a background measurement (with the SPAC evacuated) must be performed followed by a measurement with the SPAC containing a known amount water vapour. This section aims to describe how the experimental setup given in the last section was configured during each stage of the measurement process.

Stage 1 - Background
Valves open: 3,4,5,6
Valves closed: 1,2,7

The SPAC was evacuated using the turbo pump whilst keeping the SPAC isolated from the water vapour sample. Once the measured pressure inside the SPAC was less than 0.002 mb a background measurement was performed. A typical background measurement consisted of 50 scans and took 15 minutes. At this point the agreement between the pressure gauges was also checked. During sample measurements some water molecules may be absorbed onto the inner surface of the SPAC. Therefore, during the background measurement there was a trace amount of water in the SPAC even during evacuation (as can be seen in Figure 3.3). However, the contribution of this small amount of water vapour to spectroscopic absorption was found to have a negligible effect on any spectra derived from these measurements. This was because this absorption only occurred in the strongest water line centres which were completely saturated during all sample measurements.

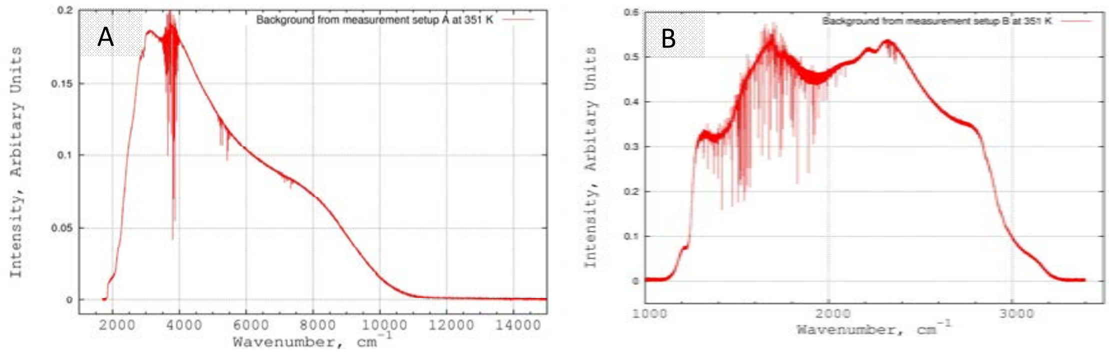

Figure 3.3 Background measurements from setup A (panel A) and setup B (Panel B) conducted at 351 K. The shape of the curve is determined by a mixture between the Planck function of the radiation source, the range of the detector and absorption by various windows along the ray path.

Stage 2 – Filling

Valves open: 1,2,3 (only at 296 K) ,4,5,6

Valves closed: 7

The valve to the pumps (5) and that to the 1,10 and 1000 Torr MKS-390 gauges (3) (this was only done for temperatures above 296 K where condensation becomes a problem) are closed. Valves 1 and 2 are opened to let water vapour enter the cell from the source until the desired vapour pressure was obtained.

Stage 3 – Sample Measurement

Valves open: 3 (only at 296 K) ,4

Valves closed: 1,2,5,6,7

Once the required pressure was reached the valves to the water sample (1 and 2) were closed. Time was allowed for the water vapour pressure to stabilise (typically 10 minutes). A variation of less than 0.2 K in temperature 0.1 mb in pressure and 1% relative humidity constituted stable conditions. The water vapour was assumed to be well distributed once the difference between the humidity sensors was less than 5%. When these conditions are satisfied a sample measurement was then conducted (normally 100 scans). The vapour pressure, humidity and temperature are recorded once at the beginning, once in the middle and once at the end of each measurement. If the temperature was observed to change by more than 0.2 K or the pressure by more than 0.5 mb or 0.5% of its value, whichever is greater, then the measurement was discarded.

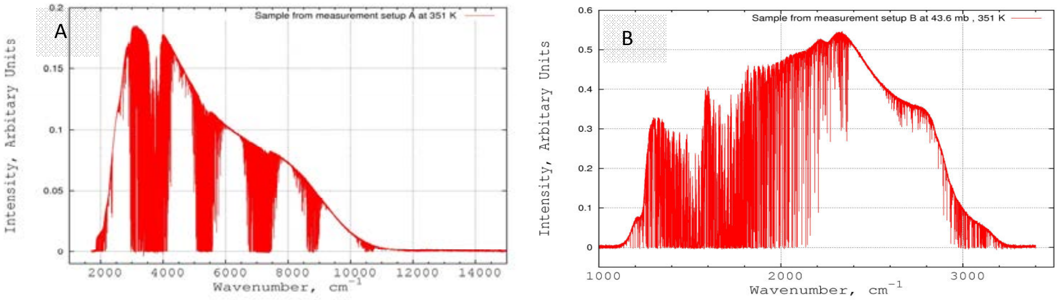

Figure 3.4 Sample measurements of pure water vapour using setup A (panel A) at 351K and 40.3 mb and from setup B (Panel B) at 351 K and 43.6 mb.

3.1.3. Calculating the measured optical depth

Once the background and sample measurements had been made it was possible to obtain the measured optical depth (τ_m) using the relationship of Beer's law,

$$\tau_m(\nu) = -\ln\left(\frac{I_m(\nu)}{I_b(\nu)}\right), \tag{3.2}$$

where I_m is the measured intensity of a sample measurement and I_b is the intensity of a background measurement. Typical spectra obtained from measurement setups A and B are shown in the corresponding panels Figure 3.5 Due to the small signal recorded at the edge of the measured spectral regions, the derived optical depth data are only useful between 2000 and 8000 cm^{-1} and 1200 and 2800 cm^{-1} for setups A and B respectively.

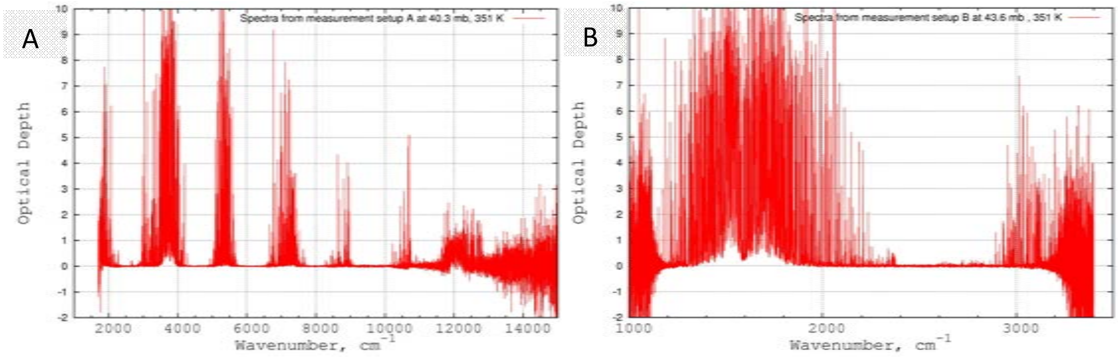

Figure 3.5 Optical depth spectra obtained for a pure water vapour sample measurement using setup A (panel A) at 351K and 40.3 mb and using setup B (Panel B) at 351 K and 43.6 mb.

3.1.4. Maintaining a stable vapour pressure

In order to obtain an accurate representation of the continuum it is important to have both stable vapour pressure and temperature throughout a measurement. There were two possible causes of pressure changes during a measurement; a leak or condensation at cold spots in the system. Detecting a leak during the measurement process was fairly straightforward, as it is showed as an increase in the measured pressure without a corresponding change in humidity. Of greater concern is air leaking in with the vapour sample during the filling of the SPAC. In this situation it was not possible to know to the required level of accuracy how much air has entered into the SPAC. The humidity sensors, while being responsive to very small changes in vapour pressure, were not accurate enough in an absolute sense to be able to measure the amount of water vapour in the SPAC.

To reduce the possibility of air entering the cell a leak test was performed every morning before measurements were made. This involved evacuating the SPAC down and then closing valve 1 (to the water sample) and valve 5 (to the pumps). The pressure of the SPAC was then monitored for 30 minutes to check that any change in pressure would be less than 0.05 mb and therefore insignificant.

The Freeze-pump-thaw technique was also performed on the sample every morning to make sure that no air was dissolved in the water sample. In addition repeat sample measurements on separate days were performed at the same pressure and temperature. If the repeat measurements agree, this is a sign that there is no leak, as it is very unlikely that exactly the same amount of air would leak into the sample each time.

3.2. The calculated spectra

To obtain the continuum it is necessary to calculate the optical depth for the measurement conditions. Section 2.5 has already detailed the process of required to calculate the optical depth. This section will explain how this optical depth is calculated for measurement conditions.

3.2.1. Calculating optical depth

In section 2.5 it is shown that the optical depth for pure water vapour assuming a Lorentzian line shape is,

$$\tau_H(\nu) = \frac{P_s L}{kT}\sum_{i=1}^{N} S(T_0,\nu_i)\frac{\alpha_i}{\pi\left((\nu-\nu_i+\delta_i)^2+\alpha_i^2\right)}, \tag{3.3}$$

where for near infrared spectra range,

$$S_i(T) \approx S_i(T_0)\frac{Q(T_0)}{Q(T)}\exp\left(-c_2\left(\frac{1}{T}-\frac{1}{T_0}\right)\right), \tag{3.4}$$

and assuming pure water vapour,

$$\alpha_i(P,T) = \alpha_i^0 \left[\frac{\mathrm{P_s}}{\mathrm{P_0}}\right]\left[\frac{T_0}{T}\right]^{n_i}. \tag{3.5}$$

The HITRAN 2004 (Rothman et al. 2005) database gives values of the partition function for different temperatures. For the temperatures investigated the empirical relation,

$$\mathrm{Q(T)} = 174.63 + 0.924(T - T_0), \tag{3.6}$$

can be fitted be fitted to the data. Table 3.2 gives the meaning and source of these parameters used in equations (3.2)-(3.6).

Quantity	Source
P Vapour pressure	Measured
T Temperature	Measured
L Path length	Measured
ν_i Line position	HITRAN 2004
S_i Line intensity	HITRAN 2004
α_i self-broadened half-width at half maximum at T_0 and P_0	HITRAN 2004
E_i lower state energy of line	HITRAN 2004
Q- Partition function	HITRAN 2004
δ_i – Pressure shift.	HITRAN 2004
n_i – temperature dependence exponent	HITRAN 2004
c_2 – Constant with value hc/k = 1.4388 cm K.	

Table 3.2 The parameters used in equations (3.2)-(3.6) and where they are sourced from.

As has been noted previously, the continuum is derived away from the line centres. In these areas, where $(\nu_i - \nu_0 + \delta_i)^2 \gg \alpha_i(P,T)^2$, the calculated optical depth is given by,

$$\tau_H(\nu) \approx \frac{P_s L}{kT}\sum_i^N S_i(T)\frac{1}{\pi}\left[\frac{\alpha_i}{(\nu_i - \nu + \delta_i)^2}\right]. \tag{3.7}$$

This form is useful as it allows one to see which parameters have the most significant effect upon the optical depth.

3.3. The HITRAN database

As can be seen from Table 3.2 the parameters not obtained from the measurement process are obtained from the HITRAN database (Rothman et al. 1987; 1992; 1998; 2003; 2005). HITRAN (the **hi**gh-resolution **tran**smission molecular absorption database) contains information about the spectral lines of 37 different molecules. Mostly the data is sourced from various experimental measurements, although when measurements are not available theoretical estimates are also used. For water vapour in the spectral region this study is mainly concerned with (1200-8000 cm^{-1}) there are at present a total of 35,088 parameterised lines. Figure 3.6 shows the position and intensities of these. Updates to HITRAN occur roughly every 4 years. The latest version is HITRAN 2004 (version 12) which superseded HITRAN 2000.

The aim of this section is to provide an overview of the accuracy of the parameters from the HITRAN database used to calculate the optical depth. This firstly will involve investigating the changes in the HITRAN 2004 database compared to the previous version. The various sources of the HITRAN data will be discussed and where possible an inter-comparison will be made between different sources. The errors associated with each of HITRAN's parameters are looked at. Finally, the effect of these errors upon the optical depth is calculated.

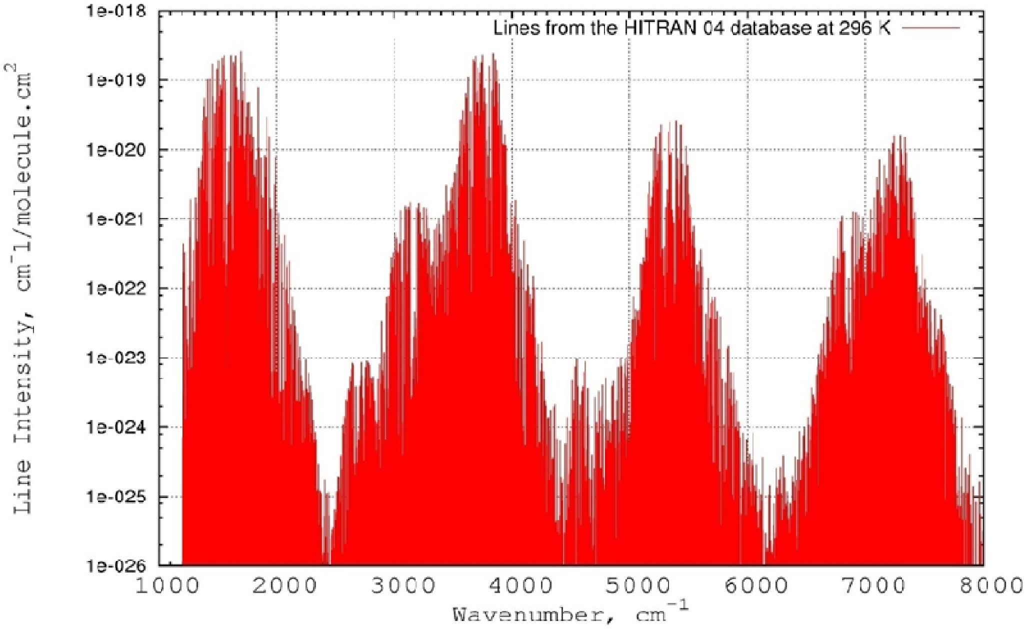

Figure 3.6 HITRAN 2004 line positions and intensities for water vapour between 1200 and 8000 cm^{-1}

3.3.1. Comparing HITRAN 2004 to HITRAN 2000

The latest version of HITRAN contains some major changes to the water vapour parameters needed to calculate optical depth. In the 2800-8000 cm^{-1} region the majority of the line positions, intensities and air broadened half-widths have been updated using the measurements of Toth, who has compiled a detailed line list of water vapour transitions (http://mark4sun.jpl.nasa.gov). In addition for the first time in the 2000-8000 cm^{-1} region pressure shifted parameters have been included.

Perhaps the most significant change as far as this work is concerned is the inclusion in HITRAN 2004 of self-broadened half-widths for water vapour between 2000 and 6000 cm^{-1}. Previously only foreign broadened half-widths were provided in this region; when calculations were performed it was often assumed that for a line the self half-width was five times the foreign. In addition, the self-broadened half-widths in the 1200-2000 cm^{-1} and 6000-8000 cm^{-1} regions have been updated. The self-broadened half-widths come from a variety of sources which will be discussed in the next section.

Figure 3.7 summarises the changes to the parameters used to calculate the optical depth between 1200 and 8000 cm^{-1}. Panel A shows the change in line positions. It can be seen that in the 1200-2800 cm^{-1} region, apart from a few weak lines, there has been no change in the line positions. Between 2800 cm^{-1} and 6000 cm^{-1} the lines positions of all the stronger lines ($>10^{-22}$ cm^{-1}/molecule.cm^{-2}) and the majority of other lines have been adjusted by less than 0.002 cm^{-1}. The changes above 6000 cm^{-1} are more significant, here some of the strongest lines ($>10^{-20}$ cm^{-1}/molecule.cm^{-2}) are shifted up to 0.03 cm^{-1}.

However, in general the effect of these changes on line positions can be ignored when deriving the continuum. This is because for the large majority of lines the change in position is far less than the spectral resolution (0.03 cm^{-1}) making it unlikely that all but these larger changes will be detectable. Furthermore, it can be shown that even for the largest shifts (~>0.01 cm^{-1}) the resulting change in the calculated optical depth is small compared to the value of the continuum.

Due to the linear dependence of optical depth upon line strength, accurate line intensities are important for correctly deriving the continuum. The ratio of the line intensities in HITRAN 2004 and HITRAN 2000 are shown in panel B. As can be seen there are no adjustments of any significance occurring below 2800cm^{-1}. In the 2800-6000 cm^{-1} region, adjustments of up to 20% have been made to the stronger lines. These adjustments are enough to have a considerable effect upon the continuum derived. However, the fact that they appear to be non systematic means that they are unlikely to lead to a large difference in the magnitude of the continuum over the whole region depending upon which version of HITRAN is used. Above 6000 cm^{-1} there appears to be a systematic shift with the lines in HITRAN 2004 being in general about 20%

stronger, suggesting that HITRAN 2004 will have less of a continuum contribution in this region. There are also in this region far greater adjustments made to the strongest lines.

Away from line centres, as with the line intensities, the optical depth varies linearly with the self-broadened half-width. Panel E shows the ratio of self broaden half widths of HITRAN 2004 to HITRAN 2000 in the regions where they exist in both databases. The adjustments made to the stronger lines are up to around 10% and for other lines up to 50%. Panel F shows the ratio between five times the foreign-broadened coefficients in HITRAN 2000 (i.e. the value used previously for the self broadened half-width) to the self-broadened half-widths in HITRAN 2004. The fact that the half-widths of numerous stronger lines are either under or over estimated by up to 50% or more, highlights the importance of having separate measurements of the self broaden half-widths.

Panel C contains the ratio of temperature dependence exponent (n_i) between the two versions of HITRAN. In HITRAN 2000 in the 2800-6000 cm^{-1} region the temperature dependence exponent had a default value of 0.64. In HITRAN 2004, these along with the values for the rest of lines have been updated. As T_0 in HITRAN is defined as 296 K, the temperature dependence exponent only starts to have a large effect when the measured temperature deviates greatly from this value. The maximum temperature at which measurements were conducted at in this work was 351 K. At this temperature, assuming the maximum difference between the two databases will result in a 5% change in the calculated optical depth. In general this is far less than the differences resulting from the line intensities or self-broadened half-widths.

The pressure shift contributions in the 1200-2000 cm^{-1} region have been updated quite significantly, as is shown in Panel D. The typical values of the shifts are about 0.01 $cm^{-1}atm^{-1}$. The average pressure used in these measurements is around 100 mb (~0.1 atm) and thus the difference between HITRAN 2004 and 2000 can be considered insignificant compared to the measurement resolution.

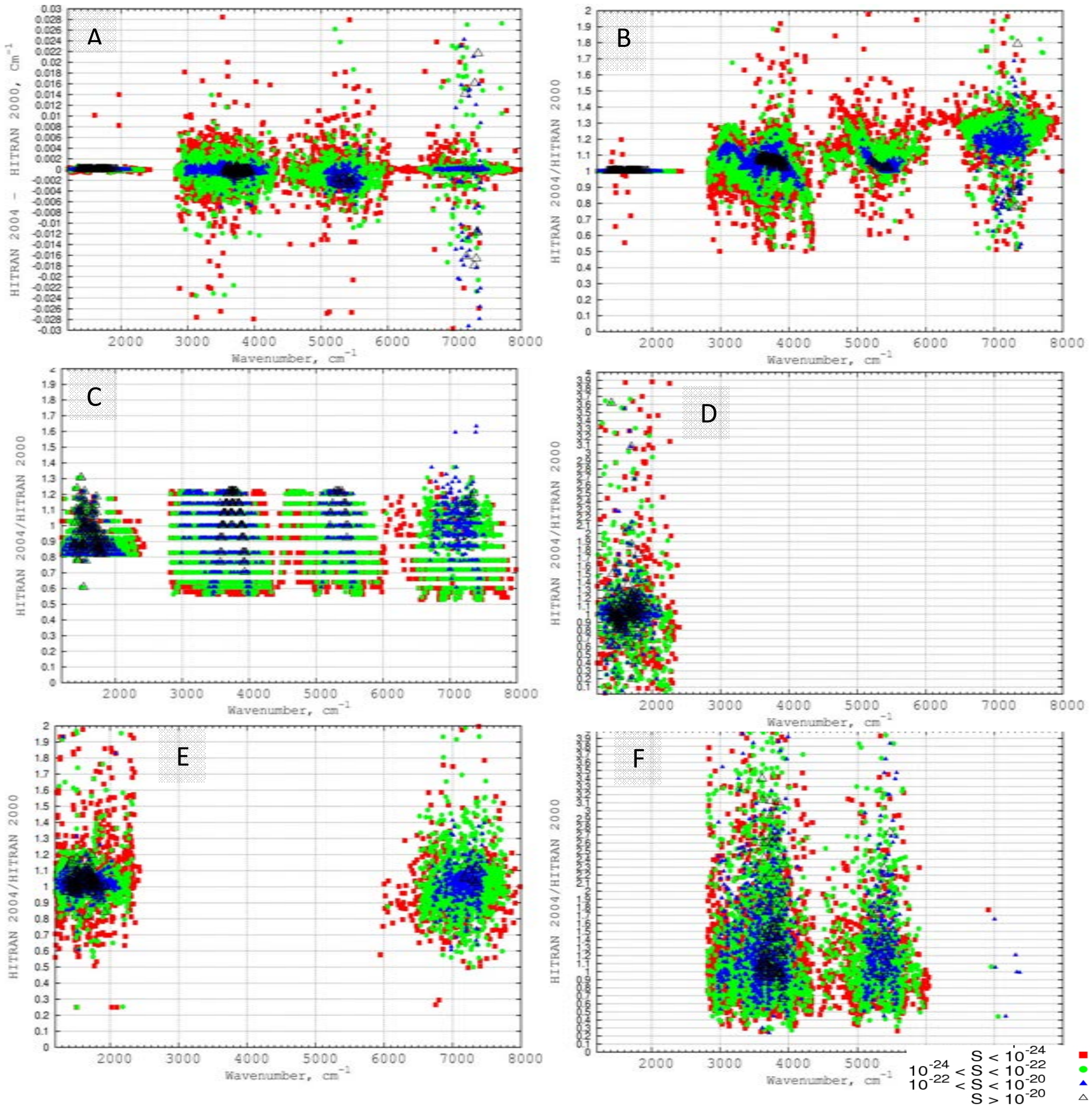

Figure 3.7 The parameters in HITRAN 2004 compared to HITRAN 2000 over the spectral region investigated in this thesis. Panel A shows the difference in line positions. The ratio of line intensities (panel B), temperature dependence exponent (n_i) (panel C), pressure shift (panel D) and self-broadened half-widths (Panel E) are shown. Panel F presents the ratio of the self-broadened half-widths in HITRAN 2004 to five times the foreign-broadened half-widths in HITRAN 2000. For all panels the different point types represent different line intensities (S) in units of $cm^{-1}/molecule.cm^{-2}$. Where there are no points it was not possible to perform a comparison, due to lack of data in HITRAN 2000.

3.3.2. Sources of HITRAN 2004 data

For each line in HITRAN 2004 the sources of the line position, line intensity, foreign-broadened half-width, self-broaden half-width, temperature dependence exponent and pressure shift is given. It is important where possible to compare the different sources in order to discover any systematic errors within them.

For the regions investigated between 1200-8000 cm^{-1} this analysis is straightforward, as the lines positions, intensities, temperature exponents and line shifts are all from the line list of Toth (http://mark4sun.jpl.nasa.gov and (Toth 1993; Toth 2005; Toth 2005)). Most of the data in the Toth line list are from measurements conducted by Toth. Occasionally, the lines do come from other sources; however, Toth does not state the source of individual lines, so it is not possible to perform a detailed analysis of the line list.

The only parameters that come from a variety of sources are the self-broadened half-width, which is mainly from the work of Mandin et al. (1982), the Toth line list and Gamache (unpublished). The HITRAN 2004 database gives priority to the work of Gamache who obtained the half-widths by averaging over a number of measurements. Where the Gamache measurements are not available either the measured values of Toth, Mandin or occasionally another source are used. Where there are no accurate measurements, what is called a smoothed half-width, which are derived by Toth are used.

A smoothed half-width is obtained by making use of a complex empirical relationship between half-width and the quantum numbers associated with that transition. By fitting measured half-widths to the quantum numbers it is possible to extrapolate the half-width of a transition even if no measurement has been made (e.g. Toth 2005). Occasionally where there are neither smoothed nor measured values a default value given by Gamache is used (which is always 0.12 $cm^{-1}atm^{-1}$).

Figure 3.8 shows the self-broadened half-widths from the different sources discussed above as a function of both wavenumber and line intensity. Table 3.3 contains details how many lines each source contributes in different regions. This is shown for all lines and those lines with intensity greater than 10^{-21} $cm^{-1}/molecule.cm^{-2}$. Stronger lines are particularly important as errors in these can significantly affect the magnitude of the derived continuum over a wide spectral region.

The analysis reveals that at any wavenumber in the spectra the self-broadened half-widths come from a variety of sources. This is especially so in the 3000 - 4500 cm^{-1} region, where there is a substantial number of lines from all four sources. In the other regions, aside from some of the strongest lines measured by Gamache between 6600 and 7500 cm^{-1}, the data are mainly either the smoothed or measured Toth values.

There are a few discrepancies in the data worth noting. Firstly, as can be observed in Figure 3.8 panel C and D, the values of Mandin et al. (1982) appear to be on average generally higher than the other lines in the 3100-4500 cm^{-1} region. This finding is backed up by measurements of self-broadened half-widths by Zou and Varanasi (2003). They found that upon comparing 46 of their measured half-widths to those measured by Mandin et al. (1982), the Mandin et al. values were up to 40% higher.

In addition, the Toth line list also contains alternative values to those of Mandin et al. (1982). These lines are mainly either smoothed or measured values by Toth, although some values are from the afore-mentioned measurements of Zou and Varanasi (2003). The ratio of Mandin et al. (1982) lines to those provided by Toth are presented in Figure 3.9 panel A demonstrates this bias clearly for lines of all intensities.

Another noticeable feature from the analysis presented in Figure 3.8 is that the Gamache default value lines all have half-widths of 0.12 $cm^{-1}atm^{-1}$. These values are considerably smaller than most of the other self-broadened lines. The Toth line list provides alternative values for these half-widths. It can be seen in Panel B of Figure 3.9 that most of the Gamache values are only one quarter those of Toth.

Region/Author	**Toth Measured**	**Mandin et al measured**	**Gamache measured**	**Toth Smoothed**	**Gamache Default Value**	**Other**
1200-2000 cm^{-1}	2767/245	0	145/26	843/9	2/0	135/40
3000-4500 cm-^{1}	1121/0	896/63	1559/216	3170/103	12/2	0
5000-5600 cm-^{1}	1981/79	0	155/42	683/5	3/0	3/1
6600-7500 cm^{-1}	3629/66	0	173/47	932/5	43/0	27/9

Table 3.3 The number of lines in HITRAN 2004 which each source of the self broadened half-widths contributes. The first value is the number of lines with S> 10^{-25} cm^{-1}/molecule.cm^{-2}. The second value is for S > 10^{-21} cm^{-1}/molecule.cm^{-2}. These stronger lines are likely to have the greatest effect on deriving the continuum.

The Toth line list also provides alterative values for the measured Gamache lines used in HITRAN 2004. The results of this comparison show that there is a significant difference between the two sets of data, with numerous of the stronger lines disagreeing by up to 20%. The HITRAN database does not specify why the Gamache half-width values are favoured over those of Toth. If both datasets are considered of equal quality than we cannot be certain of the half-widths to any better than at best a 10% accuracy for the stronger lines.

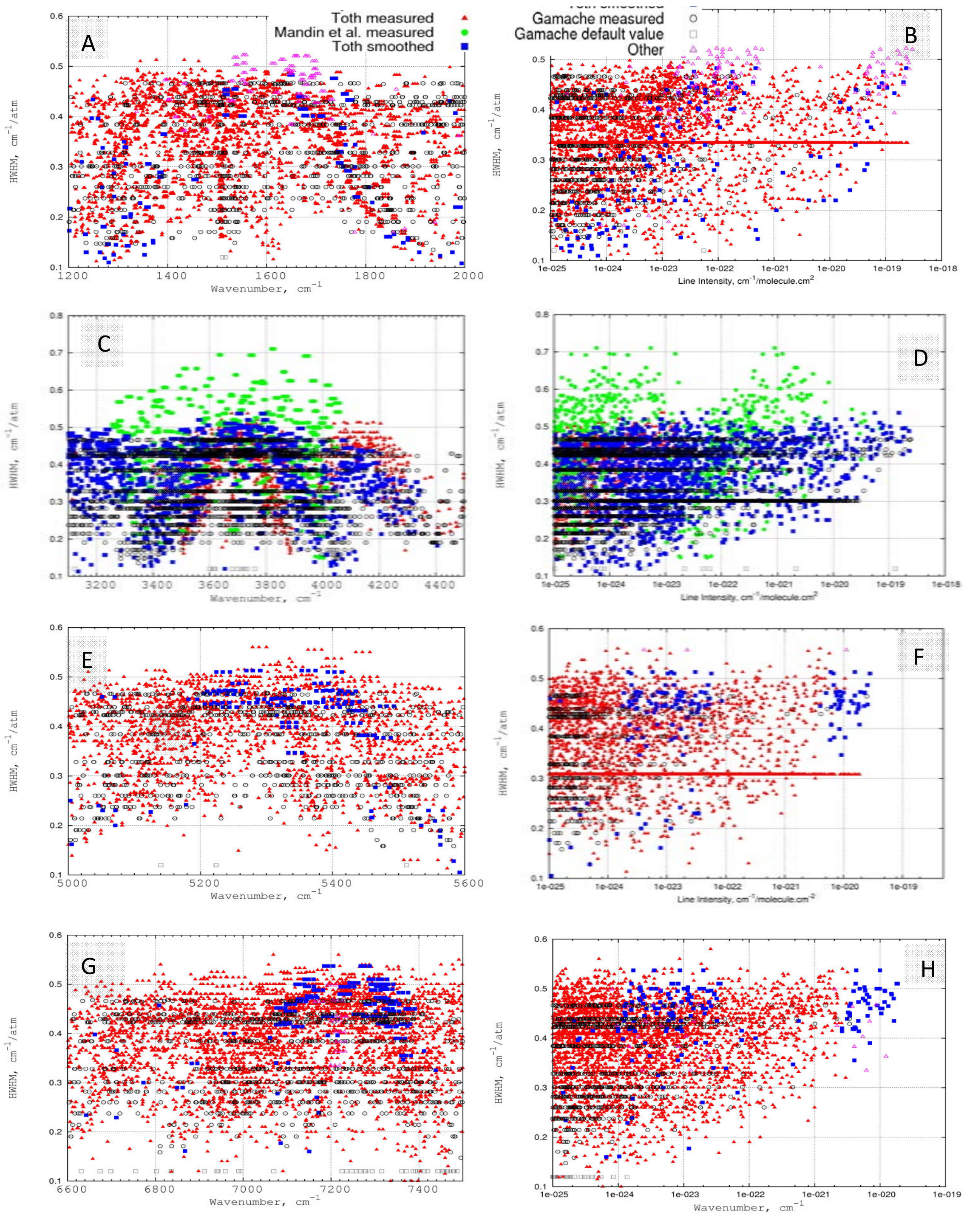

Figure 3.8 HITRAN 2004 self-broadened half-widths for different spectral regions, shown as a function of wavenumber (panels A,C,E,G) and of line intensity (panels B,C,F,H) for the wavenumber region in the preceding panel. The different points represent different sources of the half-widths, as shown on the key.

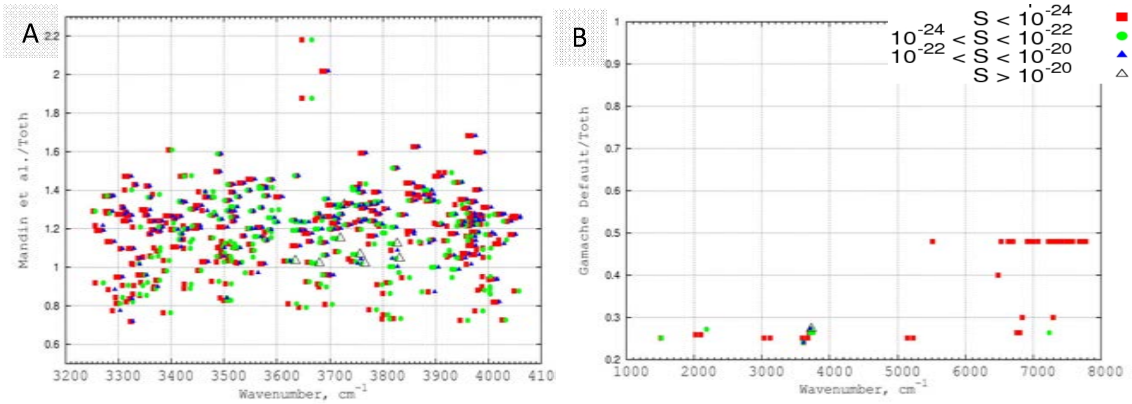

Figure 3.9 Panel A: The ratio of the measured self-broadened half-widths of Mandin et al. (1982) used in HITRAN 2004 to those in the Toth line list. Panel B: The ratio of the Gamache default value self-broadened half-widths used in HITRAN 2004 to those provided in the Toth line list. For both panels the different point types represent different line intensities in cm^{-1}/molecule.cm^{-2}

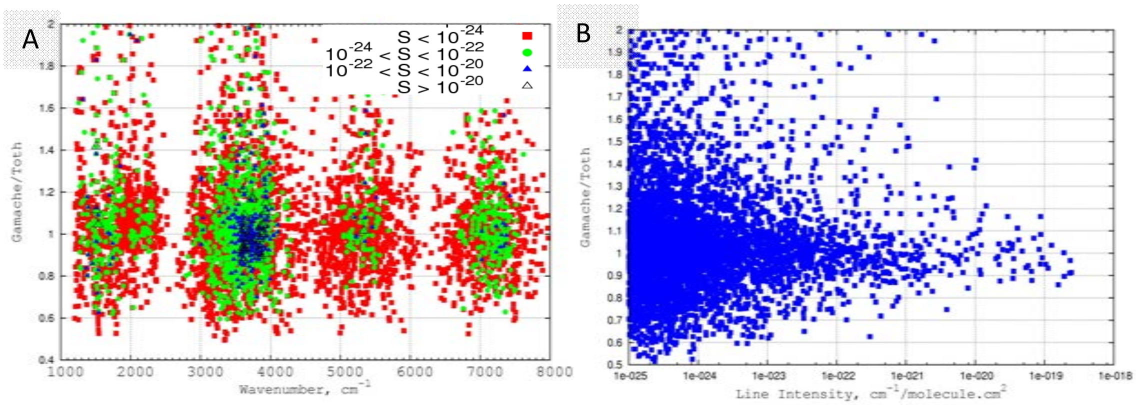

Figure 3.10 The ratio of the measured self-broadened half-widths of Gamache used in HITRAN 2004 to those in the Toth line list. In panel A these are plotted against wavenumber and in Panel B against line intensity. For panel A the different point types represent lines intensities in units of cm^{-1}/molecule.cm^{-2}.

In the region between 5000 and 5600 cm^{-1} Ptashnik et al. (2005) have conducted measurements of the line positions, intensities and self broadened half-widths of the 320 strongest lines with an intensity greater than 1.5×10^{-23} cm^{-1}/molecule.cm^{-2}. They found that for the Toth measured self-broadened half-widths, there was a systematic overestimate of the widths which increased with intensity. This result is presented in Figure 3.11, where it can be seen that for the strongest lines this disagreement was as large as 20%. A better agreement was discovered with the stronger Toth smoothed lines. For all lines they also found that the strength was underestimated between 5 and 2% (Figure 3.12). However, this value is within the experimental 10% uncertainty stated by Toth.

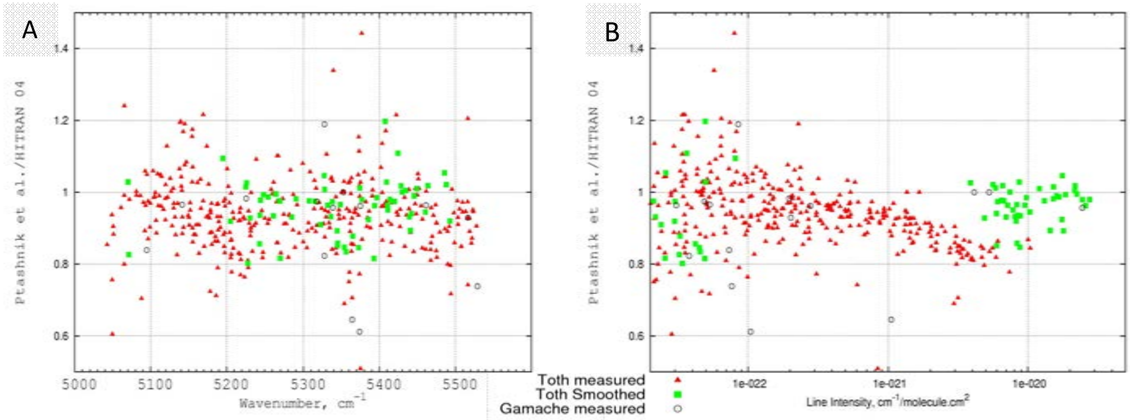

Figure 3.11 The ratio of the self-broadened half-widths of the lines measured by Ptashnik et al. (2005) to those in HITRAN 2004. The different point types represent different sources of the lines, as shown in the key. Panel A and B show this ratio plotted against wavenumber and line intensity respectively.

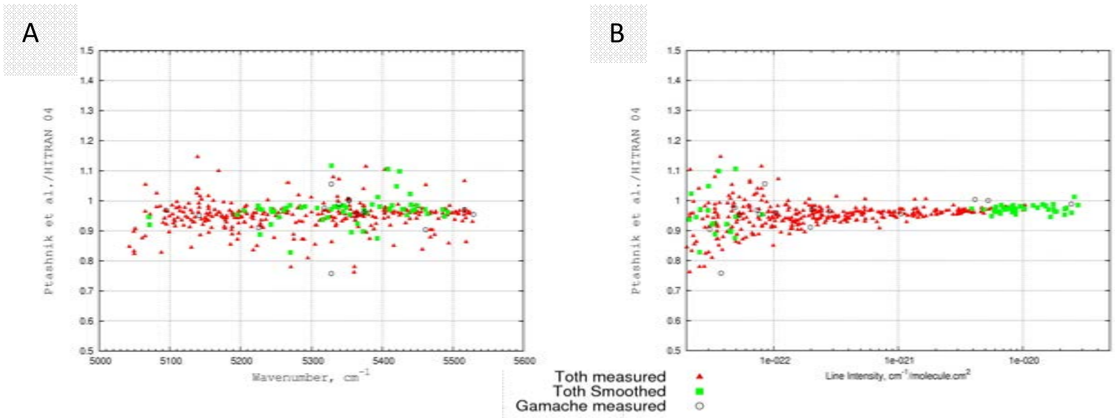

Figure 3.12 The ratio of the line intensities measured by Ptashnik et al. (2005) to those used in HITRAN 2004. The different point types represent different sources of the lines. Panel A and B show this ratio plotted against wavenumber and line intensity respectively.

3.3.3. Error codes in HITRAN

For each spectral line in HITRAN an error code is provided. These codes relate to a certain error category (see Table 3.4). All of the line positions lie in the error category of 0.001-0.01 cm^{-1}. As discussed in Section 3.3.1 errors of this size are unlikely to have any effect upon the derived continuum. All of the line intensities have an error between 5-10%. The temperature dependence exponent has an uncertainty between 10% and 20%. As also discussed in 3.3.1 this should translate into less than a 5% error in the optical depth calculation at 351 K.

Uncertainty Code	Uncertainty range
0	Unreported
1	Default Value
2	Average or estimate
3	>20%
4	>10% and < 20 %
5	>5% and <10%
6	>2% and <5%
7	>1% and <2%
8	<1%

Table 3.4 The percentage error categories relating to the uncertainty codes given in HITRAN 2004.

The error codes of the self-broadened half-widths (see Figure 3.13) are slightly more complex. The Gamache values and default values do not seem to have any error estimates. The results of Mandin et al. (1982) either have an error of 10-20% or greater than 20%. This value is less than the possible errors suggested in the previous section. The regions in which these lines may affect the continuum is discussed in section 4.1. The Toth smoothed values all lay within the 5 -10 % category. As can be seen this is similar to the differences with the measurements Ptashnik et al. (2005), suggesting this is a reasonable estimate. The Toth measured values have a whole range of error values. Mostly, they are assumed to be accurate within 10%, which as can be seen in the last section is slightly less than the differences with Ptashnik et al.

In summary, the variation in error codes tells us that the uncertainty in the derived continuum resulting from the self-broadened half-width will vary throughout of the spectral region investigated. It also apparent from the previous section that the uncertainty in the Mandin et al. (1982) lines, some of the measured Toth lines and all of Gamache default value is larger than that reported by HITRAN.

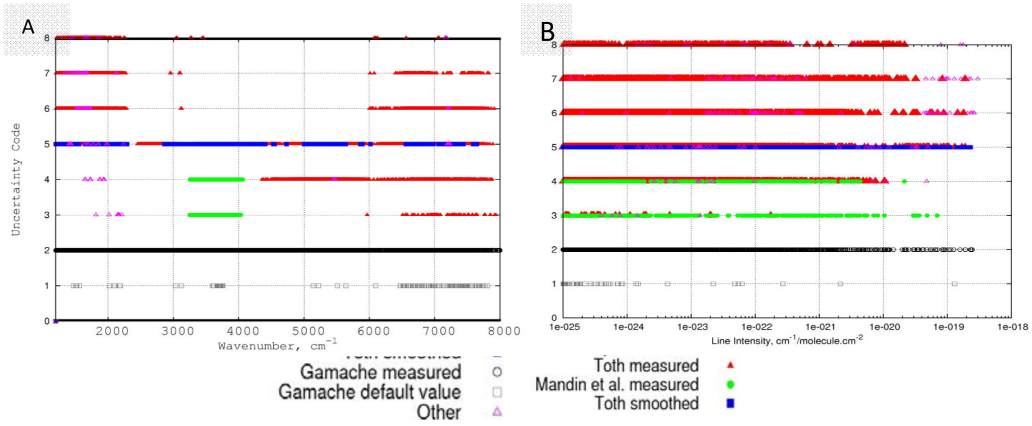

Figure 3.13 The error codes in HITRAN 2004 for the self broadened half-widths. The different point types represent different sources of the lines. Panel A and B show this ratio plotted against wavenumber and line intensity respectively.

3.3.4. The effect of HITRAN errors upon optical depth

The last two sections noted that the two dominant sources of errors in HITRAN likely to cause the most significant uncertainty when calculating the optical depth, are those in the line intensities and self-broadened half-widths. In this section how the uncertainty in these two parameters translates into uncertainty in the optical depth will be derived. The errors in the optical depth caused by errors in other parameters given by HITRAN are considered negligible and are therefore ignored. The error in the optical depth calculation is simply defined as the difference between the optical depth calculated with or without the error. The assumption is made here that the effect of a negative error in a variable is the same as a positive one. For example, let us say that we are considering the error (β_ϵ) in an arbitrary variable β. Then the modulus of the error in optical depth resulting from an error in β is,

$$\tau_\epsilon(\beta_\epsilon) = |\tau(\beta + \beta_\epsilon) - \tau(\beta)|, \tag{3.8}$$

where it is assumed that,

$$|\tau(\beta + \beta_\epsilon) - \tau(\beta)| \approx |\tau(\beta - \beta_\epsilon) - \tau(\beta)|. \tag{3.9}$$

So that when considering solely errors in β, it can be said that we know the optical depth within an accuracy,

$$\tau(\beta) \pm \tau_\epsilon(\beta_\epsilon). \tag{3.10}$$

Following this principle and using the expressions for optical depth laid out in equations (3.2)-(3.5) the error in the optical depth due to errors in the line strength (*S*) is,

$$\tau_\epsilon(S_\epsilon) = \mu \frac{PL}{kT} \sum_i^N S_i(T) \frac{1}{\pi} \left[\frac{\alpha_i}{(\nu - \nu_i + \delta_i)^2 + \alpha_i^2} \right] = \mu \tau_H. \tag{3.11}$$

whist for self-broadened half-width (α_i) it is

$$\tau_\epsilon(\alpha_\epsilon) = \frac{PL}{kT} \sum_i^N S_i(T) \frac{1}{\pi} \left\| \left[\frac{\alpha_i}{(\nu - \nu_i + \delta_i)^2 + \alpha_i^2} \right] - \left[\frac{(1+\varphi_i)\alpha_i}{(\nu - \nu_i + \delta_i)^2 + \left((1+\varphi_i)\alpha_i\right)^2} \right] \right\|. \tag{3.12}$$

Here μ and φ_i are the fractional errors in S_i and α_i respectively. As it would seem unrealistic that all lines had the maximum error, it was decided that the middle value of each category would be assumed as an error. If a line has an uncertainty code of 3 or less then it is assumed there is an error of 20%. As noted in the last section the error codes for intensities are the same for all lines (5-10 %). This means that μ has a value of 0.075 for all lines between 1200-8000 cm^{-1} and thus is brought outside of the summation term. So, if we assume that other sources of error in HITRAN can be neglected and that all errors are independent, then the total error resulting from HITRAN is,

$$\tau_\epsilon(HITRAN) = \sqrt{(\tau_\epsilon(S_\epsilon)^2 + \ \tau_\epsilon(\alpha_\epsilon)^2)}. \tag{3.13}$$

Figure 3.14 shows $\tau_\epsilon(\alpha_\epsilon)$, $\tau_\epsilon(S_\epsilon)^2$ and $\tau_\epsilon(HITRAN)$ between 3591 and 3600 cm^{-1} compared to the measured optical depth and the optical depth predicted using HITRAN 2004. Apart from in the line centres the errors due to the half-widths are dominant. It can be seen that while the errors are large they are still not as large as the continuum (i.e. the difference between the measured and predicted) in some of the micro-windows. A similar picture was found in all spectral regions investigated.

It should also be noted that HITRAN does not include parameters of some very weak lines (~S <10^{-26} cm^{-1}/molecule.cm^{-2}). Schwenke and Partridge (2000) database have produced an *ab initio* water vapour line list, which includes such weak lines. However, it can be shown (Ptashnik, Personal communication) that the contribution of these lines is negligible when deriving the continuum using HITRAN 2004. For this reason the errors due to these lines not being included are ignored.

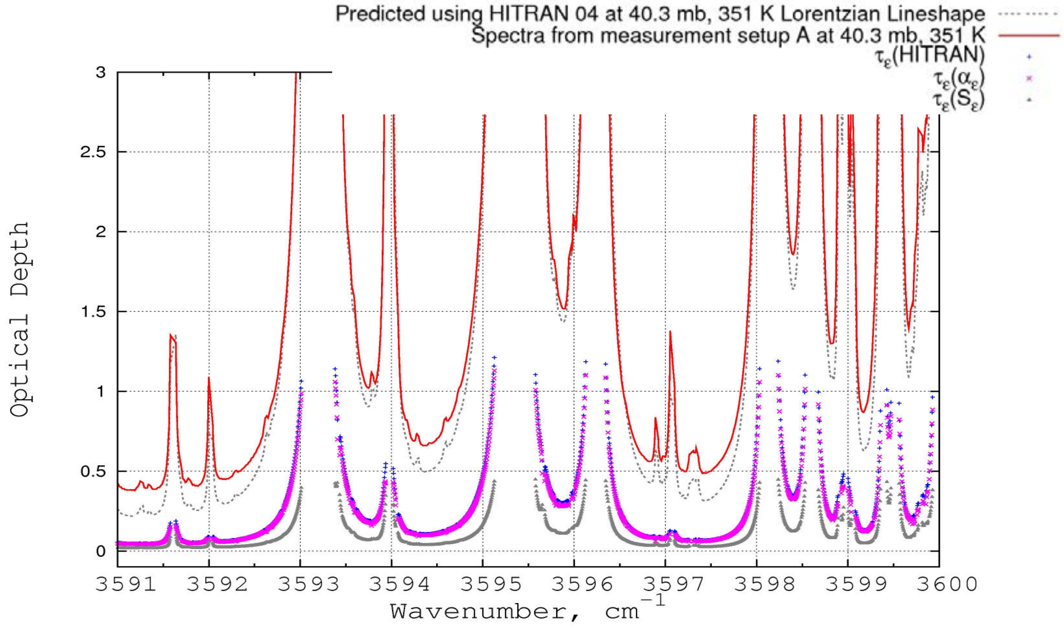

Figure 3.14 The measured optical depth (red line) and the optical depth calculated for the measurement conditions using HITRAN 2004 (light grey line). The uncertainty in the calculated optical depth resulting from uncertainties in HITRAN 2004 line intensities (dark grey dots), self broadened half-widths (purple dots) and the combination of the two (blue dots) is also shown.

3.4. Analysis of measured spectra

As was stated at the beginning of this chapter, the continuum is defined as the difference between an accurately measured optical depth and the optical depth calculated for the measurement conditions using the HITRAN line list. This section will show examples of this difference and then investigate sources of error that could explain them. The effects of the instrument line shape, and whether there is any advantage over using a Voigt profile compared to a Lorentzian when deriving the continuum, is then discussed. The possibility of some CO_2 detected in the cell affecting the derivation of the continuum is then looked at. Finally each of the errors resulting from pressure and temperature, noise and baseline is then modelled and their impact upon the continuum discussed.

3.4.1. Comparing measured and calculated spectra

Figure 3.15 shows the measured optical depth between 3351 and 3358 cm^{-1} at 40.3 mb and 351 K and that predicted using the parameters in HITRAN 2004 with a Voigt profile convoluted with a Sinc function instrument line shape (see 2.11.3). Apart from at the very line centre, there is good agreement between the two spectra. This slight disagreement at the line centres is most likely the result of the resolution of the measurements being not quite high enough to resolve the peak properly. As Figure 3.6 tells us, this region of the spectrum is shifted away from the strongest water vapour absorption lines. In Figure 3.16 the same comparison is made, but between 3591 and 3600 cm^{-1}, where there are far stronger water vapour lines. In this area the measured absorption is greater than that predicted. The difference between the two, while varying slightly from one micro-window to the next, is apparent throughout the spectrum. It is this slowly changing and unstructured absorption that typifies the continuum. The properties of the continuum will be studied in more detail in the next chapter. This rest of the section will deal with sources of errors that could affect the continuum.

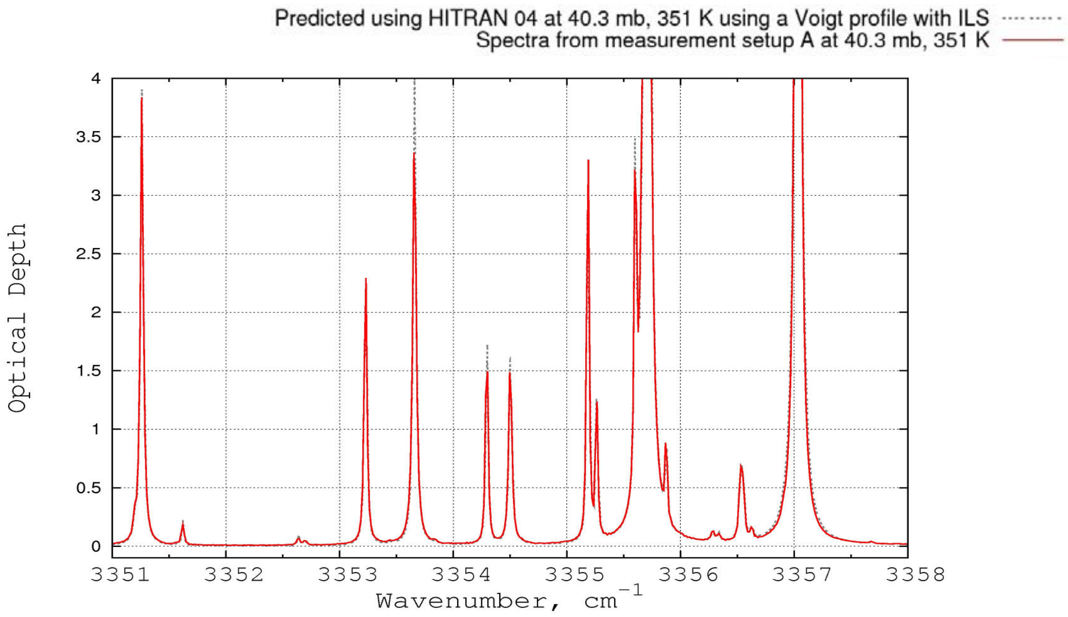

Figure 3.15 The measured optical depth (red line) compared to that predicted using HITRAN 2004 for the measurement conditions (grey line). Note in most areas the two lines are indistinguishable.

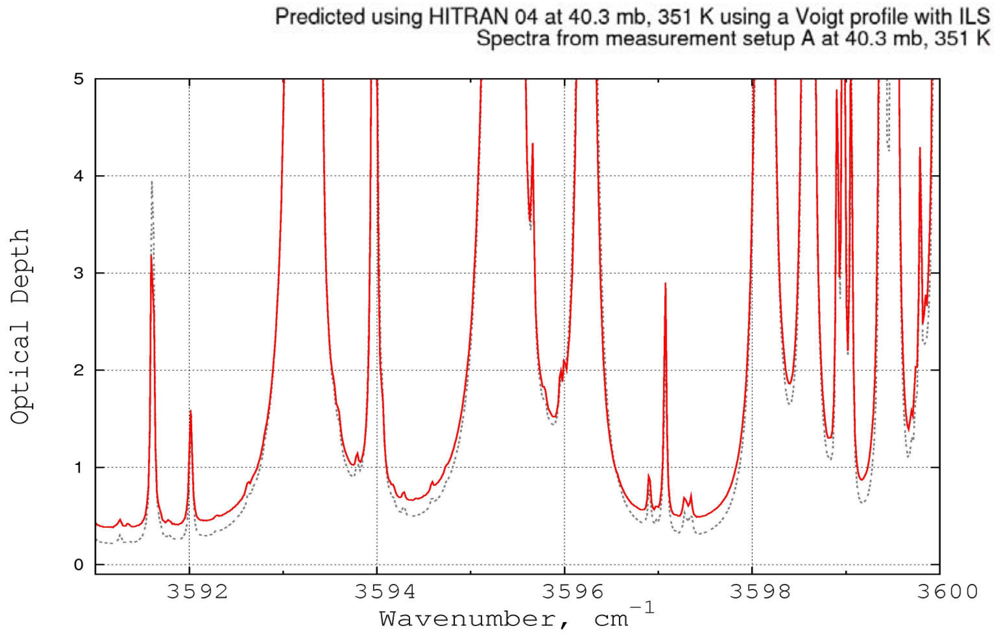

Figure 3.16 The measured optical depth (red line) compared to that predicted using HITRAN 2004 for the measurement conditions (grey line).

3.4.2. The effect of instrument and Voigt line shapes

The formulation presented in section 3.2 for calculating the optical depth makes the assumption that broadening is solely caused by collisions and that the effects due to Doppler broadening and instrument line shape (ILS) can be neglected. As discussed in section 2.4 when both Doppler and pressure broadened half-widths are of a similar value, a numerical convolution of the two called a Voigt line shape is used. The Doppler half-width is given by,

$$\alpha_{D_i} = v_i \sqrt{\frac{2ln2kT}{mc^2}}, \tag{3.14}$$

where the symbols have their usual meanings and v_i is the line centre. Due to the temperature and wavenumber dependence, the value for α_D varies over the measured region from a minimum of 0.002 cm^{-1} at 1200 cm^{-1} and 296 K to a maximum of 0.012 cm^{-1} at 8000 cm^{-1} and 351 K. As can be observed from Figure 3.8, the value for the Lorentzian self-broadened half-widths vary from about 0.15 cm^{-1}atm^{-1} to 0.5 cm^{-1}atm^{-1}. The lowest pressure at which measurements were made was around 20 mb. This translates to the narrowest Lorentzian half-widths being around 0.003 cm^{-1}; which suggests for low pressure measurements at least, that Doppler broadening will have an effect upon the line shape. However, as can be seen in Figure 3.17 even when the Doppler half-width is significantly broader than the Lorentzian, Doppler broadening will only dominate near the line centre; as soon as one moves greater than five Doppler half-width (~0.06 cm^{-1}) away from the line centre nearly all of the line contribution is Lorentzian. As the continuum is derived in the micro-windows which are normally at least 3 or 4 half-widths away from the line centres, neglecting the Doppler component is a valid assumption. This is demonstrated in Figure 3.19 panel A, where the difference between the optical depths calculated using a Voigt and Lorentzian line shapes is seen to be negligible.

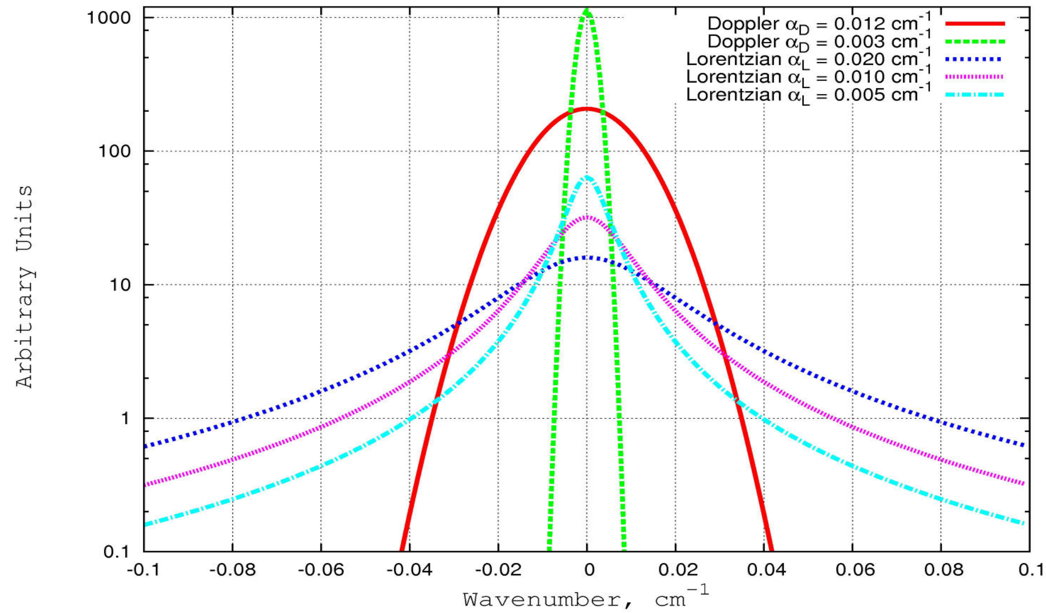

Figure 3.17 The Doppler lines shape predicted at 7000 cm^{-1} and 351 K (α_D=0.012 cm^{-1}) and at 1600 cm^{-1} and 296 K (α_D = 0.003 cm^{-1}) compared to various Lorentzian line shapes calculated with typical self-broadened half-widths for water vapour lines at 20 mb and 296K.

The ILS will cause the line shape to be convoluted with a Sinc function of the form,

$$ILS = 2\frac{0.9}{R}sinc\left(\frac{2\pi(v - v_i)}{R}\right), \tag{3.15}$$

where the v_i is the line centre and R is the spectral resolution, which is 0.03 cm^{-1} for these measurements, This results in an ILS half-width 0.02 cm^{-1}. The estimated ILS is shown in Figure 3.18. As with the Doppler half-width this is of a similar value to the Lorentzian half-widths at lower pressures. However, also similar to the Doppler line shape its effect on the line shape diminishes away from the line centre. As can be seen in Figure 3.18, in this region the ILS results in a periodic oscillation in the spectrum which decreases further away from the lines centre. It is important that these oscillations are not of a similar magnitude to the continuum. Panel B of Figure 3.19 shows the effect of ILS in a micro-window where the continuum absorption is very weak. The ILS clearly models the measured spectrum better than if it is not included, but even in weak absorbing regions the oscillations are less than the difference between the measured and calculated spectra.

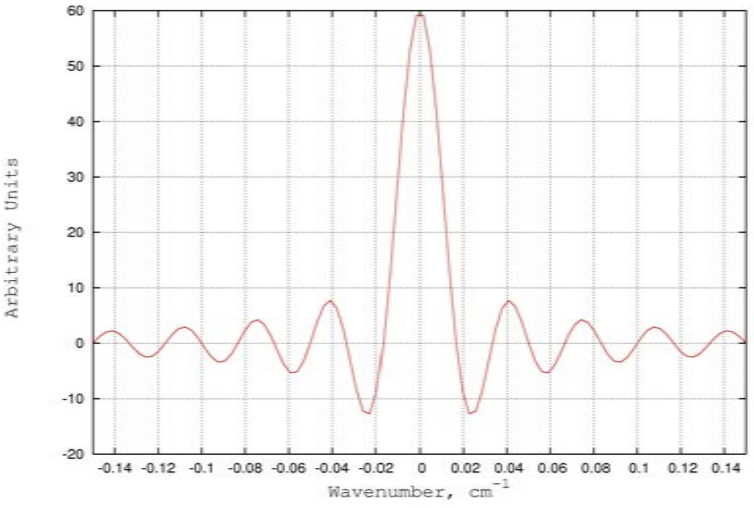

Figure 3.18 The estimated ILS for a line centred at 0 for boxcar apodization at the resolution of 0.03 cm^{-1}.

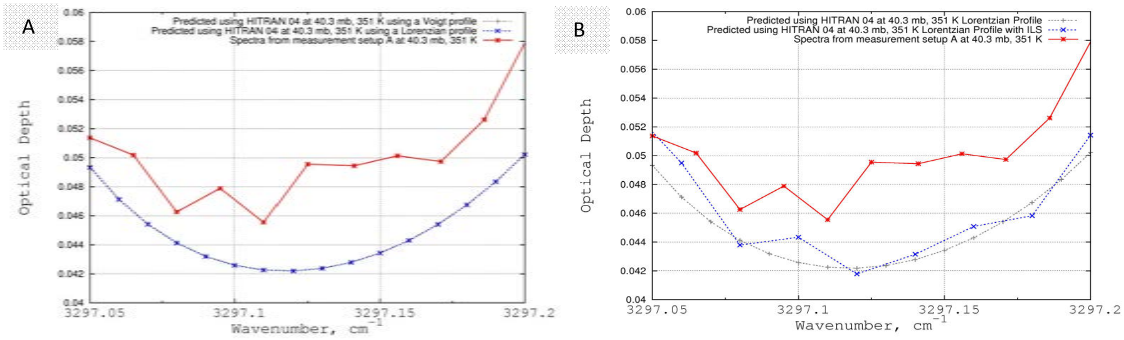

Figure 3.19 Panel A compares the measured water vapour spectrum (red line) to that predicted using HITRAN 04 with a Lorentzian line shape (grey line) and a Voigt line shape (blue line). Panel B compares the same, but the effect of the ILS is also are included (blue line).

In summary, whilst both Doppler and ILS broadening clearly have an effect on the measured spectra near the line centres, for the measurement condition as soon as one moves beyond about 5 half-widths from the line centres Lorentzian broadening does becomes dominant and it is these areas which are of interest. This point is highlighted in Figure 3.20 which shows that the difference between the spectra calculated using Voigt and ILS profiles and just a simple Lorentzian is very small compared (in fact undetectable on the scale of this figure) to the difference between theoretical and measured spectra.

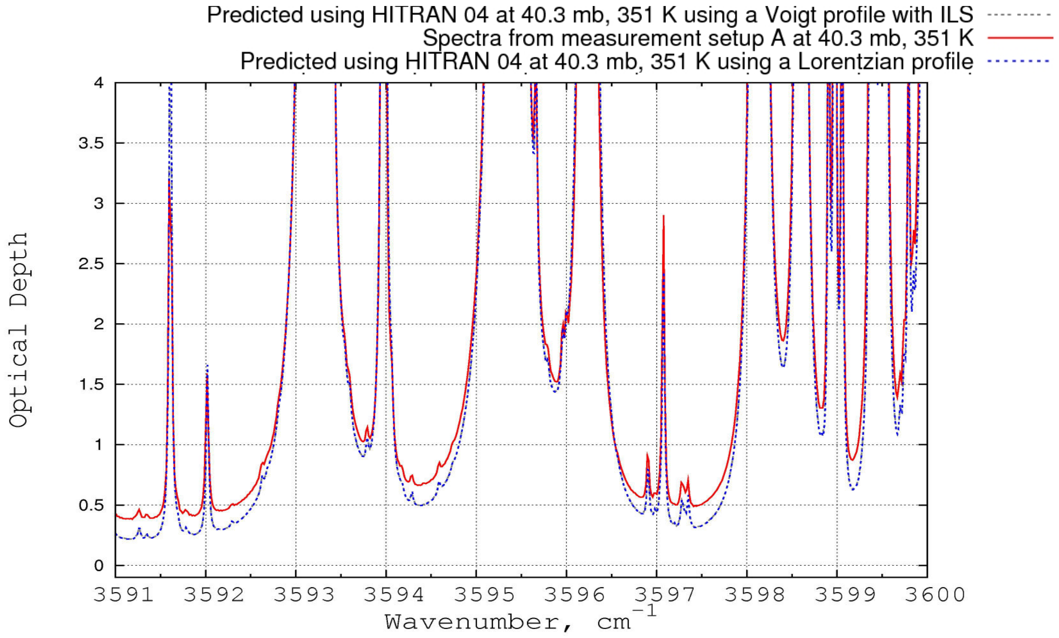

*Figure 3.*20 *The measured spectra (red line) compared to that calculated for the measurement conditions using a Lorentzian line shape (grey line) and secondly calculated using a Voigt line shape convoluted with the ILS shown in Figure 3.18 (blue line). Note, that the blue and grey lines are indistinguishable.*

3.4.3. Excluding the line centres

In order to derive the continuum accurately the line centres are excluded. This is firstly because, as has been previously discussed, near the line centres errors from HITRAN, the Voigt profile and ILS are all significant. Secondly at the resolution which these measurements are conducted, the line centres are not properly resolved, this could result in unphysical artefacts appearing when the continuum is derived. Thus, in common with other authors (Burch 1982; Burch 1984; Burch 1985; Tobin et al. 1996; Ptashnik et al. 2004) the line centre is excluded when deriving the continuum to minimise the effect of these errors.

On potential way of doing this is to derive the continuum only in regions where, when calculating the optical depth the α_i^2 term in the denominator can be ignored and equation (3.7) can be considered a valid approximation. Consider that the optical depth calculated using HITRAN for the measurement conditions is given by $\tau_H(\nu)$. A point is allowed if the difference between the optical depth calculated with and without the α_i^2 term in the denominator less than a certain fraction (F) of the calculated optical depth. That is to say we allow a point in the spectra if,

$$\mathrm{F}\tau_H(\nu) > \frac{P_s L}{kT}\sum_{i}^{N} S_i(T)\frac{1}{\pi}\left\{\left[\frac{\alpha_i}{(\nu_i - \nu + \ \delta_i)^2}\right] - \left[\frac{\alpha_i}{(\nu_i - \nu + \ \delta_i)^2 + \alpha_i^2}\right]\right\}, \tag{3.16}$$

is satisfied, where the symbols are as defined previously. However, such a method does not account that for very narrow lines the ILS or Doppler broadening could cause a deviation away from the Lorentzian. For this reason an additional value of 0.03 is added to the α_i in the dominator. This results in a filter of,

$$\mathrm{F}\tau_H(\nu) > \frac{P_s L}{kT}\sum_{i}^{N}\frac{1}{\pi}\left\{\left[\frac{\alpha_i}{(\nu_i - \nu + \ \delta_i)^2}\right] - \left[\frac{\alpha_i}{(\nu_i - \nu + \ \delta_i)^2 + (0.03 + \alpha_i)^2}\right]\right\} \ = \tau_\epsilon(lineshape) \tag{3.17}$$

Figure 3.21 shows an example of how the filter works for the narrow line with a α_i value of 0.005 cm^{-1}. Here the difference is shown (light blue line) between the line calculated with the α_i in the denominator set to zero (dark blue) and with it set to 0.035 cm^{-1} (i.e. 0.005 +0.03) (purple). The width of the line is also shown without the extra 0.03 cm^{-1} added to the denominator (green) along with the widest Doppler line for this work (red). It can be seen that the difference is sufficient that by setting an appropriate value of F so to exclude the region around the line centre of even the narrowest line that might be affected by Doppler broadening or ILS. In this work F is set to 0.02 unless mentioned otherwise. Figure 3.22 shows how the $\tau_\epsilon(lineshape)$ function behaves between 3591 and 3600 cm^{-1}. Notice how between the lines it is much smaller than the difference between the measured and calculated optical depth.

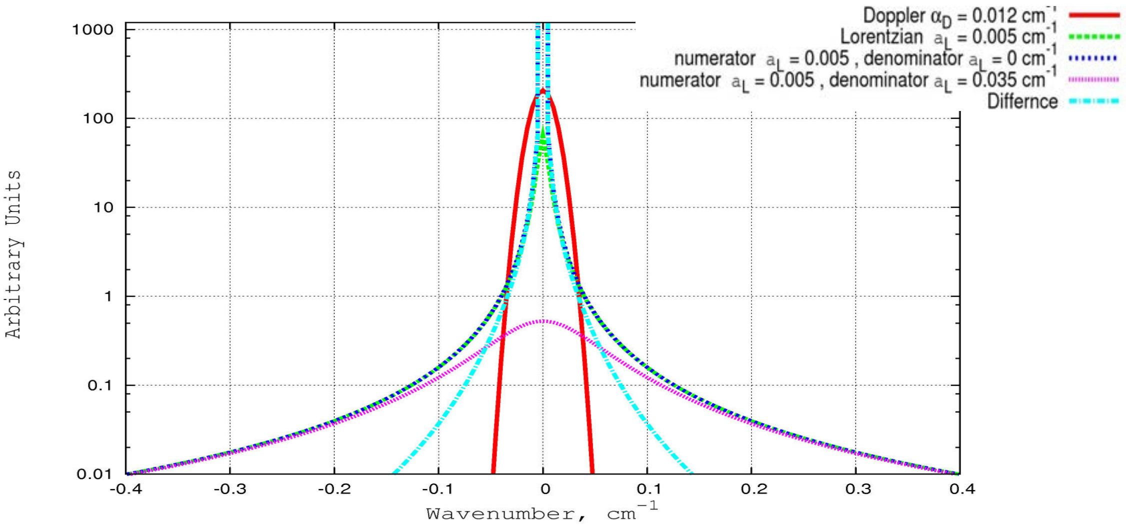

Figure 3.21 The difference (light blue line) between a Lorentzian line shape with a half-width of 0.005 cm^{-1}, but with the half-width value in the dominator set to zero (dark blue line) and it set to 0.035 cm^{-1} (purple line). The line shape of this line without these alterations is also shown (green line) along with the widest Doppler line for the spectral region measured (red).

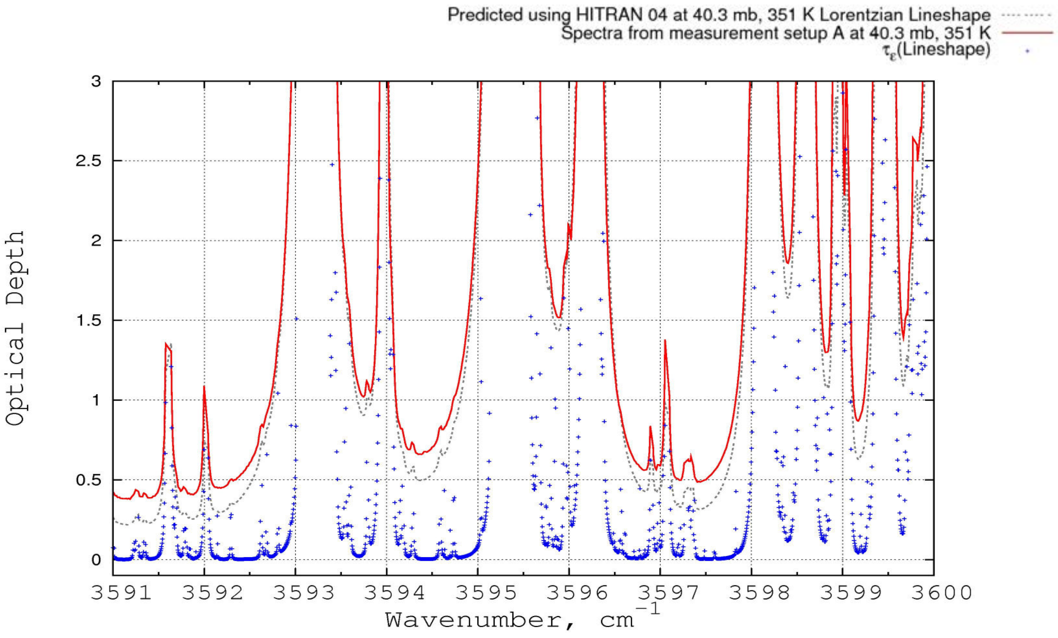

Figure 3.22 The measured spectra (red line) compared to that calculated for the measurement conditions using a Lorentzian line shape (grey line). The optical depth of the line shape filter function (τ_ϵ(lineshape)) for the measurement conditions is shown. It can be seen that between the line centres this error is very much smaller than the difference between the measured and calculated spectra.

3.4.4. CO_2 Spectra

It can be seen that in both panels of Figure 3.5 between 2200 cm^{-1} and 2400 cm^{-1} there is a noticeable amount of CO_2 in the spectra. Figure 3.23 Panel A shows an example of the spectra observed in a typical measurement. As this is not present in the background measurement it is assumed that it is leaking in with the water vapour. It could enter the cell either from being absorbed in the water vapour or through air leaking into the cell. Observing CO_2 in the spectra is troubling for two reasons. Firstly, its presence in the spectra could lead to inaccuracies in deriving the continuum. And secondly because if it is caused by an air leak then it could cause a falsely high measurement of cell vapour pressure (i.e. one is measuring air pressure rather than vapour pressure).

For these reasons, it is important to quantify the amount of CO_2 present. The strength of the CO_2 lines seemed to vary for different water vapour measurements, but in general it increased proportionally to the pressure of the water vapour. Determining the amount of CO_2 in the cell by fitting the lines using HITRAN 2004 data proved difficult. Fitting to the line width resulted in too strong absorption in the line centres. Likewise, if one tried to fit the line centres, the widths were found to be too narrow. This result is shown in Figure 3.23 Panel B. Hence, it appeared that the lines in HITRAN were too narrow. This should not be too surprising as when calculating the optical depth foreign broadening half-width are used. These are measured for CO_2 in air, not in water which has a larger dipole moment and thus results in broader lines.

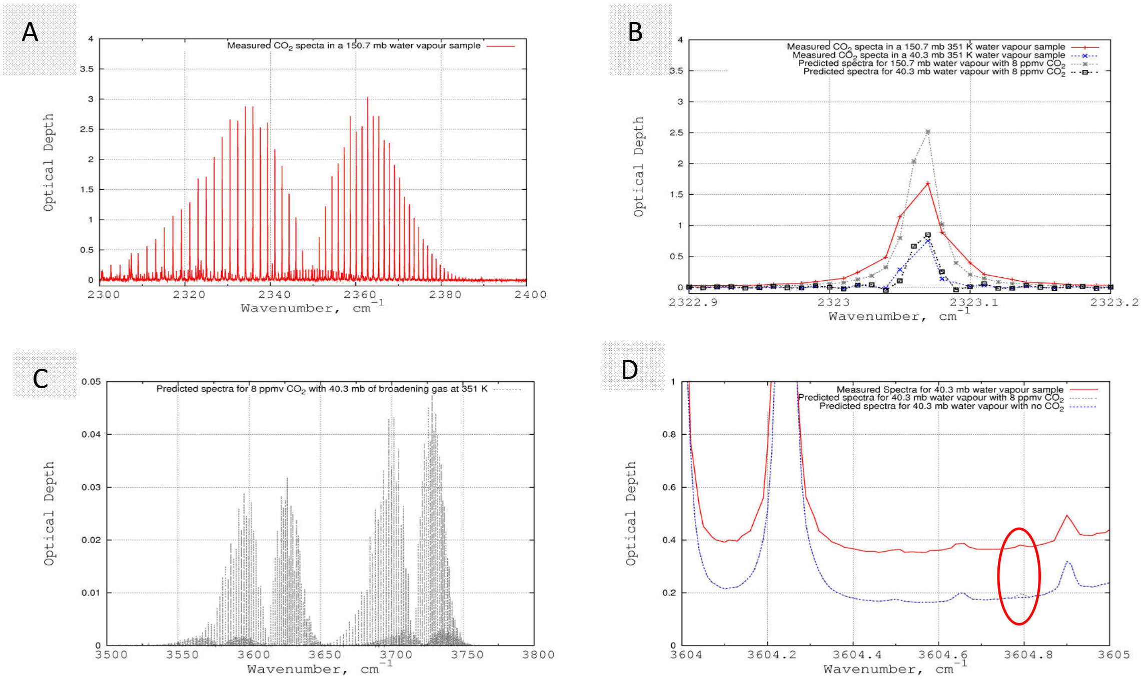

Figure 3.23 Panel A: A typical measured spectrum of CO_2 from these measurements. Panel B: The attempts to fit a spectrum calculated using HITRAN 04 to that measured. However, it can be seen that the measured line width are wider than those predicted. Panel C: The calculated spectrum between 3500 and 3800 cm^{-1} for 8ppmv of CO_2 in a non-absorbing broadening gas. Panel D: The measured spectrum (solid red line) compared to that predicted using HITRAN 04 with (dotted grey) and without 8ppmv CO_2 (dotted blue). Within the circled area a slight deviation between the two calculated lines is observed (grey is higher than blue). In the same area a slight deviation in the measured spectra is also seen.

For this reason it was not possible to estimate the amount of CO_2 by fitting the lines per se. Instead, the amount of CO_2 was estimated by equating the integrated area under the calculated and measured spectra. Through this analysis it was found that the amount of CO_2 varies between 4 ppmv and 8 ppmv. This can then be used to estimate the maximum amount of air that could have leaked into the cell. If one assumes that there is there is 380 ppmv CO_2 in the ambient air, then is possible that about 2% of the total measured pressure is air. If this was the case, it would lead to an underestimate of the continuum.

However, for the reasons listed in section 3.1.4 (i.e daily leak tests performed and the repeatability of measurements) it seems unlikely that there was an air leak during the measurement process. Therefore, it is more likely that some CO_2 was absorbed in the water vapour sample.

The next issue is whether the amount of CO_2 found in measurements will affect the derived continuum. In the region between 2200-2400 cm^{-1} the CO_2 does not present a problem, as the water vapour absorption here is too weak to obtain a continuum. However, there is another weaker band between 3500-3800 cm^{-1}. In Figure 3.23 Panel C the predicted optical depth for CO_2 with 8 ppmv in 40.3 mb of broadening gas is shown. It can be seen that some of the strongest lines have an optical depth of almost 0.05, which should be detectable. This is confirmed in Panel D where the measured water vapour spectrum between 3604 and 3605 cm^{-1} is compared to the spectra calculated for the measurement conditions with and without CO_2. The circled area highlights where a CO_2 line is detectable in both the measured and calculated spectra. However, the value is very small compared to the difference between the measured and calculated spectra and only covers a very small wavenumber range. Compared to other possible sources of error discussed in the next sections this one is regarded as small enough to ignore.

3.4.5. Errors in pressure and temperature measurements

It is very important to know accurately both the temperature and pressure at which the measurements are conducted. Errors in either would result in the optical depth being calculated not for the actual measurement conditions and thus lead to an incorrect continuum. This section will investigate the magnitude of pressure and temperature errors and then investigate their effect upon the calculated spectra.

The Baratron 625B pressure gauge used has an accuracy of 0.25%. However, this accuracy was also limited by the digital display read out that would only give the pressure in 0.1 Torr (0.133 mb) increments. There was also a potential offset error, because after a measurement when the cell was pumped down it was also observed that the pressure gauge would return to either -0.1 Torr or 0.1 Torr.

During the FTS measurement process, a small drop in the vapour pressure was observed as the measurement progressed. In general the vapour pressure was very stable with an average decrease of 0.6 %, although for a few measurements above 200 mb, a decrease of up to 2% was observed. However, as the recorded pressure is actually the average of ten pressure measurements taken throughout the measurement process, the effect of this change is to some degree minimised. This decrease in pressure is most likely a mixture of water vapour distributing around the cell, water vapour being absorbed by the cell walls and water vapour condensing on cold spots in the cell. It is most likely that the latter two processes are dominant, as the two humidity sensors in the cell also measured a decrease. The effect of water vapour condensing is only a problem when the amount of water vapour in the cell nears saturation vapour pressure. This is most likely why the measurements at higher pressures have a larger decrease.

Given these various factors it would seem fair to assume that there is an error in pressure measurements of ±1% or ±0.5 mb depending on which is greater.

The temperature thermistors have a stated accuracy of ±0.2 K. There are 6 thermistors distributed throughout the cell. The temperature in the cell is obtained by taking the average of the temperature from these. Throughout the measurement process the temperature was observed to be very stable, varying less than 0.2 K. Themistors near each other in the cell agreed within the specified accuracy. For all measurements thermistors T2-T5 (see Figure 3.1 for positions) had a range no greater than 0.3 K. However, sometimes T1 would have a value of up 0.5 K greater or less than the average of T2-T5. This gradient was caused by not quite getting the heater at the base of the cell in equilibrium with the temperature of the immersion heater. Given these various factors it is assumed that the temperature error is ± 0.5 K.

Following the same method for defining errors resulting from HITRAN, the error in calculated optical depth (τ_ϵ) resulting from an error in pressure P_ϵ at a pressure P_s can be defined as,

$$\tau_\epsilon(P_\epsilon) = |\tau(P_s) - \tau(P_s + P_\epsilon)|. \tag{3.18}$$

Likewise, as with the HITRAN errors the modulus notation is used, as this analysis assumes that a negative value of P_ϵ will have a same magnitude of effect upon the optical depth as a positive one. That is to say that,

$$|\tau(P_s) - \tau(P_s + P_\epsilon)| \approx |\tau(P_s) - \tau(P_s - P_\epsilon)|. \tag{3.19}$$

In the micro-windows away from the line centres using equation (3.3) - (3.7) it can be seen that the optical depth has a squared dependence on pressure. This allows us to say that,

$$\tau(P_s + P_\epsilon) = \frac{(P_s + P_\epsilon)^2}{P_S^2}\,\tau(P_s), \tag{3.20}$$

and that can be written as,

$$|\tau_\epsilon(P_\epsilon)| = \left|\tau(P_s)\left(1 - \frac{(P_s + P_\epsilon)^2}{{P_s}^2}\right)\right| = \tau(P)\frac{2P_sP_\epsilon + P_\epsilon^2}{P_s^2}, \tag{3.21}$$

and as $P >> P_\epsilon$ the approximation can be made that,

$$|\tau_\epsilon(P_\epsilon)| \approx \left(\frac{2P_\epsilon}{P_s}\right)\tau(P_s). \tag{3.22}$$

Furthermore, if the assumption is made that that $P_\epsilon = 0.01P$ leave us with the end result that,

$$|\tau_\epsilon(P_\epsilon)| \approx 0.02\tau(P_s). \tag{3.23}$$

The error in temperature dependence is more complex as the abundance, self-broadened half-width and the line intensity all have temperature dependences. Furthermore, this error will vary across the spectra as these latter two vary depending on the spectral line. Suppose we want to find the error in optical depth $\tau_\epsilon(T_\epsilon)$ resulting from an error in temperature, making the same assumptions as with pressure this can be written as,

$$|\tau(T_\epsilon)| = |\tau(T) - \tau(T - T_\epsilon)|. \tag{3.24}$$

Making use of equations (3.3) - (3.6) we can write the optical depth in terms of a temperature independent variable (A) and 3 variables that reflect the temperature dependence of the different parameter. When calculating the optical depth for N lines, we can say that

$$\tau_{\mathrm{H}}(\mathrm{T}) = \mathrm{Q}(\mathrm{T})\sum_i^N \mathrm{A_i}(\mathrm{T})\beta_\mathrm{i}(\mathrm{T})\gamma_\mathrm{i}(\mathrm{T}), \tag{3.25}$$

where $\mathrm{A_i} = \frac{1}{\pi}\ \frac{\mathrm{P_s L}S_i(T_0)\left(\frac{\mathrm{P}}{\mathrm{P_0}}\right)\alpha_\mathrm{i}^0}{\mathrm{k}(v_i - v_0)^2}$, $\mathrm{Q(T)} = \frac{(174.63+0.924(T-T_0))}{174.63\,T}$, $\beta_\mathrm{i}(\mathrm{T}) = \left(\frac{T_0}{T}\right)^{n_i}$,

$$\gamma_\mathrm{i}(\mathrm{T}) = \exp\left(-c_2E_i\left(\frac{1}{T_0} - \frac{1}{T}\right)\right).$$

This means that,

$$|\tau_\epsilon| = \left|\sum_i^N \mathrm{A_i}[\mathrm{Q(T)}\beta_\mathrm{i}(\mathrm{T})\gamma_\mathrm{i}(\mathrm{T}) - \mathrm{Q}(\mathrm{T}+\mathrm{T}_\epsilon)\beta_\mathrm{i}(\mathrm{T}+\mathrm{T}_\epsilon)\gamma_\mathrm{i}(\mathrm{T}+\mathrm{T}_\epsilon)]\right|. \tag{3.26}$$

The values of the different variables for a 1 K error in temperature at 351 K, assuming typical values for a water vapour line (n= 0.64, T = 351 K, E = 300 cm^{-1}) are presented in Table 3.5. It can be seen that to some degree these cancel each other out. In Figure 3.24 the percentage error in the calculated spectra arising from both errors in temperature and pressure as a function of wavenumber is shown. Double the error value suggested in this chapter is used to give a better idea of the sensitivity. This demonstrates that the error due to temperature is less than that due to pressure, especially at 40 mb, but that the percentage error in temperature is far more variable than pressure. In fact the error due to temperature can change by almost an order of magnitude over small spectral regions.

Variable	T	$T + T_\epsilon$
$T_0\alpha$	1.088	1.097
β_i	0.896	0.893
γ_i	1.233	1.237
$\alpha_i\beta_i\gamma_i$	1.204	1.213

Table 3.5 The value of the different temperature dependent variables calculated at T= 351K and T+T_ϵ, where T_ϵ = 1 K, n = 0.64. and E= 300 cm^{-1}

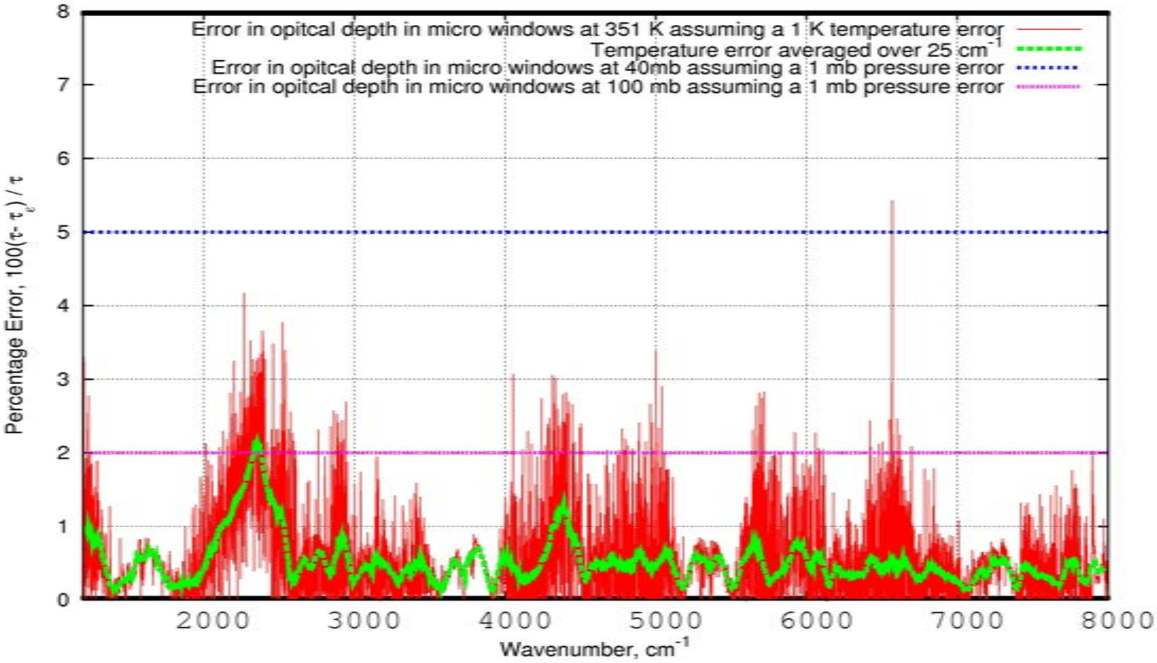

Figure 3.24 The percentage error in optical depth, resulting from two times the estimated errors given in the text, for temperature (red) and pressure (error at 40 mb shown in blue, 100 mb in purple).

Figure 3.25 Panel A and B shows the typical effect of the errors in pressure and temperatures respectively upon the calculated spectra compared with the measured spectra. It illustrates that in this region at least the error due to temperature is very small compared to the difference between the calculated and measured spectra. However, while this is the case for pressure in most micro-windows, in a few the errors in pressure is as big as the difference between the two.

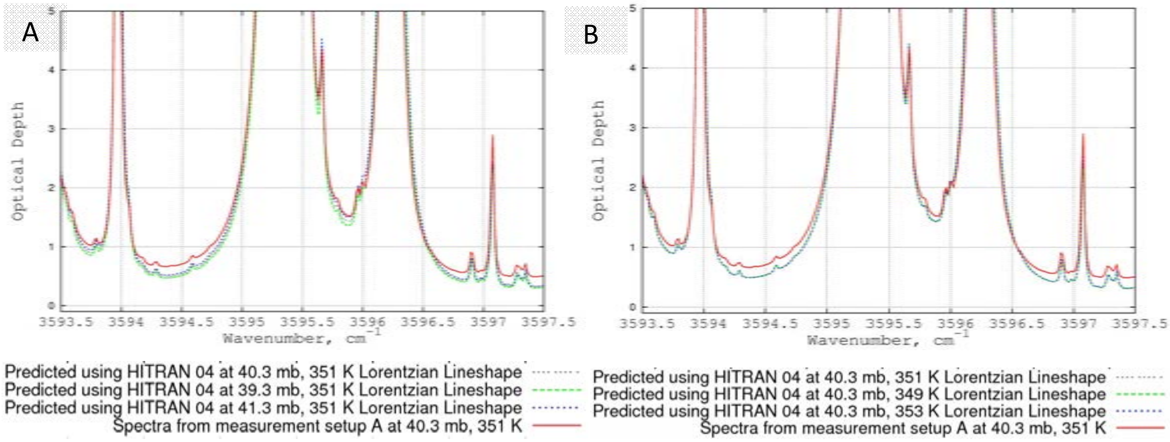

Figure 3.25 The measured spectra compared to the spectra calculated for the measurement conditions using HITRAN 2004 with the minimum and maximum pressure (Panel A) and temperature (Panel B) for the measurement In panel B the error in temperature is small enough to make the different lines indistinguishable. Note in panel B four times the actual estimated temperature error is assumed to test the sensitivity.

3.4.6. Errors due to Noise

Noise has the most effect on the accuracy of the measured absorption at large and small optical depths. In the latter case this is due to there being very little signal, while in the former saturation causes the measured transmittance to be almost zero. More formally the error in the continuum resulting from noise can be derived by considering the relationship,

$$\tau_m = -\ln\left(\frac{I_m}{I_b}\right), \tag{3.27}$$

where I_m and I_b are the measurement intensity and background intensity respectively (see Figure 3.6 to see how these vary with wavelength across the spectrum). If the magnitude of the noise in both I_m and I_b is defined as I_ϵ, the maximum error in the optical depth (τ_ϵ) can be estimated as,

$$\tau_\epsilon(noise) = \left|\ln\left(\frac{I_m + I_\epsilon}{I_b - I_\epsilon}\right) - \tau_m\right|. \tag{3.28}$$

A value of I_ϵ is obtained as the difference between the minimum and maximum value in the recorded intensity when there is no absorption measured. Figure 3.26 shows the percentage error in optical depth ($100|\tau_\epsilon(I_\epsilon) - \tau_m|/\tau_m$) as a function of optical depth assuming I_ϵ = 0.0002 for experimental setup A and I_ϵ = 0.002 for setup B. The reason for the difference in noise in setup A compared to setup B is that the former consisted of 100 scans, whilst the latter only of 50.

Because noise is a random error which varies rapidly with wavenumber and the continuum generally varies gradually with wavenumber means that until $\tau_{\epsilon} \sim \tau_c$ it should still be possible to detect the continuum. As often 30% of the measured optical depth is the continuum even with noise levels of 10% it should be possible to detect features. For experimental setup A it was generally possible to detect features providing the optical depth is greater than 0.01 and less than 6. Due to the greater amount of noise for setup B the tolerance value is between 0.04 and 5.

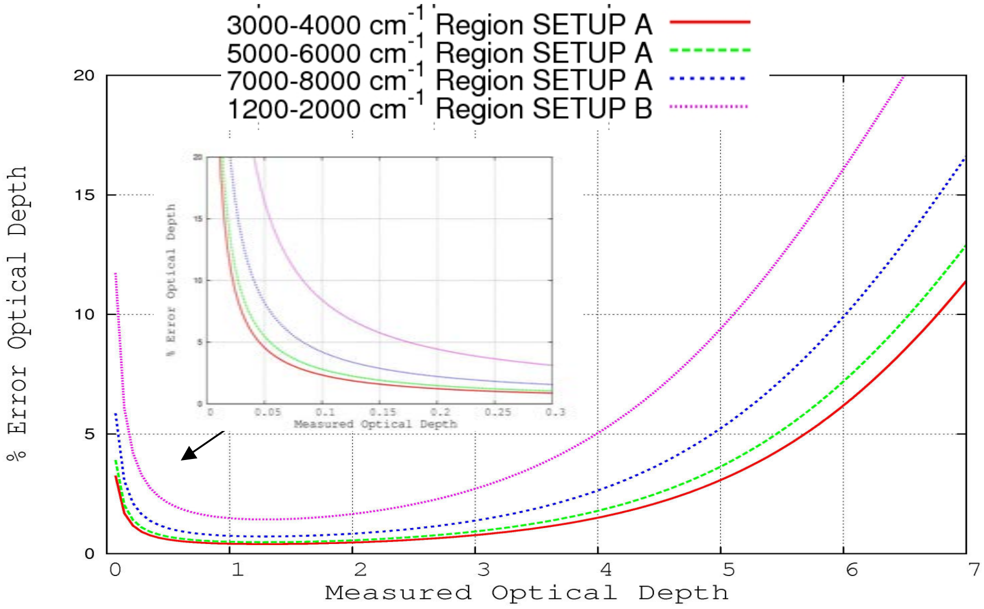

Figure 3.26 The percentage error in optical depth resulting from noise for the different experimental setups. The insert shows the expanded plot for low optical depths.

Therefore, when analysing individual measurements of the continuum taking into the account the error due to noise in general is not important; it will be readily apparent when noise is affecting the result. However, when comparing the same individual point from different measurements or looking at continuum features derived from small number of spectral points (i.e where it is not possible to cancel out the effect of noise through averaging) it is important to take noise into account.

3.4.7. Baseline error

A baseline error is caused when the measured intensity value for the same point in the spectrum drifts between the time of the background and sample measurement. There are numerous possible causes, such as changes in the light source intensity, changes in the mirror alignment (caused either by inputting of water vapour or air into the cell or small changes in temperature) and small amounts of condensation on the mirrors.

The drift of the baseline over the length of a 3 and 6 hour period for three separate measurement days is shown in Figure 3.27. Typically the drift in optical depth was around 0.01 to 0.02, although sometimes as much as 0.10. To minimise any possible effect of this drift, the time between the background and sample measurement should be as short as possible. However, this need has to be balanced with that of allowing the water sample to be distributed properly before a measurement is conducted (this typically took about 10 minutes). Originally it was proposed that for increased accuracy, the background used would be an average of background measurements taken before and after the sample measurement.

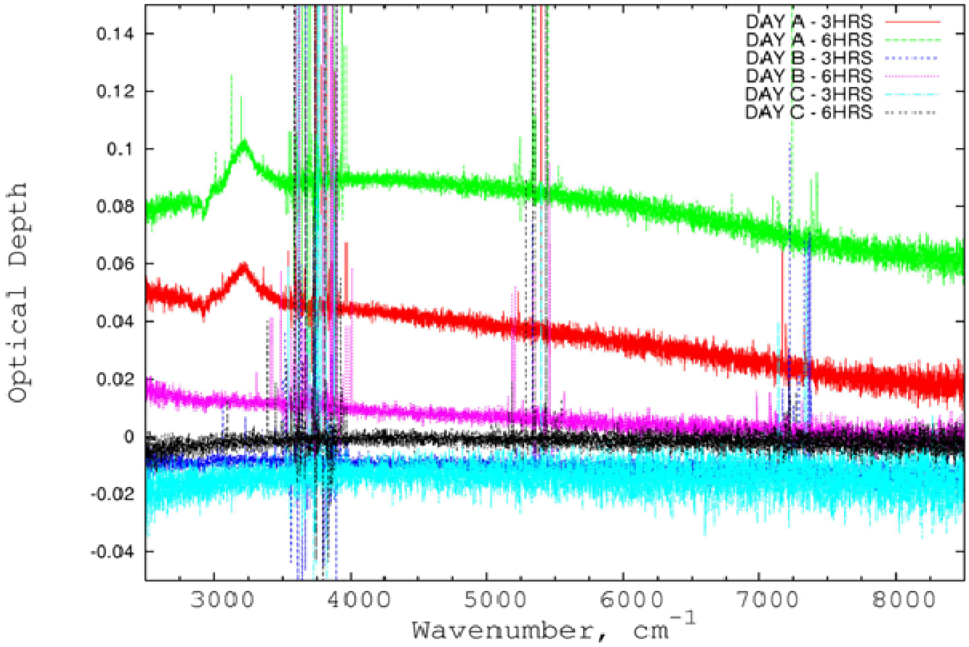

Figure 3.27 The optical depth of the baseline drift for 3 different days on which measurements were made. It can be seen that the amount of baseline drift varies with wavenumber. There is also a feature at 3200 cm^{-1} present in DAY A, which appears to be caused by ice forming on the detector.

However, it was soon discovered that due to the amount of time it took to pump down the cell after measurements, that it would take at least about hour to evacuate the cell by a sufficient amount. As can be seen from Figure 3.27 over this time period the drift in baseline could be significant.

There is a noticeable peak in the background around 3200 cm^{-1} in DAY A. This spectral feature was present in both background measurements and sample measurements and could be seen to increase in magnitude with time. Comparing this feature to the findings of Theocharous et al. (2005) it seems apparent that this is caused by ice growing on the detector. Indeed once the detector was properly evacuated the feature was seen to disappear, as can been seen for Day B and C. As the continuum is very weak in this region it is important to make sure that this is not present in the spectrum, as such a smooth broad feature could be mistaken for a water dimer.

Even when the time between background and measurement is reduced to a minimum, some baseline drift is still present. Some of this drift could result from changes in pressure and temperature causing the mirror alignment to change. Some backgrounds were attempted using N_2 in the cell at the same pressure at which the measurement is made. However, this seemed to have no effect upon the baseline shift. Most of the baseline error can be removed by assuming that at a certain wavenumber in the window region the measured absorption should be zero. A polynomial can be fitted to these zero points and then subtracted away from the measured absorption spectrum.

For setup A three points between 4300 cm^{-1} and 9000 cm^{-1} were chosen at 4680 cm^{-1} , 6225 cm^{-1}, 7990 cm^{-1} and a second order polynomial was fitted. Figure 3.28 shows four examples of baseline correction. In general the correction was around +/-0.005. Due to the sharp decrease in signal strength between 2500 and 2000 cm^{-1} and because of strong absorption beyond 3000 cm^{-1} the only other suitable points to set to zero in this region appears to be around 2490 cm^{-1}. Simply extrapolating the polynomial fitted in other regions seems to underestimate the required adjustment. Therefore, due to the lack of another 'zero' point a linear line between this point and the 4680 cm^{-1} point was fitted, the magnitude of these corrections is ~0.01. How accurate this is at correcting the baseline in the band is unclear.

For measurement set up B there are a few additional complications to fitting the baseline. At the lower wavenumber side of the spectrum the intensity of the source decreases significantly, even though there is still possible continuum absorption. As there is no ideal point to set to zero if was decided that 1200 cm^{-1} had the best balance between weak absorption and strong signal. The other side of the band, where there is far stronger signal and less absorption, a point at 2500 cm^{-1} is chosen. As there is only one main area of absorption for these measurements a linear fitting was performed to these two points.

In the case of lower pressure measurements (generally less than 100 mb) where any absorption in the wings can be considered negligible, setting the baseline to zero can be considered accurate. At higher pressures, where absorption in the band wings becomes strong enough to measure the continuum, applying a baseline correction could result in removing or adding to the continuum absorption. Therefore, in these cases the measurements are analysed with and without baseline correction. However, in general the effect of baseline correction upon the spectra is very small. As can been seen in Figure 3.28 the magnitude of the correction applied to the baseline is generally very small. A value of $\tau_{\epsilon(baseline)} = 0.01$ is assumed.

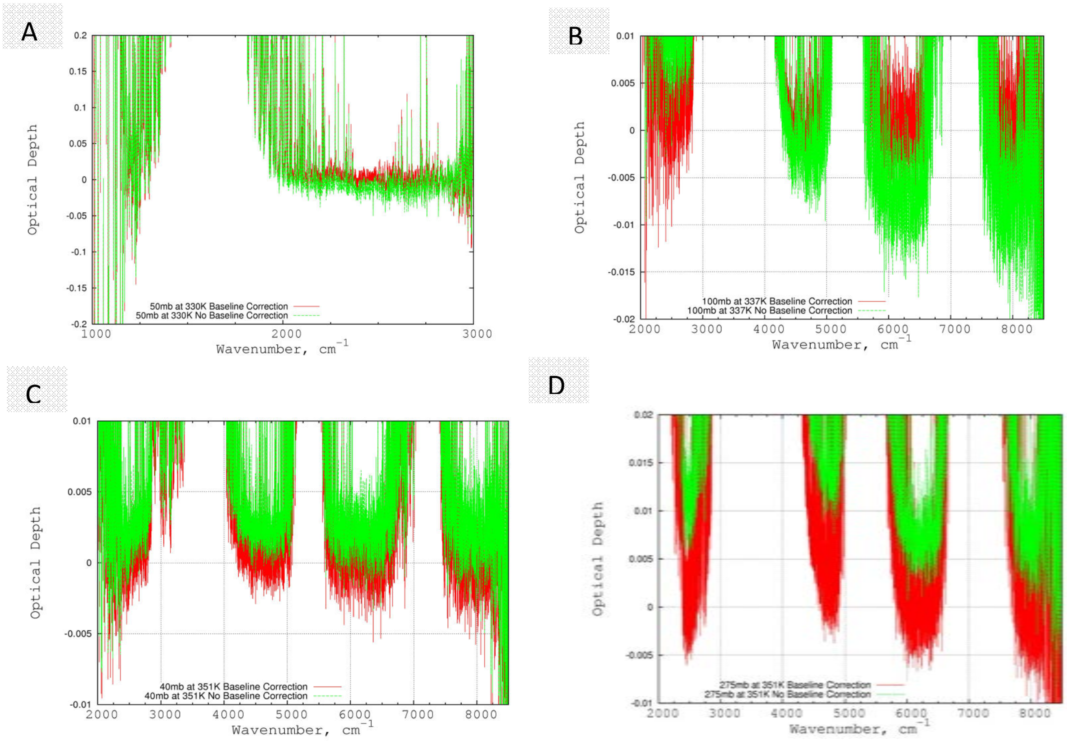

Figure 3.28 The measured optical depth with (red) and without (green) a baseline correction applied for different measurements. The measurement conditions are listed on each panel. Panel A was measured using setup B, and panels B-C with setup A.

3.5. Measureable areas of the spectrum

It is now possible to get a better idea in which spectral regions the continuum can be accurately derived using either setup A or B. Due to baseline errors and noise, in general it will not be possible to accurately measure optical depths below 0.05 or above 5 to more than a 20% accuracy. If it is assumed that the measured optical depth in the micro-windows will be approximately twice the MT_CKD continuum at 351 K, the pressure which corresponds to these bounds can be estimated at each wavenumber. This analysis is shown in Figure 3.29, where the area is coloured depending on the optical depth calculated at each wavenumber-pressure coordinate. If the value is less than 0.05 then it is deemed that it might not be possible to accurately measure the continuum in this region. These areas are shown in black. In the yellow areas where the optical depth is greater than 5 the continuum cannot be regarded as accurate, because of the effects of noise. In addition the value of 75% SVP is also shown, which can be seen as a maximum amount of vapour that can be put in the cell at a particular temperature, whilst still ensuring condensation does not occur.

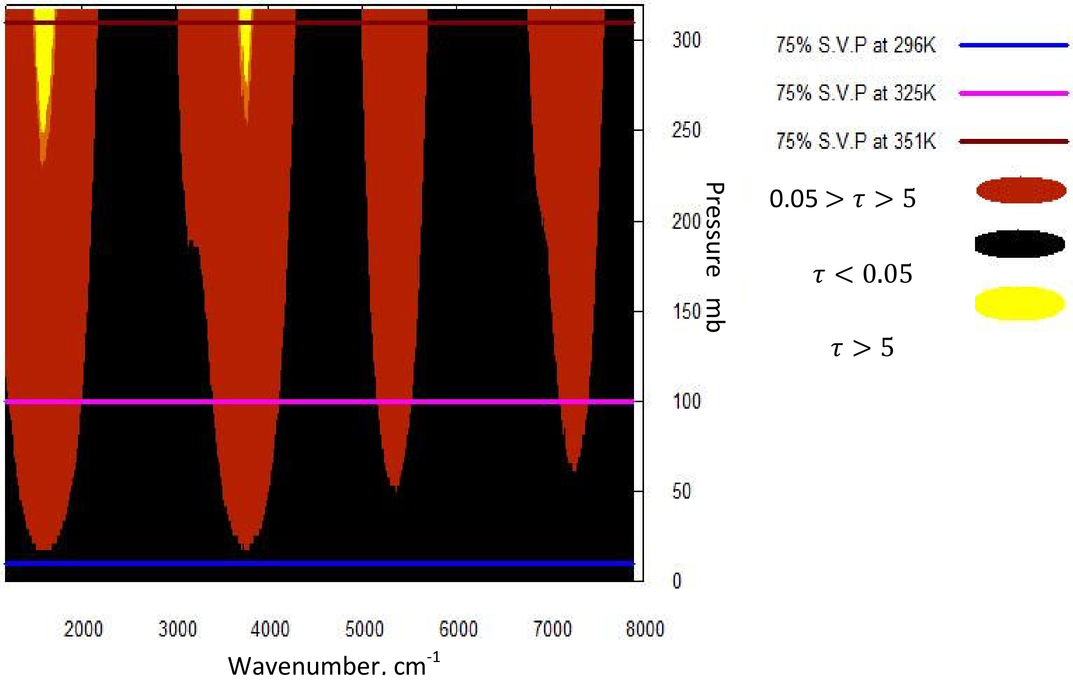

Figure 3.29 Estimated spectral regions where continuum measurements are possible using the experimental setup. The lines represent the maximum pressure attainable in the cell at different temperatures. The yellow and black shaded areas represents where the optical depth is estimated too great or too low to measure the continuum respectively. The red areas are where it should be possible to obtain the continuum in the micro-windows at a given pressure.

It is apparent that at temperatures below 325 K it is only possible to perform accurate continuum measurements in the bands between 1400 -1800 cm^{-1} and 3400-4000 cm^{-1}. The bands between 5000-5600 cm^{-1} and 6900-7500 cm^{-1} are only achievable with temperatures above 325 K. Given that the maximum temperature obtainable in the cell is 351K this does not allow for very accurate derivation of the temperature dependence of these bands or any weaker areas of the spectrum. It is also noticeable that even at the highest attainable pressures it is still not possible to accurately measure the continuum between the major absorption bands.

It should be noted that this analysis is only designed to give a rough idea of in what regions it is possible to measure the continuum with the experimental setup used. The assumption that the measured optical depth is twice the MT_CKD optical depth is quite a basic one, which may significantly over or underestimate the actual optical depth. For example at 296 K the self continuum is roughly twice the magnitude as at 351 K, which will make the absorption in the micro-windows greater than estimated. For this reason, even though this plot suggest the optical depth should be too low, it is actually possible to derive the continuum in the strong absorbing regions at 296 K in the 1300-1900 cm^{-1} and 3500-4000 cm^{-1} regions.

3.6. Data Filtering

If it was possible to have a completely accurate measured and calculated spectra then deriving the continuum would be as simple as subtracting one number from another. However, as the previous three sections have demonstrated, neither the measured nor calculated spectra can be regarded as accurate. For this reason the strategy is adopted where a point is only included in the continuum if the errors associated with that point is below a certain value. This section will discuss how the total error of each point is calculated and then how it is decided whether a point is included in the continuum or not.

3.6.1. Calculating the total error

Consider that, assuming that all errors are independent, the total error for the continuum derived for an arbitrary wavenumber is.

$$\tau_\epsilon^2 = \tau_\epsilon(P_\epsilon)^2 + \tau_\epsilon(T_\epsilon)^2 + \tau_\epsilon(HITRAN)^2 + \tau_\epsilon(Lineshape)^2 + \tau_\epsilon(noise)^2 + \tau_\epsilon(Baseline)^2. \tag{3.29}$$

In reality $\tau_\epsilon(HITRAN)^2$ is also effected by P_ϵ and T_ϵ, but as it has been shown that both $P_\epsilon \ll P$ and $T_\epsilon \ll T$, equation (3.28) is a valid approximation for the accuracy desired. Figure 3.30 shows the contribution of each these errors compared to both the calculated and measured optical depth for the region between 3591 and 3600 cm^{-1}. It is clear that of the all of errors investigated the dominant source is that due to the HITRAN database. These errors are greatest near the line centre.

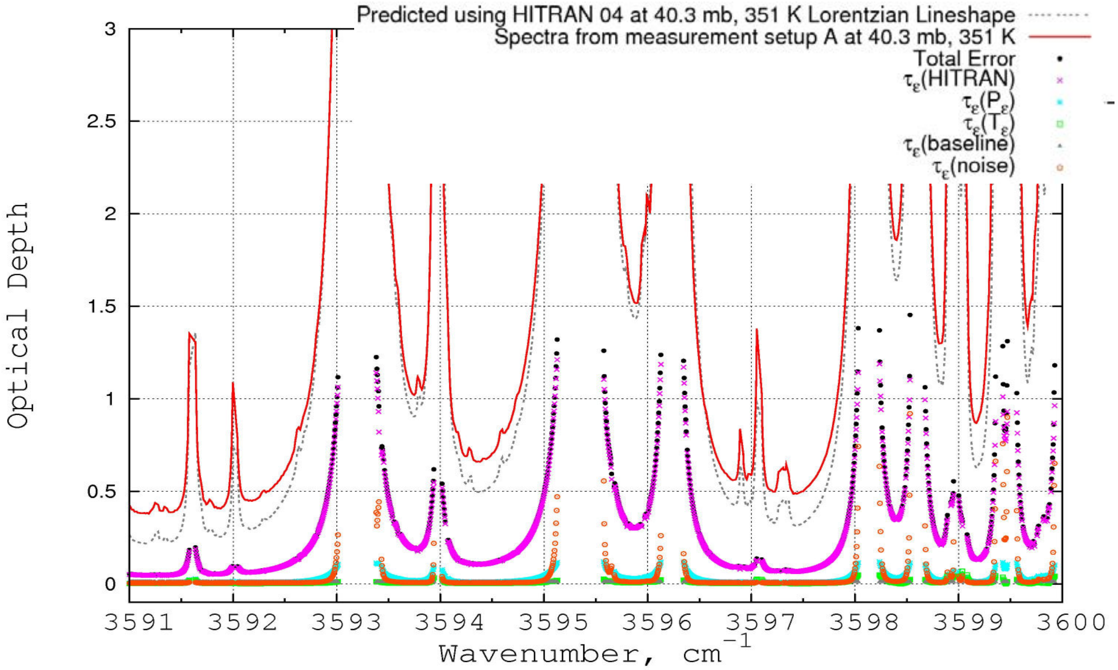

Figure 3.30 The measured optical depth (red line) and the optical depth calculated for the measurement conditions using HITRAN 2004 (light grey line). The uncertainty in the calculated optical depth resulting from uncertainties in HITRAN 2004 (purple), pressure (light blue), temperature (green), baseline (grey) and noise (orange) are compared. The total sum of these errors is shown by the black points.

Following the example of Burch (1981) the continuum coefficient ($C(v,T)$) is used when presenting the majority of results in the next chapter. The continuum coefficient has units of $cm^2 molec^{-1} atm^{-1}$. For the self continuum this is calculated from the optical depth as follows,

$$C_s(v,T) = \frac{kT\tau_c}{P_s^2 L}. \tag{3.30}$$

It is widely accepted that the self continuum optical depth has a pressure squared dependence. By using the continuum coefficient this pressure dependence is removed. This is beneficial as it allows measurements made at different pressures to be directly comparable (providing they are conducted at the same temperature). In other words the continuum coefficient should have the same value regardless of the pressure at which a measurement is made. The continuum coefficient can be written for the average of n different measurements as,

$$C(v,T) = \frac{kT}{L(\sum w_i)} \sum_{i=1}^{n} \frac{w_i \tau_{c_i}}{P_{S_i}^{\ 2}}, \tag{3.31}$$

where w is a weighing function. The weighting function is introduced as different measurement conditions will result in differing confidences for the same point in the derived continuum. There is no obvious appropriate weighting function. It is well known from basic statistics (e.g. Bevington 1969) that if there is a large data set of measured values, with a normalised distribution of random errors and standard deviation σ_i, then 66% of the measured values will lie within plus or minus one standard deviation of the mean and 95% within two. If one wants to average together numerous datasets when measuring the same quantity then the weighting function for each dataset would be defined as the inverse of the variance for that dataset,

$$w_i = \frac{1}{\sigma_i^2}, \tag{3.32}$$

where ${\sigma_i}^2$ is the variance (the square of the standard deviation) of the i^{th} data set. Applying this theory to this work would require the continuum coefficient to be derived for the same experimental conditions enough times to achieve a confident value of σ_i. This could be repeated again at other pressures to obtain different datasets (i.e. different values of σ_i). Such an approach presents two problems. Firstly, it would not be possible to conduct the number of measurements required for this analysis at the number of different pressures required to categorise the continuum. For example, it might require a minimum of 20 measurements to get a basic estimate of σ_i and it would be ideal to obtain the continuum on average at 10 different pressures each at 5 different temperatures. This would result in a 1000 measurements having to be made. For the lab time available for this work it was only possible to perform 50 measurements. The second problem is that this analysis would assume that the only sources of experimental error are random errors. As has been discussed there is also the possibility of systematic errors too affecting measurements too.

For these reasons, such an approach is not really plausible for these measurements. Another way of looking at this problem is to consider that the estimate for experimental error given in this chapter so far is equal to twice σ_i. This implies that for the continuum optical depth obtained from a single measurement there is a 95 % probability that the actual value will lie within two standard of the predicted experimental error.

This approach assumes that any systematic errors or random error in τ_ϵ

are normally distributed about the obtained value of τ_c. This seems like a better assumption for some experimental quantities than others. For example, with pressure the error in optical depth is directly proportional to the error in pressure and there is no good reason to believe that a positive systematic error is any more likely than a negative. While for temperature the relationship between optical depth is more complex, so even if the errors in measured temperature had a normal distribution the resulting error in optical depth may not. However, as the pressure error for most regions is the dominant experimental error in most regions this is not a bad approximation.

We can consider that all of the errors investigated so far, apart from those resulting from HITRAN, are experimental. Thus, for the ith measurement the error in experimental optical depth is given by,

$$\tau^2{}_{exp,i} = \tau^2{}_{\epsilon,i} - \tau^2{}_{\epsilon,i}(Hitran). \tag{3.33}$$

From the proceeding discussion we will define the weighting function as,

$$w_i = \frac{1}{\tau^2_{exp,i}}. \tag{3.34}$$

This means that the definition for the continuum coefficient now becomes,

$$\overline{C(v,T)} = \frac{kT}{L}\left(\sum_{i=1}^{n}\frac{1}{\tau^2_{exp,i}}\right)\left(\sum_{i=1}^{n}\frac{\tau_i}{\tau^2_{exp,i}\,{P_s}_i^{2}}\right) \tag{3.35}$$

Following the same line of argument the total error for an averaged point is

$$\overline{C_\epsilon(v,T)} = \frac{kT}{L}\left(\sum_{i=1}^{n}\frac{1}{\tau^2_{exp,i}}\right)\left(\sum_{i=1}^{n}\frac{\tau_{\epsilon,i}}{\tau^2_{exp,i}\,{P_s}_i^{2}}\right) \tag{3.36}$$

This is of course, assuming that that the errors in P_s can be neglected. As it has been shown that $P_s >> P_\epsilon$, given the relative size of other errors this can be considered a valid assumption. Using the weighting function it is also calculate the standard deviation of the results. One would expect this value to be less than $C_\epsilon(v,T)$

$$\overline{C_\sigma(v,T)} = \sqrt{\left(\sum_{i=1}^{n}\frac{1}{\tau^2_{exp,i}}\right)^2 \sum_{\mathrm{i=1}}^{\mathrm{n}}\left(\frac{kT}{L}\frac{\tau_i}{\tau^2_{exp,i}\,{P_s}_i^{2}} - \overline{C(v,T)}\right)^2}. \tag{3.37}$$

3.6.2. Filtering results

In section 3.4.3 it was discussed that one way of improving the accuracy of the continuum is to not derive it around the line centres. While this technique is useful, there is no reason why a point in the continuum derived away from the line centre may not be subject to a substantial error. For this reason, there is also the need to not include a point in the continuum if it has a predicted error above a certain value. Obviously, the value at which the cut-off is decided is arbitrary. Choosing the best function to decide the cut off value is not straightforward. Allowing the maximum allowed error base solely on the magnitude of a continuum point would potentially allow large values with large errors. Another possibility is one filter which would not allow any points with errors above a certain value. Such a filter would be ideal if all continuum values were the same, but this would allow for smaller continuum values to have an error far greater than their magnitude.

One solution to the problem is a filter that varies depending upon the value of C_s, but with a maximum cut off value. The filter used here is defined as such that,

$$\overline{C_\epsilon(v,T)} < A\,exp\left(-\frac{B}{\overline{C(v,T)}}\right) + \overline{C(v,T)}\,D\,exp\left(-\frac{\overline{C(v,T)}}{B}\right), \qquad (3.38)$$

where A, B and D are constants. When ($\overline{C(v,T)}$>> B) the first term tends to A(i.e. a maximum cut off value of error) and the second to zero. When $\overline{C(v,T)}$ << B then the this first term tends to zero and the second to $\overline{C(v,T)}\,D$. This then allows the maximum error value to be defined as a function of the value of $\overline{C(v,T)}$. As example of the filter is showed in figure 3.31.

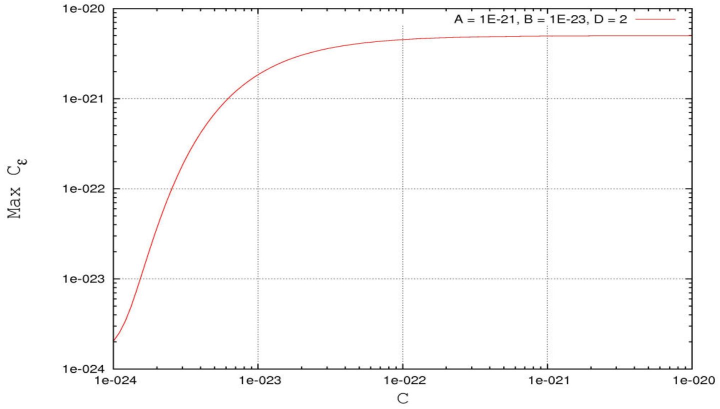

.

Figure 3.31 An example of the filter function used. This shows the allowed maximum value of the error in the continuum coefficient as a function of the continuum coefficient (C).

3.7. Conclusions

This chapter has explained how the measurements of the pure water vapour spectra were conducted. The way that the HITRAN database was used in conjunction with a line by line code to calculate the spectra for the measurement conditions was then demonstrated. The various sources of the major parameters used in HITRAN 2004 were discussed. Here it was shown that while most sources come from the Toth line lists, the self broadened half-widths came from a variety of different sources. It was noted that the measurements of Mandin et al. (1982) appeared to overestimate the half-widths compared to other measurements for the same lines. Furthermore, some lines have a default half-width of 0.12 $cm^{-1}atm^{-1}$, which was up to 400% narrower than the same lines measured by Toth. The effect of both of these inconsistencies upon the continuum will be discussed in the next chapter.

The error parameters given in HITRAN 2004 and their effect upon the calculated optical depth were also discussed. It was demonstrated that these errors affected all parts of the spectrum, especially nearer the line centres. Various experimental errors that could affect the continuum were also investigated and formulas for expressing them developed. In some micro-windows it was demonstrated that the combination of errors due to HITRAN and experimental errors was still not as large as the difference between the measured and calculated optical depth. This suggests that it should be possible to observe the continuum in the band centres. In the next chapter the uncertainty in the continuum caused by these errors will be investigated.

This chapter also discussed a method by which it may be possible to use the errors associated with each point in the continuum to average the continuum derived from measurements at different pressures. Methods of filtering the continuum results by not including areas derived near line centres or which have an estimate error value over a certain amount were also introduced. The effectiveness of these filters will be discussed in the next chapter

4. Self Continuum

The aim of this chapter is to present the results of the analysis of the self continuum. It will begin by investigating the robustness of the continuum to the various errors discussed in the previous chapter. Different measurement sets are then introduced and analysed. The next section then performs a least squares fit to the relationship between the continuum coefficient and vapour pressure. This analysis is useful for determining the pressure dependence of the continuum in all parts of the spectrum. The continuum derived in this work is then compared to measurements made by others, where they are known to exist. The results are then compared to various theories and models for explaining the continuum.

4.1. Analysing errors in the continuum

Before all of the measurements of the continuum are investigated it is worthwhile taking a look at a few measurements across the spectral region and investigating how robust the continuum signal is to various possible errors. The continuum derived in the 3400-4000 cm^{-1} region from a single measurement without any filtering of the data is showed in Figure 4.1 Panel A. It contains a very wide range of both negative and positive values and appears to lack any structure. The reader will recall from sections 3.4.3 and 3.6.2 that it was suggested that the continuum should be filtered to exclude any point in wavenumber space if it has an error greater than a certain value or it is too near a line centre. Let us now look at the effect of each of these filters in turn.

Panel B shows the effect of filtering the continuum by errors only (i.e. excluding a point in the continuum if has an associated error above a certain value). This involves a filter similar that in 3.6.3, but using optical depth units rather than the continuum coefficient (as it is more convenient when looking at just a single measurement),

$$\tau_{\epsilon}(\nu) < A\, exp\left(-\frac{B}{\tau_c(\nu)}\right) + \ \tau_c D\, exp\left(-\frac{\tau_c(\nu)}{B}\right). \tag{4.1}$$

It can be seen in panel B that this method of filtering gives a smoother continuum with more of structure in the band centre, but the continuum still lacks structure and has a large range of values at the edge of the band. This is most likely the resultant of a failure of the filter function being used. It allows large values of the continuum to have larger errors than smaller values. Around the edges of the band, errors resulting from a mixture of ILS and HITRAN cause large residuals to occur nearer the line centres, which appear not to be properly excluded. This is not such a problem in the bands, as most of the line centres are saturated and the resulting residual errors are large enough to be filtered out.

The continuum without the error filter of equation (4.1) applied, but with the line centres removed is shown in panel C. It can be seen that the spread at the edge of the band disappears when this filter is applied, suggesting that they are the result of errors near the line centres. However, due to experimental and HITRAN errors, some of these areas of the continuum are most likely still subject to a large amount of uncertainty. Therefore, the logical approach is to combine the two filters together to obtain a continuum like that shown in panel D. This results in the smoothest continuum with the clearest structure.

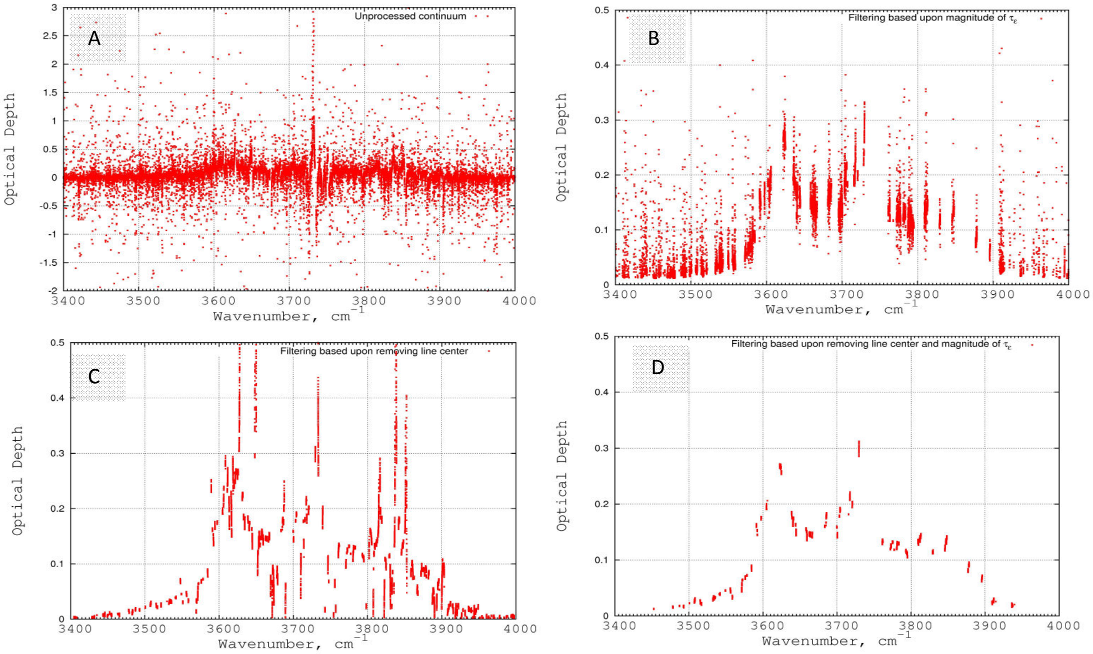

Figure 4.1 Panel A: The derived continuum with no data processing (filtering). Panel B: Only allowing points with τ_ϵ below a certain value. Panel C: Only allowing points away from the line centres. Panel D: Only allowing points with τ_ϵ below a certain value and away from the line centres. For panel B and D the parameters for equation 4.1 are, $A = 0.1$, $B = 0.05$ and $D = 1$ and F *=0.02 for removing line centres.*

Figure 4.2 panel A shows the measured and calculated optical depth along with the resulting continuum before any filtering is applied between 3600 and 3635 cm^{-1}. This further demonstrates how the 'noise' in the continuum results from near the line centres. Panel B shows a breakdown of the various sources of errors. The errors due to HITRAN, noise, temperature and pressure all increase nearer the line centres. As was noted in the last chapter, the dominant source of error affecting the continuum is the errors resulting from HITRAN. Even in the micro-windows the magnitude of this error compared with the continuum does vary considerably. This supports the concept that it is important to remove both the line centres and to filter by errors and not just to trust a point because it was derived in a micro window.

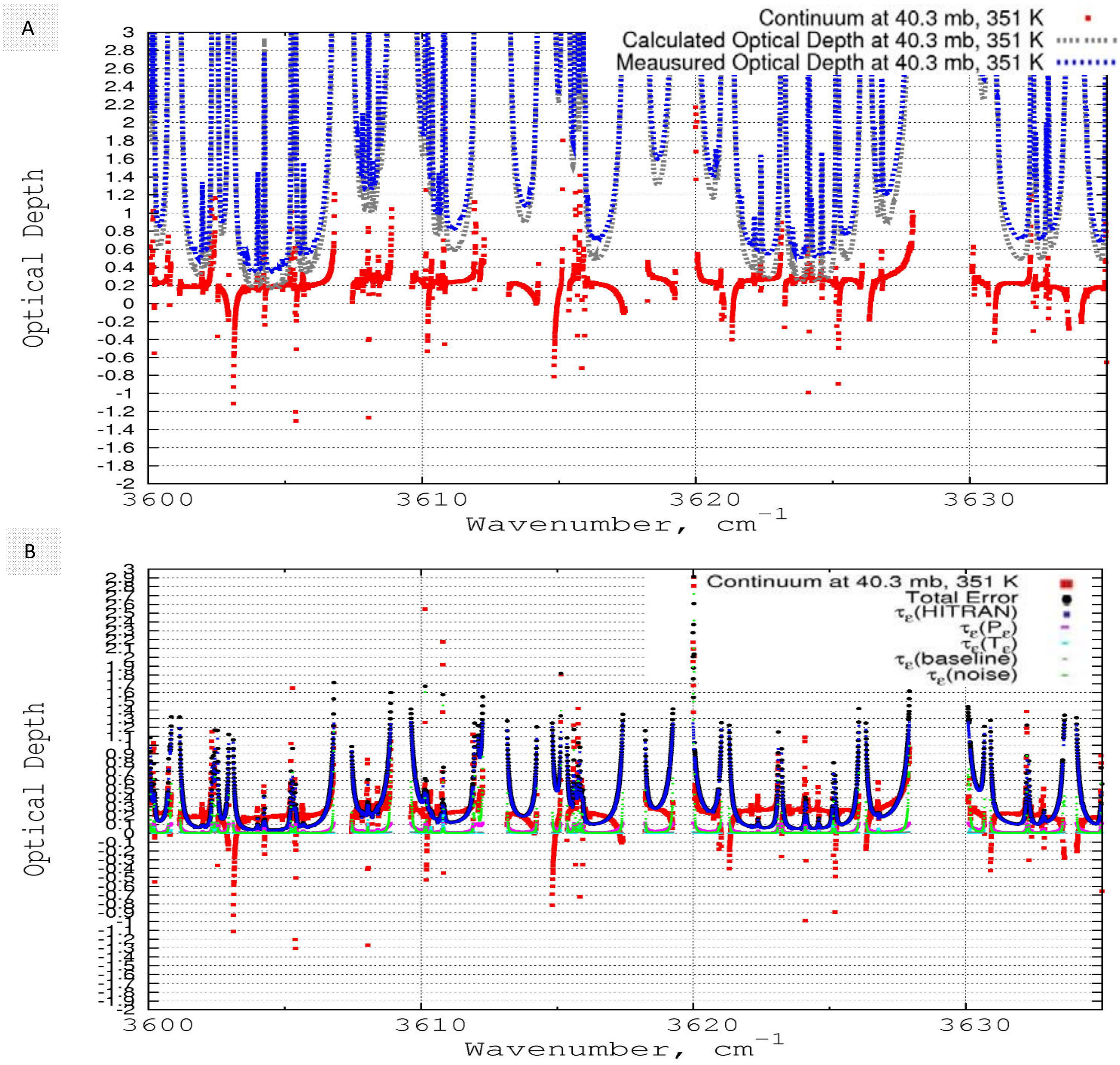

Figure 4.2 Panel A: The measured and calculated optical depth, along with the resulting continuum before any processing. Panel B: The derived continuum in the same region compared to the estimated optical depth of various errors affecting the continuum.

Figure 4.3 shows the same error analysis, but this time over the broader 3500-3900 cm^{-1} spectral region and for the continuum filtered as in Figure 4.1 panel D. It shows that the magnitudes of the errors are smaller than the continuum features. It is also interesting to note that the errors do not mirror the continuum. This suggests that the continuum, in this region at least, cannot be seen as arising from systematic errors in the line parameterisation in HITRAN alone. The errors from HITRAN away from the line centres are directly proportional to the optical depth of the calculated spectra. Thus, the fact that the continuum does not mirror the errors in HITRAN also tells us that the continuum absorption is not strongest where the calculated absorption in the micro-windows is strongest.

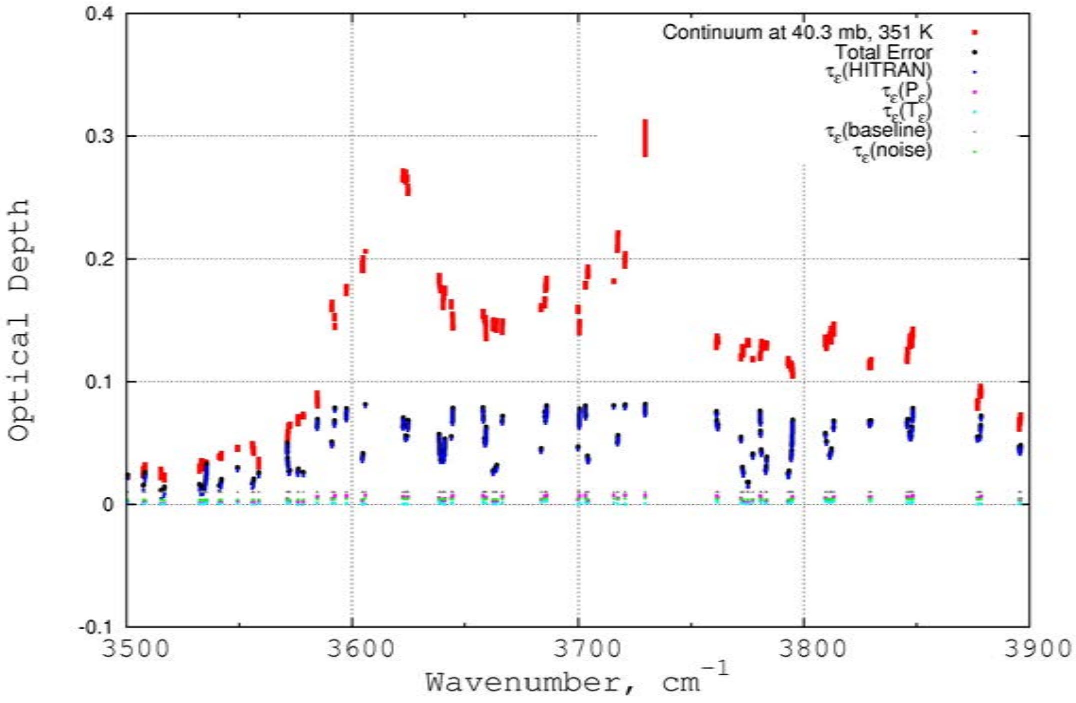

Figure 4.3 The derived continuum between 3500 cm^{-1} and 4000 cm^{-1} along with the estimated optical depth of various errors affecting the continuum. Same filtering parameters as Figure 4.1 Panel D.

Figure 4.4, Figure 4.5 and Figure 4.6 present the same analysis carried out for the other major bands investigated. The results are similar to the 3400-4000 cm^{-1} region, with the filtering giving a structured continuum. The magnitude of the errors compared to the continuum is slightly greater in these three regions than in the 3400-4000 cm^{-1} region. This is especially the case between 6900 and 7500 cm^{-1} (Figure 4.6). An interesting feature lies around 1600 cm^{-1} (Figure 4.4) where the errors due to HITRAN are very much smaller than the continuum. This, like the features around 3620cm^{-1}, provides strong evidence that the continuum cannot be simply the result of errors in the half width or absorption strength of lines alone.

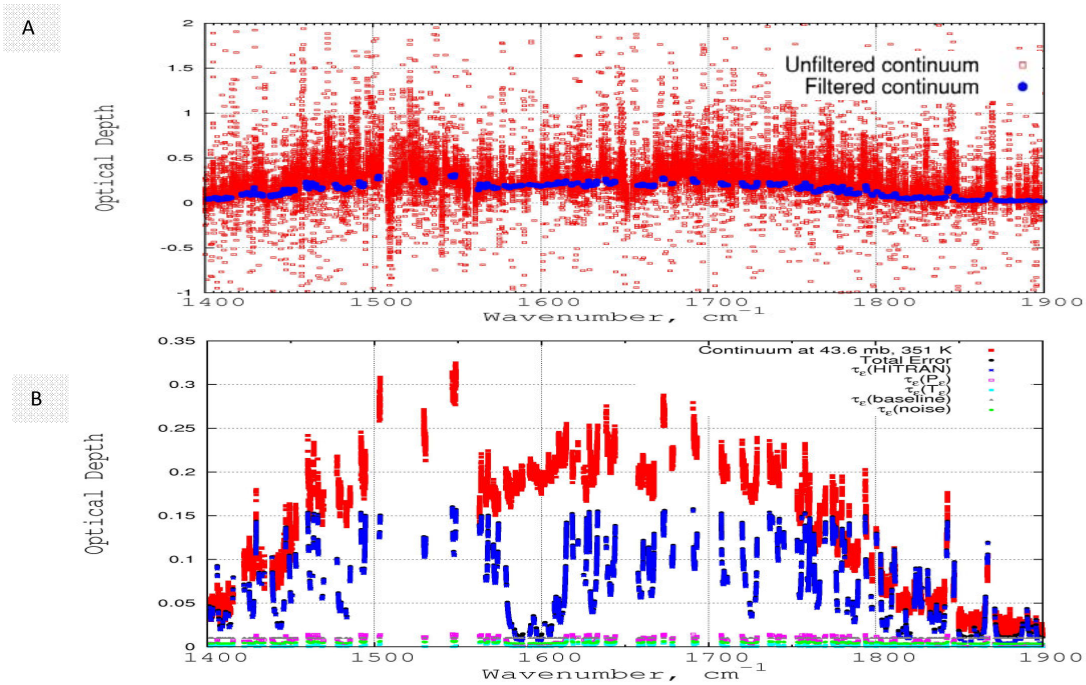

Figure 4.4 Panel A: The continuum between 1400 and 1900 cm^{-1} *before any filtering (red) and when filtered (blue) to only allow points with* τ_ϵ *below a certain value and* away *from the line centres. For the filters A =0.15, B = 0.05, D = 1 and* F *=0.02. Panel B: The continuum derived using the filtering in panel A (red!) compared to the estimated contribution of various errors.*

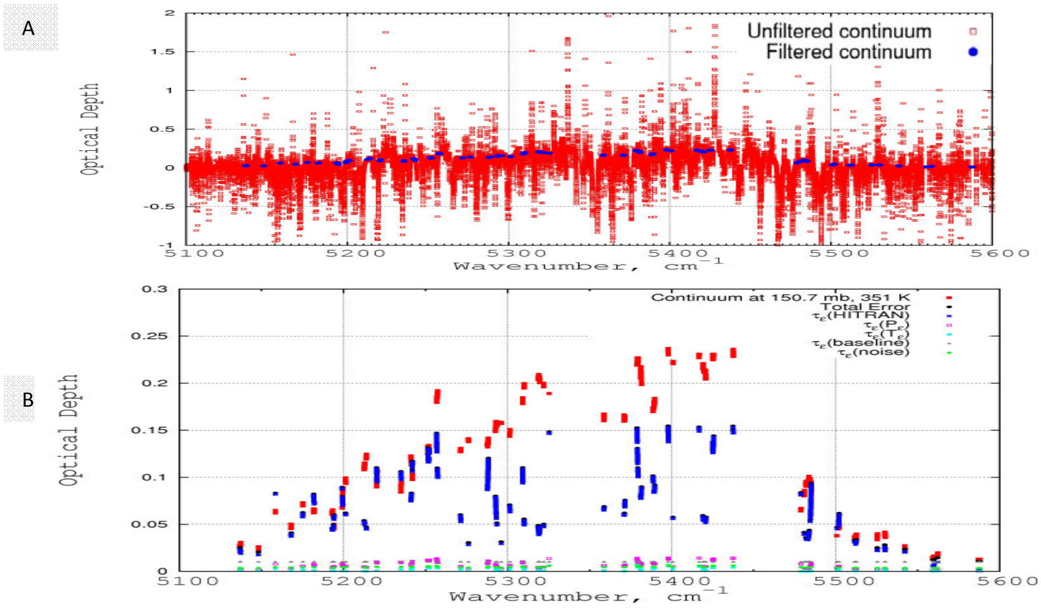

Figure 4.5 Panel A: The continuum between 5100 and 5600 cm^{-1} *before any filtering (red) and when filtered (blue) to only allow points with* τ_ϵ *below a certain value and* away *from the line centres. For the filters A =0.15, B = 0.05, D = 1 and* F *=0.02. Panel B: The continuum derived using the filtering in panel A compared to the estimated contribution of various errors.*

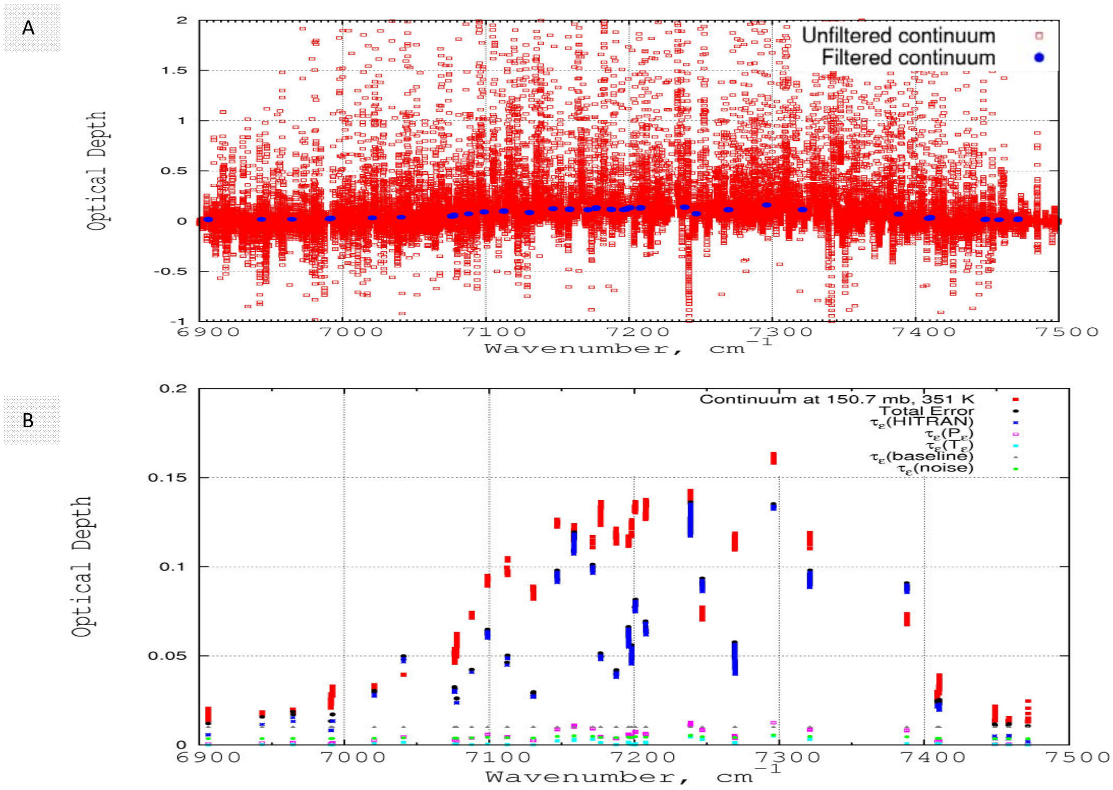

Figure 4.6 *Panel A: The continuum between 6900 and 7500 cm^{-1} before any filtering (red) and when filtered (blue) to only allow points with τ_ϵ below a certain value and* away *from the line centres. For the filters A =0.15, B = 0.05, D = 1 and* F *=0.02. Panel B: The continuum derived using the filtering in panel A compared to the estimated contribution of various errors.*

4.1.1. Using different versions of HITRAN

In Section 3.3, the differences between HITRAN 2000, HITRAN 2004 and other line lists were investigated. It was clear that there were some significant differences between the two databases. The most major of which was the inclusion of self-broadened half-widths between 2000 and 6000 cm^{-1} in HITRAN 2004. It was also noted in section 3.3 that Toth has a line list for water vapour. This contains the same values as HITRAN 2004 for all parameters apart from the self-broadened half-widths.

It was also discussed how in HITRAN 2004 the self-broadened half-widths came from a variety of different sources. Figure 4.7 shows, for the derived continuum, which source of self-broadened half-width is dominant when calculating the optical depth. If at any point in the spectrum over 50% of the calculated optical depth is from lines whose half-width is from a particular source then the continuum point is coloured to identify that source. This is important as it allows any features that could be the result of the bias in one source of self-broaden half-with measurements to be observed. This method is far from perfect, as it may not capture the situation where a source contributes less than 50 %, but still has a significant effect upon the continuum. For example, an underestimated half-width may cause the continuum to be significantly overestimated, but only contribute less than 50%

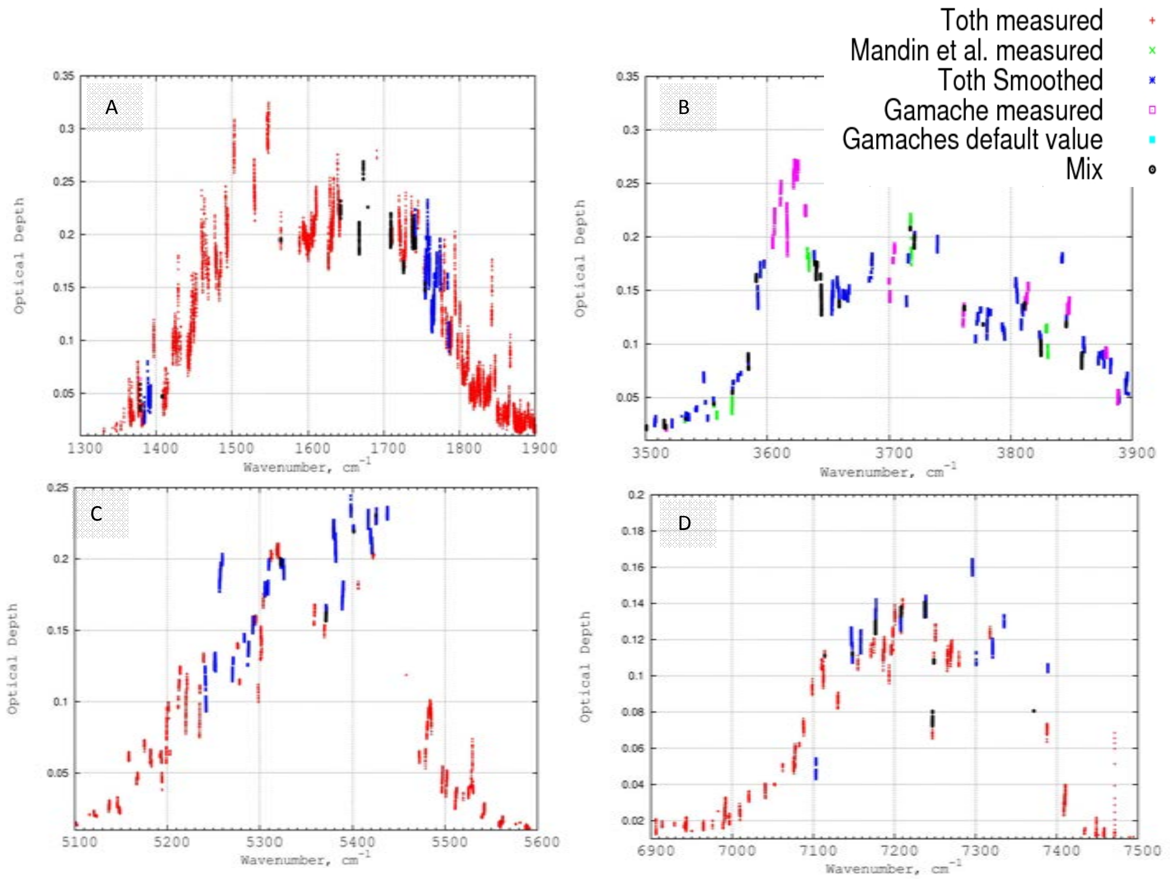

Figure 4.7 The continuum derived in different spectral regions, coloured to represent which source of self-broadened half-widths in HITRAN 2004 contributes most to the calculated optical depth. If the lines from a particular source contribute to over 50% of the calculated optical depth then the point is coloured using the scheme shown in the key. Panel A: This analysis for 1300-1900 cm^{-1} *for a pressure of 43.6 mb and temperature of 351 K with the parameters of A= 0.2, B=0.05, D = 1. Panel B: 3500-4000* cm^{-1} *at 40.3 mb,351 K, A =0.15, B= 0.05. Panel C 5100-5600* cm^{-1} *region 40.3 mb, 351 K, A =0.10, B= 0.05. Panel D 6900-7000*cm^{-1} *region 40.3 mb, 351 K A =0.10, B= 0.05.* F =0.02, D =1 *for all panels.*

The analysis in section 3.6 suggested that the measurements of Mandin et al. (1982) may overestimate the half-widths for some lines between 3400 and 4000 cm^{-1}. However, Panel B tells us that the Mandin et al. values do not have a large affect upon the continuum. The peak found around 3620 cm^{-1} seems to be dominated by the measurements of Gamache. There was no evidence either from this work or other studies that the Gamache measured half-widths are subject to any systematic error.

In the 5000-5600 cm^{-1} region, Ptashnik et al. (2005) claims that the Toth measured values were up to 20 % too high. Here the analysis suggests that this could be significant in this region as a large number of errors are dominated by this source. Furthermore, it can be seen in all regions, bar 3400-4000 cm^{-1} region, that the Toth measured lines dominate. As additional measurements have only been performed in the 5000-5600 cm^{-1} region, it is not possible to know for certain whether this could result in an underestimate of the continuum in other areas. However, Panel D suggests this might be the case in the 6900-7500 cm^{-1} region, as continuum values which are more influenced by the smoothed Toth values (which were found not to be subject to obvious bias, see section 3.3.2) do appear to be slightly higher than those more influenced by the measured Toth values. However, this evidence certainly cannot be seen as conclusive without further measurements of the lines in this region.

Figure 4.8 shows the continuum derived using the HITRAN 2004, 2000 and the Toth line list. The same filter values of A, B and D (from equation (1)) are used for each database. Panel A contains this analysis for the 1200-2000 cm^{-1} region. It can be seen that there is very little difference between the continua derived using the three databases. This is consistent with the analysis in chapter 3 that shows there is little difference in this region between HITRAN 2000 and HITRAN 2004.

As there are no self broadened half-width measurements beyond 2000 cm^{-1} in HITRAN 2000, the assumption is made that the self half-widths are equal to five times the foreign. In Panel B, C and D this results in a far noisier continuum than that derived using HITRAN 2004. This is most likely the result of underestimating the half-width of lines and thus causing excess absorption in the continuum. This suggests that the inclusion of self-broadened half-widths for all regions allows a more accurate continuum to be derived. The fact in all regions there is very little difference between the Toth line list and HITRAN 2004 is consistent with the fact that the Toth measured and smoothed values dominate the calculated spectra.

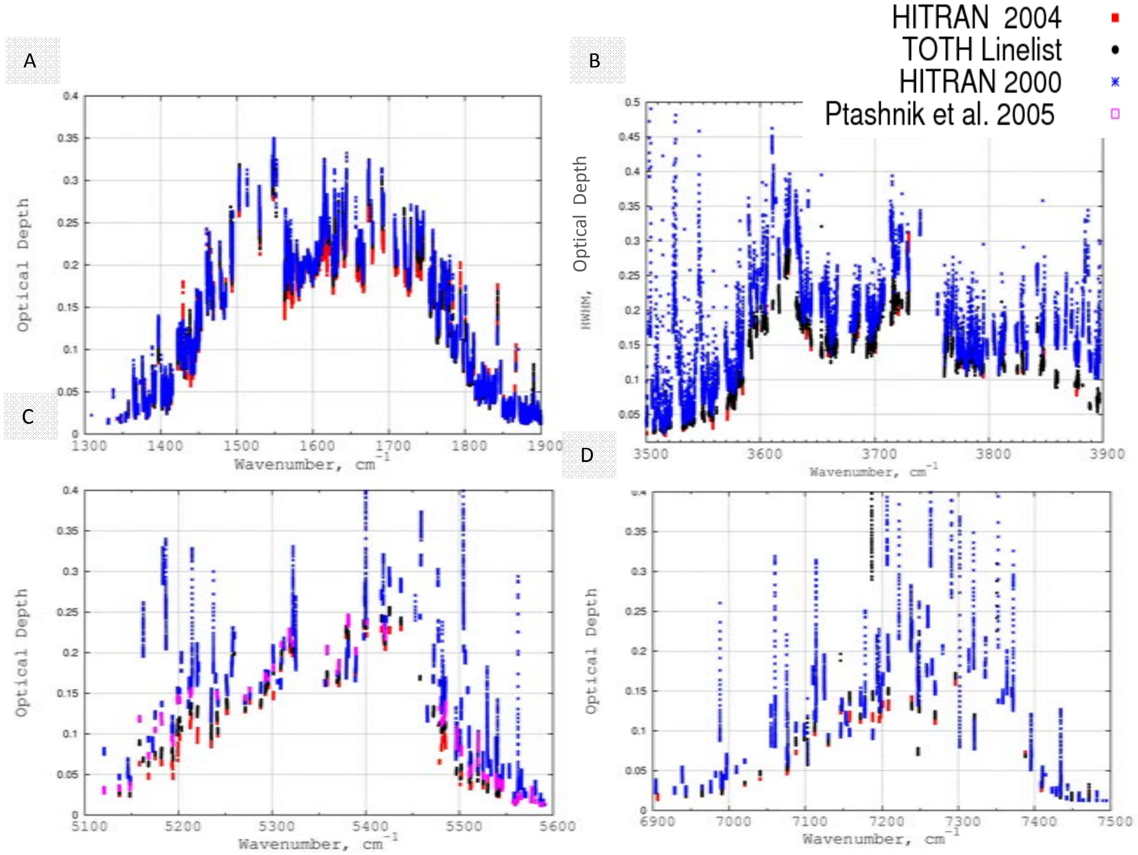

Figure 4.8 Panel A: The continuum derived using HITRAN 2004 (red), the Toth line list (black) and HITRAN 2000 (blue) between 1300 and 1900 cm^{-1} at 43.3 mb and 351 K using parameters A=0.15 and B =0.05. Panel B: The same as A, but for the 3500-3900 cm^{-1} region and measurement conducted at 40.3 mb, 351 K. Panel C: Same as A but for the 5100-5600 cm^{-1} region measurement conducted at 150.3 mb, 351 K A =0.10, B= 0.05 and including the line list of Ptashnik et al.(2005) (purple). Panel D: Same as panel C, but 6900-7500 cm^{-1} region. F =0.02, D=1 *for all panels.*

One problem in the HITRAN 2004 database, which clearly affects the continuum, but is not immediately apparent from this analysis, is the narrow half-width of a strong line at 3732.134 cm^{-1}. The source of the half-width in HITRAN is listed as having a Gamache default value. As was noted in this last chapter all of these lines have a half-width of 0.12 $cm^{-1}atm^{-1}$. Figure 3.9 panel B demonstrated that the Gamache values were up to 400% narrower than the same lines given in the Toth line list. In general most of the lines effected were weaker ones that would have little effect upon the continuum, but the line at 3730.1343 cm^{-1} has a strength of $1.3x10^{-19}$ $cm^{-1}/(molecule.cm^{-2})$. Toth gives a half-width for this line as 0.4390 $cm^{-1}atm^{-1}$. Figure 4.1 Panel A shows a large increase in the value of the continuum around this area which is consistent with the line being narrower. As can be seen in Figure 4.1 Panel D even after filtering this feature leads to a peak in the spectra around 3730 cm^{-1}. Figure 4.9 shows the difference in the calculated optical depth and the derived continuum when the Toth value (black points) is used rather than that of Gamache (purple points). Using the more realistic Toth value causes a significant reduction in the continuum in this region. Due to the presence of numerous strong lines, this area of the continuum is very sensitive to errors in HITRAN. For that reason between 3700 cm^{-1} and 3800 cm^{-1} even using the Toth value it is difficult to obtain many values of the continuum which we have much confidence in.

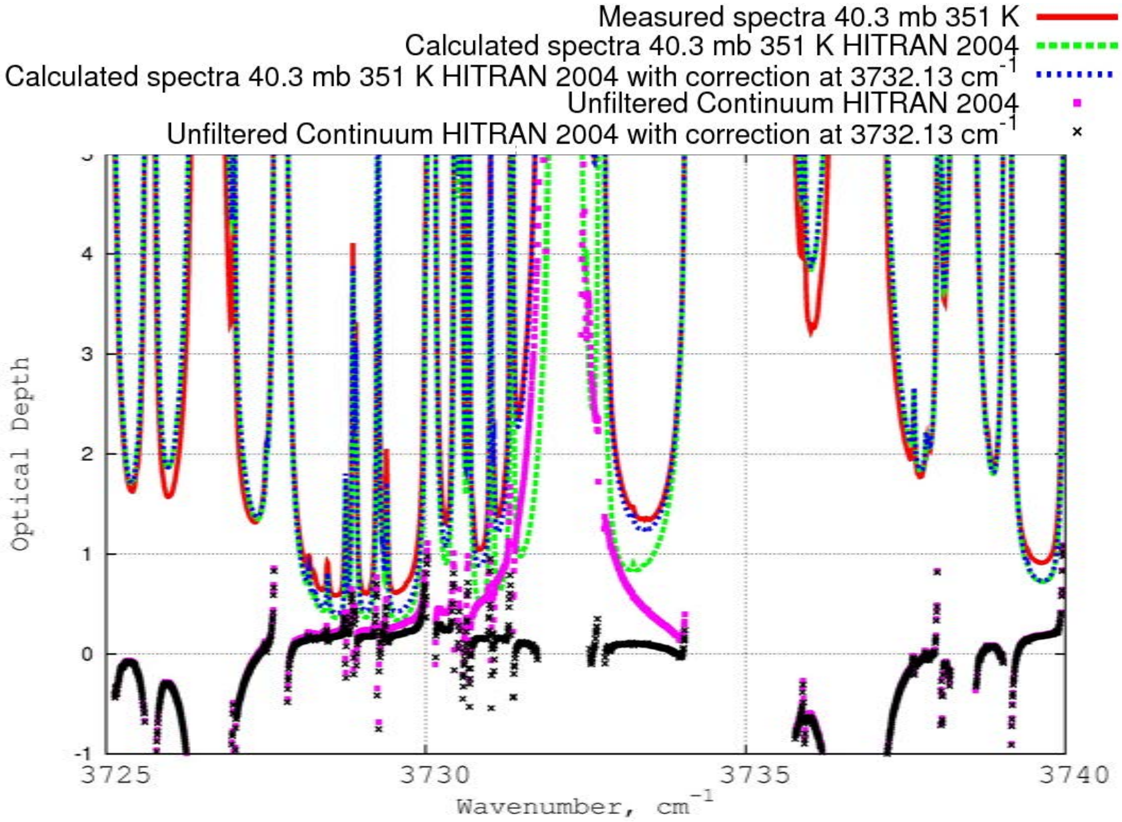

Figure 4.9 The spectra calculated (green line) with HITRAN 2004 using the given self-broadened half-width value of 0.12 cm^{-1}atm^{-1} for the line at 3732.134 cm^{-1}, compared to the same calculation, but using the value of 0.4390 cm^{-1}atm^{-1} given in the Toth line list (blue line). The measured spectra (red solid line) and the resulting unfiltered continuum when the Toth value is used (black points) and when it is not used (purple points) are shown to illustrate the large difference in the continuum resulting from this badly catalogued line.

4.2. Measurement sets

In order to characterise the continuum correctly, pure water vapour measurements were made at different pressures and temperatures. The temperature at which measurements were made varied from 296 K to 351 K, while the pressures ranged from 20 mb to 275 mb. As has been discussed the optical depth of the continuum is expected to scale with the vapour pressure squared. For this reason it is expected that when it is placed in the units of continuum coefficient (C_S) (i.e by dividing through by pressure squared) all measurements will yield the same value at a particular wavenumber. This is demonstrated in Figure 4.10, where Panel A shows the continuum derived at three different pressures given in units of optical depth. Panel B shows the continuum derived from the same measurements, but in units of the continuum coefficient.

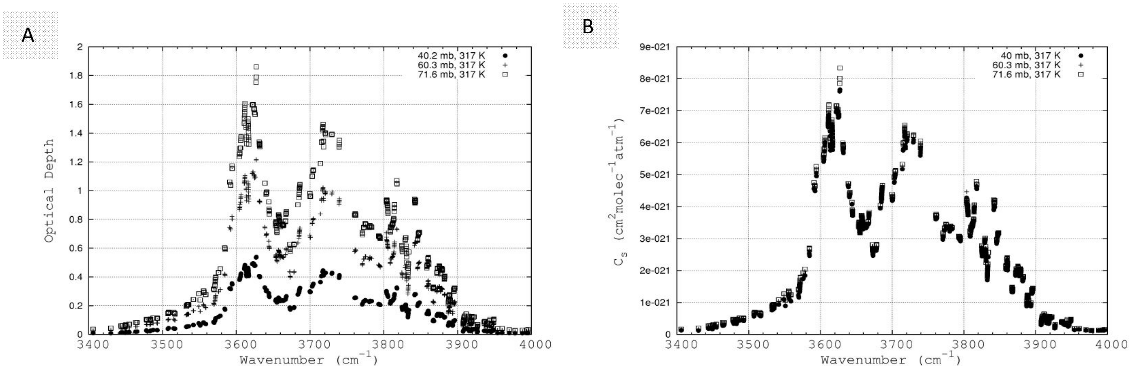

Figure 4.10 Panel A: The continuum derived from measurements at 40.2 mb, 60.3 mb and 71.6 mb in units of optical depth. Panel B: The same measurements, but converted into the units of the continuum coefficient (cm^{2}molec^{-1}atm^{-1}).

As was mentioned in section 3.6, to make full use of all of the measurements, and to obtain an as accurate continuum as possible, measurements conducted at the same temperature are grouped together to form measurement sets. From each set, an average continuum coefficient for each point in the spectrum (i.e. a point in wavenumber space where each measurement has a value) can then be calculated using the formula given in section 3.2. That is to say, it is calculated as a weighted average of the continuum coefficients obtained from different measurements of the water vapour spectra Table 4.1 outlines the different measurement sets used in this work.

In fact, even at the same temperature, it is necessary to split the measurements conducted at different pressures into different sets. This is because the strength of the continuum varies by several orders of magnitude over the spectral region in which the measurements are made. In the stronger areas, the lower pressure measurements will be most suitable, whilst the higher pressure measurements will be too saturated to yield any data. In the weaker areas the lower pressure measurements will be too noisy, but the higher pressure measurements will have a better signal. In Table 4.1 the region(s) which the different sets are used in is shown.

Set	Spectral Region (cm^{-1})	Temperature (K)	No. Measurements	Pressures (mb)
A296	1200-2000	296	2	13.5, 17.8
A330	1200-2000	330	4	22.7, 44.8, 53.3, 71.9
A351	1200-2000	351	4	43.3, 50.3, 67.2,91.3
B296	3400-4000	296	2	12.1, 14.1
B304	3400-4000	304	3	24.2,19.8, 19.5
B317	3400-4000	317	9	29.2, 30.2, 30.6 , 39.8, 40.2,40.1, 59.3,60.3 71.6
B327	3400-4000	327	2	20.1, 40.3
B337	3400-4000	337	9	30.2, 39.5, 40.0, 40.9, 59.8, 61.4, 85.0, 94.9, 99.9
B351	3400-4000	351	17	30.0, 40.0, 40.3, 42.1, 60.3, 60.4, 62.1, 70.5, 71.5, 100.1, 102.4, 111.1,124.1, 125.4, 150.3, 152.2,156.5
C317	5000-5600, 6900-7500	317	3	59.3, 60.3, 71.6
C337	5000-5600, 6900-7500	337	4	94.9, 99.9,146.1,152.7
C351	5000-5600, 6900-7500	351	9	102.4, 111.1,124.1, 125.4, 150.3, 152.2,156.5, 195.4 199.3
D351	3000-3500, 3900-5100, 5500-7000, 7500-8000,	351	4	267.1,276.6, 264.6, 199.3

Table 4.1 A summary of the different sets resulting from the pure water vapour measurements. Note that sometimes the same measurement will exist in more than one set.

Figure 4.11 shows the derived continuum coefficients for six of the sets. The error bars represent the range of the continuum coefficients obtained from individual measurements within the set. In general the range of the continuum derived from different measurements within the sets is smaller than the errors due to HITRAN and is on a similar scale to the predicted experimental errors. This good agreement between repeat measurements suggests that there can be considerable confidence placed in the experimental accuracy of the derived continuum in this work.

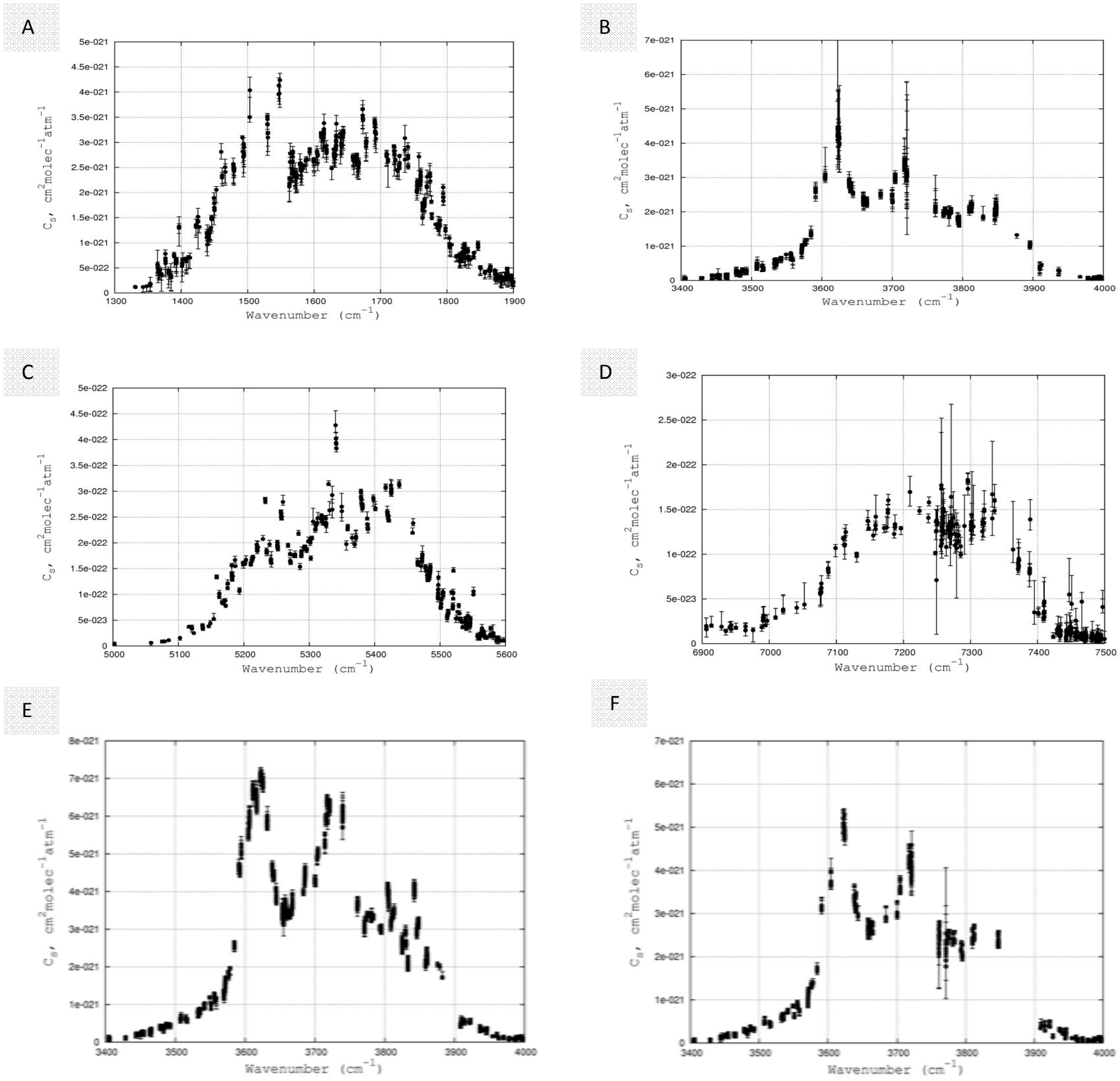

Figure 4.11 The continuum derived from different measurement sets given in units of the continuum coefficient. The error bars represent the range of each set. Panel A: Set A351, using parameters of A = 3E-21, B = 3E-22, D = 1. Panel B: Set B351, using the same parameters as panel A. Panel C and D: Set C351 in the 5000-5600 and 6900-7500 cm^{-1} regions respectably, using parameters of A = 2E-22, B = 3E-23, D = 1. Panel E: Set B317, using parameters of A = 2E-21, B = 3E-22, D = 1. Panel F: Set B337, using parameters of A = 3E-21, B = 3E-22, D = 1. F *=0.02 for all panels.*

4.3. Pressure dependence of the continuum

The fact that there is such good agreement between the continuum derived from different measurements within the same set means that in general, the optical depth of the continuum scales with the vapour pressure squared. However, it is possible that this analysis could miss any subtle linear or cubic trends. Indeed, in chapter 3 it was suggested that if the spectra calculated using

HITRAN are not properly subtracted this could result in some of the continuum having a linear component. There is also a possibility of trimers or pressure broadened dimer lines contributing to the continuum, which would result in a pressure cubed component. A more detailed approach is to perform a least squares fit of optical depth to pressure for each member of a measurement set at each point in wavenumber space. Hence, a quadratic of the following form is fitted to the measurements,

$$\tau_C(\nu, P_s, T) = a(\nu)P_S + b(\nu){P_s}^2 + c(\nu){P_s}^3, \tag{4.2}$$

where $a(\nu)$, $b(\nu)$ and $c(\nu)$ are constants fitted to every point in wavenumber space at which the continuum was derived. This expression can be written in terms of the continuum coefficient to give,

$$C_s(\nu, P, T) = \frac{kT}{L}\left(\frac{a(\nu)}{P_s} + b(\nu) + c(\nu)P_s\right). \tag{4.3}$$

Multiplying through by the vapour pressure gives the form,

$$PC_s(\nu, P, T) = \frac{kT}{L}(\mathrm{a}(\nu) + \mathrm{b}(\nu)\mathrm{P_s} + c(\nu){P_s}^2). \tag{4.4}$$

Consider that we refer to the ith member of a measurement set as being conducted at pressure P_{S_i} and having an associated continuum coefficient C_{s_i}. If we want to fit (4.4) to an arbitrary point in the continuum (ν_n) it is useful to make the following substitutions,

$y_i = P_{s_i} C_{s_i}(\nu_n, P_i, T)$, $\qquad x_i = P_{s_i}$,

$\beta_s = \frac{kT}{L}\mathrm{a}(\nu_n)$, $\qquad \alpha_s = \frac{kT}{L}\mathrm{b}(\nu_n)$,

$\gamma_s = \frac{kT}{L}\mathrm{c}(\nu_n)$.

This then allows us for that point to perform a least squares fit to the equation,

$$y_i = \alpha_s + \beta_s x_i + \gamma_s x_i^2. \tag{4.5}$$

Where it can be shown that (Bevington 1969),

$$\alpha_s = \frac{1}{\Delta_s}\begin{vmatrix} \sum\frac{y_i}{\sigma_i^2} & \sum\frac{x_i}{\sigma_i^2} & \sum\frac{x_i^2}{\sigma_i^2} \\ \sum\frac{x_i y_i}{\sigma_i^2} & \sum\frac{x_i^2}{\sigma_i^2} & \sum\frac{x_i^3}{\sigma_i^2} \\ \sum\frac{x_i^2 y_i}{\sigma_i^2} & \sum\frac{x_i^3}{\sigma_i^2} & \sum\frac{x_i^4}{\sigma_i^2} \end{vmatrix} \qquad \beta_s = \frac{1}{\Delta_s}\begin{vmatrix} \sum\frac{1}{\sigma_i^2} & \sum\frac{y_i}{\sigma_i^2} & \sum\frac{x_i^2}{\sigma_i^2} \\ \sum\frac{x_i}{\sigma_i^2} & \sum\frac{x_i y_i}{\sigma_i^2} & \sum\frac{x_i^3}{\sigma_i^2} \\ \sum\frac{x_i^2}{\sigma_i^2} & \sum\frac{x_i^2 y_i}{\sigma_i^2} & \sum\frac{x_i^4}{\sigma_i^2} \end{vmatrix} \tag{4.6}$$

$$\gamma_S = \frac{1}{\Delta_s}\begin{vmatrix} \sum\frac{1}{\sigma_i^2} & \sum\frac{x_i}{\sigma_i^2} & \sum\frac{y_i}{\sigma_i^2} \\ \sum\frac{x_i}{\sigma_i^2} & \sum\frac{x_i^2}{\sigma_i^2} & \sum\frac{x_i y_i}{\sigma_i^2} \\ \sum\frac{x_i^2}{\sigma_i^2} & \sum\frac{x_i^3}{\sigma_i^2} & \sum\frac{x_i^2 y_i}{\sigma_i^2} \end{vmatrix} \qquad \Delta_s = \begin{vmatrix} \sum\frac{1}{\sigma_i^2} & \sum\frac{x_i}{\sigma_i^2} & \sum\frac{x_i^2}{\sigma_i^2} \\ \sum\frac{x_i}{\sigma_i^2} & \sum\frac{x_i^2}{\sigma_i^2} & \sum\frac{x_i^3}{\sigma_i^2} \\ \sum\frac{x_i^2}{\sigma_i^2} & \sum\frac{x_i^3}{\sigma_i^2} & \sum\frac{x_i^4}{\sigma_i^2} \end{vmatrix}$$

where $\sigma_i = \ uncertainty\ in\ y_i$) i.e. the experimental error and the summation is over the number of measurements within a measurement set.

Let us now relate this fitting back to what it means in terms of the relationship between optical depth and pressure. If the α_s term dominates in the fitting then the optical depth of the continuum at that wavenumber will scale with the vapour pressure. If the β_S term dominates then the continuum optical depth can be said to have a pressure squared dependence (this is what is expected). Finally if the γ_s term dominates then at that point the continuum optical depth will have pressure cubed dependence.

4.3.1. Pressure dependence of 3400-4000 cm^{-1} region

The quality of this fitting will be discussed in some detail for measurement set B351. This set was chosen as it includes the largest range of pressures at which the continuum was derived. It can be seen that the contribution each term makes to the continuum coefficient is given by,

$$C_{s,\alpha} = \frac{\alpha_S}{P} \ , \qquad C_{s,\beta} = \beta_S \ , \qquad C_{s,\gamma} = P\gamma_S. \tag{4.7}$$

Hence, one would expect both the $C_{s,\alpha}$ and $C_{s,\gamma}$ terms to be pressure dependent. This means when comparing the continuum estimated using these coefficients to that measured a pressure value has to be assumed. A value of 100 mb was chosen as this appeared to allow enough 'signal' from both coefficients to detect any features. Figure 4.12 shows the continuum derived as a weighted average of all of the measurements within the set B351, The error bars on the continuum are two standard deviations within the set. Figure 4.12 panel A also has a value for the continuum coefficient estimated using equations (4.5) and (4.6) assuming a pressure of 100 mb (i.e the sum of $C_{s,\alpha}$, $C_{s,\beta}$ and $C_{s,\gamma}$) Panel B,C and D show the averaged continuum compared to the contribution from the α_s, β_s, γ_s components at 100mb. In order to make any trends in the data more apparent these components are averaged over 15 cm^{-1}.

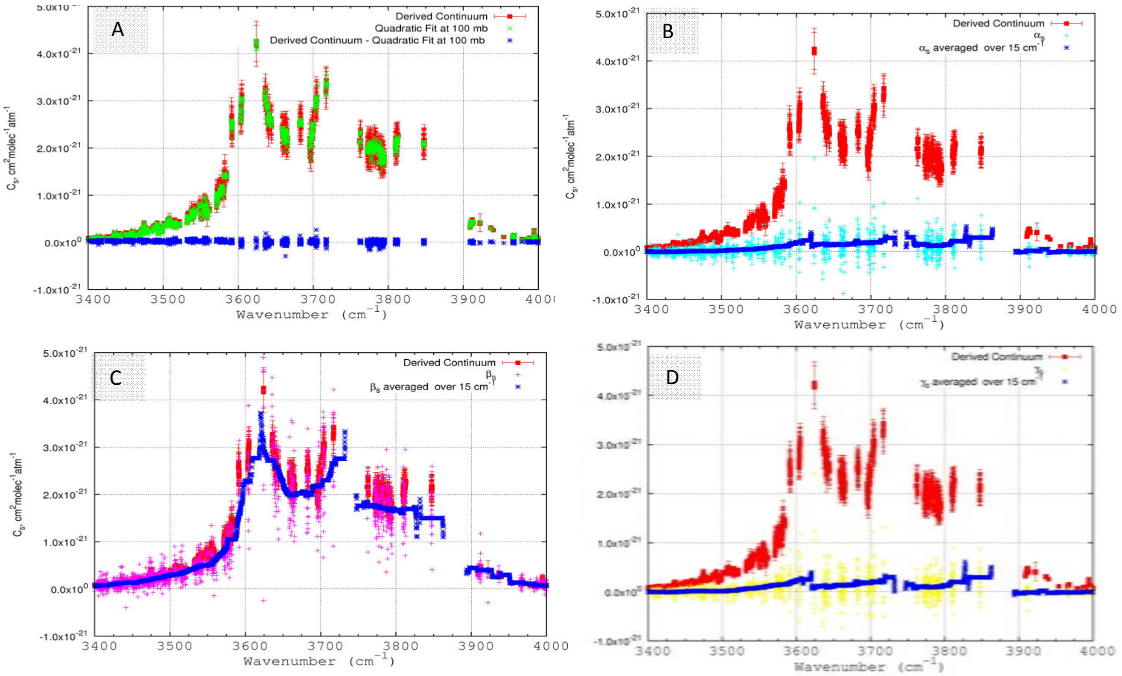

Figure 4.12 Panel A: The derived continuum from set B351 (red) compared to the estimated continuum using a second order least squares fit (green). The difference between the two is shown in blue. Panels B, C and D compare the derived continuum (red) from set B351 to the contributions for the α_s, β_s and γ_s components respectively. In the panels B-D the blue lines is the average of the contribution over 15 cm^{-1}. The error bars are two times the standard deviation of the set.

If the optical depth of the continuum is to have an ideal squared dependence one would expect the α_s and γ_s terms to tend to zero. As can be seen in Figure 4.12 this is not the case. What is apparent though is that fitting this form to the continuum can result in an accurate estimate of the continuum coefficient throughout the region at a pressure of 100 mb, but often with a significant contribution from both α_s and γ_s terms. However, once averaged out over 15 cm^{-1} there is no noticeable positive or negative contribution to the continuum from either coefficient. There is a clear β_s signal that has a similar form to that of the continuum.

One possible reason for the contribution from both the α_s and γ_s terms could be that a quadratic fit over parameterises the problem. That is to say it is possible that slight biases in data caused by experimental errors might result in the α_s and γ_s terms having an artificially large value.

A way to test this would be to neglect the γ_s term and perform a linear least squares fit (i.e only fit the α_s and β_S terms). Hence (4.5) can be simplified to the linear form,

$$y_i = \alpha_l + \beta_l x_i, \tag{4.8}$$

where, following the example of Bevington (1969), it can be shown that,

$$\alpha_l = \frac{1}{\Delta_l}\left(\Sigma\frac{x_i^2}{\sigma_i^2}\Sigma\frac{y_i}{\sigma_i^2} \ - \Sigma\frac{x_i}{\sigma_i^2}\Sigma\frac{x_i y_i}{\sigma_i^2}\right), \tag{4.9}$$

and,

$$\beta_l = \frac{1}{\Delta_l}\left(\Sigma\frac{1}{\sigma_i^2}\Sigma\frac{x_i y_i}{\sigma_i^2} \ - \Sigma\frac{x_i}{\sigma_i^2}\Sigma\frac{y_i}{\sigma_i^2}\right), \tag{4.10}$$

where,

$$\Delta_l = \Sigma\frac{1}{\sigma_i^2}\Sigma\frac{x_i^2}{\sigma_i^2} - \left(\Sigma\frac{x_i}{\sigma_i^2}\right)^2. \tag{4.11}$$

With the non-linear fit there was little point in testing the goodness of fit as this would have not helped to decipher between the β_s and γ_s coefficients. For a linear least squares fit the goodness of fit is, defined as (e.g. Bevington 1969),

$$R^2 = \beta_l \beta_l^*, \tag{4.12}$$

is useful as it gives information about the correlation between the derived continuum and β_l. β_l^* is defined by solving x in terms of y,

$$x = \alpha_l{}^* + \beta_l{}^* y, \tag{4.13}$$

where,

$$\mathrm{\beta}^* = \frac{\Delta_\mathrm{l}}{\Delta_\mathrm{l}^*}\mathrm{\beta}, \tag{4.14}$$

and

$$\Delta_\mathrm{l}^* = \Sigma\frac{1}{\sigma_i^2}\Sigma\frac{y_i^2}{\sigma_i^2} - \left(\Sigma\frac{y_i}{\sigma_i^2}\right)^2. \tag{4.15}$$

As such R can be interpreted as the quality of agreement between fitting the data minimising both the x and y difference. For this fitting if the α_l term dominates then the optical depth of the continuum at that wavenumber will scale directly with the vapour pressure. If the β_l term dominates then the optical depth can be said to have a pressure squared dependence (this is what is expected).

The results of this linear fitting are shown in Figure 4.13. Panel A compares the linear fit at 100 mb to the derived continuum. Panels B and C shows the contribution of both the α_l coefficients at 100 mb and the β_l coefficient, compared to the measurements, while panel D shows the value of R^2 for the different fitting. It can be seen that the linear fit does just as well at fitting as the non linear fit. Furthermore, the obtained values of β_l are far less noisy and closer to the derived continuum than β_s .

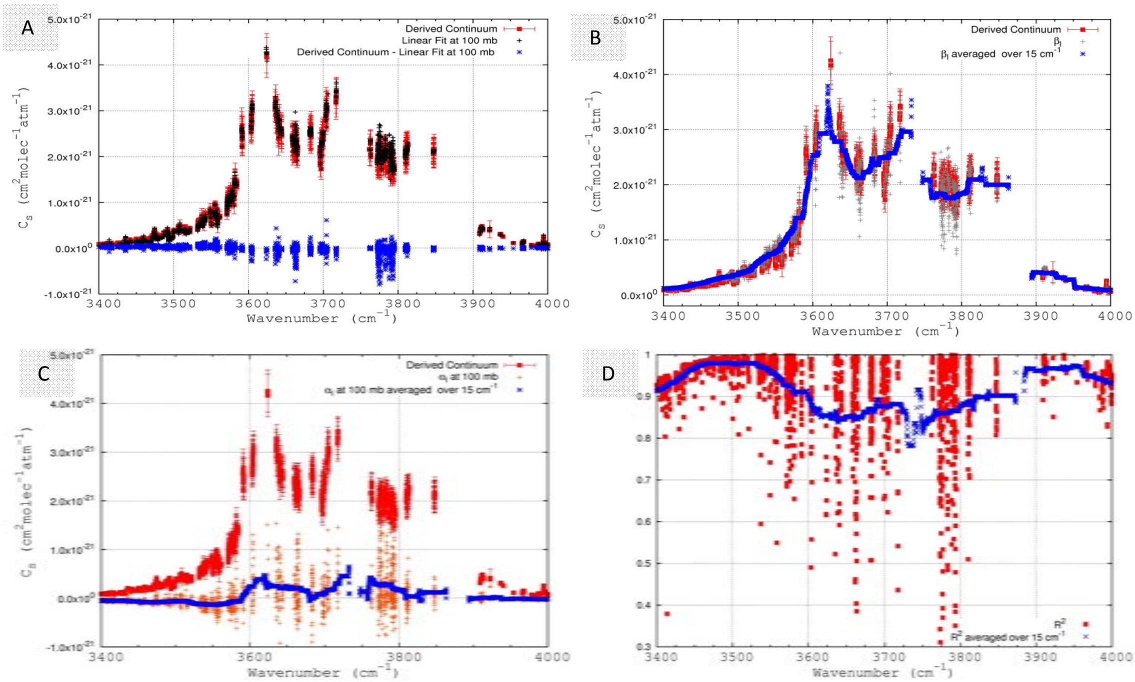

Figure 4.13 Panel A: Comparing the derived continuum from set B351 (red) to the estimated continuum from a linear least squares fit (black). The difference between the two is shown in blue. Panel B and C compare the derived continuum from set B351 (red) to the contributions from the $\boldsymbol{\beta_l}$ *and* $\boldsymbol{\alpha_l}$, *components respectively. Panel D: The value of* R^2. *In the panels B-D the blue lines are the average of the contribution over* $15cm^{-1}$. *The error bars are two times the standard deviation of the set.*

Further evidence that the linear fit least squares method is the best method for fitting the pressure dependence of the continuum can be seen in Figure 4.14. Here for an individual point in the spectrum, the estimate of both the linear and non-linear fits along with the contribution of each individual component are compared to the actual value of the continuum coefficient obtained from each measurement multiplied by the vapour pressure. In other words at a certain wavenumber the estimates of equation (4.5) and (4.8) and the individual components making up these equations are compared to values that are fitted to. These plots show that for each of the four chosen wavenumbers the linear fit is equally as good as, if not superior to the non-linear fit.

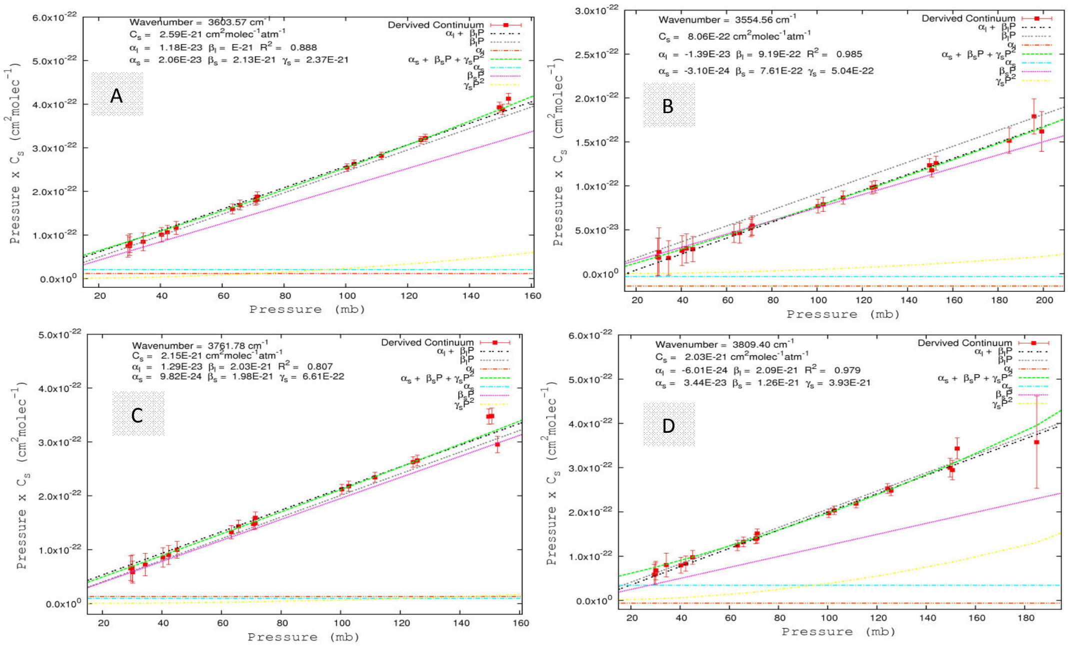

Figure 4.14 Panels A-D comparing derived continuum from set B351 multiplied by vapour pressure to the contribution of both the linear and non-linear fit along with the individual components of these fittings. The black dashed line is the result of the linear fit. The grey dotted line is the result of the β_l component of the linear fit (if this value agrees with the continuum coefficient multiplied by the vapour pressure then it shows that the continuum optical depth that scales with the vapour pressure squared). The orange dotted line is the α_l component of the linear fit.

4.3.2. Pressure dependence of 1400-1900 cm^{-1} , 5000-5600 cm^{-1} and 6900-7500 cm^{-1} regions.

A similar analysis to that performed at 351K in the 3400-4000 cm^{-1} region has been performed in other regions. The assumption is made from the previous section that it is adequate to fit the continuum using a linear least squares fit. Figure 4.15 shows the derived continuum between 1400 and 1900 cm^{-1} at 351 K using set A351. This, along with Figure 4.16, which presents the linear fitting of the continuum at a few selected wavenumbers, demonstrates that the β_l component is dominant.

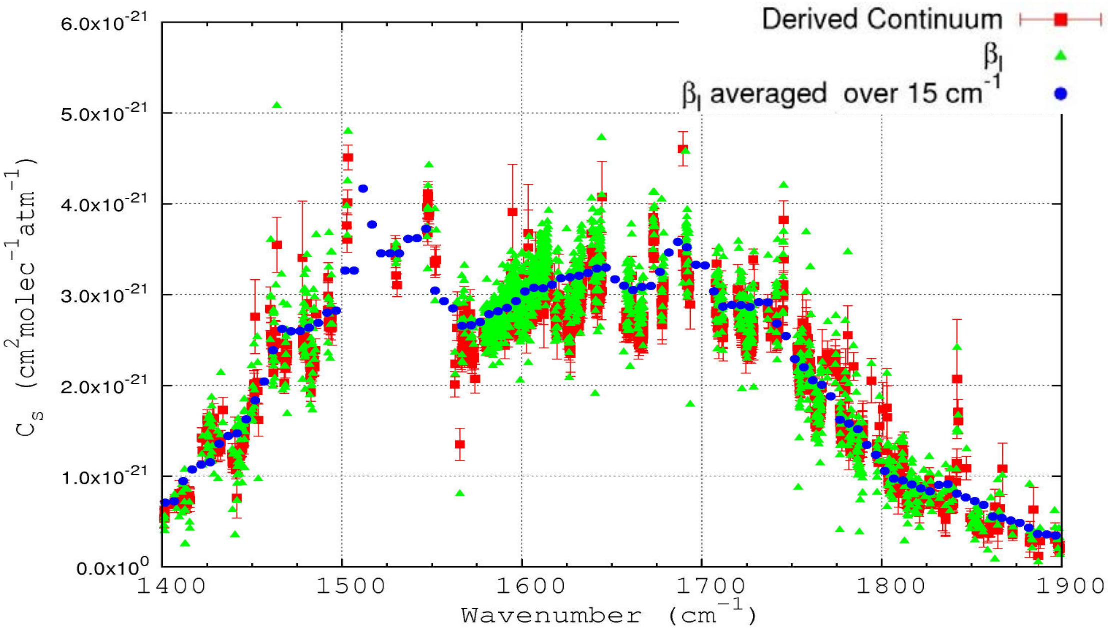

Figure 4.15 The self continuum derived at 351K between 1400 cm^{-1} and 1900 cm^{-1} from set A351 compared to β_l derived from a linear fit as described earlier in the chapter. An average over 15 cm^{-1} is also shown to make any trends clearer. The error bars are the 2 times the standard deviation of the A351 measurement set.

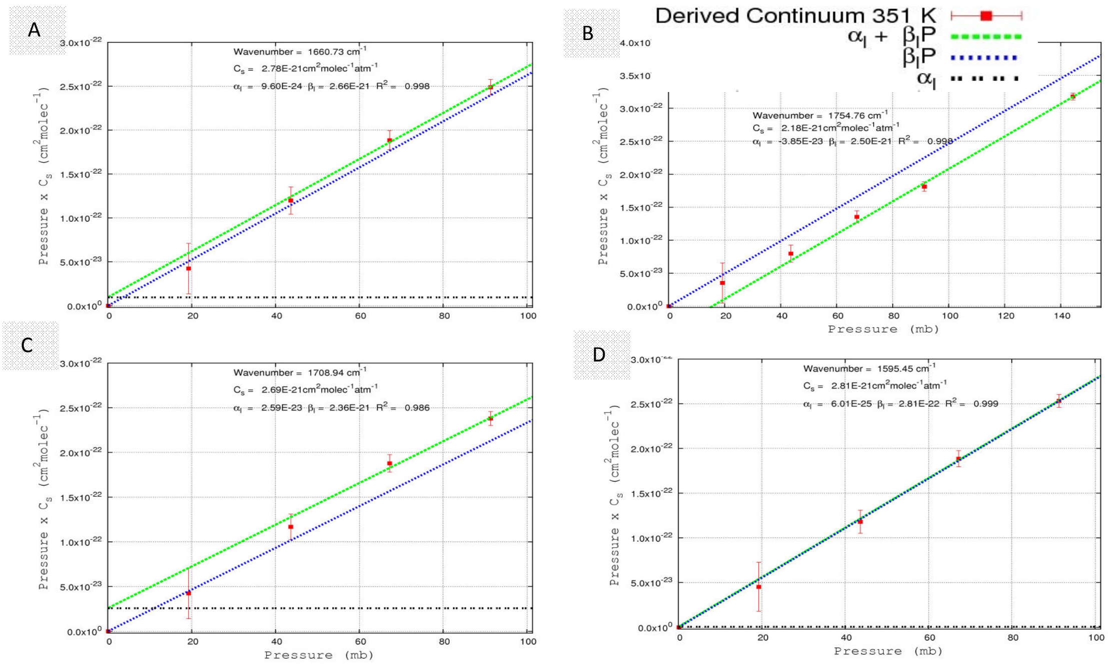

Figure 4.16 Panels A-D compare the continuum coefficient derived from different measurements making up set A351 multiplied by the vapour pressure (red points), to the linear fit to this (green line). The individual $\boldsymbol{\beta_l}$ *and* $\boldsymbol{\alpha_l}$ *components are also shown (blue and black lines respectively). The error bars are estimated experimental errors. The error bars are the estimated experimental error.*

Exactly the same analysis is performed for the two other bands.

Figure 4.17 has the fitting for the region between 5100 and 5600 cm^{-1} with Figure 4.18 containing the fitting for individual points in the spectrum Figure 4.19 and Figure 4.20 present the same analysis for the region between 6900 and 7900 cm^{-1}. In summary for all three regions it is clear that within the accuracy for which it is possible to derive the continuum, it is only possible to deduce a pressure squared dependence of the optical depth. This tells us that whatever mechanism is used to explain the continuum in the region studied it must have a pressure squared dependence. It also suggests that the filtering discussed in the previous chapter does accurately exclude line centres from the derived continuum, as no significant linear component is observed.

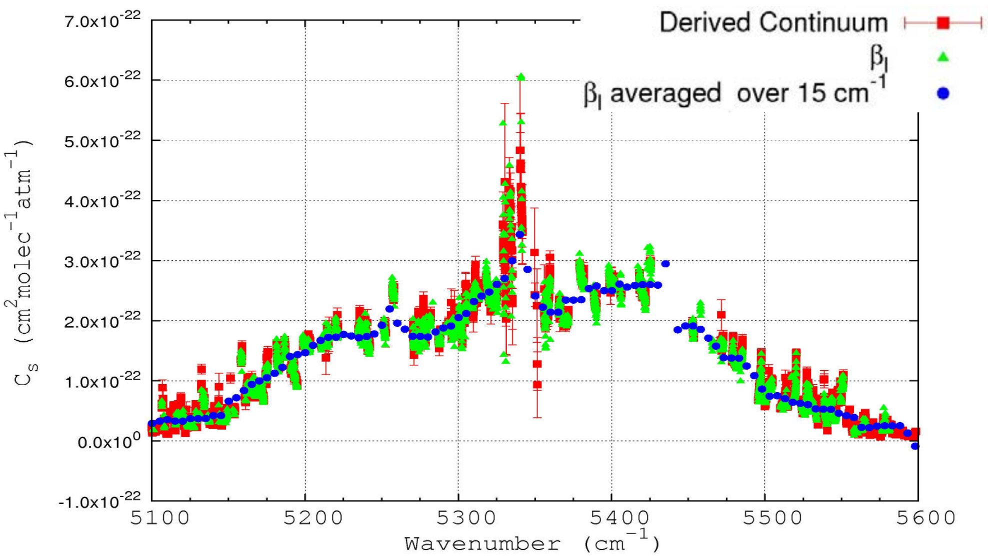

Figure 4.17 The self continuum derived at 351K between 5100 cm^{-1} and 5600 cm^{-1} from set C351 compared to β_l derived from a linear fit as described earlier in the chapter. An average over 15 cm^{-1} is also shown to make any trends clearer. The error bars are the 2 times the standard deviation of the C351 measurement set. The line corrections to HITRAN 2004 by Ptashnik et al.(2005) are used for the calculated spectrum. The error bars are 2 times the standard deviation of the C351 measurement set.

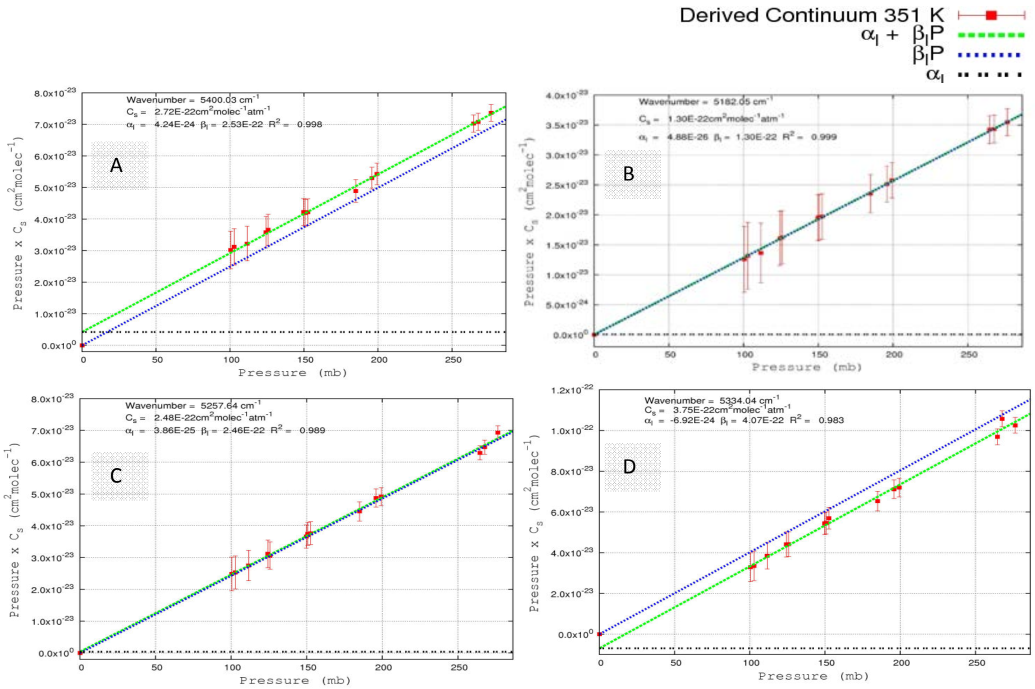

Figure 4.18 Panels A-D compare the continuum coefficient derived from different measurements making up set C351 multiplied by vapour pressure (red points), to the linear fit to this (green line). The individual β_l and α_l components are also shown (blue and black lines respectively). The error bars are the estimated experimental errors.

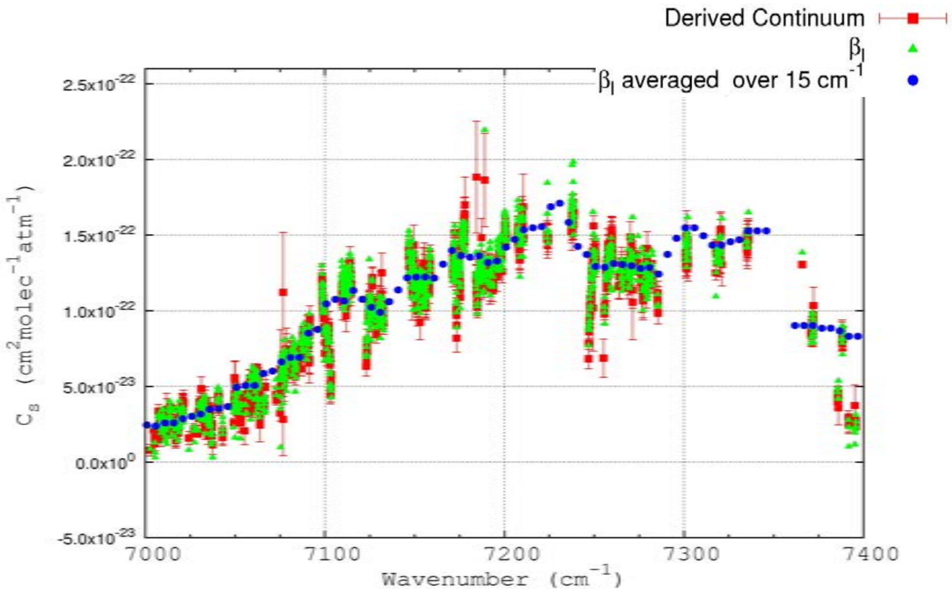

Figure 4.19 *The self continuum derived at 351K between 7000 cm^{-1} and 7400 cm^{-1} from set C351 compared to β_l derived from a linear fit as described earlier in the chapter. An average over 15 cm^{-1} is also shown to make any trends clearer. The error bars are the 2 times the standard deviation of the C351 measurement set.*

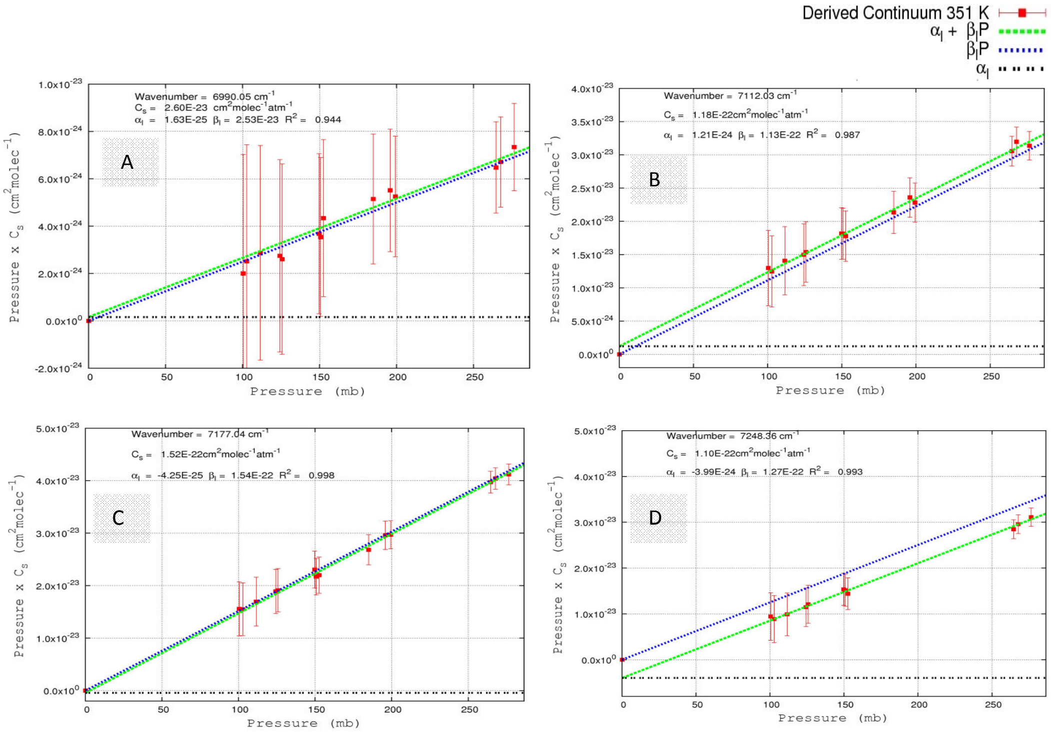

Figure 4.20 Panels A-D compare the continuum coefficient derived from different measurements making up set C351 multiplied by the vapour pressure (red points), to the linear fit to this (green line). The individual β_l *and* α_l *components are also shown (blue and black lines respectively). The error bars are estimated experimental errors.*

4.4. Comparison with other works

As discussed in chapter 2 there are four known previous sets of laboratory measurements of the pure water continuum in the 1200-8000 cm^{-1} spectral region. There are some low spectral resolution measurements (~1 cm^{-1}) of Burch (1981) conducted between 1200 cm^{-1} and 2200 cm^{-1} and between 3100cm^{-1} and 4400 cm^{-1} (1985). Tobin et et al. (1996) conducted higher resolution (0.04 cm^{-1}) measurements between 1300 and 2200 cm^{-1}. Ptashnik et al. (2004) also conducted high resolution measurements between 5000 and 5600 cm^{-1}. Burch in the region between 3100 and 4400 cm^{-1} and Tobin et al. derived the continuum at 296 K only. Between 1200 cm^{-1} and 2200 cm^{-1}, Burch derived the continuum at 308 K only. Ptashnik et al. derived the continuum at 296 K and 342 K.

4.4.1. Burch and Tobin measurements

Figure 4.21 compares the measurements of Burch and Tobin et al. to this work at 296 K in the 1300-1900 cm^{-1} region. For this comparison the continuum derived from set A296 is used. It is apparent that the continuum derived from this work agrees very well with the measurements of Tobin et al. The Burch values in general seem to be slightly lower. Given the negative temperature dependence of the continuum, as the Burch measurements were conducted at 308 K one would expect this. This does not explain the large discrepancies of the two points between 1500 and 1600 cm^{-1}. Figure 4.22 shows the 3400-4000 cm^{-1} region, here the Burch values appear to be consistently larger than the values in this work.

One possible explanation for this and the differences between 1500 and 1600 cm^{-1} could be because Burch uses the AGFL database to calculate the optical depth. This database dates from 1980 and therefore is considerably less accurate than the more modern HITRAN 2004. In his papers Burch actually provides data tables of both the measured and calculated absorption. This makes it possible to use HITRAN 2004 to calculated the absorption and thus to improve Burch's estimate of the continuum. Rather unfortunately the only available version of the 1981 paper from the British Library was damaged, making it impossible to obtain the data to perform this calculation in the 1300-1900 cm^{-1} region. Figure 4.22 shows the adjustment in the 3400-4000 cm^{-1} region where it was possible to perform the analysis. Here there is a noticeable reduction to the Burch continuum upon using HITRAN 2004 which brings it into better agreement with this work.

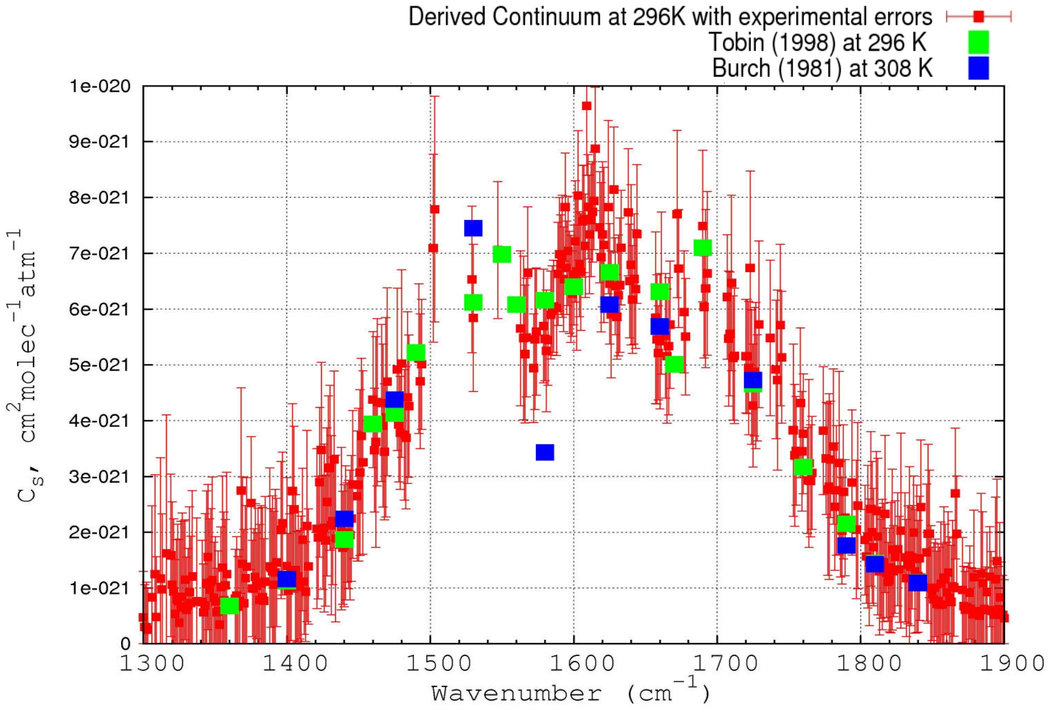

Figure 4.21 Comparing the continuum derived from set A296 in the 1300-1900cm^{-1} region (red) to the continuum derived by Tobin et al. (1996) and Burch(1981). Error bars are experimental errors.

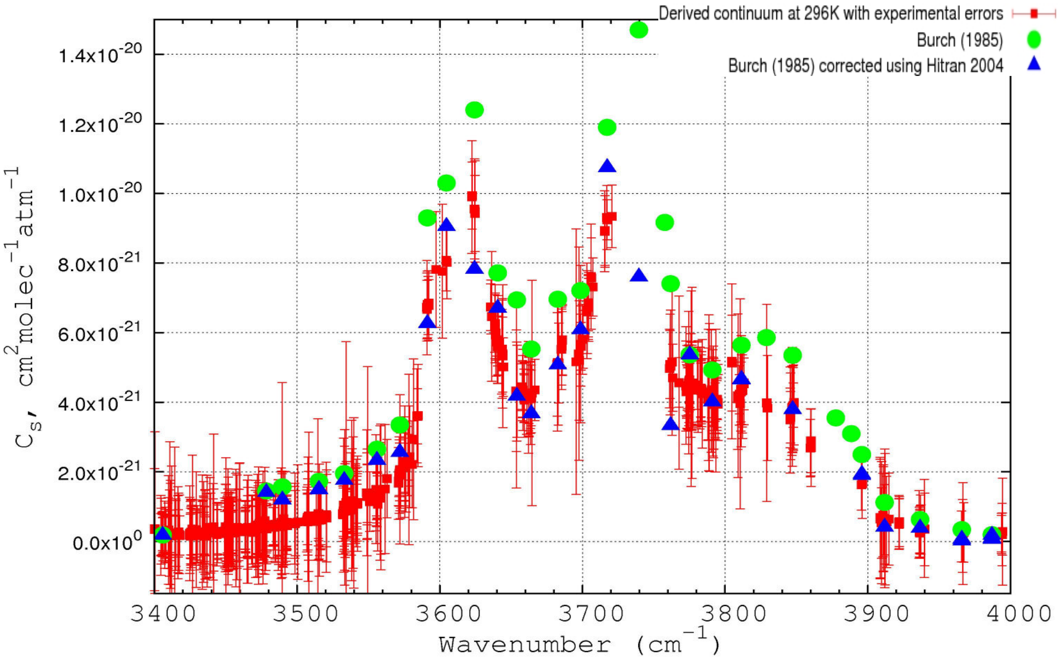

Figure 4.22 Comparing the continuum derived from set B296 (red) in the 3400- 4000 cm^{-1} region to the continuum derived by Burch (1985) and the corrected version of the Burch continuum using HITRAN 2004. The error bars are estimated experimental errors.

4.4.2. Ptashnik et al. measurements

In order to get the most accurate comparison of the continuum measured by Ptashnik et al. (2004) it is necessary to change slightly how the continuum is derived. Ptashnik et al. neglect data points based upon the gradient between one point in the calculated spectra and the next. If the gradient of the calculated absorption is above a certain value it is neglected. This technique, as with the error filter technique used in this work, rules out points in the spectrum near line centres. In addition Ptashnik et al. include the 'line base' (see section 2.7.1) in their definition of the continuum. Once the continuum is derived in their work it is also averaged over 25 cm^{-1}. To make a better comparison with Ptashnik et al. the continuum in this work was also processed in a similar manner.

As has already been discussed, using their measurements of pure water vapour lines Ptashnik et al. (2005) have corrected the strongest 530 lines in the HITRAN 2004 database in this region. For my work, these corrected lines have been inserted into the HITRAN 2004 database, while for the continuum derived by Ptashnik et al. (2004) a corrected version of HITRAN 2001 is used. This could be another possible cause of difference between the two continua.

Another problem in performing a comparison was that in this region it was not possible to derive the continuum accurately at 317K in this region. This made it only possible to perform a realistic comparison with the Ptashnik et al. continuum derived at 342 K. The closest temperatures to this that the continuum was derived at were 337 K and 351 K. This meant that it was necessary to scale the continuum derived in this work slightly. The detail of the temperature dependence of the continuum will be discussed in chapter 5.

Figure 4.23 shows the comparison in 5000 - 5600 cm^{-1} spectral region between the continuum derived in this work and Ptashnik et al. The derived continuum in all cases had the 'line base' included and adjusted from the continuum derived at 337 K to estimate the value at 342 K. Neither adjustment makes a large difference to the continuum: adding on the base adds about 10% to the value of the continuum, while the temperature adjustments results in about an 8% adjustment. As can be seen, there is virtually no difference between the continuum derived using the gradient technique and that derived using the error filter (i.e. the technique used in this work). The difference between using a modified version of HITRAN 2004 and HITRAN 2000 is also small. Although HITRAN 2000 can be seen to lead to a larger peak around 5330 cm^{-1}.

Figure 4.24 shows the same as Figure 4.23 but without any averaging. This reveals that despite using the same gradient, the HITRAN 2001 database allows more 'noisy' data points. This is in agreement with the analysis in section 4.1.1 which showed that a 'noisier' continuum results when HITRAN 2000 is used. As discussed this is most likely due to the fact that (apart from the stronger lines measured by Ptashnik et al. 2005) there are no self broadened half-width in HITRAN resulting in the rough assumption that the self half-width is five times the foreign being used.

Overall, it appears that the measurements of the continuum agree well with those of Ptashnik et al. However, there are a couple of notable differences. Ptashnik et al. predicts considerably more absorption between 5400-5500 cm^{-1}. The cause of this difference is currently unknown. It would seem unlikely that this would result from an error in pressure or temperature measurements, as this would manifest itself across the whole spectrum. As the same calculated spectrum is subtracted in both cases this rules out errors due to HITRAN as a possible explanation. This work also seems to estimate a smaller peak at 5330 cm^{-1}: this is significant, as this is the feature that Ptashnik et al. fit the dimer spectrum to in order to obtain an equilibrium constant. As can be seen in Figure 4.24 this work does predict that there should be a peak in this region of almost the same value as that predicted by Ptashnik et al., but once averaged with the surrounding points it gets reduced in magnitude and width. As in this area the water vapour lines are very strong any error in pressure of the measurement is going to have a larger effect than elsewhere in the band (see *Figure 4.5* panel B). This implies that we have to be very careful before drawing any conclusions about the dimer or contributions to the continuum when fitting to this feature.

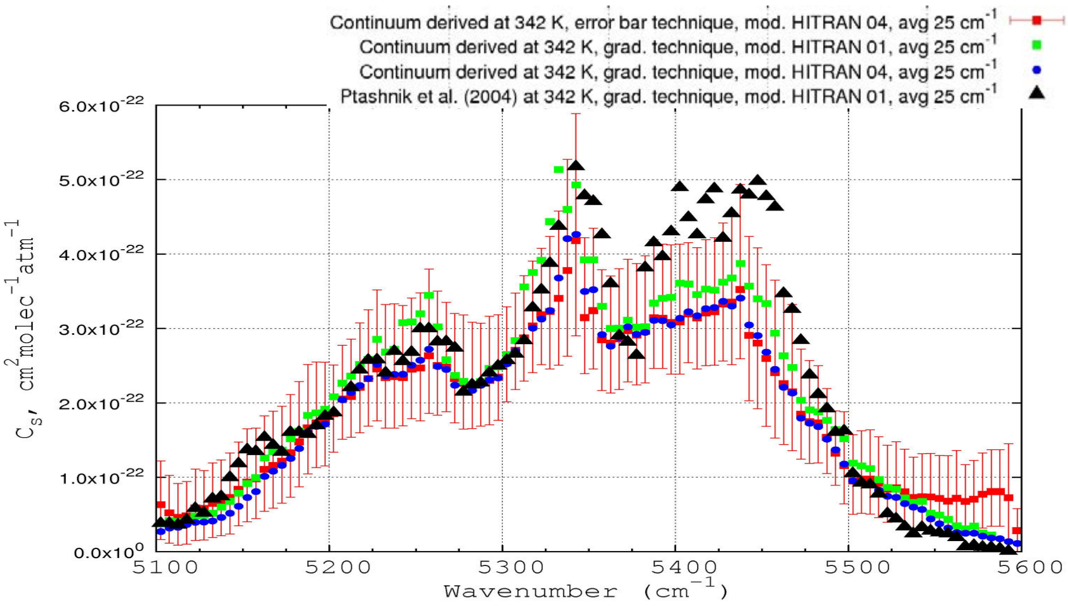

Figure 4.23 This continuum derived by Ptashnik et al. (2004) (black triangles) compared to that derived in this work with HITRAN 2004 and using the error bar technique (red squares) and the gradient method (Blue circles). Using the gradient technique the continuum was also derived using HITRAN 2001(green circles). In all cases the version of HITRAN was modified to make use of corrections to the strongest lines suggested by Ptashnik et al. (2005). The error bars represent the experimental error estimated for this work. A cut off value of 3 cm is used for the gradient. The continuum is averaged over 25cm^{-1}

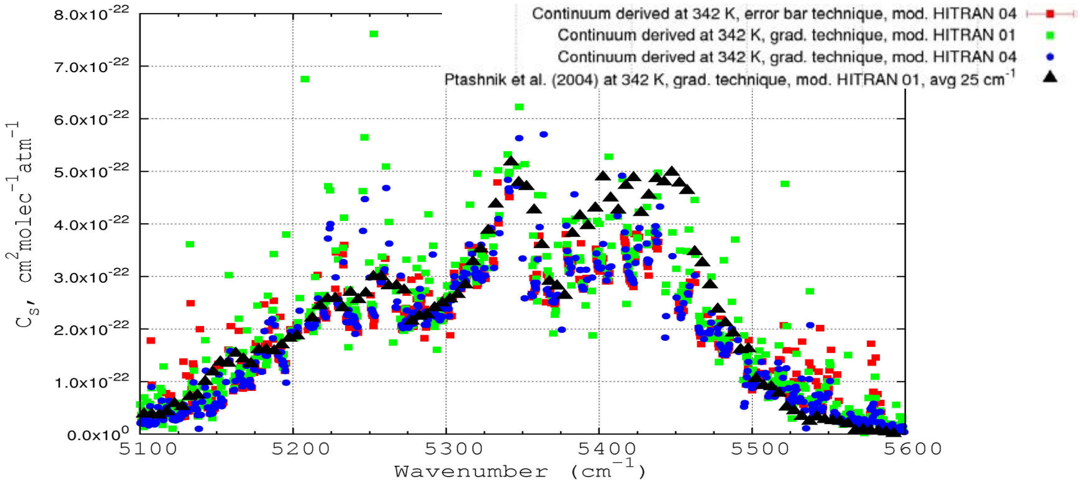

Figure 4.24 same as figure 25, but not averaged.

4.5. Comparing the continuum to other models

The three main continuum models are CKD, MT_CKD and the Ma and Tipping continuum. Even though CKD has been superseded by MT_CKD, it is included in this analysis, as it extrapolates the continuum using a different method than MT_CKD and thus does predict slightly different amounts of absorption (see section 2.7.1 and 2.8 for a discussion on the different continuum models). Both the CKD and MT_CKD continua provide predictions of the continuum for all of the bands and temperatures measured in this work. The Ma and Tipping continuum provides estimates from 2000 cm^{-1} upwards.

Figure 4.25 shows the CKD and MT_CKD continuum compared to the derived continuum from sets A296 (panel A) and A351 (panel B) in the 1300-1900 cm^{-1} region. It can be observed in both panels that while the CKD model roughly captures the peak in the continuum around 1550 cm^{-1}, the continuum does not dip as significantly around 1600 cm^{-1} as predicted and nor is the peak at 1700 cm^{-1} quite as pronounced. MT_CKD more accurately predicts the magnitude of the absorption around 1600 cm^{-1}, but does not capture the shape and some of the finer detail of the continuum absorption as well as the older CKD model. Both of the CKD and MT_CKD appear to underestimate the absorption more at 351 K compared to 296 K. This suggests that maybe the temperature dependence for both models is slightly too high.

The derived continuum from sets B296 (panel A) and B351 (panel B) between 3400 and 4000 cm^{-1} is presented in Figure 4.26. In this region the continuum contains two distinct peaks around 3620cm^{-1} and 3730cm^{-1} which are present in the continuum derived at both 296 K and 351 K. Here it can be seen that while both MT_CKD and CKD at both temperatures agree well with the derived continuum between 3750 cm^{-1} and 3900 cm^{-1}, neither predict these peaks. The Ma and Tipping model underestimates the continuum throughout this region. This is expected because their formulation of the continuum has not been developed to explain the continuum in the band centres (see section 2.7.2). The predicted dimer features of Schofield and Kjaergaard (2003) are shown here for comparison. The details of how these were fitted will be discussed in more detail in the next section. The negative temperature dependence of the self continuum is highlighted by the significantly stronger continuum at 296 K compared to 351 K observed in both Figure 4.25 and Figure 4.26. This is discussed in more detail in chapter 5.

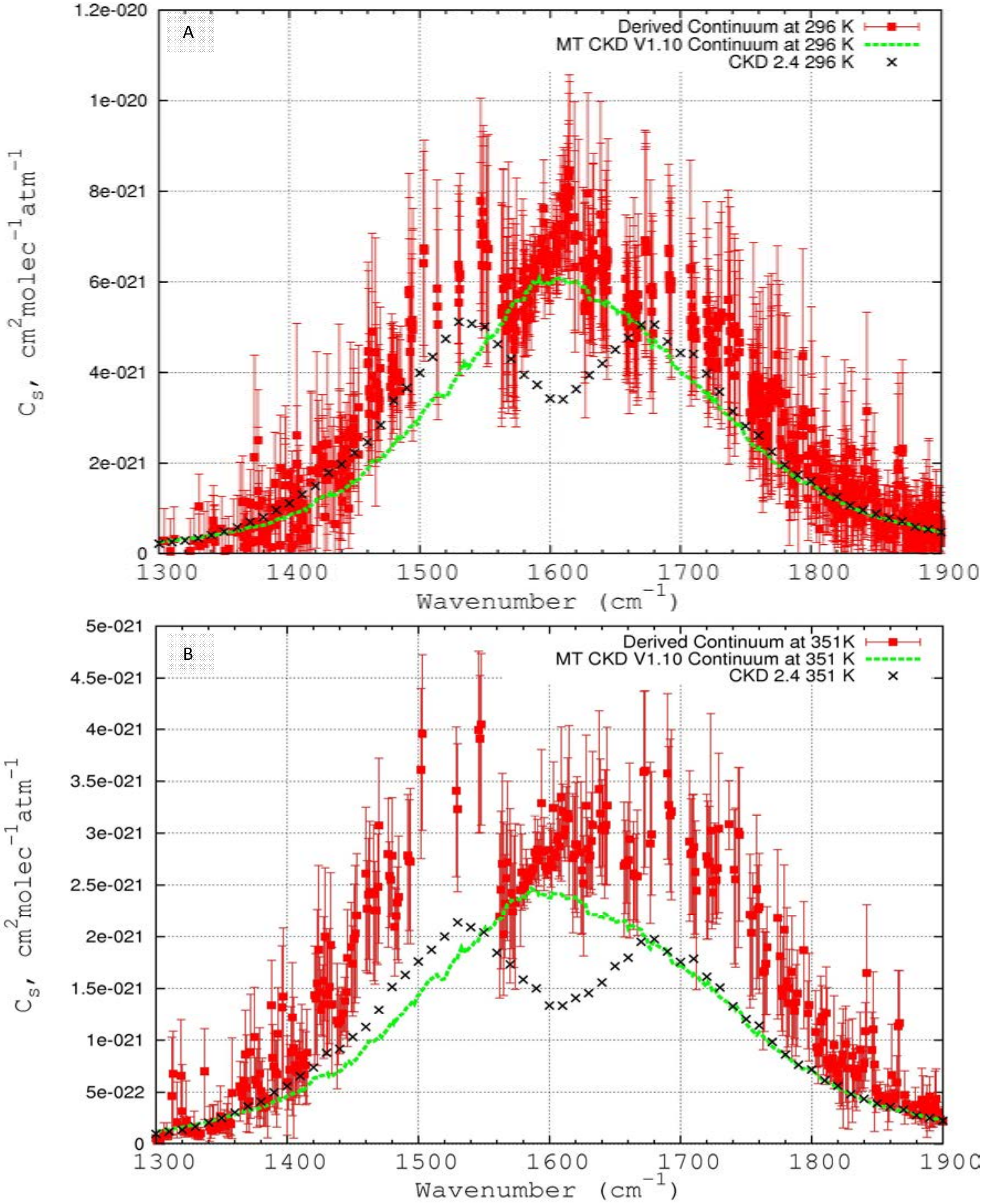

Figure 4.25 Panel A: The continuum derived between 1300 and 1900 cm^{-1} *using measurement set A296 compared to the predicted continuum at 296 K from MT_CKD and CKD. The errors bars are the result of uncertainties in HITRAN and experimental errors. Panel B is the same as panel A, but the continuum is derived from set A351 and the continuum from MT_CKD and CKD are at 351 K . For both panels; A = 1.5E-21, B= 0.5E-21 and D = 1 and* F *=0.02.*

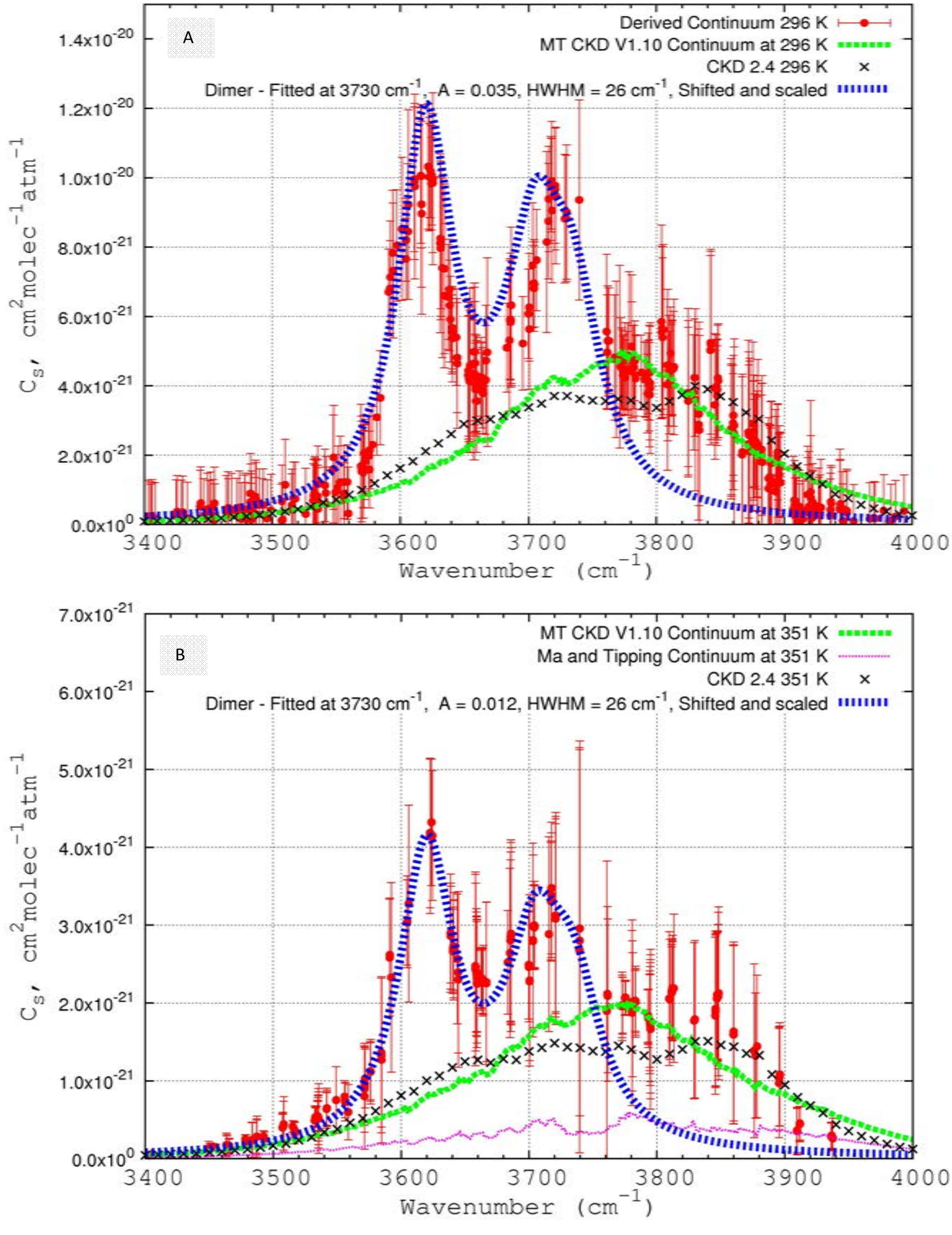

Figure 4.26 The continuum derived between 3400-4000 cm^{-1} using measurement set B351 compared to CKD, MT_CKD, Ma and Tipping and the water dimer theory of Schofield and Kjaergaard. The errors bars are the result of uncertainties in HITRAN and experimental error.. Panel A shows this result at 296 K and panel B at 351 K. For both panels A = 1.5E-21, B= 0.5E-21, D = 1 and Γ *=0.02.*

Figure 4.27 and Figure 4.28 show the comparison between the models and the continuum derived from set C351 in the 5000-5600 cm^{-1} and 6900-7500 cm^{-1} regions respectively. In both these regions the MT_CKD and CKD continua appear to capture the general shape and magnitude of the continuum. Overall, the older CKD model captures the shape of the continuum better than the newer MT_CKD. However, around 5300 cm^{-1} the MT_CKD continuum predicts the absorption slightly more accurately in the band centres than CKD. Neither predict the peaks around 5330 cm^{-1} and 5250 cm^{-1}, although as can be seen, both peaks are subject to large uncertainty. The possibility of water dimer contributing to these peaks will be discussed in the next section.

In all four bands both MT_CKD and CKD predict a gradually varying continuum. However, the derived continuum varies from micro-window to micro window. Thus, it appears that the derived continuum has a far finer structure than predicted by either version of CKD. Given the large errors due to HITRAN parameters, it is not possible to tell whether these are actually parts of the continuum or just the result of badly parameterised line half-widths and intensities in HITRAN.

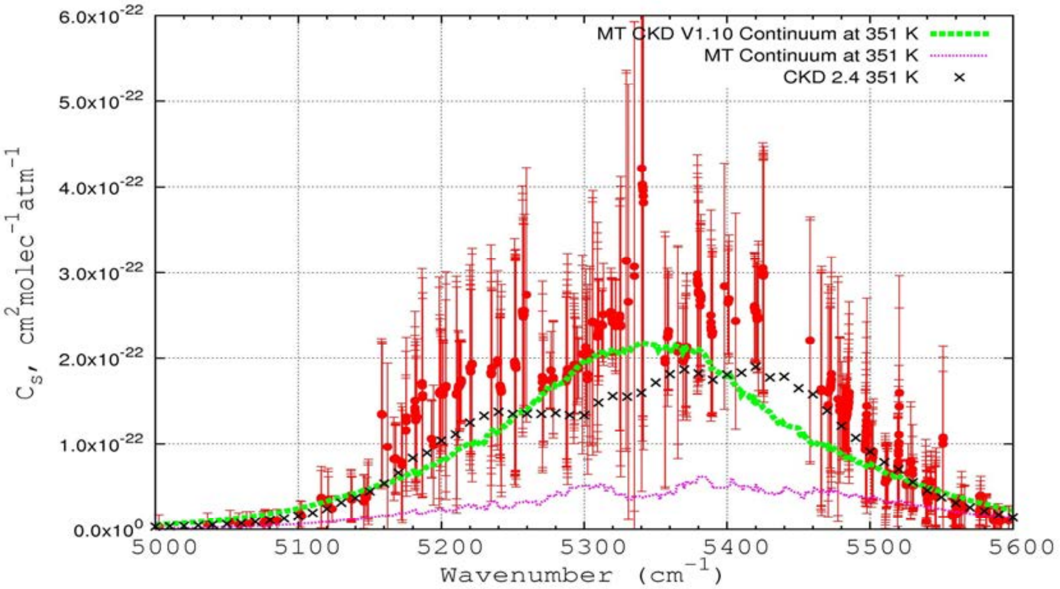

Figure 4.27 The continuum derived between 5100-5600 cm^{-1} using measurement set C351 compared to the MT_CKD, CKD and Ma and Tipping (MT) models. The error bars estimate the total possible error in the continuum resulting from experimental errors and HITRAN. A = 1.5E-22, B= 0.5E-23, D = 1. The line corrections to HITRAN 2004 by Ptashnik et al.(2005) are used for the calculated spectrum and F =0.02

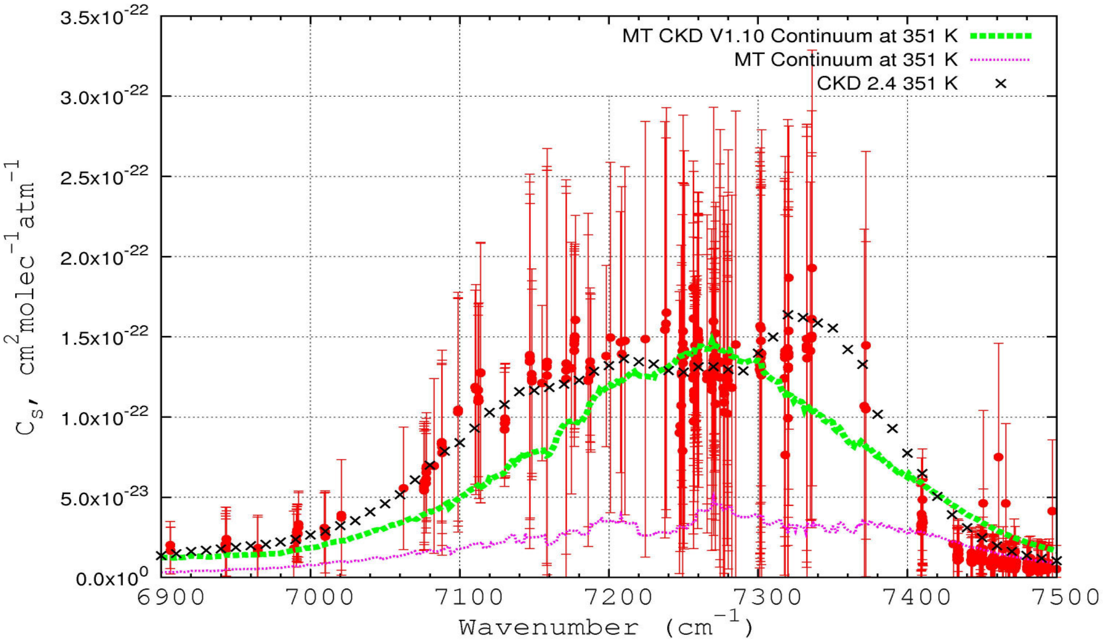

Figure 4.28 The continuum derived between 6900-7500 cm^{-1} using measurement set C351 compared to the MT_CKD, CKD and Ma and Tipping (MT) models. The error bars estimate the total possible error in the continuum resulting from experimental errors and HITRAN. A = 2.5E-22, B= 1E-23, D = 1 and F *=0.02.*

4.6. The continuum between the major bands

Even though the continuum is far weaker, the regions in-between the major water vapour bands are very important when estimating the atmospheric absorption by the continuum. Therefore, as will be discussed in chapter seven, it is vital in these regions to know the continuum accurately. The relatively short path length used in these experiments meant it was not possible below 190 mb and below 351 K to derive the continuum outside of the main band regions already shown so far in this chapter. However, even at the highest pressure obtained of 276.6 m, it was not possible to accurately derive the continuum in large areas between the bands.

Figure 4.29 shows the same analysis for the errors as in section 4.1 for the continuum derived from a pure water measurement conducted at 276.6 mb and 351 K. It is clear from panels A and B that at this pressure, it is possible to detect continuum absorption in the 3100-3400 cm^{-1} and the 4000-4300 cm^{-1} regions. The errors due to HITRAN generally are less significant away from the band centre, due to decreased monomer line absorption. Instead, errors due to noise and baseline become more important. In fact, between 4300 and 4700 cm^{-1} the errors due to noise and baseline become very significant, making it impossible to have much confidence in the continuum derived in this region.

Beyond 5600 cm^{-1} there are two separate problems. First, as can be seen in both Panel C and D, nearer the band the errors from HITRAN lead to large uncertainties in the continuum. Secondly, further away from the bands the optical depth is small enough that the error due to baseline and noise become greater than the derived continuum.

Rather unfortunately, it was not possible to measure the continuum either side of 1200 and 2000 cm^{-1} band, as measurements were not conducted at a high enough pressure.

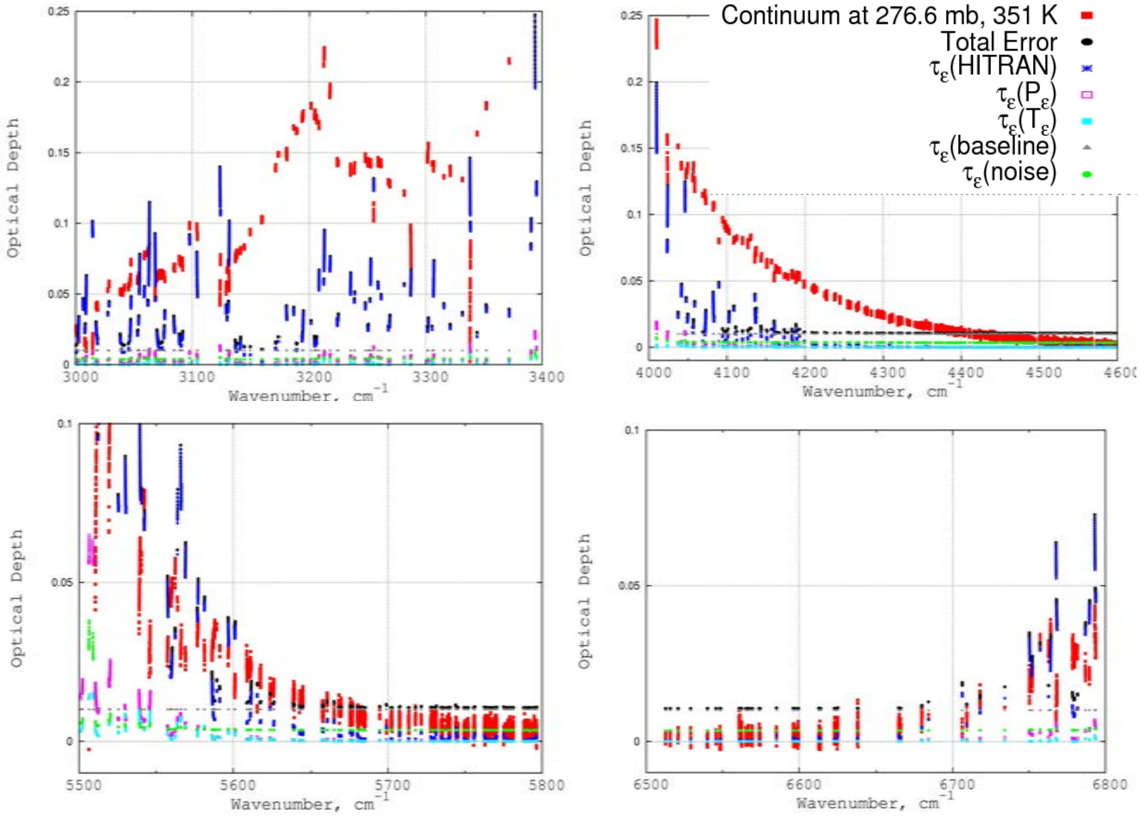

Figure 4.29. The continuum derived at 276.6 mb, 351 K in various regions. A baseline correction has been applied. The contribution of various errors is also shown for each derived point.

4.6.1. Baseline corrections

In Figure 4.29 the estimated error in optical depth due to baseline correction was set at 0.01. The actual baseline correction (i.e. the value subtracted from the derived continuum) to the four measurements making up set D351 is shown in Figure 4.30. The exact form of the baseline correction used when deriving the continuum is discussed in section 3.4.7. It can be seen that for two of the measurements the continuum actually dropped below zero, whilst for the other two it was considered too large. This disagreement between different measurements highlights the importance of correcting for baseline errors when presenting continuum results in weakly absorbing regions.

To correct for baseline error requires the setting of certain points of the measured optical depth to zero. These points are chosen where both the MT_CKD and Ma and Tipping continuum models suggest that the absorption should be so small, that it can be safely assumed that the measureable continuum absorption by this experimental setup would be zero. However, with no independent verification of either model in these regions there is no way of knowing whether they underestimate the amount of absorption. These measurements clearly do not help to solve that problem. For example at 4880 cm^{-1} where the baseline correction is performed, both models predict that there should be no detectable absorption, but as Figure 4.30 demonstrates before baseline correction a value for the continuum between +0.012 and -0.010 is obtained from the four different measurements making up set D351. The trouble with then setting the continuum to zero at some point is that it is unclear how much actual absorption is being removed. For this reason it is likely that the continuum obtained after baseline correction is a lower estimate.

Another problem with the baseline correction is whether or not the form of correction chosen is valid. The form the baseline subtraction takes (see section 3.4.7.) is only an approximation. It is possible that the baseline correction required is more complex. This could lead to certain areas where the continuum is under or over estimated. However, it was found that after baseline correction the continuum coefficients calculated from different measurements are in good agreement. This implies that the form of the baseline correction is valid. This is because it shows that the optical depth of the continuum is scaling with the vapour pressure squared and it is very unlikely that any baseline error would have a similar form.

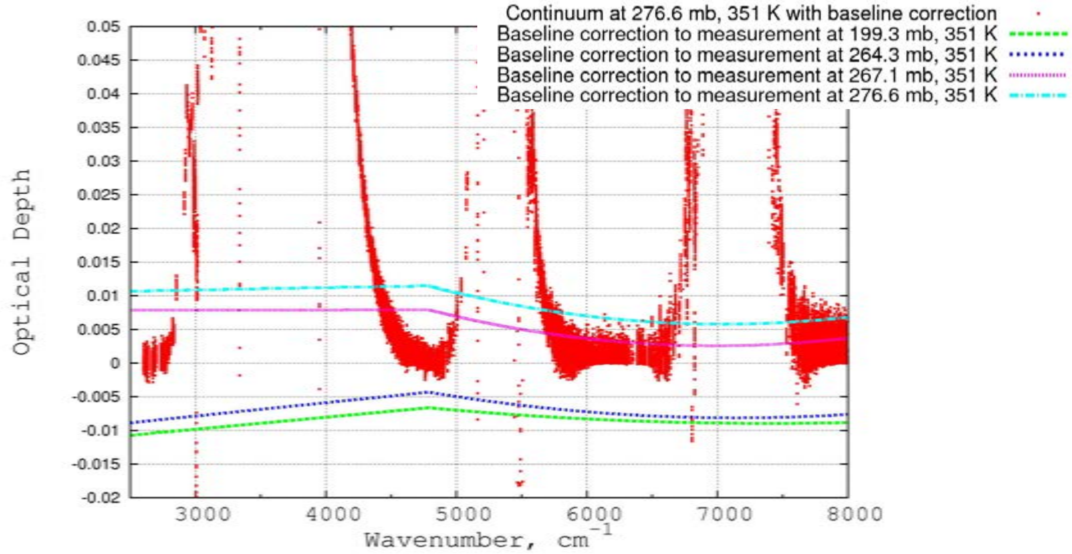

Figure 4.30 The continuum derived from a pure water vapour measurement at 276.6mb, 351 K after baseline correction (red points). The function subtracted from the continuum to correct the baseline for this measurement and the function used for three other measurements is shown.

4.6.2. Comparison with other models

The measurement set used for studying between the bands (D351) consists of four measurements. This set is analysed like the other sets in section 4.2. That is by taking a weighted average of the measurements derived at different pressures. In order to maximise the amount of data, the results here are only filtered to remove the line centres. These results are shown in Figure 4.31. Here the error bars represent the range of the continuum coefficient throughout the set. These show that there is very good agreement between the four different measurements, with the range between the four sets similar to the level of noise present. As noted this implies that the baseline correction applied to the continuum is of a satisfactory form. In addition this agreement between four separate measurements can give us confidence in the accuracy of the continuum.

The derived continuum between 3000 and 3400 cm^{-1} shown in panel A of Figure 4.31 is considerably greater than that predicted by either Ma and Tipping or either version of CKD. There is also a noticeable 'bump' around 3200 cm^{-1} that is not present in any of the continuum model, but is predicted by the *ab initio* calculation for the water dimer of Schofield and Kjaergaard (2003) (see section 4.7).

The opposite is seen between 4000 and 4200 cm^{-1} (panel B) where both

Ma and Tipping, MT_CKD and CKD overestimate the amount of absorption. Figure 4.29 shows that in this region for some points the total error only accounts for approximately 20% of the continuum value. As the MT_CKD continuum is approximately 100% greater than the measured continuum adjustments are need to the MT_CKD continuum in this region. The difference with the CKD and the Ma and Tipping continua is not so large, but still greater than the total error in some regions. Beyond 4200 cm^{-1} all continua models appear to underestimate the amount of absorption. However, as can be seen in Panel C in this region the disagreement between measurements starts to become rather large, so this result beyond 4400 cm^{-1} cannot be considered accurate.

In the regions between 4900 and 5100 cm^{-1} (panel D) MT_CKD and to a lesser degree CKD overestimate the amount of absorption and here the Ma and Tipping theory seems to fit best. This is not the case between 6500 and 7000 cm^{-1} (panel F) where MT_CKD seems to estimate the continuum more satisfactorily. The two regions on the 'far side' of the bands between 5500 and 5900 cm^{-1} (panel E), 7500 and 7700 cm^{-1} (panel G) show a very similar pattern to the 4000 - 4200 cm^{-1} region, with all three continuum theories overestimating the amount of absorption(especially MT_CKD) .

In summary, none of the models estimates the continuum satisfactory in all the regions between the bands at 351 K. In most regions near the bands the MT_CKD continuum appears to consistently overestimate the amount of absorption. In fact the older CKD continuum is far closer to the derived continuum than MT_CKD. In general it can be seen that the Ma and Tipping continuum does best at predicting the continuum between the bands. This is not surprising, as the Ma and Tipping continuum is designed to describe the line shape away from the line centres.

It should be noted that all of the continuum models predict a strong temperature dependence in-between the bands. This means that some of these discrepancies between the derived continuum and the models observed at 351 K may well not be so significant at lower temperatures. Therefore, before any firm conclusions can be drawn about corrections that need to be made, the continuum needs be measured in these regions at a range of temperatures.

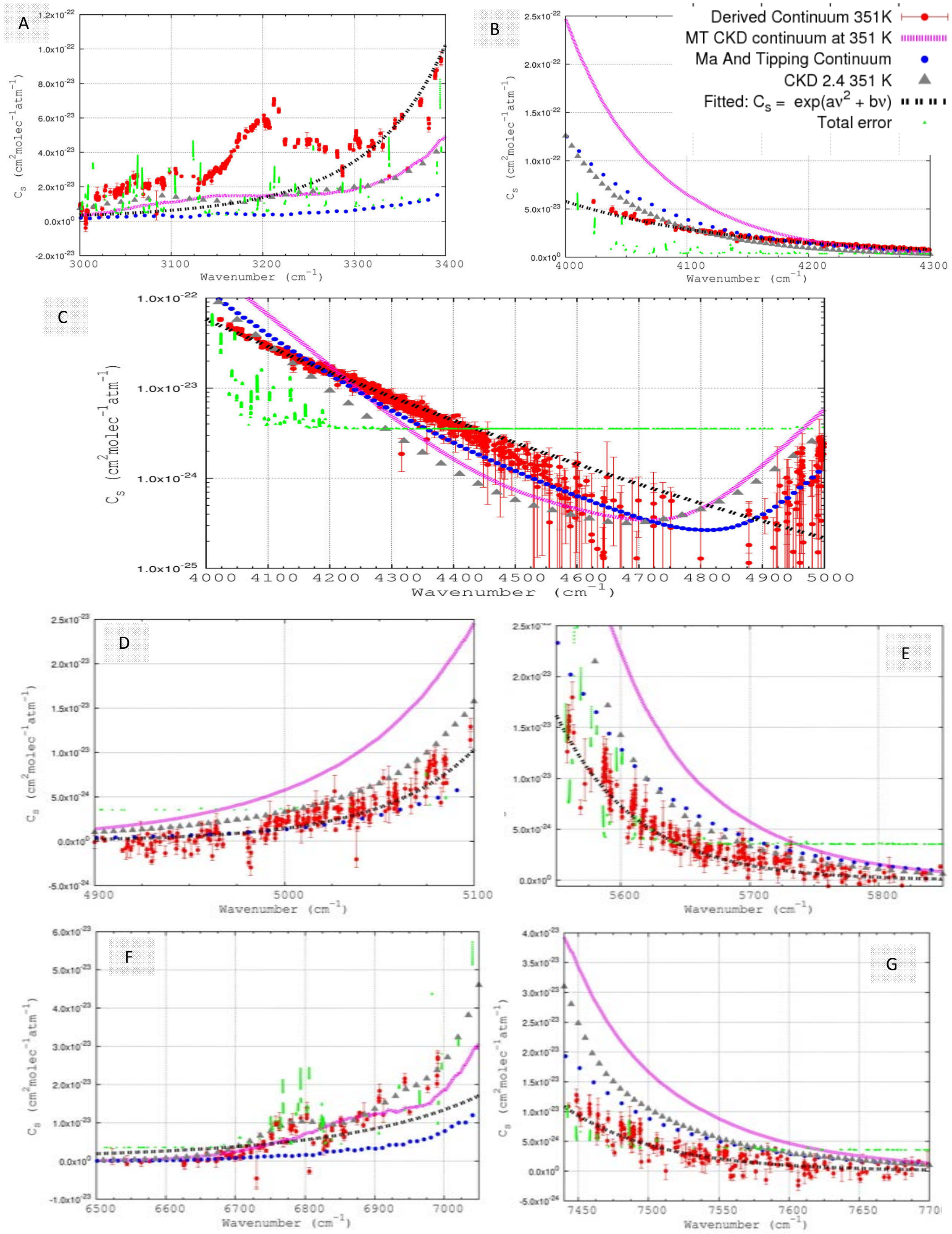

Figure 4.31. The continuum absorption between different bands derived from set D351. compared to the CKD, MT_CKD and the Ma and Tipping models. The error bars represent the range within the set. For filtering $\mathrm{F} = 0.03$.

4.6.3. Fitting to the shape of the wings

A function of the form,

$$\mathrm{C_S}(\nu) = \exp(a\nu^2 + b\nu), \tag{4.16}$$

was found to fit well to the continuum between 4000 and 4300 cm^{-1}. This form has no theoretical basis and can be seen purely as an empirical fit to the continuum. However, by fitting it to where there are data, it made it possible to estimate the contribution of the continuum in regions where it was not possible to derive the continuum from measurements. As Figure 4.31 demonstrates this form also fits well to most of the other regions. Given the uncertainty in wings beyond 5000 cm^{-1}, this means that there is a large amount of uncertainty attached to this fitting.

Fitting a Lorentzian like function to this decrease was also attempted. However, in all cases it was found to decrease too slowly with wavenumber and thus ended up overestimating the absorption the further away one moved from the band. This result is also interesting, because some authors such as Ptashnik et al. (2004) and Daniel et al. (2004) suggest that the water dimer might have a Lorentzian like band shape. This will be discussed more in the next section.

4.7. Fitting water dimer features to the continuum

As was discussed in section 2.8, various authors have speculated that the water dimer could contribute to the pure water vapour continuum. The search for the water dimer contribution has been greatly aided by recent theoretical advances predicting the strength and position of dimer transitions.

Schofield and Kjaergaard (2003) (from here on referred to as S&K) have produced a list of band positions and strengths for the bending and stretching transitions of the water dimer. This section will compare the water dimer bands predicted by S&K to the derived continuum at 351 K. For this, the method used by Ptashnik et al. (2004) to fit the water dimer to the continuum, as discussed in section 2.8.2 is employed. They assume that the dimer component ($C_D(\nu,T)$) of the continuum can be obtained from the S&K band strengths predictions using the following formula,

$$C_D(\nu,T) = \mathrm{A(T)} \sum_{\mathrm{i=0}}^{\mathrm{N}} \mathrm{S}_{\mathrm{band}_{\mathrm{d_i}}}(\nu_i, T_0) F_{band_{d_i}}(\nu, T_0), \tag{4.17}$$

Where there are N transitions, $\mathrm{S}_{\mathrm{band}_{\mathrm{d_i}}}$ is the band strength, $\mathrm{F}_{\mathrm{band}_{\mathrm{di}}}$ is the band shape and A(T) is,

$$A(T) = K_{eq}(T)\left(\frac{T_0}{T}\right)^{\frac{3}{2}} \exp\left[-C_2 E_{d_{avg}}\left(\frac{1}{T}-\frac{1}{T_0}\right)\right], \tag{4.18}$$

where $E_{d_{avg}}$ is the average lower state energy for the water dimer and $K_{eq}(T)$ is the dimer equilibrium constant. It can be seen that by applying a band shape to the S&K band strengths and then using A(T) as a scaling factor (which is independent of wavenumber) it is possible to attempt to fit $C_D(\nu,T)$ to the derived continuum.

This process assumes that there is no spectral variation in the temperature dependence of the dimer, which implies that if the S&K features are fitted to the continuum at 296 K (i.e. T_0) then one would expect the fit to work at 351 K by simply changing the value A(T). However, as section 5.2 and 5.3 will show, there is spectral variation in the temperature dependence of the continuum. This level of spectral variation is not enough to cause any features in the continuum which exist at 296 K to not be detectable at 351 K. Thus, as the aim of this section is to investigate whether the continuum exhibits any of the dimer like features, this form can be seen as being perfectly adequate.

It was discussed in chapter 2 that there is still some uncertainty as to whether the water dimer has a Lorentzian or Gaussian band shape or something different. For this reason the effect of fitting both will be investigated. If the water dimer has a Lorentzian band shape then,

$$F_{band_{d_i}}(\nu, T_0) = \frac{\alpha_{d_\mathrm{i}}}{\pi\left((\nu_i-\nu)^2+\alpha_{d_i}^2\right)}. \tag{4.19}$$

If a Gaussian band shape then,

$$F_{band_{d_i}}(\nu, T_0) = exp\left(-\frac{(\nu-\nu_i)^2}{\alpha_{d_i}^2}\right), \tag{4.20}$$

where α_{d_i} is the half-width half maximum of each transition (HWHM).

4.7.1. Water dimer features in the 3400-4000 cm^{-1} region

For the 3400-4000 cm^{-1} region Figure 4.32 panel A shows the dimer band strengths predicted by S&K with a Lorentzian band shape fitted. The peak at 3600 cm^{-1} is caused by the $|0\rangle_f|1\rangle_b|0\rangle$ transition, whilst the peak at 3730 cm^{-1} is caused by both the $|1\rangle_f|0\rangle_b|0\rangle)$ and $|01\rangle_-|0\rangle$ transitions. The fit is performed by choosing a value of A (T) and a Lorentzian half-width such that the value of $C_D(\nu,T)$ matches the peak in the derived continuum at 3730 cm^{-1}. However, fitting this feature causes an over estimate in the magnitude of the feature in the derived continuum at 3620 cm^{-1}. The 3620 cm^{-1} feature also appears to be slightly shifted away from the position predicted for the dimer by S&K. Thus, by shifting and scaling the predictions of S&K (i.e. changing the value of S_{band_d}), as shown in panel B, a better fit can be obtained. The details of the shifts and scaling are given in Table 4.1. As the values of the derived continuum are more accurate around the 3620 cm^{-1}, it was decided to fit a value of A(T) to this peak and then increase the strengths of the $|1\rangle_f|0\rangle_b|0\rangle\rangle$ and $|01\rangle_-|0\rangle$ transitions to scale up $C_D(\nu,T)$ around 3730 cm^{-1} to fit the derived continuum. This shifting and scaling can be justified by the fact that there is still considerable uncertainty in the calculations of S&K. All of the scaling performed lies within the expected uncertainties. (*Kjaergaard, personal communication).*

It can be seen that once these adjustments are made, the water dimer predictions of S&K agree well with the derived continuum between 3400 and 3750 cm^{-1}. Between 3750 cm^{-1} and 4000 cm^{-1} the water dimer theory under predicts the amount of continuum absorption. A theoretical explanation for this extra absorption is currently lacking from water dimer theory.

One possible explanation could be that the water dimer is not the only mechanism contributing to continuum absorption. As discussed in chapter 2, the MT_CKD continuum estimates the continuum by assuming an adjustment to each water monomer line. Even though this adjustment is empirically fitted, it does give an idea of where an adjustment in the absorption of the monomer line would result in continuum absorption. Hence, it is interesting to note that once the MT_CKD continuum is subtracted away from the continuum, as is shown in panel C, it is still possible to fit a dimer spectrum without any scaling required to the band strength (although at smaller value of A(T) is used). This exercise also goes some way to showing that the features detected cannot be explained by applying the same adjustment to every monomer line in the way that MT_CKD does. Subtracting MT_CKD also seems to remove some the continuum between 3750 cm^{-1} and 4000 cm^{-1}.

Panel D has the dimer features fitted with a Gaussian band shape. This does seem to fit the centre of the two peaks as well as the Lorentzian, but decreases too rapidly with wavenumber moving away from the band between 3400-4000 cm^{-1}. Thus, it can be said that the Lorentzian captures the structure of the continuum around the peaks better than the Gaussian does.

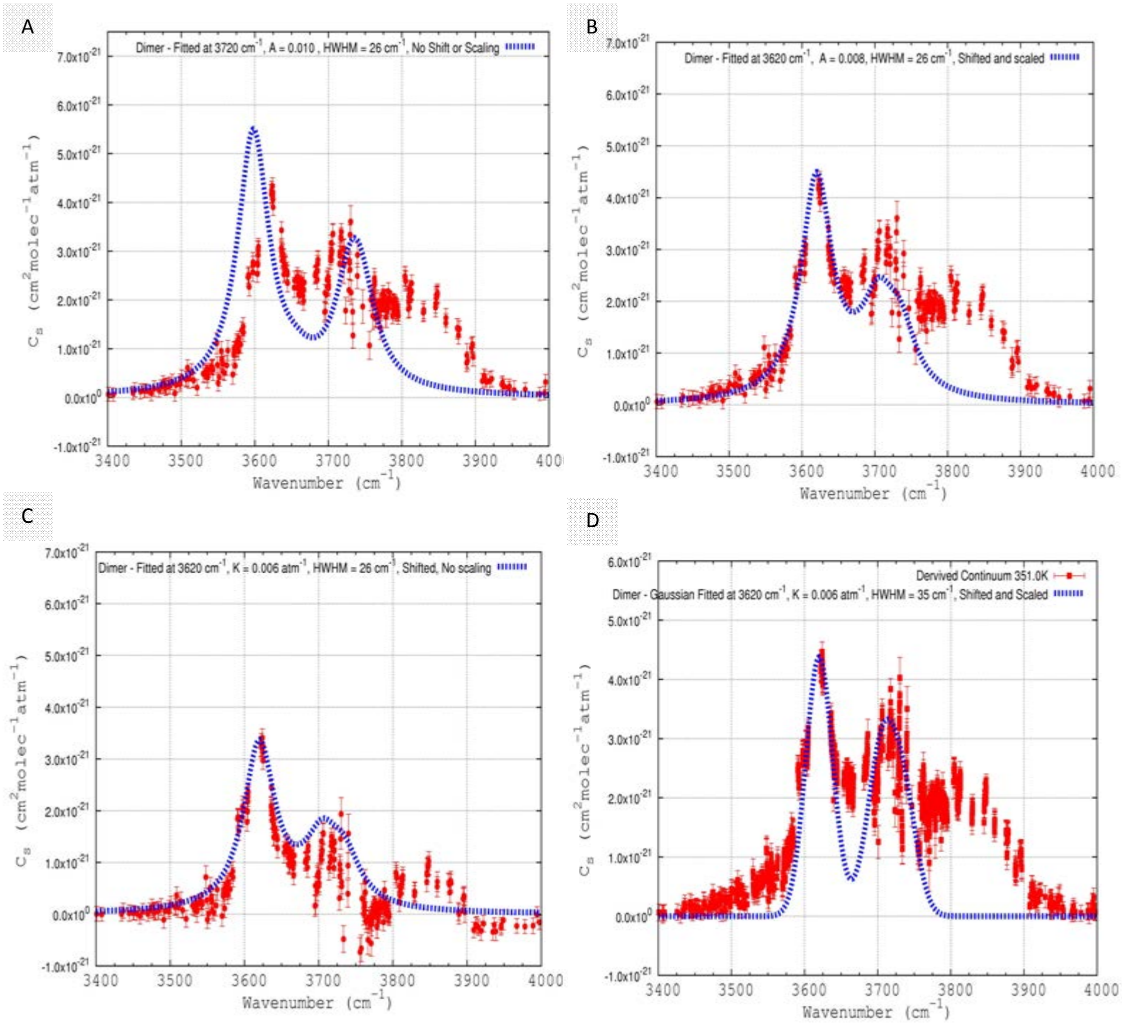

Figure 4.32 The S&K dimer features fitted to the derived continuum from set B351. Panel A: S&K bands fitted with Lorentzian bandshape, but with no scaling or shifting. Panel B: Same as A, but with shifting and scaling as described in the text. Panel C: The derived continuum with the MT_CKD continuum subtracted, the dimer feature fitted and not scaled. Panel D: The same as B, but with a Gaussian band shape fitted. The errors bars are two standard deviations of the set B351 as calculated using equation 3.37

4.7.2. Water dimer features in other regions

Figure 4.33 shows the dimer features predicted by S&K in the other bands studied compared to the derived continuum. Between 1300 and 1900 cm^{-1} S&K predict that there should be two features situated near each other at 1596 cm^{-1} and 1627 cm^{-1}, which correspond to the $|00\rangle|1\rangle$ and $|0\rangle|0\rangle|1\rangle$ transitions respectively. It is clear from panel A that even when applying a band half-width of 30 cm^{-1} and a larger value of A(351 K) (0.02 atm^{-1}) than used previously that the feature is not broad enough to explain much of the absorption in the band. Furthermore, unlike in the 3400-4000 cm^{-1} region there are no distinct features in the derived continuum that match up specifically to those predicted by S&K.

Panel B compares the prediction of S&K to the continuum absorption between 3000 and 3500 cm^{-1}. As can be seen in Figure 4.31 in this region the continuum absorption is much larger than that predicted by either the MT_CKD or Ma and Tipping continuum. S&K predicted that there should be a dimer feature 3215 cm^{-1} caused by the $|0\rangle|0\rangle|2\rangle$ transition. By scaling the strength of the feature by a factor of 0.7 and shifting it by -20 cm^{-1} it is possible to achieve a good fit with the measured continuum. In this region there is a considerable contribution from the Lorentzian wings of the features at 3730 cm^{-1} and 3620 cm^{-1}. No adjustment had to be made to the fitting seen in panel B of Figure 4.32. This suggests that between 3000 and 3600 cm^{-1} that fitting a Lorentzian wing to the dimer features of S&K agrees well with the observed continuum absorption.

In the 5000-5600 cm^{-1} the water dimer theory seems to capture some of the continuum. Peaks around 5250 cm^{-1} agree well with the $|0\rangle_f|1\rangle_b|1\rangle$ transition and that at 5330 cm^{-1} with the $1_f|0\rangle_b|1\rangle$ and $|10\rangle_-|1\rangle$ transitions. However, either side of these regions there are large areas that cannot be currently explained. Less confidence can be placed in attributing continuum features to the water dimer in this region compared to the 3400- 4000 cm^{-1} region. This is because, as Figure 4.26 demonstrates the errors due to HITRAN, especially for the peak at 5330 cm^{-1} are quite large. In addition the peak at 5250 cm^{-1} is also from one micro window, making it vulnerable to an error in just a single strong line. In this region, a value for A(351K) used of is 0.02 atm^{-1}, which is larger than the 3400-4000 cm^{-1} region. Between 6900 and 7500 cm^{-1}, very much like in the 1300 – 1900 cm^{-1} region there is no real distinct features matching up to that predicted for the dimer. Using an A (351 K) value of 0.02 atm^{-1} does give a peak of a similar magnitude to the continuum, but still only explains a small region of the continuum.

In summary, the strategy adopted here has been to fit a value of A(351 K) such that one of the features predicted by S&K is of a similar order of magnitude to the continuum in a spectral region, even if in some cases there are no apparent dimer features. Within a region the value of A(351 K) was assumed constant and thus if fitting different S&K transitions within a region resulted in different values of A(T) the S&K features were scaled by the factor shown in Table 4.1.

This strategy resulted in a much smaller value of A(351 K) in the 3400-4000 cm^{-1} region compared to the other regions. In reality one would expect the value of A(T) to be very similar from band to band, with maybe a variation of around 15% explainable by different values of E_{avg} where the fitting occurs. One reason for this large variation may be because the continuum is actually not solely the result of the water dimer. If one assumes a smaller value of A(T) to be correct then the dimer would only contribute significantly to the continuum around 3620 and 3200 cm^{-1}. In other regions its contribution would be somewhat smaller than whatever other mechanisms are contributing to the continuum. This would explain that why, despite there being possible dimer features at 5250 cm^{-1}, 5330 cm^{-1} and maybe even 1600 cm^{-1}, water dimer theory cannot explain the whole self continuum.

	ν_i cm^{-1} S&K	$S_{band_{d_i}}$ (cm^1/(molecule.cm^{-2}) S&K	$S_{band_{d_i}}$ *scale* This work	ν_i *shift* cm^{-1} This work	HWHM cm^{-1} This work	A(351 K) atm^{-1} This work
$|00\rangle|1\rangle$	1596	1.27E-17	1	0	30	0.020
$|0\rangle|0\rangle|1\rangle$	1627	7.38E-18	1	0	30	0.020
$|00\rangle|2\rangle$	3149	2.62E-20	1	0	30	0.008
$|0\rangle|0\rangle|2\rangle$	**3215**	**7.29E-19**	**0.7**	**-20**	**30**	**0.008**
$|0\rangle_f|1\rangle_b|0\rangle$	**3598**	**4.36E-17**	**1.0**	**22**	**26**	**0.008**
$|10\rangle_+|0\rangle$	**3656**	**2.17E-18**	**1.0**	**26**	**26**	**0.008**
$|0\rangle_f|1\rangle_b|1\rangle$	**3730**	**1.54E-17**	**1.4**	**-25**	**26**	**0.008**
$|10\rangle_-|0\rangle$	**3745**	**1.16E-17**	**1.4**	**-10**	**26**	**0.008**
$|0\rangle_f|1\rangle_b|1\rangle$	**5231**	**4.80E-19**	**1.7**	**25**	**26**	**0.020**
$|10\rangle_+|1\rangle$	**5256**	**1.75E-20**	**1**	**0**	**26**	**0.020**
$|10\rangle_-|1\rangle$	**5341**	**9.82E-19**	**1**	**-7**	**26**	**0.020**
$|0\rangle_f|1\rangle_b|1\rangle$	**5357**	**8.73E-19**	**1**	**-7**	**26**	**0.020**
$|1\rangle_f|0\rangle_b|2\rangle$	6944	4.36E-21	1	0	30	0.020
$|0\rangle_f|1\rangle_b|2\rangle$	7047	2.18E-21	1	0	30	0.020
$|20\rangle_+|0\rangle$	7200	1.27E-19	1	0	30	0.020
$|20\rangle_-|0\rangle$	7239	5.72E-19	1	0	30	0.020
$|2\rangle_f|0\rangle_b|0\rangle$	7238	3.45E-19	1	0	30	0.020
$|1\rangle_f|1\rangle_b|0\rangle$	7371	3.49E-20	1	0	30	0.020
$|11\rangle_+|0\rangle$	7440	1.75E-21	1	0	30	0.020

Table 4.1 A list of the dimer features predicted by S&K in the regions studied. Where this work has detected possible features is highlighted in bold and green. Possible scaling factors in line intensity or shifts in band positions suggested by this work are also given. If a value is red, it had not been possible to detect evidence for this transition from the continuum measurements.

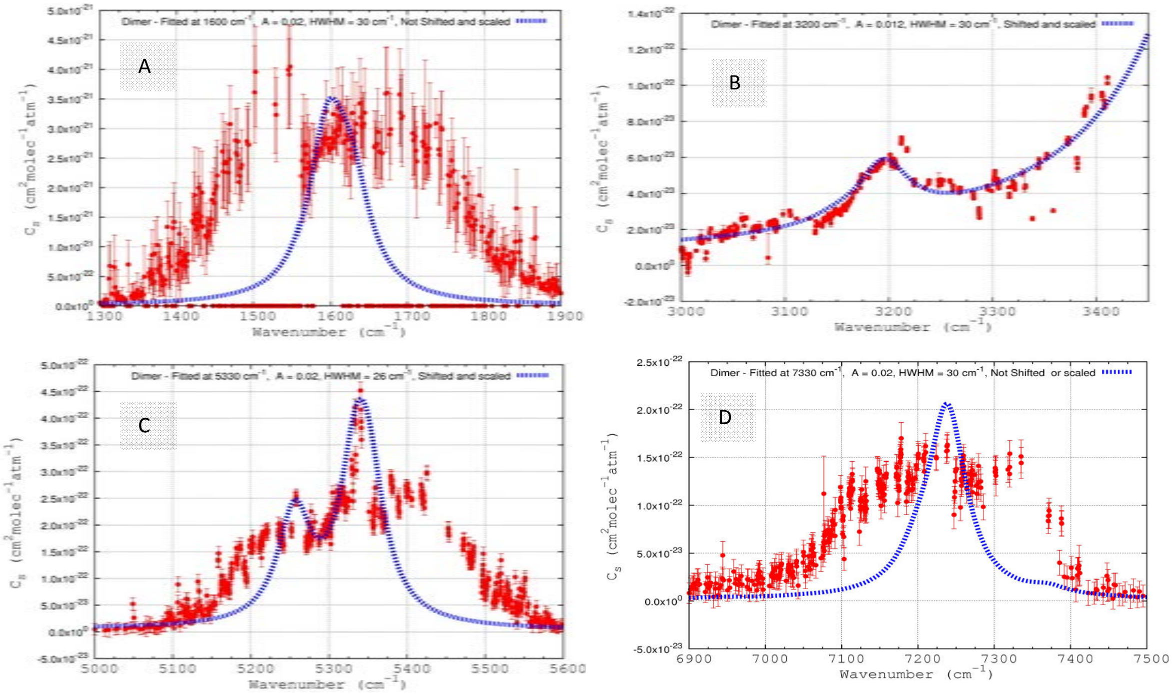

Figure 4.33 Attempts to fit the dimer transitions of S&K to the self continuum derived in different spectral regions. The fitting parameters are shown on each panel and in all cases a Lorentzian band shape is assumed. Panel A: The continuum from set A351. Panel B: The continuum from set D351. Panel C and D are from set C351.

4.7.3. Water dimer contribution between the bands.

In section 4.6.3 it was commented that between the bands the continuum between 4000 and 5000 cm^{-1} does not appear to be Lorentzian in nature. Figure 4.34 shows the absorption between for bands resulting from the S&K water dimer with a Lorentzian band shape as fitted in to the 3620 cm^{-1} feature. This is compared to the prediction between the bands of the MT_CKD and the Ma and Tipping continua. The continuum derived in this work, along with the estimated error is also shown.

It can be seen that, despite underestimating the continuum at the edge of the band centres, due to the Lorentzian band shape, the dimer theory predicts up to an order of magnitude more continuum than either other continuum model between the bands. Between 4000 cm^{-1} and 5000 cm^{-1} the amount of absorption being predicted using the Lorentzian band shape should be detectable, as it is greater than the estimated baseline error. However, it was seen that continuum measurement by this work in this region decreases far more rapidly between 4000 and 4400 cm^{-1} than suggested by the dimer theory.

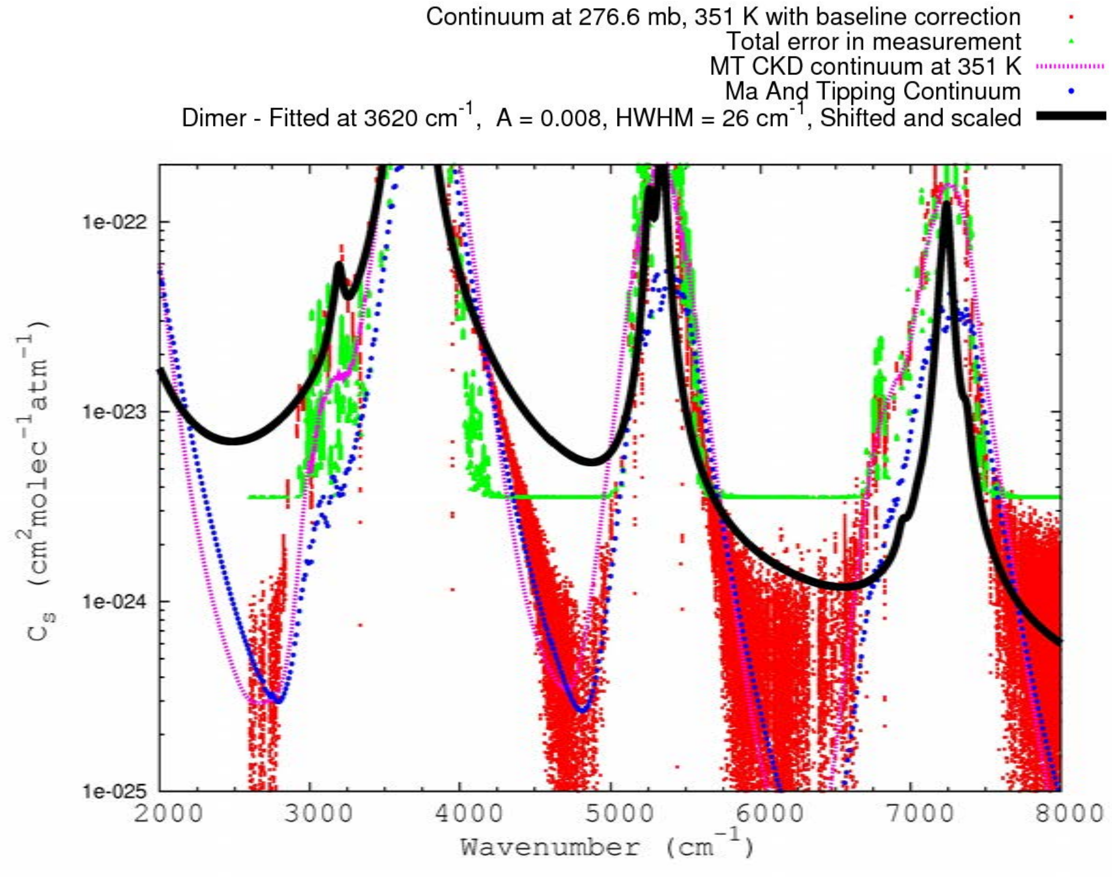

Figure 4.34 The continuum absorption predicted by S&K with a Lorentzian band shape (black solid line) compared to the MT_CKD and Ma Tipping models at 351 K. The continuum derived from a measurement at 276.6 mb and 351 K with a baseline correction applied, along with the error estimated in this measurement is also shown (green).

4.8. Conclusions

In conclusion, it can be stated that a clear self continuum has been detected in all major water vapour bands between 1200 and 8000 cm^{-1}. It was demonstrated that near the band centres the dominant source of error was those due to the HITRAN database. Over the pressure range that these measurements were conducted, in all regions the optical depth of the continuum was observed to scale with the vapour pressure squared. This allowed the measurements when expressed in terms of the continuum coefficient to be to be averaged together to create measurement sets. The agreement between the sets in general was seen to be better than the estimated experimental errors and errors due to HITRAN.

The performance of both MT_CKD and CKD was mixed. In general both MT_CKD and CKD fell within errors bars estimated for the derived continuum, but did not capture some of the finer variations seen in the continuum. The biggest failing of both models was that they did not predict the peaks detected in the continuum around 3620 cm^{-1} and 3730 cm^{-1} at 351 K.

Looking at the regions between the bands it was seen that the MT_CKD continuum overestimates the size of the continuum between 3950 - 4150cm^{-1}, 5500-5700cm^{-1} and 7400-7600cm^{-1} at the far edge of each absorption band. This to a lesser extent was also seen to be case with the CKD and Ma and Tipping models. It was shown that the decrease in the continuum away from the bands could be fitted with an exponential function.

The theoretical predictions of S&K were compared to the derived self continuum. The peak in the derived continuum around 3620 cm^{-1} agreed well with the predicted $|0\rangle_f|1\rangle_b|0\rangle$ transition and the 3730 cm^{-1} peak with the $|1\rangle_f|0\rangle_b|0\rangle)$ and $|01\rangle_{-}|0\rangle$ transitions. Whilst the latter peak was in a region of strong monomer absorption the former was found to be slightly red shifted away from the major monomer absorbing area, as one would expect for the dimer. In addition the peak around 5230 cm^{-1} agrees well with the $|0\rangle_f|1\rangle_b|1\rangle$ transition and that at 5330 cm^{-1} with the $1_f|0\rangle_b|1\rangle$ and $|10\rangle_{-}|1\rangle$ transitions.

The peak detected at 5330 cm^{-1} was about 20% smaller than that derived by Ptashnik et al. (2004). This was most likely due to a mixture of different versions of HITRAN used and the fact that in this region of the spectra, the water monomer absorption is very strong, making it highly susceptible to errors in the measured partial pressure. In this region a 2.5 times larger value of the A(T) scaling factor was required to fit the water dimer to the continuum than at 3620 cm^{-1}. The other significant feature detected was that at 3200 cm^{-1} which seemed consistent with the predicted $|01\rangle_{-}|0\rangle$ feature. In the 1200-2000 cm^{-1} and 6900-7500 cm^{-1} regions there was no detectable feature that matched up with the S&K predictions. In addition the water dimer theory could not explain the continuum between 3800 and 4000 cm^{-1} or between 5400 and 5600 cm^{-1}.

5. Temperature Dependence of the Self Continuum

So far this work has mainly concentrated on the self continuum derived at 351 K. The main reason for this is that the temperature dependence of the continuum is far more complex than the square dependence observed for pressure. Therefore, measurements at different temperatures cannot be inter-compared in the same way as those at different pressures are by simply dividing through by a certain factor. It can be seen from that there are measurement sets at different temperatures between 296 K and 351 K. The aim of this section is to compare the continuum coefficient derived from each measurement set at the same wavenumber, but at different temperatures. That is to say, to perform a wavenumber by wavenumber analysis of the temperature dependence of the continuum. This temperature dependence is then compared to that of both MT_CKD and the water dimer to help shed light on the origins of the continuum.

The continuum derived at 317 K and 351 K in the 3400 – 4000 cm^{-1} spectral region is presented in Figure 5.1 Panel A. It can be observed that there is a large negative temperature dependence even over a relatively small temperature range. This results from a stronger temperature dependence in the measured spectrum compared to that calculated using HITRAN 2004.

This is demonstrated in panel B where the ratio of the absorption calculated using HITRAN 2004 at 317 K to that calculated at 351 K is shown for the micro windows. This is calculated in the units of the continuum coefficient (i.e. optical depth multiplied (kT/PL) (red squares). It can be seen that HITRAN generally predicts there should be very little difference in the absorption in the micro-windows at the two temperatures. For the measured spectra the ratio of 317 K to 351 K, which is also show in panel B, (green triangles) is greater. As the continuum is the difference between the measured and calculated spectra, this has an even stronger temperature dependence as is shown by blue circles in panel B.

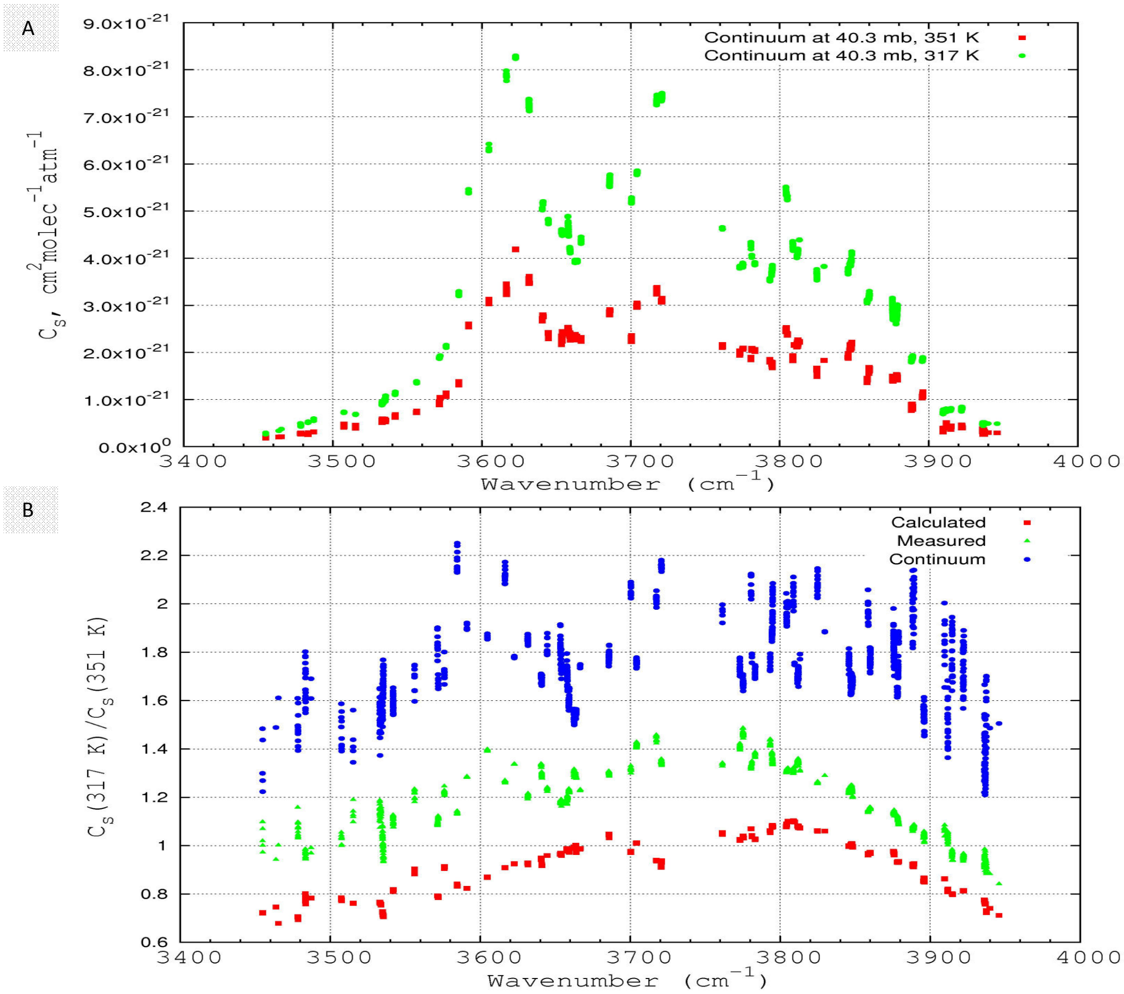

Figure 5.1 Panel A: The continuum derived from a single measurement at 351 K compared to that at 317 K absorption. Panel B: The ratio of absorption calculated using HITRAN 2004 at 317K to that calculated at 351K is shown by the red points. The green points show the ratio of the measured absorption for the same temperatures. The ratio of the continuum (i.e.(measured 351K –calculated 317 K))/(measured 351 K –calculated 351 K)) is shown by the blue points.

The temperature dependence expected for the water monomer has already been discussed in section 3.4.5. Equation (3.25) gave the temperature dependence for the absorption of the water monomer. This shows that there are three separate mechanisms which contribute to temperature dependence; the line shape, the partition function and the population of state. The first two have a negative temperature dependence, whilst the latter has a positive temperature dependence. The ratios of these temperature dependence of these mechanisms between 317 K and 351 K are shown in Table 5.1. As the half-width and population of states are line dependent, values are chosen which would maximise the negative temperature dependence (i.e. be as close as possible to that observed for the continuum). It can be seen even when these values are assumed the ratio is not as large as that seen for the continuum.

Partition function	Half-width	Population of states	Total
1.16	1.06	0.88	1.08

Table 5.1 The 317K to 351K ratio of the three contributing terms to the temperature dependence of the water monomer. The formula for each of these is given in section 3.4.5. A value of n = 0.7 and lower state energy of 200 cm^{-1} is assumed. Note that when calculating the optical depth an extra 1/T temperature dependence term needs to be included by virtue of calculating the number density.

5.1. Temperature dependence of the CKD Model

In section 2.7.1 the CKD continuum temperature dependence is introduced as a function of the continuum at 296 K and 260 K and is defined as,

$$C_S(\nu,T) = C_S(\nu,296)\left(\frac{296}{T}\right)\left(\frac{C_S(\nu,260)}{C_S(\nu,296)}\right)^{\frac{296-\mathrm{T}}{36}}. \tag{5.1}$$

Both CKD and MT_CKD have exactly the same temperature dependence. As discussed this has no apparent theoretical basis, but instead it is fitted to continuum measurements at different temperatures between 1200 and 2000 cm^{-1}. This is not a very useful form, as for the present work no measurements have been conducted below 296 K. For this reason, it is beneficial to rewrite equation (5.1) in a different form. Consider that we can perform the following two substitutions,

$$\exp(\sigma(\nu))\exp(B) = \left(\frac{C_S(\nu,260)}{C_S(\nu,296)}\right)^{\frac{-\mathrm{T}}{36}}, \tag{5.2}$$

and,

$$A = 296\left(\frac{C_S(\nu,260)}{C_S(\nu,296)}\right)^{\frac{296}{36}}\exp(B). \tag{5.3}$$

This then allows us to write,

$$C_S(\nu,T) = \frac{A}{T}\exp(-\sigma(\nu)T). \tag{5.4}$$

It then follows that the continuum at an arbitrary temperature T_1 can be derived from that at T_2 by the expression,

$$C_s(\nu,T_2) = C_s(\nu,T_1)\frac{T_1}{T_2}\exp[\sigma(\nu)(T_1-T_2)]. \tag{5.5}$$

It is possible to write this equation in linear form as,

$$\ln\left(\frac{C_S(\nu,T_2)T_2}{C_S(\nu,T_1)T_1}\right) = \sigma(\nu)(T_1-T_2). \tag{5.6}$$

Hence, the temperature dependence of the MT_CKD continuum can be defined by the variable which we will call $\sigma_{ckd}(\nu)$. It also possible to perform a least squares fit using equation (5.6) upon the continuum derived in this thesis and define its temperature dependence using the variable we will call $\sigma_D(\nu)$. The 'D' stands for that it is fitted to the derived continuum.

There are two things to test here; firstly whether the CKD form of temperature dependence agrees with that observed in this work. This will be tested by observing how well $\sigma_D(\nu)$ fits to the continuum derived in this work. Second there is the question of how good MT_CKD is at fitting the temperature dependence. This is tested by comparing the values of $\sigma_D(\nu)$ to $\sigma_{ckd}(\nu)$.

One major limiting factor was that the experimental setup was such that it was only ever possible to measure spectra between 296 K and 351 K. In addition this range was further limited for the two major absorbing bands at wavenumbers greater than 5000 cm^{-1} by the fact that continuum could only be derived at pressures above 70 mb, due to the relatively short cell path length. For this vapour pressure a temperature of at least 317 K was needed. Because of time constraints it was also only possible to obtain 3 measurement sets (C317, C337 and C351) for these regions. For the 1200-2000 cm^{-1} region it was also only possible also to obtain 3 sets (A296, A330, A351). Between 3400 and 4000 cm^{-1}, where five sets (B296, B304, B317, B337 and B351) were used in the fitting, it was possible to have more confidence in the results. In all cases, due to a rapid decrease in continuum absorption moving away from the band centre this analysis was only performed for the band centres.

The uncert in the continuum due to uncertainties in HITRAN are used to obtain the error bars. This tells us how sensitive the temperature dependence of the continuum is to HITRAN parameters. Experimental errors are not included in the analysis for the reason that at lower temperatures these errors will be larger. Hence, it can be seen that if a fitting was performed to the maximum estimated errors for each set, this would result in an artificially large or small bias in the temperature dependence.

Figure 5.3 panels A - D compare the values obtained for $\sigma_D(\nu)$ (i.e $\sigma(\nu)$ fitted to this work) to that of $\sigma(\nu)_{CKD}$ (i.e $\sigma(\nu)$ from MT_CKD) for the four major bands in which the continuum was derived. As noted, the error bars represent the fitting performed when the errors due to HITRAN are added or subtracted from each continuum set. When this error is subtracted (representing a maximum estimated value of the calculated optical depth and thus a minimum continuum), the strongest temperature dependence is observed. This is because, as is seen in Figure 5.1, the measured spectrum has a stronger temperature dependence than the calculated spectra. Thus, the greater the subtracted value of the calculated spectra the stronger the temperature dependence.

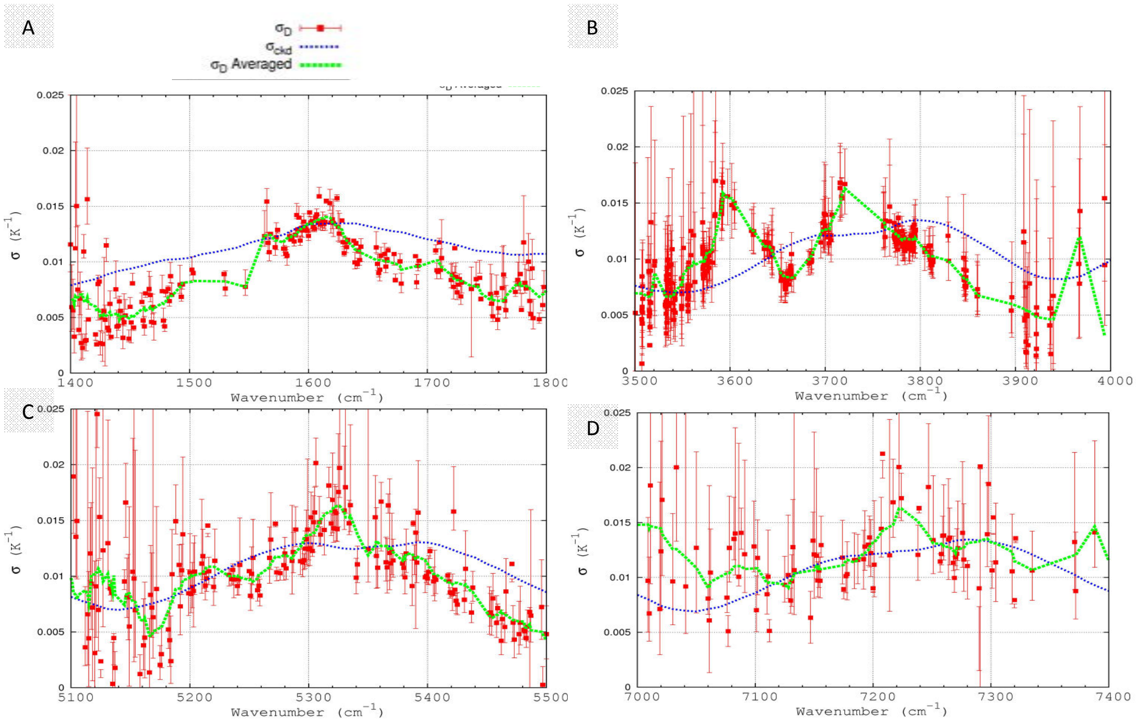

Figure 5.2 The value of $\sigma_D(\nu)$ and $\sigma(\nu)_{CKD}$ for different bands. Panel A, B,C and D show the 1400-1800 cm^{-1} , 3500-4000 cm^{-1}, 5100-5500 cm^{-1} and 7000-7400 cm^{-1} regions respectively. A value of $\sigma_D(\nu)$ averaged over 25 cm^{-1} is also shown.

It can be seen that while MT_CKD does predict a similar value to that derived here, it fails to capture some of the finer detail. For example, for the peaks at 3600 cm^{-1}, 3730 cm^{-1} and 5300 cm^{-1} there is a significant difference between MT_CKD and this work. The values of MT_CKD and this work agree well around 1600 cm^{-1}, but between 1625 cm^{-1} and 1800 cm^{-1} MT_CKD predicts a stronger temperature dependence. Such an overestimate is also apparent in the 3800-4000 cm^{-1} and 5400-5500 cm^{-1} regions.

This plot is not particularly clear at showing the effect of these differences upon the continuum. A better option is to compare the estimated value of the continuum at a particular temperature to what is actually measured. Figure 5.3 Panel A shows the continuum estimated at 296 K using values of σ_{CKD}, σ_D compared to the continuum measured at 296 K between 1400 and 1800 cm^{-1}. The estimates are obtained by taking the continuum measured at 351 K and using both σ_{CKD} and σ_D to estimate its value at 296 K. Panel B shows the same as Panel A, this time for the region between 3500 and 4000 cm^{-1}. For the 5100-5500 cm^{-1} and 7000-7400 cm^{-1} region (shown in panels C and D respectively) the continuum measurement at 317 K is shown compared to that estimated for 317 K. The temperature was higher for these regions, as it was not possible to measure the continuum at 296 K. For all panels the error bars are the estimated experimental errors.

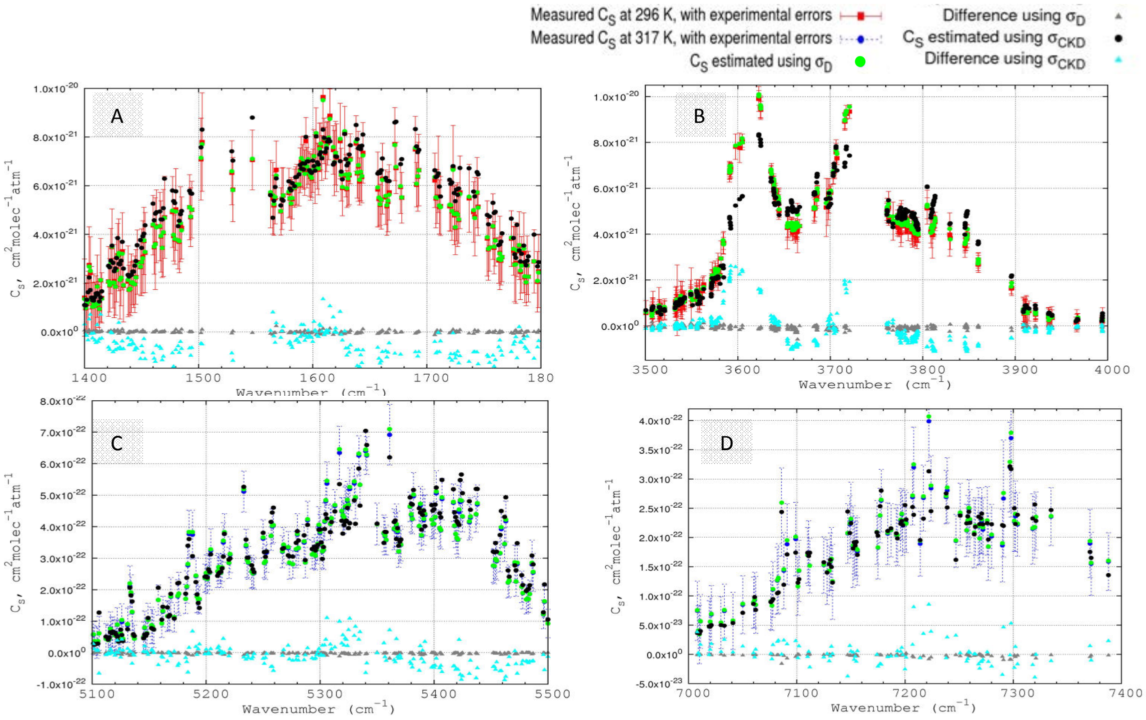

Figure 5.3 Panel A and B: The measured continuum at 296 K (red points) with experimental errors, compared to that predicted at 296 K using $\sigma_D(\nu)$ *(green points) and* $\sigma(\nu)_{CKD}$ *(black points). Panel C,D: The same as Panel A and B, but this time the measured continuum at 317 K is compared to that predicted at 317 K using* $\sigma_D(\nu)$ *(green points) and* $\sigma(\nu)_{CKD}$ *(black points). The difference between the measured and both predicted values is also shown in all panels*

It is apparent that in all bands, the continuum estimate from $\sigma_D(\nu)$ does a remarkably good job at predicting the continuum. This suggests, that over the limited range of temperatures studied, that the form of MT_CKD continuum temperature dependence is proficient at describing the behaviour of the continuum. The results show that while the values of $\sigma_D(\nu)$ and $\sigma(\nu)_{CKD}$ do differ, when it comes to predicting the measured continuum this difference does not result in an estimate of the continuum that lies outside the error bars of measurements. This implies that while indeed in some places the MT_CKD temperature dependence might need adjusting, from the quality of measurements available from this work it is not possible to improve upon the MT_CKD estimate. The key exceptions are the two spectral features around 3620 cm^{-1} and 3730 cm^{-1}. Here (see Figure 5.3 panel B) the MT_CKD temperature dependence considerably underestimates the amount of absorption.

5.2. Water dimer temperature dependence

In chapter 2 it was shown that the optical depth for the dimer can be given by,

$$\tau_d(\nu,T) = \left(\frac{T_0}{\mathrm{T}}\right)^{\frac{3}{2}} \frac{P_s^2 L}{kT} \exp\left(\frac{\Delta S^0}{R} - \frac{\Delta H^0}{RT}\right) \sum \left[S_{d_i}(T_o) \exp\left(-c_2 E_{d_i}\left(\frac{1}{T} - \frac{1}{T_0}\right)\right) f_{d_i}(\nu) \right] , \tag{5.7}$$

where the symbols are as described in chapter 2 (note that unlike earlier in chapter 4 S_{d_i} refers to the dimer line strength and $f_{d_i}(\nu)$ the line shape). When written in terms of the continuum coefficient this becomes,

$$C_d(\nu,T) = \underbrace{\left(\frac{T_0}{T}\right)^{\frac{3}{2}}}_{\mathrm{W}} \underbrace{\exp\left(\frac{\Delta S^0}{R} - \frac{\Delta H^0}{RT}\right)}_{\mathrm{X}} \Sigma \left[\underbrace{S_{di}(T_o) \exp\left(-c_2 E_{d_i}\left(\frac{1}{T} - \frac{1}{T_0}\right)\right)}_{\mathrm{Y}} \underbrace{f_{d_i}(\nu,T)}_{\mathrm{Z}} \right]. \tag{5.8}$$

This form is discussed in more detail in section 2.9.2, so what follows is just a brief summary. The temperature dependence can be broken down into four terms. Term W relates to the partition function, which like for the water monomer, can be approximated as proportional to $T^{-3/2}$. Term X is the equilibrium constant (K_{eq}). This has strong negative temperature dependence, but there is still considerable disagreement over its exact value (see Figure 2.10). The term Y relates to the population of states. This term is of the same form as for the monomer and results in a positive temperature dependence and is dependent upon the lower energy state of the transition. Term Z relates to the temperature dependence of the line shape. This term is subject to very large uncertainty, as little is known about the line shape of the dimer let alone the nature of its temperature dependence.

As there is currently no line list for the water dimer, the position, half-widths, and lower state energy of the water dimer transitions are not known. Due to the smooth nature of the continuum, the water dimer contribution at any wavenumber is most likely a superposition of numerous broad lines. Therefore, even if we knew the value of the equilibrium constant, knowledge of the continuum would not be useful for finding out the properties of individual lines. Conversely, as we are not certain of the dimer's spectral properties then it is not possible to deduce the equilibrium constant direct from this work using equation (5.8). Another problem is that it is also currently not known how much of the self continuum is the due to water dimer and how much is the result of other mechanisms.

Despite these uncertainties, in section 4.7 it was shown that it was possible using the band strengths and positions predicted by S&K to fit a Lorentzian band shape to the dimer features at 3620, 3730 and 5330 cm^{-1} at 351

K by assuming that,

$$C_d(\nu,T) = \mathrm{A(T)}\sum_{i=1}^{N} S_{d_{band_i}}(T)\frac{\alpha_\mathrm{d}}{\alpha_\mathrm{d} + (\nu - \nu_\mathrm{i})^2}. \tag{5.9}$$

Whilst performing this fitting it was mentioned that A(T) could be seen as a scaling constant. However, as discussed in section 2.9.2 Ptashnik et al. (2004) performed a similar fit to the feature 5330 cm^{-1} by assuming that A is given by,

$$A(T) = \left(\frac{T_0}{\mathrm{T}}\right)^{\frac{3}{2}}\left[-c_2 E_{d_{avg}}\left(\frac{1}{T}-\frac{1}{T_0}\right)\right]\exp\left(\frac{\Delta S^0}{R}-\frac{\Delta H^0}{RT}\right). \tag{5.10}$$

Thus, it can be seen that an estimate of the equilibrium constant can be achieved by writing the expression for water dimer absorption in terms of band strengths (i.e. as in equation (5.9)) rather than the line strength (as in (5.8)). This is provided that two assumptions are made: firstly that there is no temperature dependence of band shape and secondly that the lower state energy can be seen as being independent of wavenumber.

This method is a useful way of getting around the uncertainties and has been shown to achieve good agreement with theories. However, it does seem to have numerous shortcomings. Firstly, it assumes that the work of S&K is more accurate than the predictions of the equilibrium constant. This thesis has shown that (see section 4.7.1) actually there is an uncertainty of up to 50 % in the predicted band strengths; this seems to be of a similar magnitude as the uncertainty in the equilibrium constant (see Figure 2.10). The second problem is that at the moment there are large areas of the continuum which cannot be explained by the S&K prediction. This creates an issue when a feature is detected, like that at 3620 cm^{-1}, of not knowing how much of it is the result of water dimer and how much of it is the result of another mechanism.

The final problem is that taking an average value of the lower state energy across the band assumes that the water dimer has no spectral temperature dependence. This is not case because different dimer lines will have different lower states energies and thus different spectral regions will have different temperature dependences.

Due to these shortcomings, a slightly different approach is taken in this work. This method involves reconsidering the form of equation (5.8). Consider that the lower state energy is removed from the summation term, but once removed it still has a spectral dependence. That is to say we make the following approximation,

$$\sum\left[S_{d_i}(T_o)\exp\left(-c_2E_{d_i}\left(\frac{1}{T}-\frac{1}{T_0}\right)\right)f_{d_i}(T,\nu)\right] \sim \exp\left(-\gamma_{dimer}(\nu)\left(\frac{1}{T}-\frac{1}{T_0}\right)\right)\sum_{\mathrm{i=1}}^{\mathrm{N}}\mathrm{S_{d_i}}\,f_{d_i}(\nu,T). \tag{5.11}$$

For the water monomer values for $\gamma(\nu)$ can be calculated by rearranging this equation and using parameters from HITRAN 04. Indeed, over the temperature range investigated this approximation can be seen as being very good for the monomer. It is assumed that any temperature dependence of line shape can be neglected, but may be captured by $\gamma(\nu)_{dimer}$.

The reason for making these assumption is that it allows equation (5.8) to be approximated by,

$$C_s(\nu,T) \sim \left(\frac{T_0}{\mathrm{T}}\right)^{\frac{3}{2}}\exp\left(-\gamma_{dimer}(\nu)\left(\frac{1}{T}-\frac{1}{T_0}\right)\right)\exp\left(\frac{\Delta S^0}{R}-\frac{\Delta H^0}{RT}\right)\sum_{\mathrm{i=1}}^{\mathrm{N}}\mathrm{S_{d_i}}\,f_{d_i}(\nu). \tag{5.12}$$

This form on its own is not particularly useful for fitting any features, as there is still considerable uncertainty in the value of $\sum_{\mathrm{i=0}}^{\mathrm{n}}\mathrm{S_{d_i}}\,F_{d_i}(\nu)_{,}\gamma$, ΔH^0 and ΔS^0. One possible way of simplifying the problem and obtaining an estimate of $\gamma(\nu)$ and ΔH^0 is to consider the ratio of C_s at different temperatures and thus cancel out all but the temperature dependent terms. That is to say,

$$C_s(\nu,T_2)\sim C_s(\nu,T_1)\left(\frac{\mathrm{T_1}}{\mathrm{T_2}}\right)^{\frac{3}{2}}\exp\left(\epsilon(\nu)\left[\frac{1}{T_2}-\frac{1}{T_1}\right]\right), \tag{5.13}$$

where,

$$\epsilon = -\gamma_{dimer}(\nu)-\frac{\Delta H^0}{R}. \tag{5.14}$$

This can be rearranged and written in linear form as,

$$\epsilon(\nu)\left[\frac{1}{T_1}-\frac{1}{T_2}\right] \sim ln\left[\left(\frac{\mathrm{T_2}}{\mathrm{T_1}}\right)^{\frac{3}{2}}\frac{C_s(\nu,T_1)}{C_s(\nu,T_2)}\right]. \tag{5.15}$$

This allows a least squares fit to be performed and a value of $\epsilon(\nu)$ to be obtained for different points in the spectrum. Figure 5.4 (similar to Figure 5.3 panel B) shows the predicted continuum at 296 K using this fitting to set B351 compared to the actual measured continuum. The difference between the two is also shown. The small difference between the actual and fitted continuum shows that over the temperature range investigated this can be seen as an excellent approximation for fitting the continuum temperature dependence. This can also be seen to be the case for the other 3 bands investigated in this work.

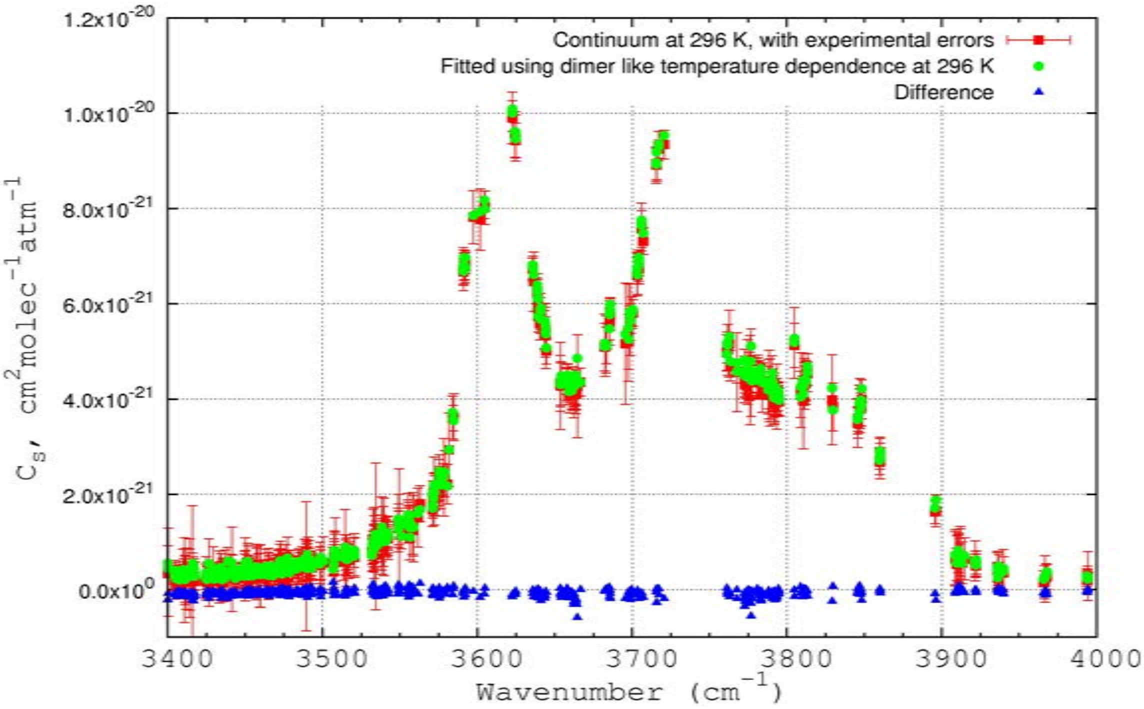

Figure 5.4 The continuum measured at 296 K compared to that estimated using a value of ϵ obtained using a least squares fit to measurement sets B351, B337,B327, B317, B304 and B296.

It can be seen that in order to obtain a value of ΔH^0 from a value of $\epsilon(\nu)$ fitted to the continuum of this work, a value of $\gamma(\nu)_{dimer}$ must be assumed. For the water monomer it can be seen that the lowest lower state energy is in the band centres. If we assume that this is also the case of the dimer then it can be said that,

$$\frac{-\Delta H^0}{R} = \gamma_{\text{dimer}}^{\text{min}} + \epsilon_{\text{max}}. \tag{5.16}$$

Hence, if $\gamma_{\text{dimer}}^{\text{min}}$ is known then it would be possible to achieve an estimate of ΔH^0 from ϵ. Let us assumes that the value of $\gamma_{\text{dimer}}^{\text{min}}$ is similar to the minimum value of γ for the monomer ($\gamma_{\text{monomer}}^{\text{min}}$) :

$$\gamma_{\text{monomer}}^{\text{min}} = \gamma_{\text{dimer}}^{\text{min}}. \tag{5.17}$$

Using the HITRAN database it is possible to obtain an estimate of $\gamma(\nu)_{monomer}$ and hence $\gamma_{\text{monomer}}^{\text{min}}$ and $\gamma_{\text{dimer}}^{\text{min}}$. However, rather than assuming that the water monomer half-widths are as in HITRAN, a half-width of 5 cm^{-1} is used. This is designed to simulate the fact that water dimer lines would be much broader than that of the monomer.

In Figure 5.5 Panel B the values of $\gamma(\nu)_{monomer}$ is plotted along with $\epsilon(\nu)$ derived from the continuum for the 3400-4000 cm^{-1} region. This region is used to obtain an estimate ΔH^0, as it contains the clearest dimer like features. From this plot it can be seen that a reasonable estimate of γ_{dimer}^{min} is 150 K and ϵ_{max} is about 1600 K. Using these values allows -$\Delta H^0/R$ to be estimated as 1750 K. This is gives a ΔH^0 of 3500 cal.mol^{-1}. This is in good agreement with the measured value of 3590±500 cal.mol^{-1} obtained by Curtiss et al. (1979), 3780cal.mol^{-1} obtained by Ptashnik et al. (2004) for fitting the water dimer feature at 5330 cm^{-1} and the theoretical value of 3860 cal.mol^{-1} of Scribano et al. (2006). However, there is a fair amount of uncertainty in this result, because there is a significant amount of deviation in values of ϵ_{max} from one micro-window to the next. One could easily argue that a value of 1400 K might be more appropriate.

Once this process is performed one can then use the -$\Delta H^0/R$ values to estimate $\gamma_{dimer}(v)$ for all other regions by,

$$\gamma_{\text{dimer}}(\nu) = -\frac{\Delta H^0}{R} - \epsilon(\nu). \tag{5.18}$$

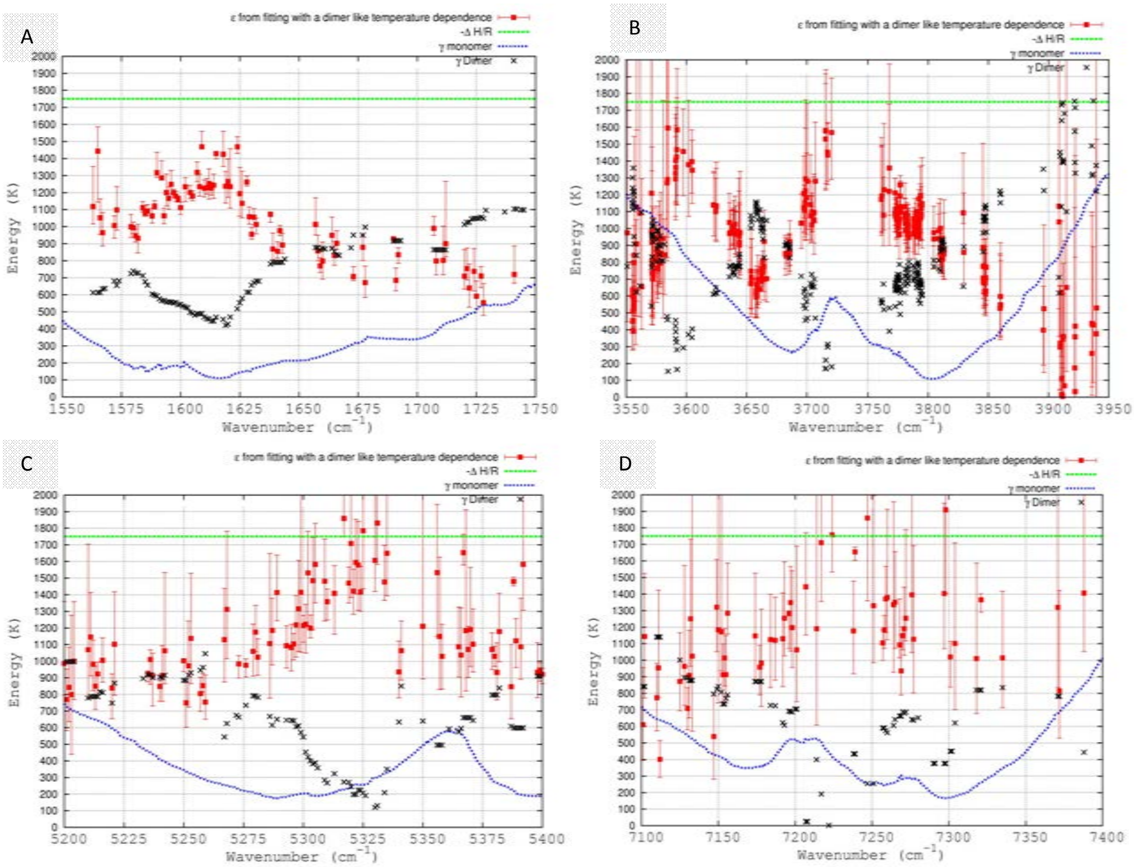

Figure 5.5 The value of $\epsilon(\nu)$ *(red squares) fitted to the derived continuum in different bands.* γ_{monomer} *(blue line) as derived from HITRAN 2004 is shown. The value of* $\frac{-\Delta H^0}{R}$ *(green line) derived as the sum of the maximum value of* $\epsilon(\nu)$ *and minimum of* γ_{monomer} *in the 3550-3950 cm*$^{-1}$ *region. This then allows* γ_{dimer} *(black crosses) to be defined as the difference between* $\frac{-\Delta H^0}{R}$ *and* $\epsilon(\nu)$ *in all spectral regions.* γ_{dimer} *is averaged over 5cm*$^{-1}$*to make any trends cleaer.*

As the value of ΔH^0 is spectrally invariant, any variation in the temperature dependence of the dimer from band to band has to be the result of γ_{dimer}. The values of $\gamma_{monomer.}$ does vary from one band to the next, but in most bands it does seem to range between around 200 K and 600 K, with larger values towards the edge of the band. The value of γ_{dimer} obtained from this analysis for each of the major bands is shown in Figure 5.5. In general γ_{dimer} has a greater band to band variation than $\gamma_{monomer}$ and has a bigger value. For example, in panel A between 1550 and 1750 cm^{-1} the value is much greater. Whilst it could be argued that maybe a lower value of $-\Delta H^0/R$ could be assumed, this would then result in some of the γ_{dimer} values being negative in the two bands beyond 5000 cm^{-1} and for the peaks at 3600 cm^{-1} and 3730cm^{-1}.

It appears that describing the spectral temperature dependence of the self continuum by variation of the lower state energy alone is not sufficient. This could mean numerous things. It could be because there is a mechanism contributing to the continuum other than water dimer which has a different temperature dependence. Therefore, in numerous regions one would not expect the continuum's temperature dependence to behave as predicted for the dimer. Or it could be because the temperature dependence of the water dimer is more complex than has been assumed in this rather simple analysis.

5.3. Integrated band temperature analysis

It seems to be the case that the present level of theoretical understanding of the water dimers cannot satisfactory explain all of the spectral features or temperature dependence observed in the self continuum. A slightly different approach, rather than focus on specific spectroscopic features, is to investigate whether the integrated band properties of the self continuum are consistent with those expected for the water dimer. The benefit of this approach is that it makes fewer assumptions about the properties of the water dimer. Consider integrating, the LHS and RHS of (5.13) over wavenumber,

$$\int_{\nu_0}^{\nu_1} C_s(\nu,T)d\nu \sim \int_{\nu_0}^{\nu_1} \left(\frac{T_0}{\mathrm{T}}\right)^{\frac{3}{2}} \exp\left(\frac{\Delta S^0}{R}-\frac{\Delta H^0}{RT}\right)\exp\left(-\gamma(\nu)\left(\frac{1}{T}-\frac{1}{T_0}\right)\right)\sum_{\mathrm{i}=0}^{\mathrm{N}} \mathrm{S}_{\mathrm{di}}\,(\mathrm{T},\nu_{\mathrm{i}}) f_{\mathrm{d_i}}(\nu)d\nu. \tag{5.19}$$

where ν_1 and ν_0 are the upper and lower wavenumber value of the band respectively. As the area under the line shape is unity, the integral of the cross section over a band is equal to the band intensity so that,

$$\int_{\nu_0}^{\nu_1} \exp\left(-\gamma\left(\frac{1}{T}-\frac{1}{T_0}\right)\right)\sum_{i=0}^{n} S_{d_i}(T,\nu_i)f_{d_i}(\nu)d\nu \approx \sum_{\mathrm{i=0}}^{\mathrm{n}} \mathrm{S}_{\mathrm{band}_{\mathrm{d_i}}}(\mathrm{T},\mathrm{\nu_i})\int_{\nu_0}^{\nu_1} \exp\left(-\gamma(\nu)\left(\frac{1}{T}-\frac{1}{T_0}\right)\right)\mathrm{d\nu}. \tag{5.20}$$

In addition it can be seen that the lower state energy when integrated over the band will give an average value,

$$\int_{\nu_0}^{\nu_1} \exp\left(-\gamma(\nu)\left(\frac{1}{T}-\frac{1}{T_0}\right)\right)\mathrm{d\nu} = \exp\left(-\gamma_{avg}\left(\frac{1}{T}-\frac{1}{T_0}\right)\right)\mathrm{d\nu}. \tag{5.21}$$

Let us assume that the average dimer lower state energy is of a similar magnitude to that of the monomer (500 K). If this is case then over the temperature range investigated the lower state energy term cancels out the partition function temperature dependence because,

$$\left(\frac{T}{\mathrm{T_0}}\right)^{\frac{3}{2}} \sim \exp\left(-500\left(\frac{1}{T}-\frac{1}{T_0}\right)\right). \tag{5.22}$$

This then allows us to simplify equation (5.20) to the form,

$$\int_{\nu_0}^{\nu_1} C_s(\nu,T)d\nu = \exp\left(\frac{\Delta S^0}{R}-\frac{\Delta H^0}{RT}\right)\sum_{\mathrm{i=0}}^{\mathrm{n}} \mathrm{S_{d_i}}(\mathrm{T_0},\mathrm{\nu_i}). \tag{5.23}$$

Hence, by rearranging we can get the following formula,

$$\Delta S^0 - \frac{\Delta H^0}{T} = R \cdot ln\left(\frac{\int_{\nu_0}^{\nu_1} C_s(\nu,T)d\nu}{\sum_{\mathrm{i=0}}^{\mathrm{n}} \mathrm{S_{d_i}}(\mathrm{T},\mathrm{\nu_i})}\right). \tag{5.24}$$

This form is useful as it allows one to predict the values of ΔH^0 and ΔS^0 by using the band strengths of S&K and integrating the area under the self continuum measured at different temperatures. Thus, by performing a least squares fit to the RHS of (5.24) calculated using the self continuum derived from sets at different temperatures (i.e. calculating $\int_{\nu_0}^{\nu_1} C_s(\nu,T)d\nu$ using sets A351, A330 etc.) it was possible to obtain an estimate of ΔH^0 and ΔS^0 for each band.

As $\Delta S^0$and ΔH^0 are independent of wavenumber, if the dimer is a significant contributor to the continuum it would be expected that the values achieved for each band to be similar. That is provided that S&K correctly predict the integrated band strengths.

Table 5.2 presents the values of $\Delta S^0$and ΔH^0 estimated using this technique and compares the values to those obtained from different authors. Figure 5.6 shows the equilibrium constant calculated using the various $\Delta S^0$and ΔH^0 values introduced in this table. Minimum and maximum values of the integrated self continuum are calculated assuming errors from HITRAN. These are used to estimate the uncertainty in $\Delta S^0$and ΔH^0 resulting from errors in the derived continuum.

It is clear that the values of $\Delta S^0$and ΔH^0 obtained using this technique vary greatly from one band to the next. It can also be seen that the values of ΔS^0 given in this work, with the exception of the 3400-4000 cm^{-1} region, are less than the measurements of Curtiss et al. (1979). As is shown in Figure 5.6 this results in a larger equilibrium constant. Given the analysis in section 4.7 this is not surprising, as it was seen in these bands the water dimer feature could only explain part of the continuum.

The value of ΔH^0 dictates the temperature dependence of the equilibrium constant. These values are less than those measured by Curtiss et al. (1976) and predicted by Scribano (2006). However, given that large uncertainty in the errors of ΔH^0 derived here and the reasonably large errors of Curtiss et al., there could be some overlap if for the two bands at greater than 5000 cm^{-1} the maximum ΔH^0 value from this work is taken along with the minimum Curtiss et al. value. This still leaves the problem of the 1200-2000 cm^{-1} region, where there is a considerable difference even when these values are taken.

Overall though, these results suggest that the continuum generally has a weaker temperature dependence than that predicted for the water dimer. This result is consistent with what was seen in the last section, where in numerous spectral regions the temperature dependence observed was weaker than that estimated using the dimer model.

Region ν_0, ν_1 cm^{-1}	ΔH^0 **(cal mol^{-1})**	ΔS^0 **(cal mol^{-1}K^{-1})**	**K$_{eq}$(296)/K$_{eq}$(351)**
1200-2000	**2592**	**13.3**	**1.96**
Min $\int_{2000}^{1200} C_s(\nu,T)d\nu$	2769	13.9	2.05
Max$\int_{2000}^{1200} C_s(\nu,T)d\nu$	2437	12.6	1.88
3400-4000	**3084**	**17.7**	**2.23**
Min $\int_{4000}^{3400} C_s(\nu,T)d\nu$	3351	18.7	2.40
Max$\int_{4000}^{3400} C_s(\nu,T)d\nu$	2868	16.8	2.10
5000-5600	**2983**	**15.3**	**2.17**
Min $\int_{5600}^{5000} C_s(\nu,T)d\nu$	3351	16.4	2.34
Max$\int_{5600}^{5000} C_s(\nu,T)d\nu$	2745	14.4	2.04
6900-7500	**3425**	**16.0**	**2.44**
Min $\int_{7500}^{6900} C_s(\nu,T)d\nu$	3972	18.04	2.81
Max$\int_{7500}^{6900} C_s(\nu,T)d\nu$	3016	12.68	2.20
Curtiss et al. (1979)	**3590±500**	**18.6 ±1.3**	**2.60**
Scribano et al. (2006)	**3860**	**19.3**	**2.77**
Ptashnik et a. (2004)	**3780**	**18.9**	**2.71**

Table 5.2 ΔH^0 and ΔS^0 estiamted from the area under the different bands. The ratio of the equilibrium constant achieved at 296 K to 351 K is also shown

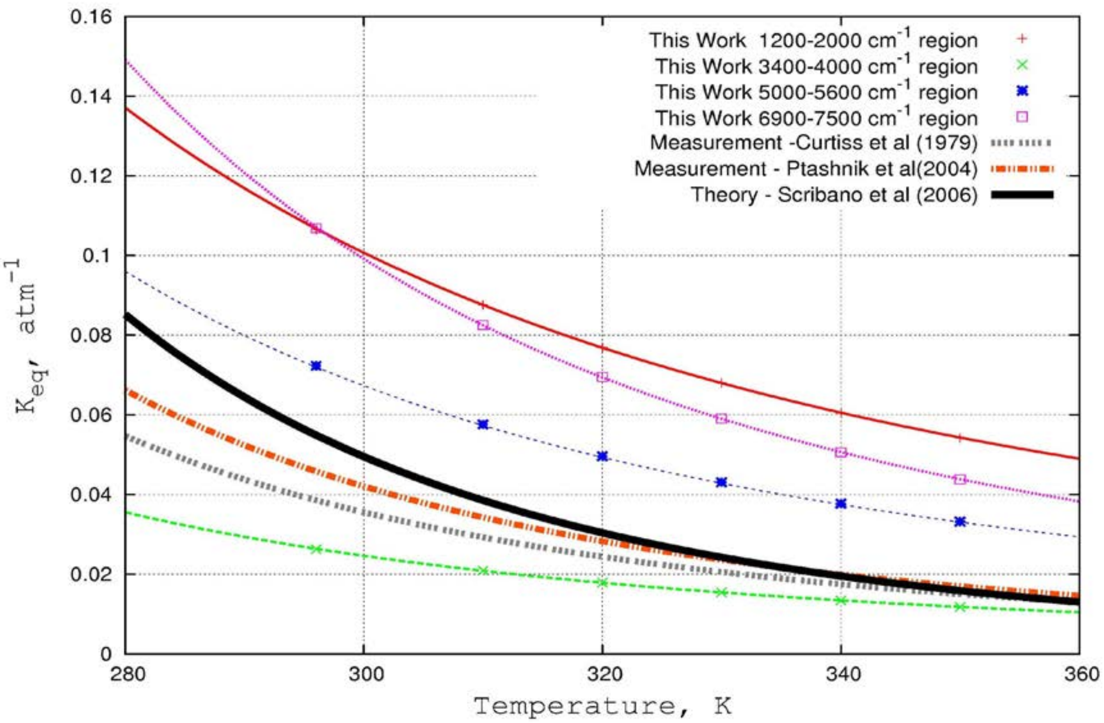

Figure 5.6 The values of equilibrium constant obtained from integrating the derived continuum in different spectral regions, compared to the equilibrium constant from other works.

This result either suggests that the entire continuum is solely not due to the water dimer or that the band strengths of S&K need to be adjusted. However, even if the S&K values were adjusted to obtain a better agreement, this would still leave the problem of the weaker temperature dependence. However, this difference is not quite so significant, as can be seen from the ratio of the equilibrium constant calculated at 351 K to 296 K as given in column 4 of Table 5.2.

Ptashnik et al. (2004), fitting a dimer feature at 5330 cm^{-1}, obtained a value of the equilibrium constant in better agreement with Curtiss et al. (1979). This is most likely to be because, rather than fitting the dimer feature to the whole band, it was fitted to a specific feature. As can be seen in Figure 4.32 and Figure 4.33 there is quite a lot of area in the self continuum that is not accounted for by this fitting. Thus, when one tries to explain the whole of the self continuum using the integrated cross sections of S&K, one gets a correspondingly smaller value of the equilibrium constant. The fact that the value of ΔH^0 is larger, can be explained by looking at Figure 5.5. It can be seen that in the spectral region around 5330 cm^{-1},the temperature dependence is indeed stronger than in other parts of the band and thus fitting in this region will result in a larger value of ΔH^0 than integrating across the band.

Given that S&K band strengths appear to give such differing values of ΔS^0, maybe a better approach is to use the value of ΔS^0 and of ΔH^0 of Curtiss et al. (1979) to correct the band strengths of S&K. This is achieved by calculating the area under the derived continuum from each band at 296 K. By then rearranging equation (5.24) a value of $\sum_{i=0}^{n} S_{d_i}(T, \nu_i)$ is achieved. The results of this analysis are presented in Table 5.3.

Region ν_0, ν_1 cm^{-1}	$\int_{\nu_0}^{\nu_1} C_s(\nu,T)d\nu$ **(cm^{-1}/molecule.atm) At 296 K**	$\sum_{i=0}^{n} S_{d_i}(T,\nu_i)$ **From S&K (cm^{1}/(molecule.cm^{-2}) At 296 K**	$\sum_{i=0}^{n} S_{d_i}(T,\nu_i)$ **(cm^{1}/(molecule.cm^{-2}) Assuming ΔS^0=18.89 cal mol^{-1}K^{-1})**	$\sum_{i=0}^{n} S_{d_i}(T,\nu_i)$ **(cm^{1}/(molecule.cm^{-2}) monomer HITRAN 04**	$\frac{\int_{\nu_0}^{\nu_1} C_S(\nu,T)\,d\nu}{\sum_{i=0}^{n} S_{d_i}(T,\nu_i)}$ **Atm^{-1} Column 2/5**
1200-2000	**2.40E-18** +0.5E-18 -0.5E-18	**2.1E-17**	**5.1E-17**	**1.07E-17**	**0.22**
3400-4000	**1.90E-18** +0.36E-18 -0.30E-18	**7.3E-17**	**3.9E-17**	**8.22E-18**	**0.23**
5000-5600	**1.84E-19** 0.5.E-19 -0.6E-19	**2.4E-18**	**3.2E-18**	**8.68E-19**	**0.21**
6900-7500	**1.15E-19** +5.71E-20 -3.88E-20	**1.1E-18**	**3.3E-18**	**6.50E-19**	**0.18**

Table 5.3 The integrated absorption under the different regions (column 2) compared to the sum of the integrated band strengths predicted by S&K in the same region (column 3). If a value ΔS^0=18.89 cal mol^{-1}K^{-1} and ΔH^0=3780 cal mol^{-1} is assumed the correction required to be made to the S&K integrated band strengths is given in column 4. The integrated band strength for the water monomer as calculated from HITRAN 04 is given in column 5. The ratio of this value to the integrated absorption from the derived continuum is given in column 6.

These suggested updates to the S&K band strengths (column 4) point to some rather significant changes that need to be made if we assume that the entire self continuum is the result of the water dimer. As such these values can be seen as an upper limit for the band strengths of the dimer.

The values of the integrated intensity for the water monomer as calculated from HITRAN 04 are also given for the same region (column 5). This shows the interesting result that the amount of continuum absorption is proportional to the water monomer band strength (column 6). This could suggest that CKD and MT_CKD which assume that the continuum is proportional water monomer absorption are indeed correct.

5.4. Conclusions

It has been shown that the self continuum has a strong negative temperature dependence with a quite strong spectral signature. When fitted to the continuum derived in this work, the form of the CKD temperature dependence does an excellent job at capturing the temperature dependence of the continuum over the temperature range studied. However, the actual temperature dependence given by CKD does not capture the finer detail of the spectral variation. In general it was shown that these differences are not significant when extrapolating the continuum at 351K to 296 K. The exception being the two peaks detected in the self continuum around 3620 cm^{-1} and 3730 cm^{-1}.

A simple dimer model was fitted to the continuum. It appeared that the spectral variation in the continuum could not be captured by this model. This could be because either the dimer model is too simple or the water dimer is not the only contributor to the continuum.

Finally, the integrated band strengths of S&K along with the integrated area under the continuum were used to obtain an estimate of ΔS^0 and of ΔH^0. These results showed that there was considerable variation in the values derived from one band to the next. This could be because the S&K band strengths are wrong or because the dimer is not the only contributor to the continuum. Possible corrections to the S&K band strengths are proposed. It was also noted that the ratio of the continuum band strengths to the integrated water monomer band strength are very similar from band to band. This may favour a monomer explanation for at least part of the continuum. However, presently there is no apparent physical explanation for the stronger temperature dependence observed for the continuum compared to that of the monomer.

6. Foreign Continuum

The foreign continuum results from the interaction between water molecules and other gases in the atmosphere. The majority of spectral measurements made for this work were conducted with only pure water vapour. However, some measurements were also conducted with zero air (80% nitrogen, 20% oxygen) added to the water vapour. These measurements have allowed the foreign continuum to be derived. Less effort has been placed on analysing these measurements and accordingly the presentation in this chapter is more basic than previous chapters.

This chapter will start by explaining the differences in the experimental technique and data processing used in deriving the foreign continuum compared to the self. Potential errors contributing to the continuum are then investigated. The results of this work are presented and compared to previous measurements by other authors and other continuum models. Finally a comparison with the self continuum is then made and the temperature dependence is briefly investigated.

6.1. Techniques for deriving the foreign continuum

The measurement technique used to derive the foreign and self continua are almost identical. Before any zero air is added to the cell, the spectrum of pure water vapour is measured just as described in section 3.1. Once this process is complete the zero air is then pumped into the cell. It is then assumed that the measured pressure is the combination of both the zero air and water vapour. The spectrum is measured (referred to as an FTIR measurement). To increase the number of measurements made, further amounts of zero air are added and an FTIR measurement is conducted at this new pressure. Typically for a given amount of water vapour three FTIR measurements are made with different pressures of zero air added.

The process can be summarised as follows; firstly a background FTIR measurement followed by an FTIR measurement of X mb of pure water vapour are conducted. Y1 mb of zero air is then added to the cell. A FTIR measurement is then conducted with the cell containing X mb of water vapour and Y1 mb of zero air. More zero air is then added to the cell so there is now Y2 mb of zero air, another FTIR measurement is then conducted. Finally yet more zero air is then added to the cell so there is now Y3 mb, and a FTIR measurement is made. After this the cell is then evacuated and anther background is conducted.

Tobin et al. (1996) claimed that whilst performing a similar technique that they observed a systematic drop in the amount of vapour pressure in the cell by about 2-3% when nitrogen was added. They assumed that this was because the extra pressure was forcing the water to be absorbed by the cell walls. For this reason in this work every time the zero air was added to the cell the humidity was measured. It was normally found that, after the initial decrease, due to the redistribution of water vapour in the cell, the vapour humidity returned to the initial value. Sometimes the humidity was slightly larger or smaller than before the zero air was added, but there was no systematic decrease observed throughout the measurement process and the magnitude of the change appeared to have no noticeable effect upon the continuum. Indeed, the humidity sensor could be used as a guide to when the water vapour and zero air were well mixed.

6.2. Deriving the continuum

It was stated in chapter 2 that the optical depth of water vapour mixed with a foreign gas is given by,

$$\tau_H(\nu) = \frac{P_s L}{kT} \sum_i^N S_i(T) \frac{1}{\pi} \left[\frac{\alpha_{s_i}(P_s, T) + \alpha_{F_i}(P_F, T)}{(\nu - v_0 + \delta_\mathrm{i})^2 + \alpha_{s_i}(P_s, T) + \alpha_{F_i}(P_F, T)} \right], \tag{6.1}$$

where,

$$\alpha_{s_i}(P_s, T) = \alpha_{s,i}^0 \left[\frac{P_s}{P_0}\right] \left[\frac{T_0}{T}\right]^{n_i},$$

$$\alpha_{F_i}(P_F, T) = \alpha_{F_i}^0 \left[\frac{P_F}{P_0}\right] \left[\frac{T_0}{T}\right]^{n_i}$$

and P_s is the water vapour pressure and P_F is the pressure of a foreign broadening gas (in this case zero air) .

The only difference with this equation compared to that the self continuum is inclusion of the foreign broadening term. This term will cause the lines to be broader and thus for there to be more absorption in the micro windows. Typically the value of $\alpha_{F,i}^0$ is a fifth of that of $\alpha_{s,i}^0$, although this value does vary quite significantly from line (as shown in Figure 3.8)

When deriving the foreign continuum we are looking at the correction required to the calculated absorption due the interaction with water vapour and other gases. As there is a mixture of water vapour and zero air when a measurement is conducted simply subtracting the optical depth calculated using HITRAN from that measured will give a continuum caused by the interactions of water molecules with both other water molecules and with zero air. Thus, to take into account the interaction between water molecules it is necessary to remove a self continuum component.

Hence, for a measurement conducted at temperature T and water vapour pressure P_s with P_F of zero air added, the foreign continuum at particular wavenumber is defined as,

$$\tau_{c_F}(P_s, P_F, \nu, T) = \tau_m(P_s, P_F, \nu) - \tau_H(P_s, P_F, \nu) - \tau_{c_s}(P_s, \nu). \tag{6.2}$$

Where, τ_{c_F} is the optical depth of the foreign continuum, τ_m is the measured optical depth, τ_H is the optical depth calculated for the measurement conditions using data from HITRAN and τ_{c_s} is the optical of the self continuum for the measurement conditions, as derived in the previous chapter.

6.3. Analysis of errors

As for the self continuum, errors due to pressure, temperature, line shape, instrument noise, baseline and HITRAN need to be taken into account when deriving the foreign continuum. Because of the inclusion of the foreign broadening term when calculating the optical depth some of the equations developed for dealing with errors due to pressure, temperature and HITRAN introduced in chapter 3 have to be changed. Section 5.3.1 will investigate errors due to pressure and temperature and section 5.3.2. will then look at errors due HITRAN. For baseline and instrument noise errors the formulation can be considered the same as in chapter 3.

6.4. Experimental errors

Away from the line centres (6.1) can be split into two components,

$$\tau_H = \tau_s + \tau_F, \tag{6.3}$$

where,

$$\tau_s(\nu) = \frac{P_s L}{kT} \sum_i^N S_i(T) \frac{\alpha_{s_i}(P_s, T)}{(\nu - \nu_i + \delta_i)^2}, \tag{6.4}$$

and,

$$\tau_F(\nu) = \frac{P_s L}{kT} \sum_i^N S_i(T) \frac{\alpha_{F_i}(P_F, T)}{(\nu - \nu_i + \delta_i)^2}. \tag{6.5}$$

When making measurements of the foreign continuum the pressure has to be measured twice. Firstly, the amount of pure water vapour in the cell is measured and secondly the amount of pure water vapour plus zero air is measured. It is assumed that the first pressure measurement will result in an error P_{ϵ_s} in P_s and the second measurement will have an error P_{ϵ_F} in P_F.

Let us consider the effects of errors on both terms. It can be seen that,

$$\tau_s(P_s + P_{\epsilon_s}) = \frac{(P_s + P_{\epsilon_s})^2 \tau_s}{P_s^2} \approx \left(1 + \frac{P_{\epsilon_s}}{P_s}\right) \tau_s, \tag{6.6}$$

and,

$$\tau_F\left(P_S + P_{\epsilon_S}, P + P_{\epsilon_F}\right) = \frac{\left(P_S + P_{\epsilon_S}\right)\left(P_F + P_{\epsilon_F}\right)\tau_F}{P_S P_F} \approx \left(1 + \frac{P_{\epsilon_S}}{P_S} + \frac{P_{\epsilon_F}}{P_F}\right)\tau_F. \tag{6.7}$$

Hence the total error in τ_H resulting is,

$$\tau_\epsilon(\mathrm{P_S}, \mathrm{P_F}) = \tau_\mathrm{s} + \tau_\mathrm{F} - \tau_\mathrm{s}\left(\mathrm{P_s} + \mathrm{P}_{\epsilon_\mathrm{s}}\right) - \tau_\mathrm{s}\left(\mathrm{P_s} + \mathrm{P}_{\epsilon_\mathrm{s}}\right) \approx \tau_S \frac{2P_{es}}{P_S} + \left(\frac{P_{\epsilon_S}}{P_S} + \frac{P_{\epsilon_F}}{P_F}\right)\tau_F. \tag{6.8}$$

If we consider that assuming a 1% error in pressure measurement,

$$\tau_\epsilon\left(P_{\epsilon_S}, P_{\epsilon_F}\right) \approx 0.02\tau_S + 0.02\tau_F = 0.02\tau_H. \tag{6.9}$$

For error in temperature the identical to that given in 3.4.5 can be used but with $\alpha_{S_i}(P_S, T) + \alpha_{F_i}(P_F, T)$ substituted in for $\alpha_{S_i}(P_S, T)$. Unlike for pressure, the formula cannot be simplified.

6.4.1. HITRAN Errors

In addition to the errors in line intensities and self-broadened half-widths discussed in chapter 3, the effect of errors in the foreign-broadened half-widths (FHW) also needs to be considered. Like the self-broadened half-widths these come from numerous sources. In 2006 an update was issued to HITRAN 2004, which changed the FHW of some lines. This was the result of a change in the algorithm which deduces the FHW by comparing various sources. This updated version will be referred to as HITRAN 2006. The nature of these changes is discussed in Gordon et al. (2007).

The data in HITRAN 2006 come mainly from the Gamache and Hartman database (Gamache and Hartmann 2004). This is a detailed database listing values of the FHW from over 40 sources. If data from this source are not available then a value is taken from a database of calculated values of Gamache and Fisher (2003). Finally, if the data for a line was not found in any of these sources, then a database of semi-empirical calculations by Jacquemart et al. (2005) is resorted to. When searching through the Gamache and Hartman database if there is more than one measurement of a FHW then, providing the each measurement set can be trusted, an average value is taken. However, quite often there is only one measurement. In the region of interest in this work, it is the case that most values are either those measured by Zou and Varanasi (2003) or by Toth (2004).

Figure 6.1 shows the half-widths between 1200 and 8000 cm^{-1} and the various sources attributed to them in HITRAN 2006. Although it is not clear from this figure, it can be shown that unlike for the self broadened half-widths, it is found that one source dominates the calculation of τ_H in each band. In the 1200-2000 cm^{-1} region, it can be shown that τ_H is dominated (i.e. above 95% of the total optical depth in most areas) by FHW values from the Gamache and Hartmann database (2004.). In the 3400-4000 cm^{-1} region the measured values Zou and Varanasi (2003) are similarly dominant. In two bands between 5000 and 8000 cm^{-1} more than 90% of τ_H is made up by the measurements of Toth.

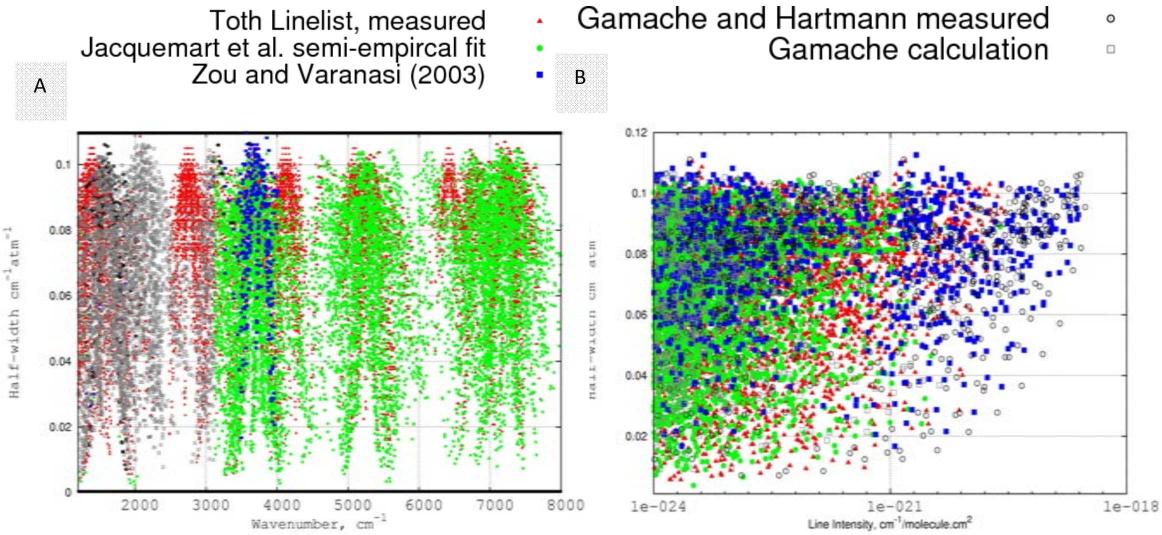

Figure 6.1 The foreign-broadened half-widths from HITRAN 2006 plotted as a function of wavenumber (Panel A) and of intensity (Panel B). The key shows which source each half-width originates from.

Figure 6.2 shows the ratio of various versions of HITRAN and the Toth list to HITRAN 2006. It can be seen that the biggest changes exist between HITRAN 2006 and HITRAN 2000 (Panel B). Although for the stronger lines this variation is less than 10%. The changes between HITRAN 2004 and HITRAN 2006 (Panel C), especially for the stronger lines, are far smaller and are generally less than 5%. For the ratio between HITRAN 2006 and the Toth database, even for the lines that HITRAN states are from the Toth line list, a slight variation of up 3% is seen between the two. The cause of this is not known, although the size of this error is far smaller than the variation seen in general between the different versions of HITRAN.

The FHW like other major parameters in HITRAN have an associated uncertainty code. These are shown in Figure 6.3 (refer to table Table 3.13 for meaning of codes). It can be seen that confidence in the FHW is greater than in the self. For most of the measured values these are lie between 5 and 10%.

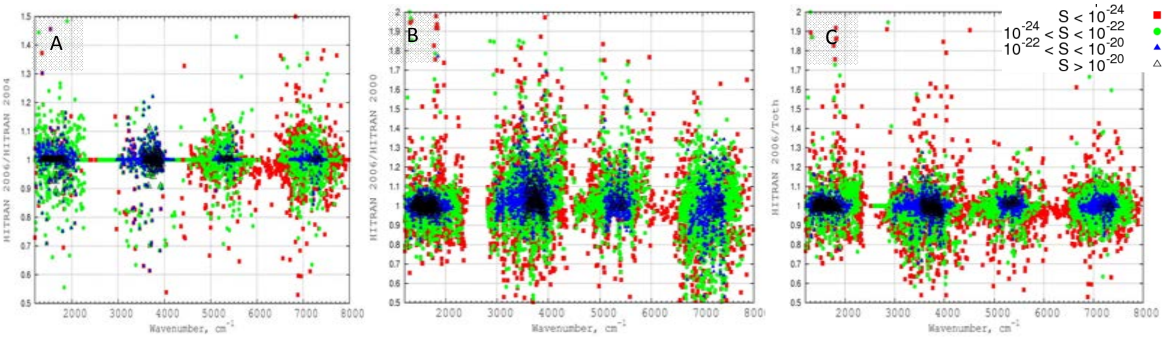

Figure 6.2. The ratio of FHW in HITRAN 2006 compared to HITRAN 2004 (panel A),2000 (panel B) and the Toth line list (Panel C). Different coloured points represent different intensities.

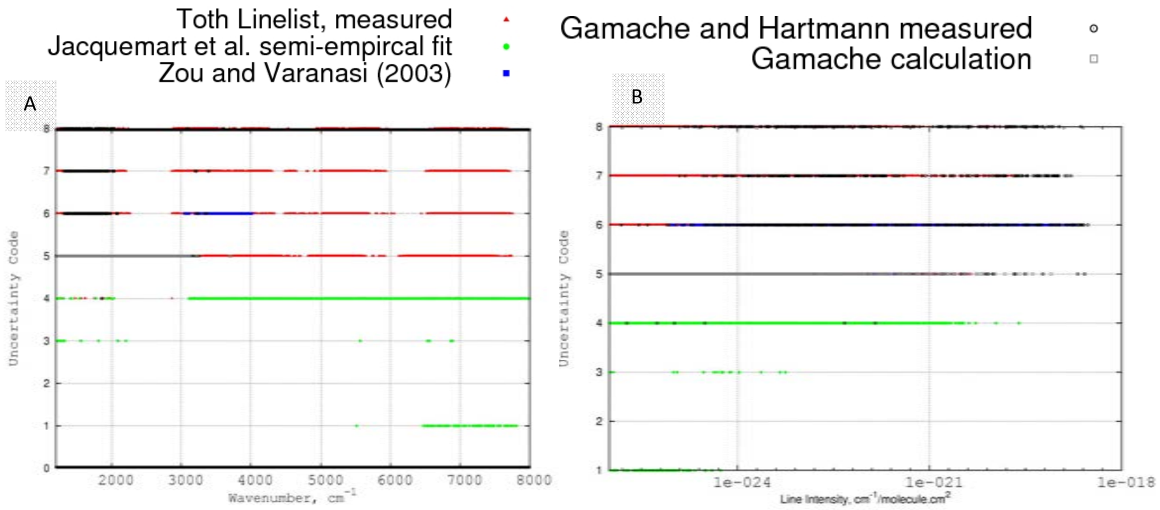

Figure 6.3 The error codes in HITRAN 2006 for the foreign-broadened half-widths. The different point types represent different sources of the lines. Panel A and B show the uncertainty code plotted against wavenumber and lines intensity respectively

The errors due to foreign half-widths are treated in exactly the same way as the self broadened errors. That is say that for a line falling in a certain error category the middle value is taken (i.e. if a line has an error between 5 % and 10 % a value of 7.5% is assumed). The error in optical depth is then assumed to be the difference between error calculated with and without these errors. That is to say that,

$$\tau_{\epsilon}(\alpha_{F\epsilon}) = \frac{P_s L}{kT}\sum_{i}^{N} S_i(T)\frac{1}{\pi}\left|\left[\frac{\alpha_{F_i}}{(\mathrm{v}-v_{\mathrm{i}}+\delta_{\mathrm{i}})^2+\alpha_{\mathrm{F_i}}^2}\right]-\left[\frac{(1+\varphi_i)\alpha_{F_i}}{(\mathrm{v}-v_{\mathrm{i}}+\delta_{\mathrm{i}})^2+\left((1+\varphi_i)\alpha_{F_i}\right)^2}\right]\right|, \tag{6.10}$$

where φ_i is the factional error (i.e. 7.5% error means that φ_i has a value of 0.075). Hence, assuming that the errors are independent, the total error in optical depth because of HITRAN is given as,

$$\tau_{\epsilon}(HITRAN) = \sqrt{}(\tau_{\epsilon}(S_{\epsilon})^2 + \tau_{\epsilon}(\alpha_{s_{\epsilon}})^2 + \tau_{\epsilon}(\alpha_{F_{\epsilon}})^2). \tag{6.11}$$

6.4.2. Errors in the self continuum

As was mentioned earlier in this chapter the self continuum is subtracted off in order to derive the foreign continuum. This obviously has errors associated with it too. However, most of these have already been taken into account by the analysis presented in this section. Consider that the continuum derived by taking the difference between τ_H and τ_m will be a mixture of self and foreign. Thus, any errors associated with τ_H and τ_m will be those associated with both the self and foreign continuum. Hence, it can be seen that the errors due to temperatures and HITRAN in the self continuum are included by virtue of calculating $\tau_\epsilon(HITRAN)$ and $\tau_\epsilon(T)$ as described in this section. The errors due to measured pressure are also included in the analysis in 5.3.1, which assumes there is error in P_S. The baseline error in the self continuum does need to be taken into account, and thus double the value for the baseline is assumed for foreign continuum measurements.

6.4.3. Basic analysis of measurements

The continuum is derived using equation (6.2). Exactly the same method for filtering the self continuum is used on the foreign. That is to say that line centres are excluded using the method described in section 3.4.3 and only points with a total error below a certain value are allowed as described in using equation 4.1. Figure 6.4 shows the foreign continuum derived in the bands investigated in this study. The contributions of various errors are also shown. It can be seen, that the major source of error comes from the HITRAN database. Because there is more confidence in the foreign than the self half-widths, the percentage error in τ_H is less when calculating τ_H for the foreign continuum than for the self.

Thus, it can be seen that one way to minimise the errors due to HITRAN would be to maximise the ratio of P_F to P_S. However, even when P_F is much greater than P_S, as Figure 6.4 demonstrates the errors due to HITRAN actually are larger for the foreign continuum than the self. This is because the foreign continuum is weaker than the self continuum (approximately a tenth the value at the same pressure). In other words the ratio of τ_{c_F} to τ_H is far less than τ_{c_s} to τ_H. This ratio for a typical measurement is shown in Figure 6.5. Here it can be seen that while τ_{c_s} is often greater than τ_H, τ_{c_F} is nearly always less than 40%. This essentially has the effect of making any errors in HITRAN more magnified for foreign continuum calculations.

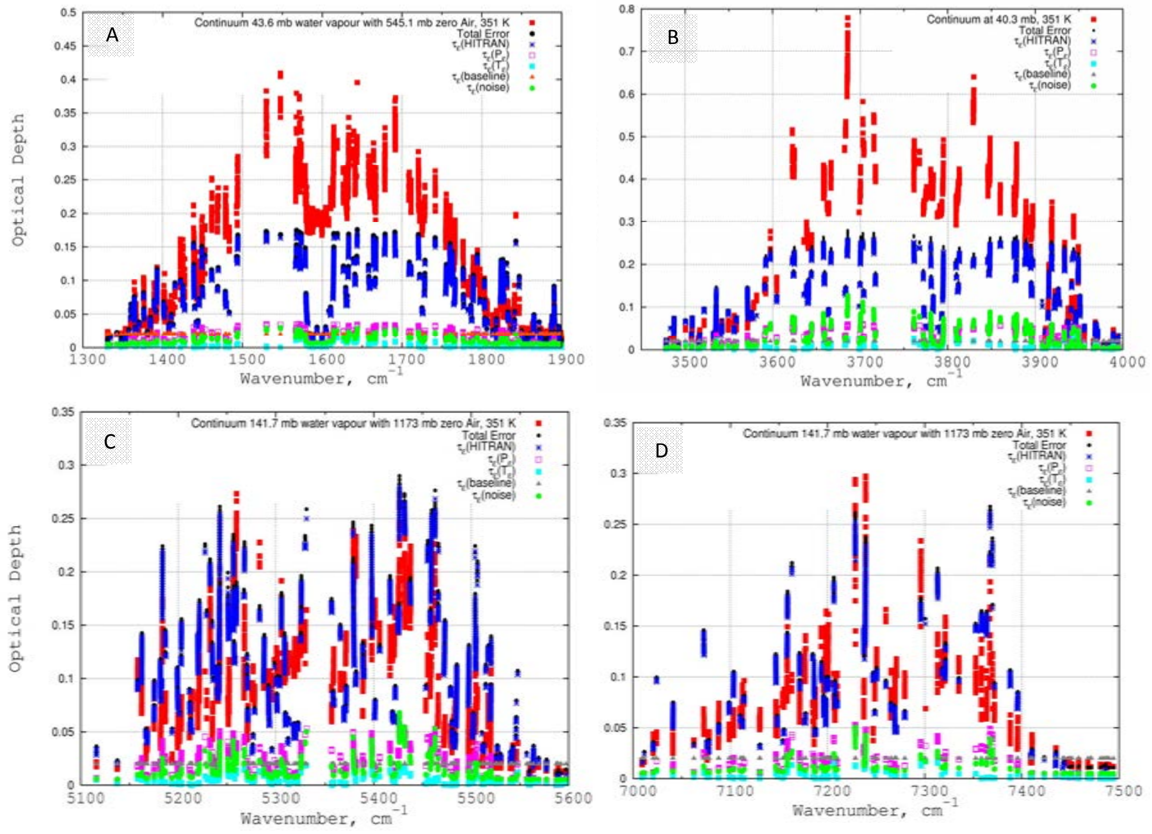

Figure 6.4 Panel A-D: The foreign continuum derived in the major bands with the contribution of various errors. The measurement conditions are shown on each panel.

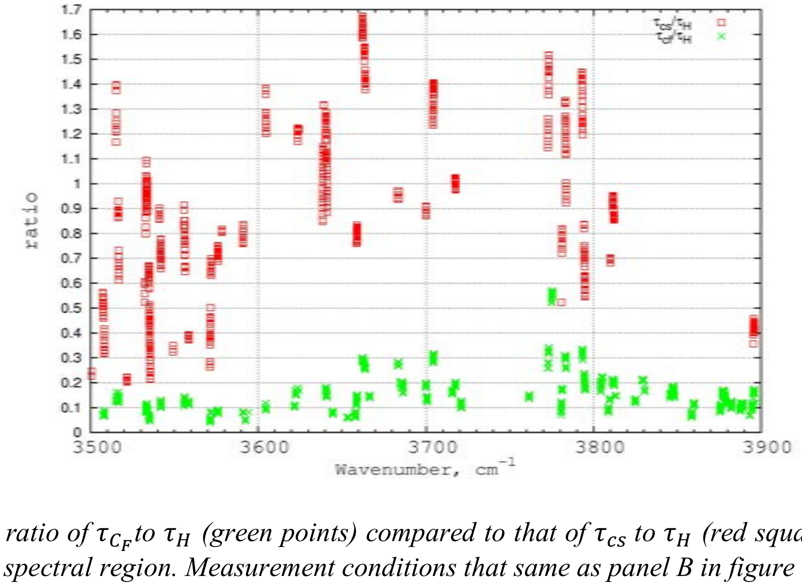

Figure 6.5 The ratio of $\tau_{C_F}$to τ_H (green points) compared to that of τ_{cs} to τ_H (red squares) for the 3500-4000cm^{-1} spectral region. Measurement conditions that same as panel B in figure 6.4.

Another consequence of the foreign continuum being less than the self, is that a greater optical depth has to be measured in order to obtain a clear continuum signal. The problem is made worse because the self continuum needs to be subtracted off before τ_{c_F} can be obtained. Thus, in order to obtain the best foreign continuum signal one has to maximise the difference between $P_F$to P_S, but whilst having P_S high enough to obtain a clear enough continuum signal. This created problems in deriving the foreign continuum in the weaker 5100-5600 cm^{-1} and 7000-7600 cm^{-1} regions. Here, due to limitations of the experimental setup (a maximum pressure of 1500mb was allowed) it was not possible obtain such a high ratio of $P_F$to P_S, whilst having P_S large enough to achieve a sufficient optical depth in τ_{c_F}. Hence, in these regions, the mixture of experimental errors and those due to HITRAN are almost as large as the continuum in most parts.

Figure 6.6 shows the effect of using different databases to derive the foreign continuum. This analysis was performed by using HITRAN 2006, HITRAN 2004, HITRAN 2000 and the Toth line list to calculate τ_H. In all cases the self continuum was derived using HITRAN 2004. It can be seen that HITRAN 2000 predicts considerably more continuum than from the other versions. In 5100-5600 cm^{-1} and 6900-7500 cm^{-1} regions the result from using HITRAN 2000 was so noisy it was decided not to included the result in order to keep the plot clearer, so it can be assumed that it is not fit for purpose in these regions. In all regions the changes between HITRAN 2006 and HITRAN 2004 seem to have very little effect upon the continuum. Likewise, the difference between the Toth line list and the two versions of HITRAN are rather similar. To some degree this should be expected given that a lot of the data in the Toth database and HITRAN are identical (especially beyond 5000 cm^{-1}). However, the fact there is good agreement between both the 1200-2000 cm^{-1} and 3400-4000 cm^{-1} region where, as can be seen from Figure 6.2, there is disagreement between the Toth database and HITRAN suggests that there is considerable amount of confidence in this result.

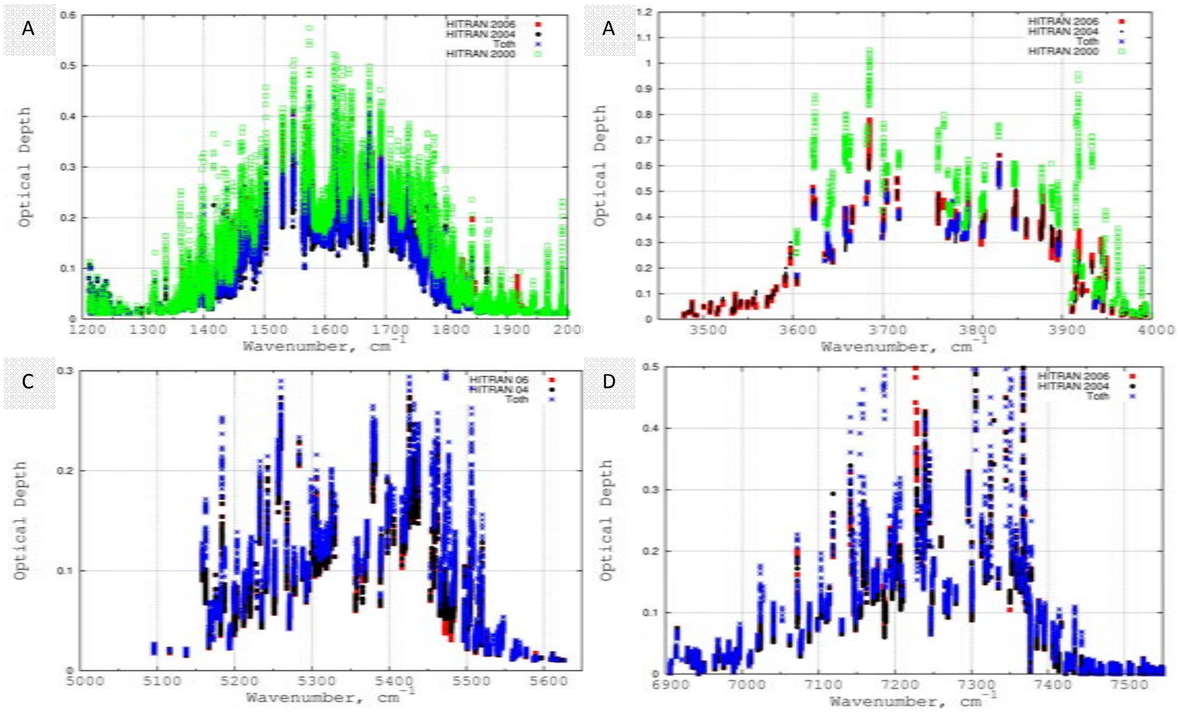

Figure 6.6 Panel A-D: The foreign continuum derived with different versions of HITRAN and the Toth line list for the major bands. The same measurement conditions and spectral regions as for the corresponding panels in Figure 6.4.

6.5. Measurement sets

The optical depth of the foreign continuum scales with the product of the vapour pressure and the broadening gas pressure. For that reason the foreign continuum, like the self, is often written in units of the continuum coefficient, but where rather than dividing the optical depth through by the vapour pressure squared, it is divided through by the product of the broadening gas with vapour pressure (i.e P_S x P_F). That is to say,

$$F(v,T) = \frac{\mathrm{k}T\tau_c}{P_S P_F L}. \tag{6.12}$$

Thus, as for the self continuum, this allows the foreign continuum measurements conducted at the same temperature to be directly comparable and placed into different measurement sets. These sets are detailed in Table 6.1. The continuum derived from each measurement can then be averaged in the same way as described in section 3.6. These sets are not as complete as for the self continuum. The greatest lack of data exists beyond 5000 cm^{-1} where there were only 3 measurements conducted, all based upon the same amount of water vapour in the cell. Due to problems with stability of the vapour pressures for this particular measurement setup it was not possible to measure at a pure vapour pressure higher than 140 mb or to perform repeat measurements. This means that if there was an error in measuring the amount of water vapour all three measurements would be wrong, leading to serious uncertainties about the continuum in this region. In addition the inability to achieve high vapour pressures has made it impossible to measure the foreign continuum between the bands. However, in the two major bands between 1200 and 5000 cm^{-1}, especially at 351 K, there are enough sets to be able to get an idea of how accurate the measurements techniques are. Figure 6.7 shows the range of the derived foreign continuum from 4 different measurement sets.

Set	**Spectral Region (cm^{-1})**	**Temperature (K)**	**No. Measurements**	**Pressures (mb) P_S (P_{F1}, P_{F2}....)**
A296F	1200-2000	296	3	13.6 (513.1,720.1) 17.9 (592.8)
A330F	1200-2000	330	5	22.7 (310.1, 905.4) 53.3 (176.3, 401.2, 712.5)
A351F	1200-2000	351	4	43.3 (208.8,361.3,534.9) 67.2 (368.4,932.4)
B296F	3400-4000	296	6	14.8 (271.6, 530.5, 817.7) 11.8 (417.6, 659.1, 1170)
B327F	3400-4000	327	2	74.8(628.1, 1010)
B351F	3400-4000	337	9	34.4(545.73, 1148,1419.9) 45.0(392.4,754.9,1356.7) 65.7(698.3,942.0,1310.0)
C351	5000-5600, 6900-7500	351	3	141.3 (443.2, 715.6, 1174.0)

Table 6.1 The different measurement sets for the foreign continuum. In the pressure column the first pressure value represents the pressure at which pure water vapour was measured. The values in brackets represent the subsequent amounts of zero air added to the cell when measurements were made. For example 13.6 (513.13,720.1) means that a spectral measurement was made with 13.6 mb of pure water vapour mixed with 513.1 mb of zero air added. More zero air was added to the cell and a measurement was conducted with 720.1 mb of zero air mixed with 13.6 mb of pure water vapour.

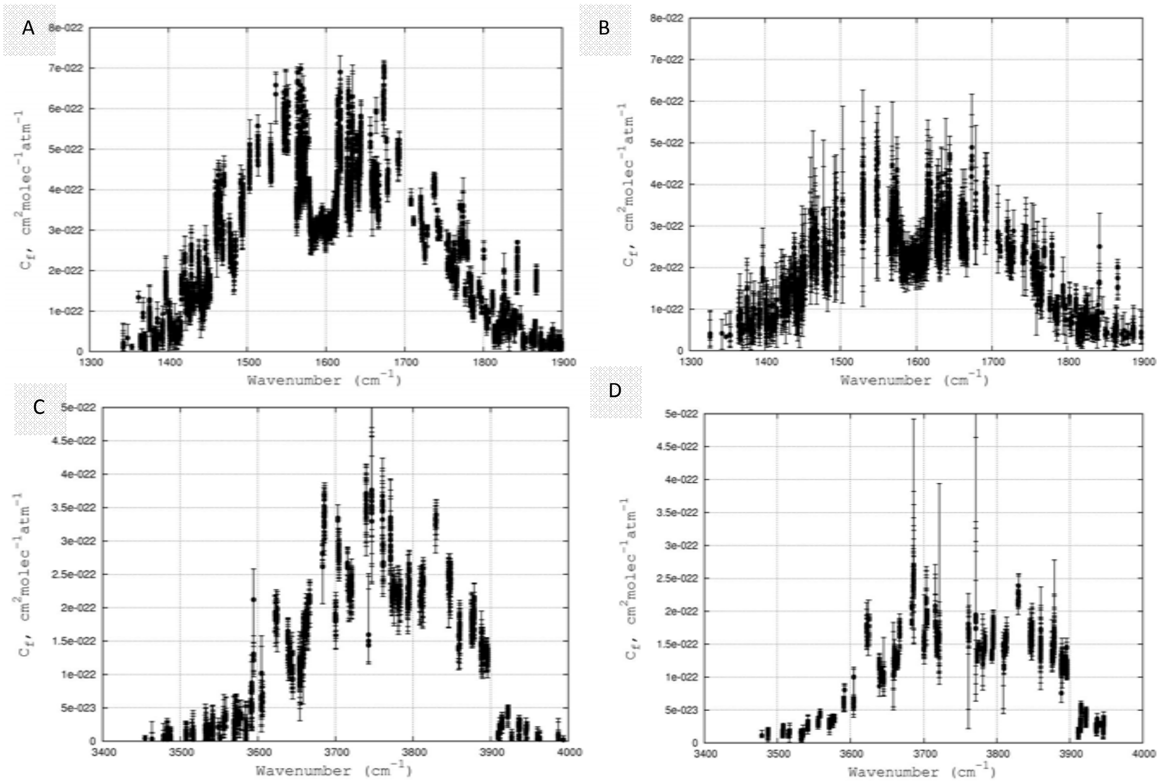

Figure 6.7 The average and range of the different measurement sets given in units of the continuum coefficient. Panel A and Panel B show set A296F and A351F respectively Panel C and Panel D shows set B296F and B351F respectively. The error bars represent the range within the measurement set.

6.6. Comparing with other results and models

The section will compare the continuum absorption in each band with other measurements already made and the main foreign continuum models.

6.6.1. 1200 – 2000 cm^{-1} region

In this region there exist two other known sets of measurements. There are some older lower resolution measurements of Burch and some newer measurements of Tobin et al. (1996). Figure 6.8 shows this work compared to Tobin measurements.

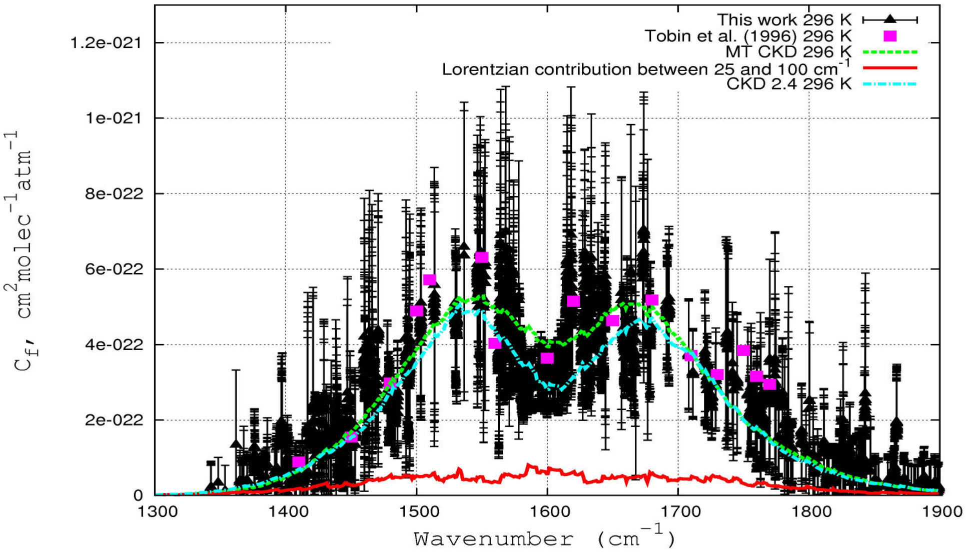

Figure 6.8 The foreign continuum derived using set A296F. The error bars are the contribution from all experimental errors. The same filtering parameters are used here as for this set in figure 7.6. The measurements of Tobin et al. (1996) are also shown, along with the MT_CKD and CKD continuum and the Lorenzian line contribution between 25 and 100 cm^{-1}.

This work shows very good agreement with the Tobin et al. measurements. Despite being fitted to the Tobin et al. data the MT_CKD continuum does not capture the shape of the continuum particularly well; missing the double peaked structure that both this work and the Tobin et al. measurements show. The CKD continuum does better at describing this structure and agrees very well with the derived continuum in this region.

6.6.2. 3400 – 4000 cm^{-1} region

In the 3400-4000 cm^{-1} region, the only previous measurements are those of Burch (1985). Unlike for the self continuum, these results have not been corrected to account for using HITRAN 2004 rather than the AGFL database as described in section 4.4.1. This was because Burch did not list the pressures at which the measurements were made, making it impossible to accurately predict τ_H. Even without the correction applied, the agreement with this work and the Burch measurements is good, although in some micro windows the Burch continuum does seem to be slightly higher. However, once the correction was applied to the self continuum it was found that the value of Burch continuum did decrease, and thus it would be reasonable to expect the same for the foreign continuum.

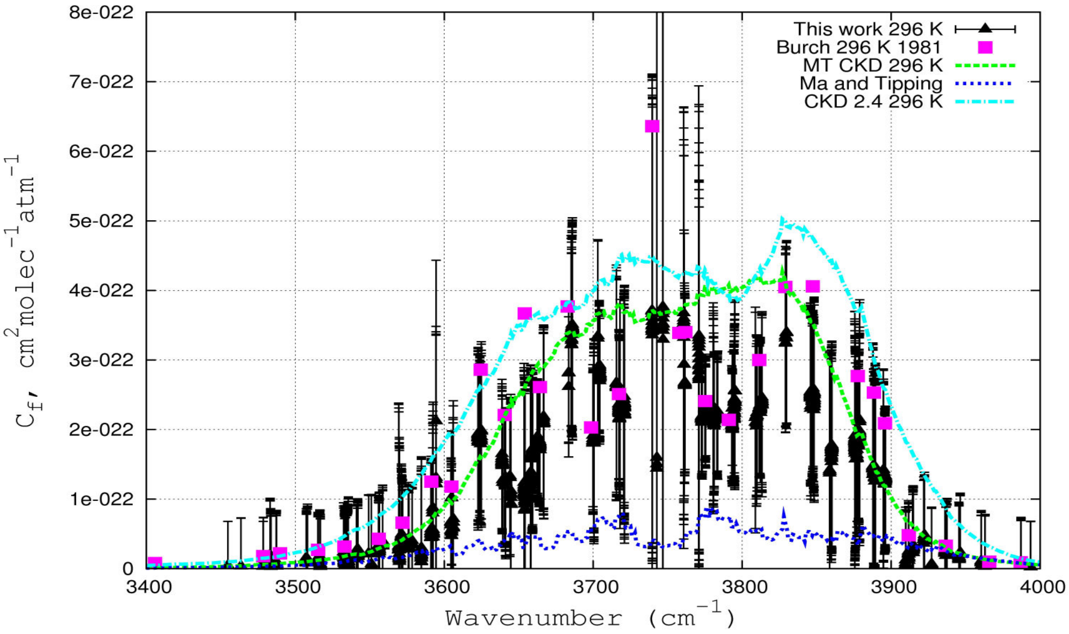

Figure 6.9 The foreign continuum derived using set B296F. The error bars are the contribution from all experimental errors. The same filtering parameters are used here as for this set in figure 7.6. The measurements of Burch (1985) are also shown, along with the MT_CKD, CKD and Ma and Tipping models at 296 K

The MT CKD continuum does capture the basic shape and magnitude of the continuum quite well here. In fact it agrees with these measurements better than it does with those of Burch. However, it could be argued that it fails to capture some of the variation in the continuum, like the dips at 3650 cm^{-1} and 3780 cm^{-1}. The CKD does not agree with the derived continuum quite as well MT_CKD and overestimates the continuum. This can especially be seen around 3850 cm^{-1}, where it predicts double the derived continuum absorption. Just as with the self continuum the Ma and Tipping continuum significantly underestimates the amount absorption. This is not surprising as the Ma Tipping continuum was not developed with the aim of explaining the continuum within the bands.

6.6.3. 5600-5600 cm^{-1} and 6900 – 7500cm^{-1}

As far as the author is aware there are currently are no other measurements of the foreign continuum in either the 5000-5600 cm^{-1} (*Figure 6.*10) or the 6900-7500 cm^{-1} (Figure 6.11) regions. In both the 5000-5600 cm^{-1} and 6900-7500 cm^{-1} region MT_CKD and CKD can be said to capture roughly the magnitude and shape of band, but there is far more structure and variation than suggested by either model. It should be remembered that, as Figure 6.4

demonstrated, the errors due to the HITRAN in this region are very significant, so it is not clear how much of this structure is actually real. Thus, until repeat measurements are made and the accuracy of the HITRAN lines improves, it is not possible to judge how well CKD models the continuum.

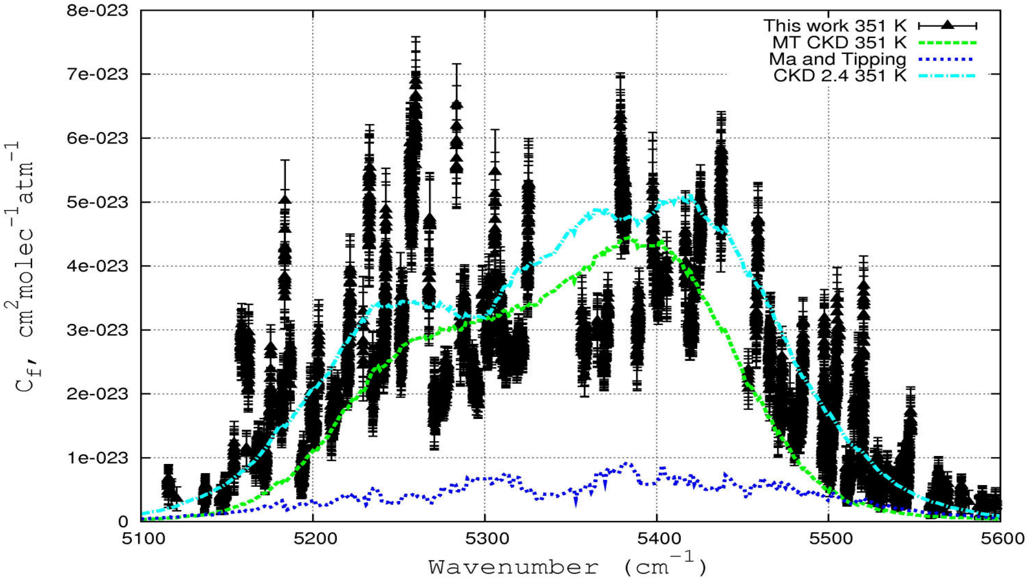

Figure 6.10 The foreign continuum derived using set C351F between 5100 and 5600 cm^{-1}. The error bars are the contribution from all errors excluding those due to HITRAN. The MT_CKD, CKD and Ma and Tipping models at 351 K are also included.

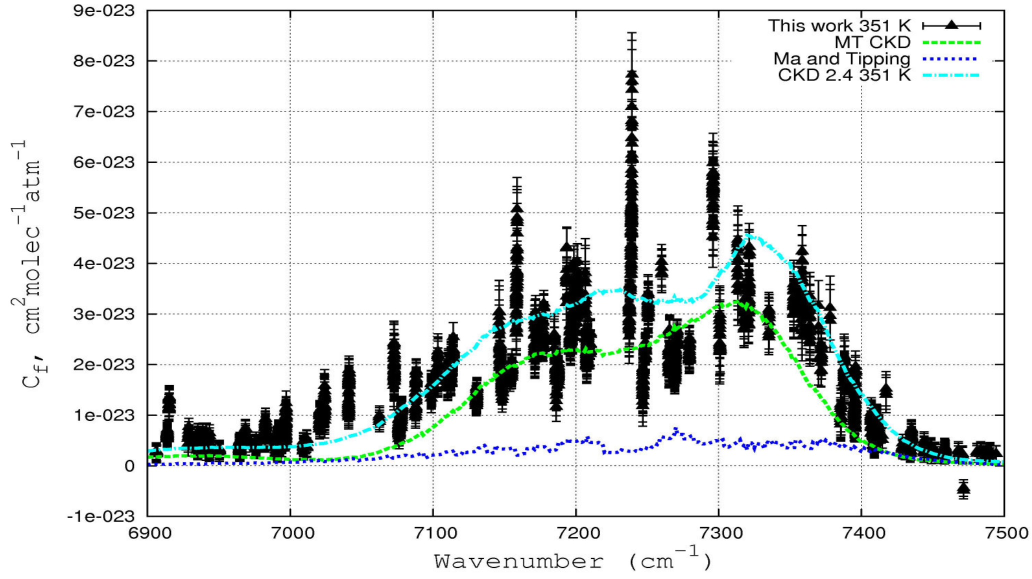

Figure 6.11 The foreign continuum derived from set C351F between 6900 and 7500 cm^{-1} The error bars are the contribution from all errors excluding those due to HITRAN. The MT_CKD, CKD and Ma and Tipping models at 351 K are also included.

6.7. Temperature dependence

As far as the author is aware there have been no measurements of the temperature dependence of the foreign continuum in the bands investigated. It is generally accepted that the foreign continuum has weaker temperature dependence than the self. In CKD and MT_CKD the temperature dependence has the simple form,

$$C_F(\nu, T_2) = \frac{T_1}{T_2} C_F(\nu, T_1). \tag{6.13}$$

Thus, unlike the self continuum the foreign continuum has no spectral variation in the temperature dependence. This section will investigate how valid an approximation this is and test whether this form is indeed the best one available. Due to the high vapour pressures required to obtain a signal for the foreign continuum in the weaker bands beyond 5000 cm^{-1} it was only possible to perform this analysis for the 1400 – 2000 cm^{-1} and 3400-4000 cm^{-1} region.

Figure 6.12 panel A and B shows the foreign continuum for both these regions derived at three separate temperatures multiplied through by T/296. To try to detect any noticeable features in the continuum, panels C and D show the ratio of the continuum derived at different temperatures. In general this is very noisy, reflecting that the signal of the temperature dependence is hard to detect above experimental errors.

If the CKD temperature dependence is correct, then the continua derived at the different temperature should be identical. In general in both regions, especially around the centres of the bands, the temperature dependence is slightly stronger than predicted by CKD. The clearest example of this is around 1600 cm $^{-1}$ and 3800 cm^{1}. There is also some evidence of spectral variation of temperature dependence, but it is not possible to be certain that this is not just noise caused by experimental/HITRAN errors

The region around 1600 cm^{-1} presents the strongest evidence that there may be a need to alter the temperature dependence of CKD. This is because in this region, the experimental errors and those due to HITRAN are smallest, but there is still a noticeable negative temperature dependence. However, as is seen in Figure 6.7, the range associated with each measurement set is of similar size to the strength of the temperature dependence detected. Hence, given that there are only measurements at three temperatures, means that it could just be chance that there is an apparent trend.

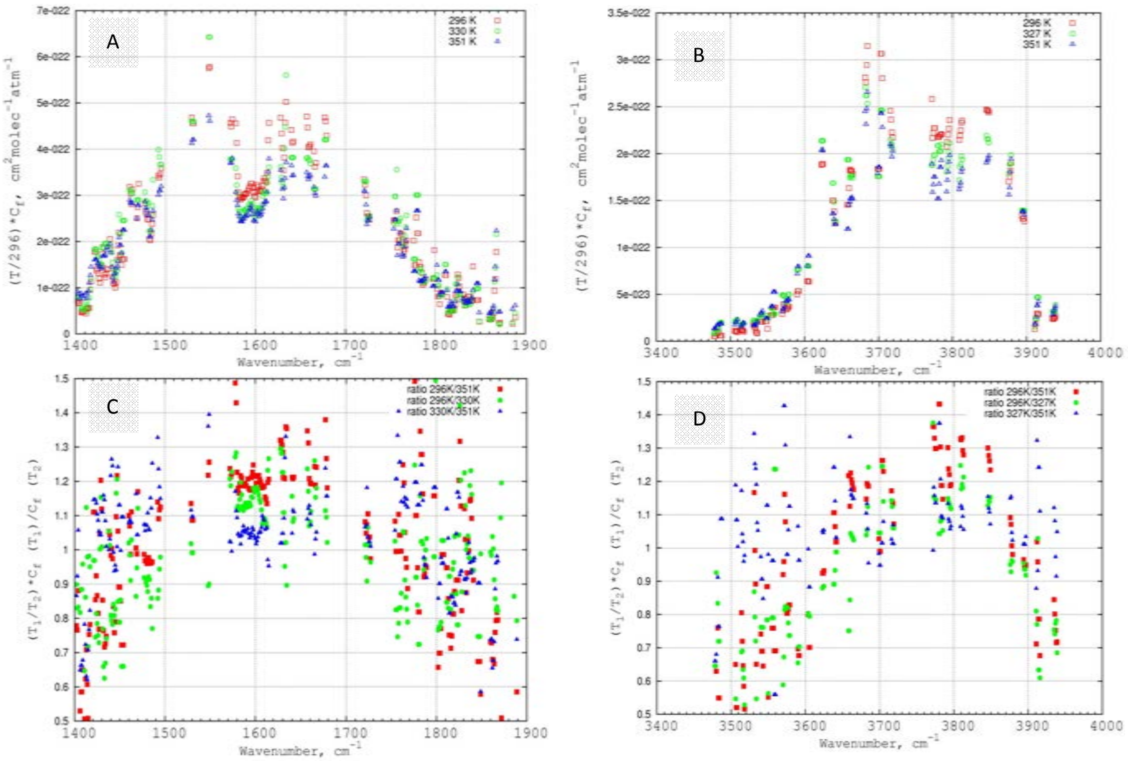

Figure 6.12 Panel A: The continuum coefficient derived from sets A296F, A330F and A351F multiplied by (T/296) in 1400-1900 cm^{-1} region. The ratio of these is shown below in panel C. Panel B and D show the same for the 3400-4000 cm^{-1} region using sets B296F, B327F and B351F.

.

6.8. Comparing the self continuum to the foreign

Comparing the self and foreign continuum can help improve understanding of whether they are caused by similar mechanisms. Figure 6.13 panels A and B show the foreign continuum compared to the self at 351 K. For the purpose of illustration the foreign continuum is multiplied by a factor of 12. The water vapour spectrum calculated using HITRAN 2004 is averaged over 50 cm^{-1}. This has been scaled to fit the continuum at 1540 cm^{-1}. This is not supposed to be an estimate of the continuum, but rather a rough indicator of where we would expect absorption if it was to result from a change in the line shape within 25 cm^{-1} of the line centre.

In the 1400-1900 cm^{-1} region (Figure 6.13 Panels A and C) the agreement between self and foreign continuum is consistent throughout the region. In general both the self and foreign continua are strongest where the water monomer absorption is strongest. The one exception is the region around 1600 cm^{-1} where the absorption from the continuum decreases far slower than the water monomer contribution. This would suggest that if the continuum in this region is due to changes in the line shape, than it would be the result of effects some distance away from the line centre.

Things are slightly different in the 3400-4000 cm^{-1} region (*Figure 6.*13 Panels C and D). Here there is a greater variation between the foreign and self continuum. This especially is the case around 3600 cm^{-1} where there was the clearest evidence of a dimer like feature in the self continuum. Here the self continuum is seen to be up to 55 times greater than the foreign.

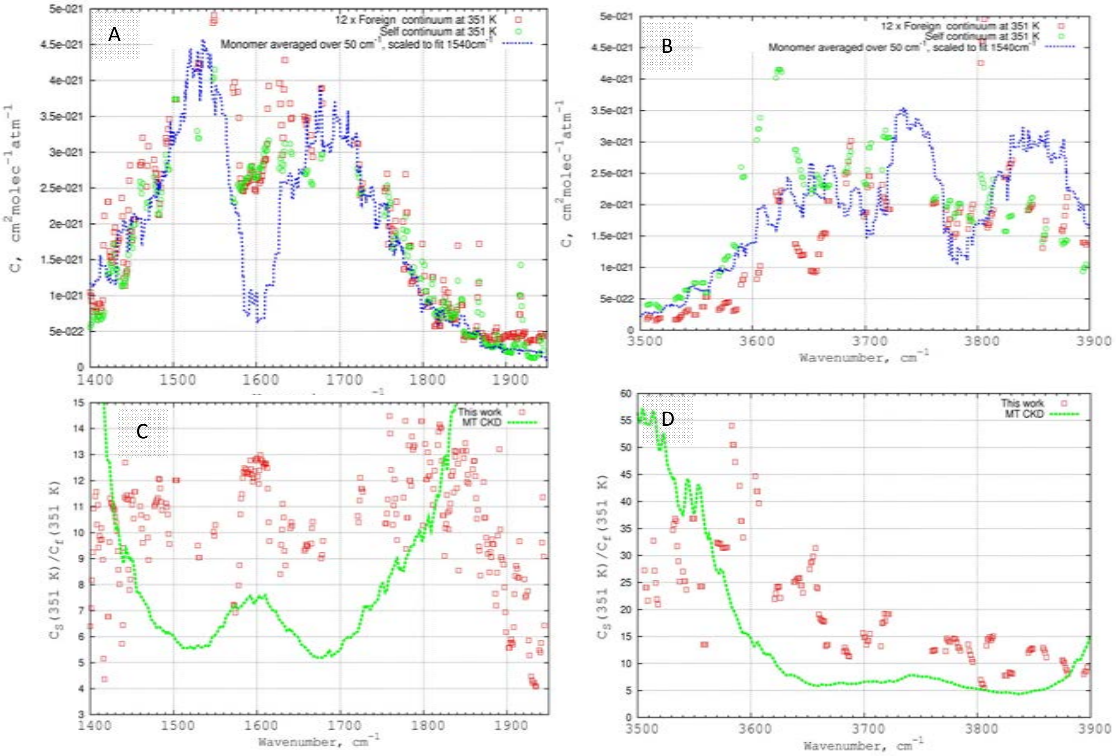

Figure 6.13 panel A and B: The self continuum compared to the foreign continuum multiplied by a factor of 12 in the 1400-2000cm^{-1} and 3500-3900cm^{-1} regions respectively. The water monomer vapour spectrum as calculated using HITRAN 2004 and averaged over 50 cm^{-1} and fitted to the continuum value at 1550 cm^{-1} is also shown. Panel C and D: The ratio between the self and foreign continuum of this work compared to MT_CKD.

There is still a small peak in the foreign continuum at 3620 cm^{-1}. One potential explanation for this could be that it is the result of the water dimer being affected by pressure broadening. However if this was the case, the feature should scale with product of the vapour pressure squared (for the abundance of dimer) and the foreign vapour pressure. However, these features like the rest of the self continuum scales with the product of vapour pressure and the foreign pressure. Another potential explanation is that this could be result of a water-nitrogen or water-oxygen complex. However, such features one would not expect to be as shifted as that of the dimer, due to the weaker nature of the bond forming.

6.9. Conclusions

This chapter has presented the foreign continuum derived from different measurements of water vapour mixed with zero air. In all of the major absorption bands between 1200 and 8000 cm^{-1} it was possible to derive a positive continuum. The experimental accuracy of the derived foreign continuum was not as good as for the self continuum. This was mainly because the foreign continuum is weaker than the self, making it impossible to obtain such high optical depths with the current measurement setup. This especially created problems when trying to derive the foreign continuum in the two bands at wavenumbers greater than 5000 cm^{-1}. In these regions even at the maximum pressure obtained it was only possible to obtain continuum optical depths of around 0.15. The fact that to derive the foreign continuum required two separate FTS measurements also affected the accuracy. The weaker continuum signal also meant that the errors due to HITRAN were more significant for the foreign continuum than for the self.

In the 1200-2000 cm^{-1} region both CKD formalisms agree well with the continuum derived in this work. The MT_CKD continuum, while predicting roughly the right magnitude of the continuum, does not seem to capture the dual peaks in this region and quite significantly underestimates the dip around 1600 cm^{-1}. In the 3400-4000 cm^{-1} region, both of the models appeared to overestimate the amount of absorption, if anything in this region MT_CKD was closer to the derived continuum. In both the 5000-5600 cm^{-1} and 6900-7500 cm^{-1} regions there was considerably more variation in the continuum than predicted by either MT_CKD or CKD. As the errors due to HITRAN were very small, it is not known how much of this variation is real and how much is the result of poorly catalogued lines in HITRAN.

In most regions it was not possible to suggest an improvement upon the simple inverse temperature dependence given in CKD and MT_CKD. However, there was evidence to suggest that around 1600 cm^{-1} the temperature dependence was perhaps slightly stronger. Further measurements are needed to confirm this.

Finally the ratio of the self to foreign continuum at 351 K was investigated for 3500-3900 cm^{-1} and 1300-1900 cm^{-1} regions. In the 1300-1900 cm^{-1} the ratio was fairly constant, although there was the hint of a peak around 1600 cm^{-1}. This was not the case in the 3500-3900 cm^{-1} region where there was a greater ratio of self to foreign between 3550 cm^{-1} and 3700 cm^{-1} than between 3700 and 3900 cm^{-1}. It was also interesting to note that this greater ratio occurred in the region where there was a suggestion of water dimer features in the self continuum. As the water dimer only contributes to the self continuum, this can be seen as more evidence that the detected features are indeed due to the water dimer.

7. Absorption of Solar Radiation in Clear Skies by the Water Vapour Continuum

This chapter investigates the contribution of both the self and foreign continua to the absorption of shortwave radiation in the atmosphere. The continuum derived in this work, CKD, MT_CKD and the Ma and Tipping models are all compared. The aim of this chapter is not to provide a detailed analysis of the effect of the continuum upon climatology; that is beyond the scope of this PhD. Instead, its aim is to give an idea of where the different formulations of the continuum presented in this work are important when investigating the Earth's radiation budget. For this reason this work will only investigate the clear sky effects of the continuum and will only consider zonal mean climatologies. Furthermore, only the effect upon shortwave radiation in the spectral regions between 1200 and 8000 cm^{-1} is investigated.

This chapter will start by explaining in more detail how the atmosphere is represented. It then presents details of how both the total shortwave absorption and heating rates are calculated. The method of preparing the data obtained in this work for atmospheric calculation is then discussed. Finally, both the shortwave absorption and heating rates for the different formulations of the continuum are presented and discussed.

7.1. Representation of the atmosphere

It was decided to perform calculations over 10^{o} latitude zonal bands. For each of these bands an atmospheric profile was obtained for the months of December, March, June and September. These atmospheric profiles consist of 20-25 layers each of which contain a homogeneous amount of water vapour, carbon dioxide, ozone, nitrogen dioxide and methane. The height, pressure, ozone and water vapour amounts in each layer come from ERA 40 climate data. Typical average values of carbon dioxide methane and nitrous oxide are included in the calculations as shown in table 1. Due to the fact that these three gases are quite well mixed and almost seasonally independent the same value is used in each layer for every season.

Gas	PPMV
H_2O	Variable see Figure 7.4
O_3	Variable, not a significant absorber in this region
CO_2	369
CH_4	1.76
N_2O	3.16

7.1.1. Calculating optical depth

In order to calculate the shortwave absorption the optical depth of each atmospheric layer must be obtained. Consider that each layer is defined to have a total pressure $\boldsymbol{P_T}$, temperature $\mathrm{T_i}$ and thickness ΔH_i and contains n absorbing gases each with a partial pressure $P_{i,m}$ and absorption cross section $\sigma_{i,m}(\nu)$. For a solar zenith angle (z) the optical depth (τ_i) for this layer is given by,

$$\tau_i(\nu, z, A_i, P_{1..n}, T_i, \Delta H_i) = \frac{\Delta H_i}{\cos(\mathrm{z})\,\mathrm{KT_i}} \sum_{\mathrm{m=1}}^{\mathrm{n}} P_{i,m}\sigma_{i,m}\left(\nu, \mathrm{P_{i,m}}, T_i, \boldsymbol{P_{T}}_m\right). \tag{7.1}$$

The total optical depth of the atmospheric profile can be obtained by simply summing the optical depths calculated for each of its constituent layers. For an atmospheric profile with K layers the transmission is given by,

$$\Gamma(\nu) = \exp\left[-\sum_{\mathrm{i=1}}^{\mathrm{K}} \tau_i(\nu, z, A_i, P_{1..n}, T_i, \Delta H_i)\right]. \tag{7.2}$$

Where i = 1 at the surface.

7.1.2. Top of the atmosphere solar flux

To calculate either flux or heating rate it is first necessary to have an accurate value for the top of the atmosphere flux. For this work the synthetic solar data of Kurucz (1994) is used. This gives the solar flux incident to the top of the atmosphere as function of wavenumber. Thus, the top of the atmosphere solar flux S at wavenumber ν for a zenith angle (z) is given by,

$$\mathrm{S}(\nu, \mathrm{z}) = \mathrm{S}(\nu, 0)\cos(\mathrm{z}). \tag{7.3}$$

Figure 7.1 shows the difference between the top and bottom of the atmosphere flux in the spectral region investigated in this work. Here the transmission in the atmosphere is calculated for an atmosphere profile centred at 5^0 latitude in March assuming an overhead sun. This irradiance with all absorbers included is shown in panel A, and with water vapour excluded in panel B. This indicates that while it is clear that water vapour is the main absorber in these regions, in some areas other absorbers are also important. This is especially the case between 2200 and 2400 cm^{-1} and between 3500 and 4000 cm^{-1} where carbon dioxide saturates the spectrum.

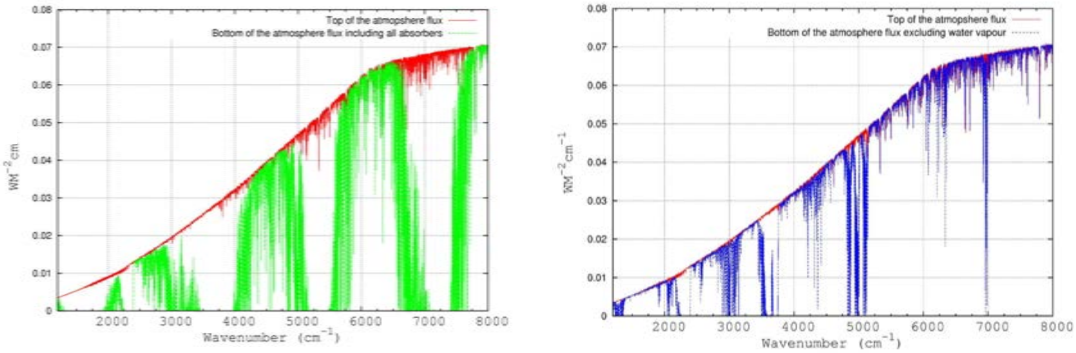

Figure 7.1 panel A: The top of the atmosphere irradiance compared to that at the bottom of the atmosphere for March at 5^0 north assuming overhead sun. Panel B: The same as panel A, but excluding water vapour in the atmosphere.

7.2. Calculating shortwave absorption

Once the transmission for the atmospheric profile is obtained, calculating the total absorbed shortwave radiation is straightforward. The absorbed shortwave radiation can be broken down into two components. The down-welling absorbed radiation (f_D), which is the difference between the downwards flux at the top and bottom of the atmosphere. The up-welling absorbed shortwave radiation (f_U), which is the difference between the upwards flux reflected from the surface and that reaching of the top of the atmosphere.

Therefore, the absorbed down-welling solar radiation $f_D(v)$ at a wavenumber v is simply is given by,

$$f_D(v, z(t)) = \mathrm{S}(v, z)[1 - \Gamma(v, z)] \tag{7.4}$$

However, some of the shortwave radiation that reaches the bottom of the atmosphere is reflected by the surface. The amount of radiation that is absorbed by the atmosphere because of this can be obtained by replacing S(v) in (7.4) with the radiation being reflected from the surface. Thus the amount of up-welling shortwave radiation absorbed given a surface albedo ϵ is,

$$f_U\big(\nu, z(t)\big) = \epsilon \mathrm{S}(\nu, z)\Gamma(\nu, z)[1 - \Gamma(\nu, z)]. \tag{7.5}$$

By adding (7.4) and (7.5) the total shortwave absorbed radiation at a particular wavenumber given as,

$$f_T\big(\nu, z(t)\big) = \mathrm{S}(\nu, z)[1 - \Gamma(\nu, z) + \epsilon\Gamma(\nu, z) - \epsilon\Gamma(\nu, z)^2]. \tag{7.6}$$

f_T gives the amount of energy absorbed per wavenumber. However, when looking at the atmosphere we are interested in the total amount of energy that the system absorbs. This is defined by integrating over a desired wavenumber range as,

$$F_T = \int_a^b f\big(\nu, z(t)\big)d\nu. \tag{7.7}$$

7.2.1. Calculating average shortwave absorption

Equation (7.7) gives the total absorbed shortwave radiation by the atmosphere at a particular solar zenith angle. However, it is useful to calculate the daily averaged shortwave radiation. This can be written as,

$$\overline{F_T} = \left(\frac{2}{86400}\right)\int_0^{D/2} F_T(\nu, z(t))\mathrm{dt}, \tag{7.8}$$

where D is the amount of time (in seconds) for which the sun is above the horizon (i.e. the day length) and t is time in seconds. The integration is only over half the day length as the absorption over the second half of the day is taken to be equal to that over the first half.

It is useful to write this in a discrete form as,

$$\overline{F_T} = \left(\frac{2}{86400}\right)\sum_{j=1}^{Q} F_T(\nu, z(t_j))\,\Delta t_j. \tag{7.9}$$

Knowledge is required of how the zenith angle varies with latitude and time throughout the day. Petty (2004) shows that the value of the cosine of the zenith angle at a certain point in time and latitude is given by

$$\cos\,(Z(t)) = sin(decl)sin(lat) + cos(decl)cos(lat)cos(Hangle_i) \tag{7.10}$$

Where the angle of declination (decl) is,

$$\begin{aligned} decl = 0.006918 &- 0.399912cos\big(\theta_{day}\big) + 0.070257sin\big(\theta_{day}\big) \\ &- 0.006758cos\big(2\theta_{day}\big) + 0.000907sin\big(2\theta_{day}\big) \\ &- 0.002697cos\big(3\theta_{day}\big) + 0.001480sin\big(3\theta_{day}\big), \end{aligned} \tag{7.11}$$

and θ_{day} is given by,

$$\theta_{day} = \frac{2\pi day}{365}. \tag{7.12}$$

Here day is the day number on which the calculation is performed.

It is also possible to define the day length at a particular day number at certain latitude and longitude as,

$$D = \left(\frac{86400}{2\pi}\right) arccos\left(-\frac{sin(decl)sin(lat)}{cos(decl)cos(lat)}\right). \tag{7.13}$$

The hour angle (Hangle), which defines how the zenith angle changes throughout the day is given by,

$$Hangle_j = \frac{\pi G_j D}{86400}. \tag{7.14}$$

Here G_i is a fraction of the day length one is interested in performing the calculation for.

Thus, using equations (7.11)-(7.14), the zenith angles (Z_i) at each required time step can be obtained. Gaussian integration is used to minimise the number of time steps required. This involves introducing a weighting function w_i such that,

$$\Delta t_j = w_j D \tag{7.15}$$

By then substituting (7.15) into (7.9) the following expression is obtained for the averaged shortwave aborbtion,

$$\overline{F_T} = \left(\frac{2D}{86400}\right)\sum_{j=1}^{n} w_j F_T(v, z_j). \tag{7.16}$$

These results shows that the average shortwave radiation can be estimated calculating the absorption for specific zenith angles at points in the day specified by G_i and using an associated weighting function (W_i). It can be shown that it is possible to achieve accurate results with calculating F_T for three points in the day using the values of W and G shown in table 2

W	**G**
5/18	9/10
4/9	½
5/18	1/10

Table 1:The weighting functions used for specific day fractions.

7.3. Calculating heating rates

To see exactly where in the atmosphere the absorption occurs it is useful to calculate heating rates for each layer in the atmosphere. To do this it is necessary to know the amount of shortwave flux absorbed by each layer. The solar flux absorbed by the ith layer of atmosphere is the difference between the radiation entering that layer (i.e that exiting the i-1 layer) and that leaving the bottom the of the layer. This can be given in terms of the shortwave flux absorbed by each layer as,

$$\Delta F_{T,i} = F_{D,i} - F_{D,i-1} + \left(F_{U,i} - F_{U,i+1}\right), \tag{7.17}$$

where $F_{D,i}$ is the amount of down-welling shortwave radiation absorbed by the atmosphere when it reaches the bottom of the ith layer and $F_{D,i-1}$ is that entering the layer. $F_{U,i}\ and\ F_{U,i+1}$ are similar terms but for the up-welling radiation reflection off the Earth's surface.

Following similar steps to when calculating the average daily shortwave absorption, the daily averaged flux across a layer is given by

$$\overline{\Delta F_i} = \left(\frac{2D}{86400}\right)\sum_{j=1}^{3} W_j \Delta F_i(\nu, Z_i). \tag{7.18}$$

By assuming the hydrostatic approximation it can be shown that the daily heating rate for the ith layer can be obtained from averaged daily flux as(e.g Petty 2004),

$$\overline{\Delta T_i} = \frac{\Delta H_i}{\mathrm{c}_p \Delta \boldsymbol{P}_i}\overline{\Delta F_i} \tag{7.19}$$

7.4. Calculating the optical depth of the continuum

When calculating the optical depth of each atmospheric layer, the self and foreign continua contributions are included by being modelled as separate absorbers with cross sections $\sigma_{s,i}$ and $\sigma_{f,i}$ respectively. These cross sections can be defined using the continuum coefficients as,

$$\sigma_{s,i}(\nu, T) = P_{i,H2O} C_s(\nu, T_i) \tag{7.20}$$

and

$$\sigma_{F,i}(\nu, T) = \left(\boldsymbol{P_i} - P_{i,H2O}\right) C_s(\nu, T_i) \tag{7.21}$$

To perform shortwave absorption calculations the continuum needs to be derived at regular wavenumber intervals. The MT_CKD continuum is defined every 10 cm^{-1} and the Ma and Tipping continuum every 1 cm^{-1}. By contrast the continuum in this work has been derived at irregular intervals mainly in the micro-windows within the major bands.

The following strategy was adopted to use these data to obtain the self continuum at regular intervals. An algorithm was devised that would go through the spectrum at single wavenumber intervals from 1200-8000 cm^{-1}. At each wavenumber it would search through the values of the derived continuum from the relevant measurement sets at 351 K. It would then define the continuum at each wavenumber as the average of the points in the derived continuum which lay 15 cm^{-1} either side. For example, the continuum at 1300 cm^{-1} would be defined as the average of all the values in the derived continuum between 1285 cm^{-1} and 1315 cm^{-1} from measurement set A351.

Occasionally, in an area of strong absorption, there is the situation where there are no values of the derived continuum within 15 cm^{-1} of a particular wavenumber. In this case, providing the gap between two nearest derived continuum values is less than 50 cm^{-1}, an extrapolation between the continuum at these two points in wavenumber space is used. This allows the continuum to be derived at all wavenumbers near the band centres.

As noted in section 4.6, it was not possible to derive the continuum between the bands. However, in these areas it was shown that, in general a Gaussian like function could be fitted to the decay in absorption away from the band centre. Thus, where there was no data available, these fits were used.

Using one of these three methods the self continuum is estimated at each wavenumber between 1200 cm^{-1} and 8000 cm^{-1}. This estimated continuum is shown in panel A of Figure 7.2. The red highlighted areas are where the continuum has been derived from the measurements in this work. The non-highlighted areas is where the continuum has been estimated using the Gaussian fit. The CKD, MT_CKD and Ma and Tipping continuum are also shown for comparison.

A similar analysis is performed for the foreign continuum using data sets A351F, B351F and C351F. However, due to accuracy issues, it was not possible to measure significant amounts of the areas between the bands and thus it was not possible to estimate this area for this work. For this reason the MT_CKD values are used where there were no data available. Panel D of Figure 7.2 shows the result of the foreign continuum derived using this technique. Here the highlighted areas is where data from the continuum derived from measurements is used, in all other areas the MT_CKD continuum is used.

As discussed in chapter 4 the experimental setup did not allow for the measurement of the continuum below 296 K, even though most of the atmosphere is colder than this temperature. However, in band centres it was possible to fit either a MT_CKD like temperature dependence or a dimer like temperature dependence. The reader will recall that the MT_CKD temperature dependence form is given by,

$$C_s(\nu,T_1) = C_s(\nu,T_o)(T_0/T_1)\exp\big(\sigma(\nu)(T_1 - T_0)\big). \tag{7.22}$$

For the dimer the dependence,

$$C_s(\nu,T_1) = \left(\frac{T_0}{T_1}\right)^{\frac{3}{2}} C_s(\nu,T_o)\exp\left(\epsilon(\nu)\left(\frac{1}{T_1}-\frac{1}{T_0}\right)\right). \tag{7.23}$$

As with the continuum coefficient, values of $\sigma(\nu)$ and $\epsilon(\nu)$ were obtained at irregular intervals. Thus, a similar technique is employed for deriving the temperature dependence of the self continuum at regular intervals For the MT_CKD like temperature form, at each wavenumber $\sigma(\nu)$ is fitted to the continuum derived from measurements and is averaged over 15 cm^{-1}. Where it was not possible to fit $\sigma(\nu)$ to the derived continuum the values of $\sigma(\nu)$ from MT CKD are used. Panel B of Figure 7.2 contains the results of this analysis. The green highlighted area represent where $\sigma(\nu)$ has been obtained by fitting to measurements, elsewhere the values are from the MT_CKD model.

Exactly, the same technique is used for the dimer like temperature dependence where data is available. Where there are no data available a different approach is taken. The reader will recall that for the dimer temperature dependence it was observed that the values of $\epsilon(\nu)$ were greatest near the areas of strongest absorption. Moving away from the band centre these values decreased. It was speculated that this could be the result of increasing influence of weaker lines away from the centre of the band, as these will typically have a higher lower state energy and have a stronger positive temperature dependence. As one moves away from the bands into the wings it is assumed that yet again the strongest dimer lines are dominant and thus the temperature dependence becomes stronger.

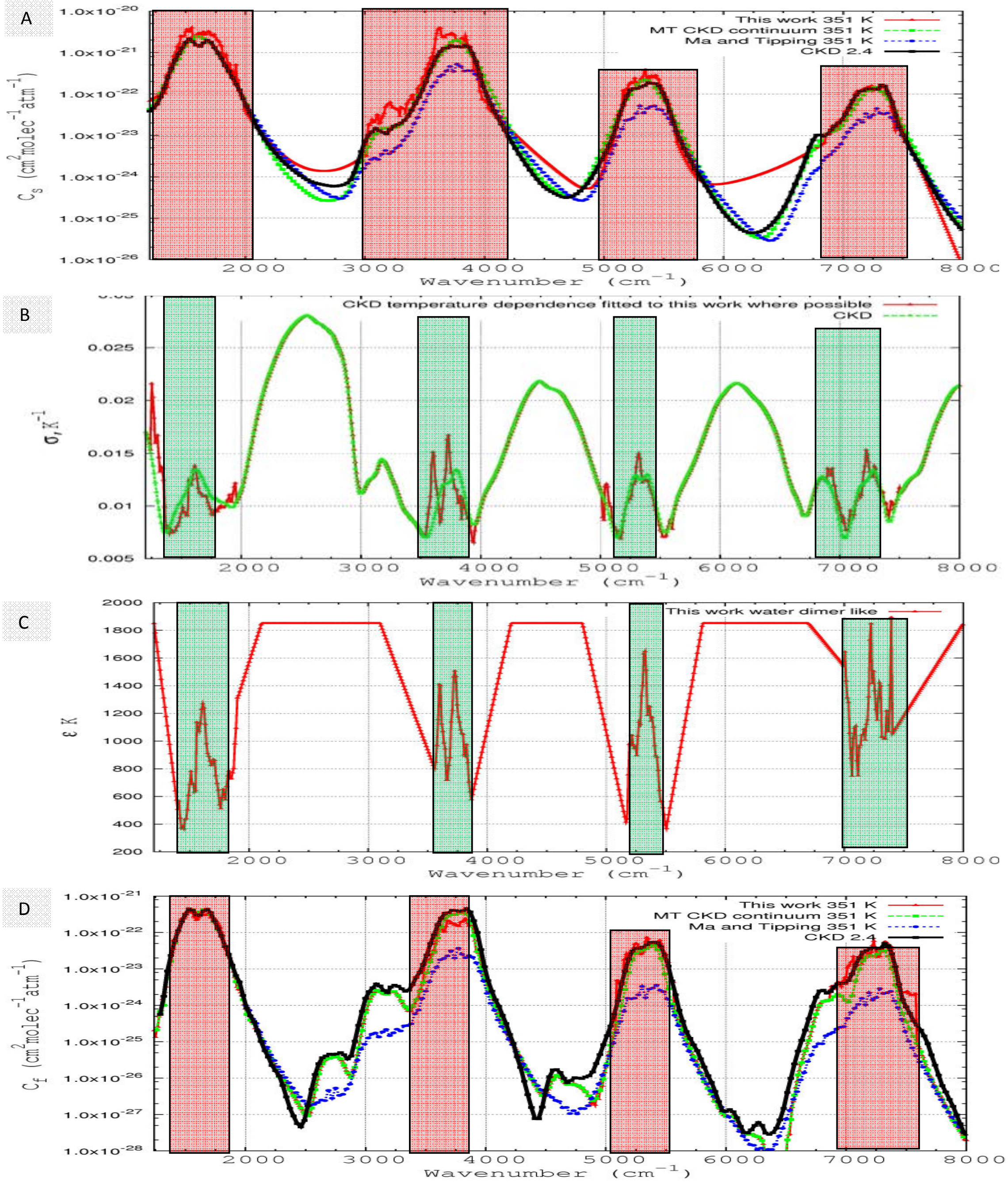

Figure 7.2 Panel A: The self continuum derived in this work at 351K. Areas highlighted in red are where it has been possible to measure the continuum. In all other areas the contribution is an estimate using a Gaussian fit. The Ma and Tipping, CKD and MT_CKD continuum are also shown. Panel B: The temperature dependence coefficient for a CKD like fit to this work. It is fitted in the green highlighted areas, elsewhere that of MT_CKD is used. Panel C: The dimer like coefficient obtained as discussed in the text, in the green highlighted areas this value is fitted directly to measurements. Panel D: The derived foreign continuum compared to CKD, MT_CKD and Ma and Tipping, areas where the foreign continuum has been obtained from measurement are highlighted in red.

This is quite simply modelled by assuming that away from the band centres $\epsilon(\nu)$ increases linearly till it reaches a maximum value between the bands. The maximum value of $\epsilon(\nu)$ was chosen as 1850 K. This is in line with the upper value obtained in section 5.2. This upper value was chosen in order to see whether at the upper limit of the dimer temperature dependence suggested in this work there are any noticeable differences in the atmospheric response to the continuum compared to when the CKD temperature dependence is used.

Figure 7.3 compares the ratio of C_s at 351 K to that 300 K, 250 K and 200 K using both the Dimer and CKD model fitted to the continuum derived in this work. In the bands at 300 K it can be seen that both predict a similar ratio. This is to be expected, as between 351 K and 296 K both theories are fitted the derived continuum of this work. However, at lower temperatures it is observed that the dimer model has a stronger negative temperature dependence than CKD. This suggests that for atmospheric conditions there is a significant difference between the dimer and CKD absorption.

Turning attention to the regions in-between the bands, it can be seen that at 300 K both the dimer theory and MT_CKD predict quite a similar amount of absorption. But, as in the bands, the dimer theory predicts a stronger negative temperature dependence, these results suggest that by measuring the continuum at atmospheric temperatures it should be possible to discriminate between the two theories.

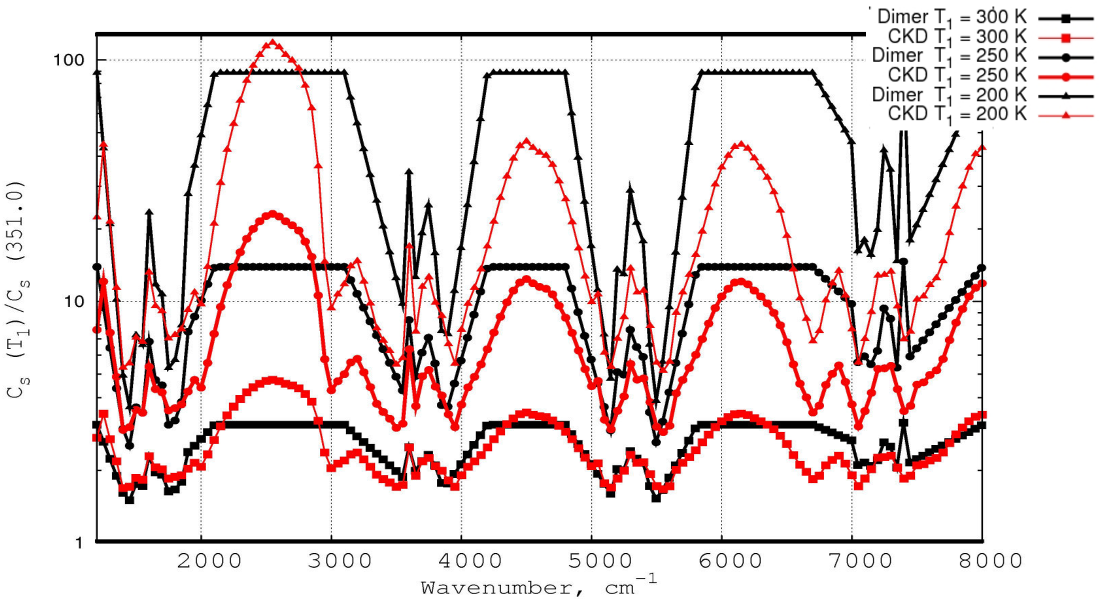

Figure 7.3 The ratio of the self continuum coefficient at different temperatures obtained using the MT_CKD style temperature dependence compared to the water dimer temperature dependence as a function of wavenumber.

7.5. Temperature and water vapour profiles in the atmosphere

As already noted, the temperature and water vapour profiles come from monthly averaged ERA-40 data. The water vapour and temperature profiles for December, March, June and September are shown in Figure 7.4 and Figure 7.5. Figure 7.4 panel E also shows the total water vapour column at each latitude for the different months.

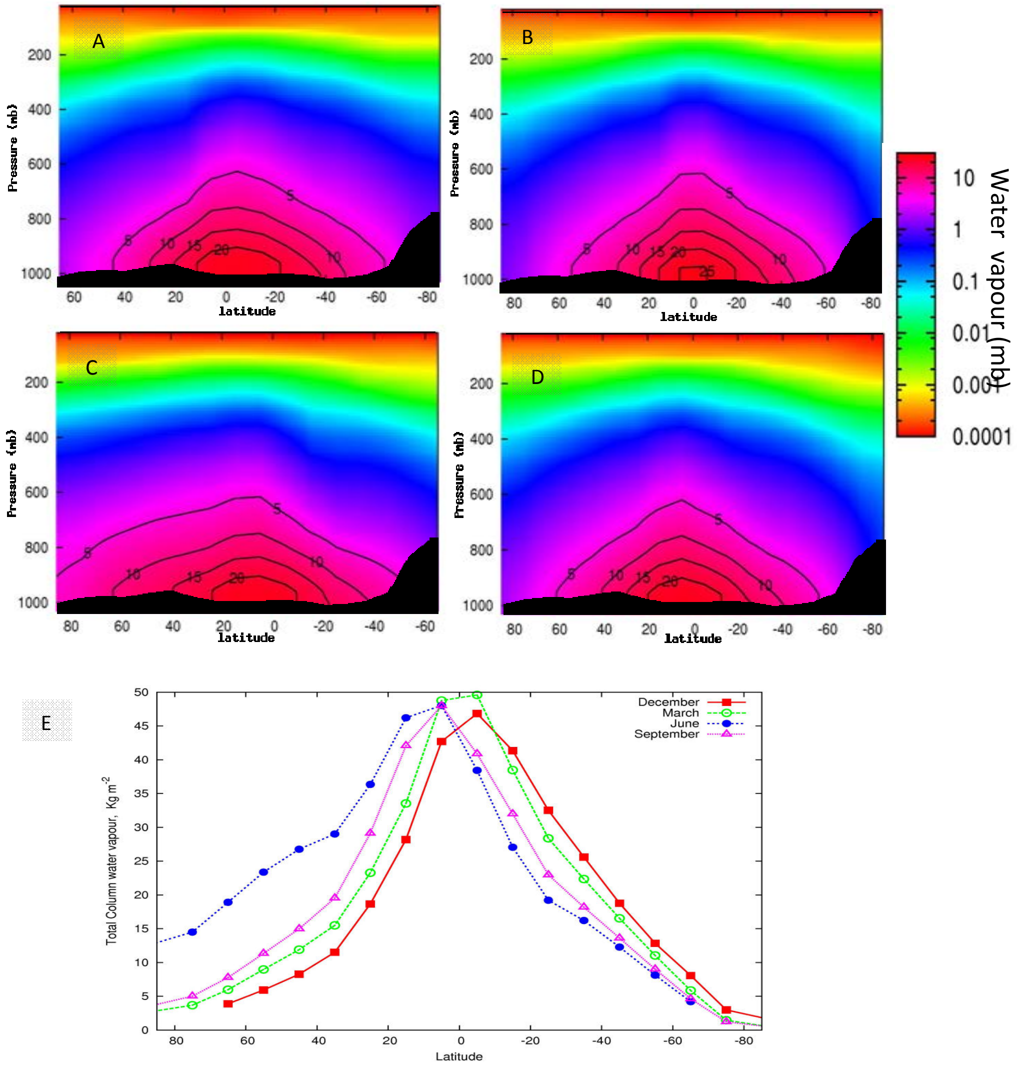

Figure 7.4 Panels A-D: The ERA 40 zonal mean distribution of water vapour pressure in mb for the months of December, March, June and September respectively. Panel E The average total water column in kg m^{-2} as a function of latitude for each of the different months at which calculations were performed.

It can be seen that the water vapour content varies many orders of magnitude with atmospheric pressure. A lesser variation is seen with latitude. However, for all seasons water vapour does increase considerably nearer the equator. As can be observed from panel F there is seasonal variation in the water vapour column at similar latitudes. The largest variation occurs in the northern hemisphere in June, where the total water column at high latitudes is double that of the other seasons.

The average temperature for each of the months is shown in Figure 7.5. It can be seen that where the greatest amount of water vapour is the temperature varies between 300 K and 250K. This is less than the temperatures at which the laboratory measurements were conducted, highlighting the importance of the process of extrapolating the continuum absorption measured in this work to lower temperatures.

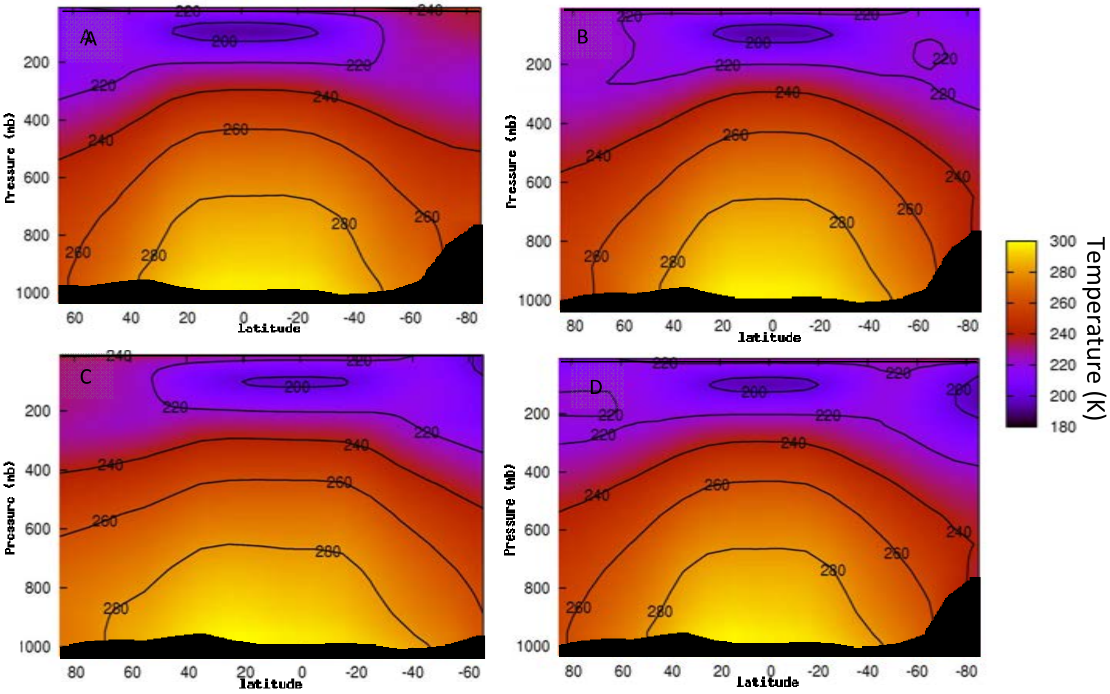

Figure 7.5 Panels A-D: The ERA 40 zonal mean monthly averaged temperature in Kelvin for the months of December, March, June and September respectively.

7.6. Clear sky globally averaged shortwave absorption

Estimating the globally averaged shortwave absorption (GSWA) provides a simple comparison of the different continuum models. This is obtained by calculating the daily average shortwave absorption using equation (7.16) every 10^0 in latitude and then averaging this value over the globe. The GSWA was calculated on either the equinox or solstice day in the months of December, March, June and September using monthly averaged atmospheric profiles. For each of these months the variation in GSWA resulting from using CKD, MT_CKD, Ma and Tipping and the derived continuum of this work has been calculated.

The GSWA for all atmospheric absorbers listed in Table 7.1 was calculated using the RFM line-by-line code at 1 cm^{-1} sample outputs between 1200 and 8000 cm^{-1}. Many water vapour lines are narrower than 1 cm^{-1}, and thus some areas of absorption may be over or underestimated. However, it can be shown that even over a relatively small spectral region (~500 cm^{-1}) that these errors cancel out and the GSWA values obtained is within 1 % of that produced taking a sample every 0.01 cm^{-1}. Most importantly the difference in this sampling rate was found to have no more than a 2% effect on the estimated contribution to the GSWA by the continuum. As will be seen this is far less than other uncertainties.

Because the exact details of the Ma and Tipping continuum temperature dependence are not published, the temperature dependence of MT_CKD continuum is used in this case. The fact that it has not been possible to estimate the temperature dependence of the continuum derived in this thesis apart from in the band centres has already been highlighted. For this reason, and because it is informative to just compare the effect on GSWA of only the spectral variation in the continuum, unless mentioned otherwise the MT_CKD temperature dependence for both self and foreign continuum (i.e. as given in MT_CKD, not fitted to this work) is assumed when calculating the GSWA.

As a test run the GSWA for all absorbers, including the MT_CKD continuum, the continuum was calculated between 1200-16000 cm^{-1} for the clear sky case assuming no scattering. A value of 59.8 Wm^{-2} was obtained. Collins et al. (2006) have shown that this region should account for about 98% of total water vapour absorption. Comparing this value with other authors' clear sky calculations is not straight-forward, as there is some ozone absorption beyond 16000 cm^{-1}. This means that the GSWA is likely to be slightly greater. Further work needs to be performed to calculate an exact value. Kiehl and Trenberth (1997) give a value for the contribution of ozone to the total GSWA of 14 Wm^{-2}. Although it is not clear how much of this absorption is already included in the 1200-16000 cm^{-1} calculations, this would suggest that model developed here predicts a clear sky absorption value somewhere between 60 Wm^{-2} predicted by Kiehl and Trenberth (1997) and 70 Wm^{-2} predicted by Collins et al. (2006).

The GSWA for the spectral region between 1200 and 8000 cm^{-1}, in which the continuum was derived, was calculated to be 35.5 Wm^{-2} without the continuum included. Unless specified the term GSWA will apply to this value calculated between 1200 and 8000 cm^{-1}. The contribution of the continuum to the GSWA (referred to from here on as C_GSWA) for each of the months is presented in Table 7.2. An estimated yearly average, which is just the average of these four months, is also given. This shows that the MT_CKD model has an average C_GSWA value of 0.79 Wm^{-2}. This is equivalent to a 2.2% increase in the value of GSWA. The older CKD continuum predicts a 23% larger value of 1.00 Wm^{-2}, giving a 2.7% increase in GSWA. There is no reason to trust the values of the newer MT_CKD more than CKD. This is because between 3000 and 8000 cm^{-1} neither model is based upon measurements of the continuum. Instead, they just use different empirical forms to extrapolate the continuum from the monomer absorption (see sections 2.7.1 and 2.8).

A smaller value of 0.47 Wm^{-2} is predicted for the Ma and Tipping continuum. This is not surprising, as it was shown in for all regions measured that the Ma and Tipping model underestimated the continuum within the band centres. For the continuum derived in this work (as defined in Figure 7.2) an average value of 1.14 Wm^{-2} is obtained. A similar small seasonal variation is seen for all four formulations of the continuum, which seems to mirror the change in GSWA.

The C_GSWA is also calculated for the minimum and maximum estimates of the continuum derived in this work by taking into account experimental errors. Where there are measurements made, then these experimental errors are simply those as estimated in chapters 4 and 6 for the self and foreign continuum respectively. As noted in sections 4.6.3 and 7.4, for the self continuum when no continuum is measured then an exponential function fitted to the derived continuum is used. In these regions the upper limit of the continuum is estimated by adding the baseline error to this fit (see Figure 4.34). Likewise, the minimum value is obtained by subtracting the baseline error away from the estimated continuum. If this value is less than zero, as often it is, then it is assumed that the continuum absorption is equal to zero. For the self continuum as such these upper and lower limits should not be seen as suggested values based upon any sort of physical insight into the continuum, but are simply showing the limits of the experimental setup used to derive the continuum in this particular instance.

For the foreign continuum, the MT_CKD model has been used where the continuum has not been derived from measurements. Because there is no obvious way to estimate the errors in these regions, no error is assumed. Therefore, for the foreign continuum presented in this work the uncertainty can only be seen as relating to where it has been derived from measurements.

Absorber	C_GSWA (Wm^{-2}) DEC	C_GSWA (Wm^{-2}) MAR	C_GSWA (Wm^{-2}) JUN	C_GSWA (Wm^{-2}) SEP	C_GSWA (Wm^{-2}) AVG	% of GSWA
All without continuum	36.93	35.00	35.79	34.30	35.51	100.0
MT_CKD	0.82	0.77	0.81	0.75	0.79	2.2
CKD	1.06	0.98	0.99	0.96	1.00	2.7
Ma and Tipping	0.48	0.46	0.49	0.44	0.47	1.3
This work Best est.	1.19	1.13	1.15	1.10	1.14	3.1
Upper bound	2.30	2.22	2.25	2.12	2.23	5.9
Lower bound	0.58	0.53	0.53	0.52	0.54	1.5
Best est. (Assuming dimer temp dep.)	1.25	1.18	1.20	1.15	1.20	3.3
MT_CKD Where Measured	0.19/0.53	0.18/0.50	0.17/0.51	0.18/0.48	0.18/0.50	0.5/1.40
CKD Where Measured	0.32/0.66	0.29/0.62	0.30/0.61	0.29/0.61	0.30/0.63	1.8/1.8
This work Best est. Where Measured	0.51/0.76	0.47/0.72	0.46/0.72	0.46/0.72	0.47/0.72	1.3/2.0
Upper bound	0.72/1.01	0.67/0.98	0.64/0.95	0.62/0.96	0.66/0.97	1.8/2.6
Lower bound	0.20/0.41	0.19/0.38	0.16/0.36	0.19/0.38	0.19/0.38	0.5/1.1
This work Best est. Where Measured (Assuming dimer temp dep.)	0.52/0.79	0.48/0.75	0.46/0.73	0.47/0.74	0.48/0.75	1.3/2.1
This work Best est. Where Measured (Assuming fitted CKD temp dep.)	0.51/0.78	0.47/0.75	0.45/0.73	0.46/0.74	0.47/0.74	1.3/2.1

Table 7.2 The difference in the globally averaged shortwave absorption (C_GSWA) resulting from different formulations of the continuum. This includes both the self and foreign continuum between 1200 cm^{-1} and 8000 cm^{-1}. When 'Where Measured' is mentioned the first value refers to the spectral region where both the foreign continuum and self continuum have been derived from measurements, as described in column one in table 7.3 (below). The second value is where just the self has been derived from measurements, but not necessarily the foreign, as described in column two in Table 7.3 (below). Thus, the format is of the form,(***spectral regions where both the self and foreign are derived from measurements)/(spectral regions where the self continuum is derived from measurements).*** *In the regions where the self continuum is measured, but not the foreign the MT_CKD foreign continuum is assumed.*

Regions where self and foreign measured (cm^{-1})	Regions where self measured (cm^{-1})
1451 - 1810	**1200 - 1981**
3481 - 3950	**3100 - 4200**
5081 - 5560	**4900 - 5700**
6861 - 7580	**6851 - 7600**

Table 7.3 The spectral regions in which the different continuums were derived from measurements

Taking these errors into account shows that although the C_GSWA predicted by this work is about 30 % more than that predicted by MT_CKD there is still a large uncertainty range. This means, rather unfortunately, that over the region as a whole is not possible to conclude whether CKD or MT_CKD provides the best estimate of C_GSWA. Using the dimer like temperature dependence with the self continuum does not have a very large impact upon the results. The reason for this will be discussed in the next section.

For the spectral regions in which both the foreign continuum and self continuum have been derived from measurements this work suggests a C_GSWA value of 0.47 Wm^{-2}. This is more than double the value of 0.18 Wm^{-2} calculated by MT_CKD and more than the 0.30 Wm^{-2} predicted by CKD. Once again this result needs to be treated with caution as there is considerable uncertainty. The lower estimated value of this work which at 0.20 Wm^{-2} is just about greater than MT_CKD.

When looking at the C_GSWA over the wider region in which the self continuum, but not necessarily the foreign continuum, has been derived from measurements, the agreement becomes better, with this work predicting a value of 0.72 Wm^{-2} compared to 0.63 Wm^{-2} of CKD. MT_CKD (0.50 Wm^{-2}), predicts a lesser value, but does still lie within the expected error. The C_GSWA when using both the dimer like temperature dependence and the MT_CKD temperature dependence fitted to this work are also presented. However, neither appears to affect the result significantly. This is because, as will be discussed, in these regions the continuum absorption is dominated by the foreign continuum.

7.6.1. The contribution to GSWA of the self and foreign continua

Table 7.4 and Table 7.5 breaks the C_GSWA result down into the self (S_GSWA) and foreign (F_GSWA) components. These are calculated by assuming that either the self or foreign continuum is included when calculating the total GSWA. In other words the S_GSWA is the difference between the GSWA calculated including both the self and foreign continuum and the GSWA calculated just including the foreign. F_GWSA is the difference between the GSWA calculated assuming both the self and foreign continua and the GWSA calculated including the self continuum

Physically this is the measure of the impact each continuum has on the GSWA. The bigger the difference between the sum of F_GSWA and S_GSWA compared to C_GSWA the less the impact of each absorber. It can be seen for the MT_CKD continuum the sum of the two contributions is 0.70 Wm^{-2} compared to 0.79 Wm^{-2} for both continuum. This suggests that the foreign continuum and self continuum in the MT_CKD model do not largely effect others output.

Focusing on S_GSWA (see Table 7.4) this work gives a wide possible range of values suggesting that the continuum could account for as little as 0.3 % of the total GWSA to as much as 3.3%. The best estimate value is towards the lower end of this range at 1.3%. When looking at the different models, it can be seen that the Ma and Tipping continuum, despite underestimating the continuum within the bands, is only around 10% lower than MT_CKD. And even though the CKD model has a larger C_GSWA, it actually has a 20 % smaller S_GSWA than that predicted by MT_CKD. The S_GSWA estimated for this work is greater than MT_CKD, with 1.3% of the total GWA value compared to 1.0% predicted by MT_CKD.

Absorber		S_GSWA (Wm^{-2}) DEC	S_GSWA (Wm^{-2}) MAR	S_GSWA (Wm^{-2}) JUN	S_GSWA (Wm^{-2}) SEP	S_GSWA (Wm^{-2}) AVG	% of GSWA
MT_CKD		0.35	0.35	0.37	0.33	0.35	1.0
CKD 2.4		0.27	0.27	0.29	0.25	0.27	0.8
Ma and Tipping		0.31	0.30	0.33	0.29	0.31	0.9
This work **Assuming MT_CKD foreign**	**Best estimate**	0.46	0.45	0.48	0.42	0.45	1.3
	Upper bound	1.18	1.17	1.18	1.10	1.14	3.3
	Lower bound	0.12	0.12	0.13	0.12	0.12	0.3
This work **Assuming this work foreign**	**Best estimate**	0.44	0.43	0.47	0.41	0.44	1.2
	Upper bound	0.98	0.96	1.04	0.91	0.97	2.7
	Lower bound	0.14	0.14	0.15	0.15	0.15	0.4
(Assuming dimer like temp)	**Best estimate**	0.50	0.49	0.52	0.46	0.49	1.4
This work **Assuming MT_CKD Foreign** **Where measured**	**Best estimate**	0.14	0.14	0.14	0.13	0.14	0.4
	Upper Bound	0.20	0.19	0.20	0.19	0.20	0.6
	Lower bound	0.09	0.09	0.09	0.09	0.09	0.3
This work **Assuming this work foreign** **Where Measured**	**Best estimate**	0.14	0.14	0.14	0.13	0.14	0.4
	Upper bound	0.20	0.19	0.20	0.19	0.20	0.6
	Lower bound	0.09	0.09	0.09	0.09	0.09	0.3
This work **Assuming this work foreign** **Assuming dimer like temp** **Where Measured**		0.16	0.16	0.17	0.16	0.16	0.5
This work **Assuming this work foreign** **Assuming fitted MT_CKD temp** **Where Measured**		0.14	0.14	0.14	0.13	0.14	0.4
MT_CKD **Where Measured**		0.16	0.16	0.17	0.15	0.16	0.5
CKD **Where Measured**		0.13	0.13	0.14	0.12	0.13	0.4

Table 7.4 The contribution to the GSWA (S_GSWA) for the spectral region 1200-8000cm^{-1} for different formulations of the self continuum. The formulation of foreign continuum assumed in obtaining this value is also stated. When 'where measured' is mentioned this refers to the spectral region where the self continuum has been measured as described in column 2 of table 7.3.

In the last section it was noted that there was a great deal of uncertainty relating to the region where the self continuum has not been derived from measurements. This is demonstrated by the larger uncertainties in the S_GSWA for all spectral regions compared to those in the regions which the continuum has been derived from measurements.

In the areas where the continuum has been derived from measurements there is good agreement between the S_GSWA of this work and MT_CKD. The table also shows the value of S_GSWA obtained using the dimer temperature dependence. This only causes a 0.2% increase in the overall GSWA value. Furthermore, when looking in the area where the self continuum is measured, the GSWA increase is less than 0.1%. Thus, overall this suggests that for the self continuum it is more important to understand the continuum absorption between the bands than the temperature dependence.

Table 7.5 shows the F_GSWA of the MT_CKD and CKD models compared to this work. It can be seen that the large difference in the C_GWSA between CKD and MT_CKD is the result of differences in the foreign continuum, with the CKD continuum predicting almost 1 % more GWSA than MT_CKD. The Ma and Tipping continuum estimates only a fifth of the absorption of CKD. The derived continuum actually predicts double the absorption of MT_CKD, although as with the self continuum, there again is considerable uncertainty in this result. The 'where measured' regions are not included here, as in regions where both the self and foreign continuum measured (i.e. in the band centres) roughly 95 % of the total absorption is due to the foreign continuum.

Absorber	F_GSWA (Wm^{-2}) DEC	F_GSWA (Wm^{-2}) MAR	F_GSWA (Wm^{-2}) JUN	F_GSWA (Wm^{-2}) SEP	F_GSWA (Wm^{-2}) AVG	% of GSWA
MT_CKD	0.37	0.35	0.33	0.34	0.35	1.0
CKD 2.4	0.72	0.67	0.66	0.67	0.68	1.9
Ma And Tipping	0.15	0.15	0.14	0.14	0.15	0.4
This work assuming MT_CKD self	0.68	0.64	0.61	0.64	0.64	1.8
This Work Best est. assuming this work self	0.69	0.65	0.62	0.65	0.65	1.8
Upper bound	1.07	1.02	0.97	1.01	1.02	2.9
Lower bound	0.15	0.15	0.14	0.15	0.15	0.4

Table 7.5 The contribution to the GSWA (F_GSWA) for the spectral region 1200-8000cm^{-1} *for different formulations of the foreign continuum. The formulation of self continuum assumed in obtaining this value is also stated.*

7.6.2. GSWA of different spectral regions

Figure 7.6 and Figure 7.7 show the S_GSWA and the F_GSWA respectively for regions that can be roughly classified as bands and in-between bands. This analysis supports that for the self continuum the regions between the bands are more important than the band centres for the absorption of solar radiation. In fact the S_GSWA contribution is almost zero in the 1400-1900 and 3400-4000 cm^{-1} regions where the continuum has been derived most accurately. The extra absorption predicted for the self continuum in this work compared to MT_CKD mainly results from the regions between 5600-7000 cm^{-1} and 1900-3400 cm^{-1}. As discussed in section 4.6, there is not that much confidence in the derived continuum in these regions, as much of these areas are based upon the an exponentially decaying curve fitted to the data nearer the band centre.

The final two columns of Figure 7.6 show the S_GSWA for the two wings regions in which it was just possible to obtain a good continuum signal from the measurements. In section 4.7 it was shown that between 3100 and 3400 cm^{-1} a dimer like feature was detected and that the continuum derived in this thesis predicted considerably greater continuum absorption than MT_CKD. This results in 0.03 Wm^{-2} S_GSWA in this region, which is double that predicted by any of the other continuum models, but still only accounts for an increase of 0.05% in GSWA. Moving away from the band centre from 4000 to 4400 cm^{-1} it was seen that the CKD, MT_CKD and the Ma and Tipping continuum all initially underestimated the amount of measured absorption and then overestimate. It appears that in general these two effects cancel each other out, with all models predicting broadly similar amounts of S_GSWA.

For the foreign continuum it can be seen (Figure 7.7) that the absorption in the bands is more significant than for the self. The bands between 5100 and 5600 cm^{-1} and between 7100 cm^{-1} and 7500 cm^{-1} contribute significantly to the total continuum absorption. As can be seen in Figure 6.10 and Figure 6.11, it is in these regions where this work does seem to suggest that there is far more spectral variation in the continuum absorption than either CKD or MT_CKD suggests, with in some regions both models underestimating the continuum and overestimating in others. However, as was stated in chapter 5, this result came from only one measurement set and there was considerable experimental uncertainty because of the weak absorption in these regions. This is reflected in the sizeable uncertainty in the foreign continuum result. The fact that CKD predicts a larger foreign continuum than MT_CKD causes a larger value of GSWA absorption in all bands. The biggest difference is observed between 5600 and

7000 cm^{-1}, where CKD predicts there should be double the absorption compared to MT_CKD.

The substantially greater solar absorption predicted between the bands above 5600 cm^{-1} by the continuum derived in this thesis compared to MT_CKD is surprising. This is because in general it was not possible to derive the foreign continuum outside of the band regions and where the foreign continuum has not been measured the MT_CKD values have been used. Hence, between the bands you would generally expect the same amount of absorption. In fact all of the difference between MT_CKD and this work between 5600 and 7000 cm^{-1} occur because of differences between 6860 cm^{-1} and 7000 cm^{-1} (i.e. the only area in this region where the foreign continuum has been derived from measurements and the MT_CKD values are not used). Likewise, the substantial difference seen between 7500 and 8000 cm^{-1} is due to differences between 7500 and 7580 cm^{-1}.

In both cases, the absorption measured is on a similar level to that of the baseline error and therefore there is great uncertainty in this result, especially between 7500 and 7580 cm^{-1}, where a very large amount of absorption is contributed over a small spectral region.

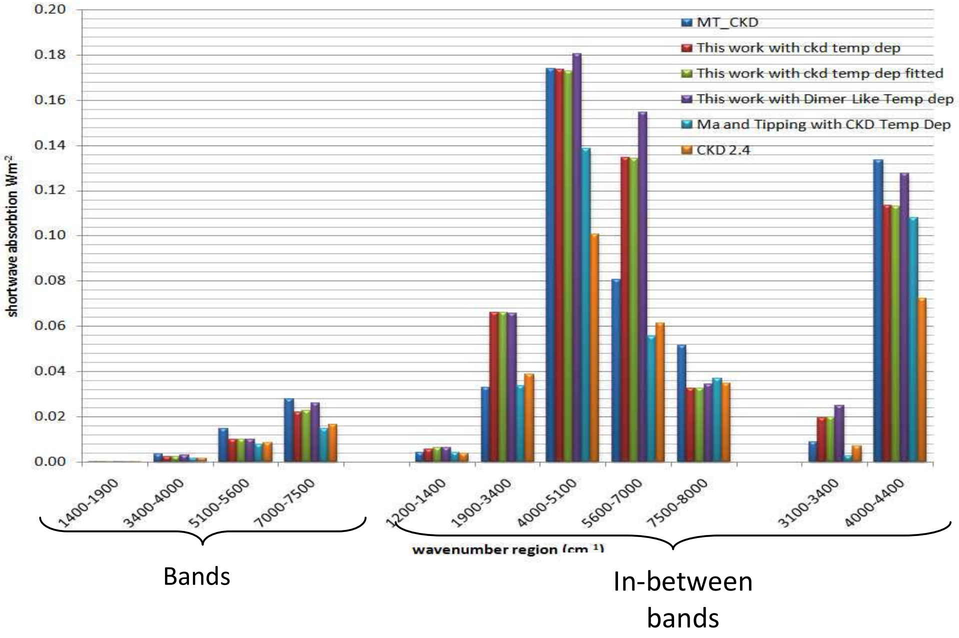

Figure 7.6 The S_GSWSA estimated for different theories and this work broken down into spectral regions that can roughly be seen as band centres and in-between the bands

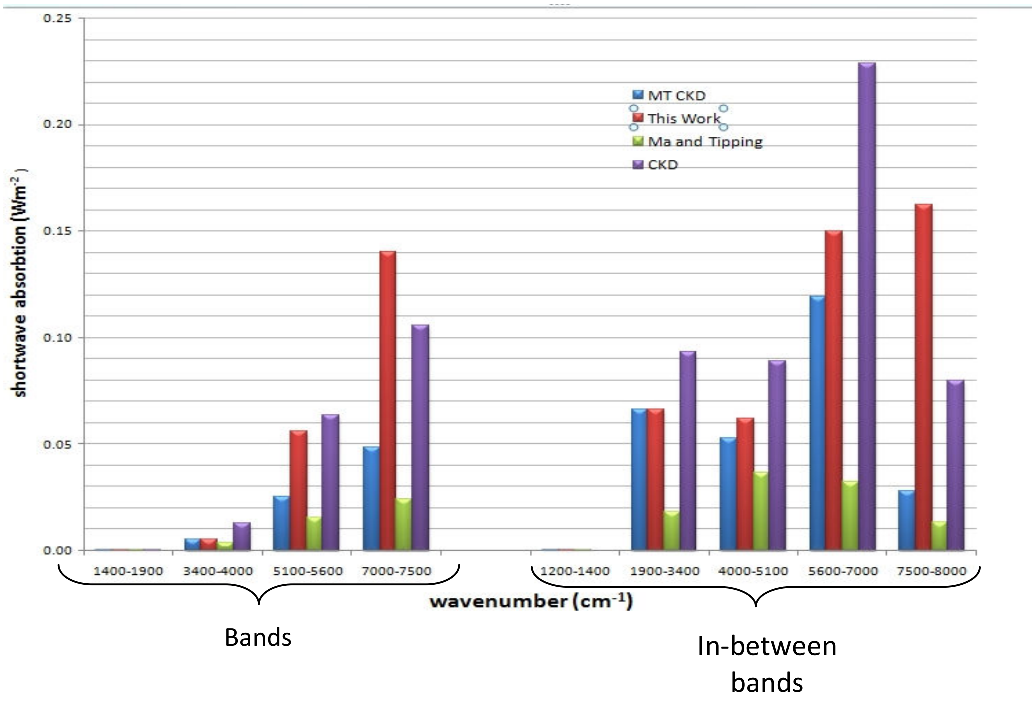

Figure 7.7 The F_GSWSA estimated for different theories broken down into spectral regions that can roughly be seen as band centres and in-between the bands .

7.6.3. Latitudinal variation

To investigate how the amount of water vapour in the atmosphere alters the contribution of the continuum it is instructive to perform shortwave calculations at a fixed zenith angle, but at different latitudes. In Figure 7.8 panel A the total shortwave absorption has been calculated assuming a solar zenith angle of 60 degrees and an albedo of 0.1 between 1200 and 16000 cm^{-1} (red upper line) and also between 1200 and 8000 cm^{-1} (green lower line). Panel B, shows for both MT_CKD and CKD the estimated continuum contribution to the total atmospheric absorption calculated in panel A between 1200 and 16000 cm^{-1}. The total continuum absorption, as well as that due to the self component is presented.

This analysis highlights the differences between CKD and MT_CKD. At high latitudes CKD predicts about 1 Wm^{-1} more absorption than MT_CKD. This is equivalent to 1.3% of the total absorption over the 1200-16000 cm^{-1} region. At the equator the difference is still about 1 Wm^{-1}, but only 0.7% of total shortwave absorption. This is due to the larger self continuum in MT_CKD cancelling out some of the differences in the foreign continuum.

Panel C shows the continuum contribution to shortwave absorption for the same atmospheric conditions as panel B, but for the 1200- 8000 cm^{-1} region.

The shortwave absorption of CKD, MT_CKD and the best estimate of the derived continuum from this work are compared. This helps to show at what latitudes the difference in GSWA predicted in the last section are important. As in Panel B, there is a relatively small difference between CKD and MT_CKD at the equator, but due to the increasing importance of the foreign continuum this become larger at higher latitudes. Because the absorption due to the foreign continuum derived in this work is of similar value to that predict for CKD and the self continuum is greater than MT_CKD that this work predicts ~30% more absorption at the equator, but at the higher latitudes, where the self continuum has little impact, it is almost identical to CKD.

Panel D shows the same as panel C, but gives the annually averaged result. This shows that the effect of the self continuum is diminished by the mixture of less water vapour in the winter and the decrease in solar zenith angle. This makes the agreement between this work and CKD better. MT_CKD appears to underestimates the total continuum absorption throughout.

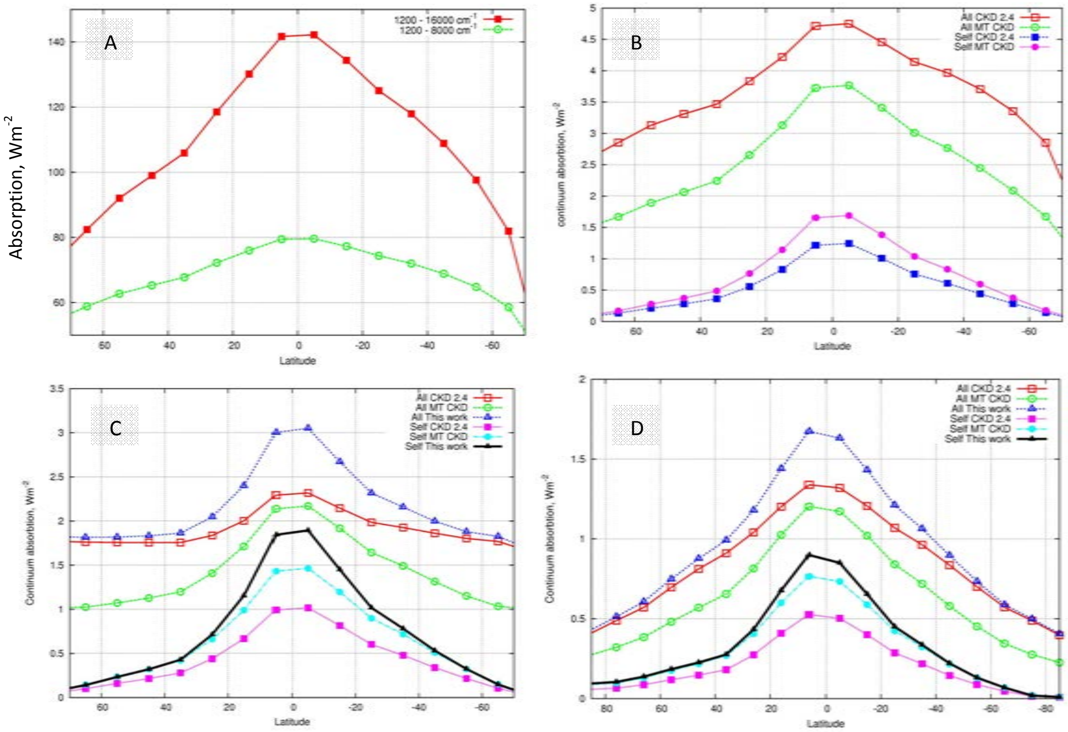

Figure 7.8 Panel A: The total shortwave absorption assuming a zenith angle of 60^o for different latitudes of the monthly mean atmosphere for March from the ERA data. Panel B: The contribution to shortwave absorption between 1200-16000 cm^{-1} as shown in panel A by the CKD and MT_CKD continuum models. The total contribution of the continuum and the self continuum contribution only is shown. Panel C: The same as Panel B, but values calculated for the spectral region 1200-8000 cm^{-1}. The estimated shortwave absorption by the continuum derived in this thesis is also shown. Panel D:The same as panel C, but estimated annually averaged values are given.

Collins et al. (2006) calculated the contribution of the continuum to shortwave absorption for different standard atmospheres (see Table 1.1) and only include water vapour in the atmosphere. They assumed a solar zenith angle of 60 degrees, an albedo of 0.1 and clear sky conditions and used the GENLN3 LBL code with the HITRAN 2000 database. They also used CKD 2.4. However, as they did not use the same atmosphere or version of HITRAN and because my work includes absorbers other than water, the results cannot be compared directly. They did detect a similar trend, with there being greater self continuum at the equator and the foreign continuum being more important at high latitudes.

7.6.4. Water dimer contribution

The derived self continuum can be compared to the predictions for water dimer absorption. Vaida et al. (2001) make use of theoretical predictions by Low and Kjaergaard (1999) and suggest a value for dimer absorption in overhead sun in the tropics between 1.6 Wm^{-2} and 3.3 Wm^{-2}. Ptashnik et al. (2004) estimate the dimer absorption for an overhead sun in tropical conditions as between 2 Wm^{-2} and 7.2 Wm^{-2}. In both of these estimates Lorentzian wings are assumed. The different bounds were obtained through changing the value of the equilibrium constant and band half-widths for the water dimer based upon the uncertainty of fitting these quantities to the dimer feature detected in the self continuum at 5330 cm^{-1}. The reason for the Ptashnik et al. upper limit being so much larger than that of Vaida et al. (2001) is mainly because they assume double the maximum value of the equilibrium constant.

Ptashnik et al. performed the dimer calculations between 1000 and 17000 cm^{-1} with an atmosphere containing 47 Kgm^{-2} of water vapour. This is similar to the 5 degree south March monthly averaged atmosphere, which has a water vapour column of 48 Kgm^{-2}. Ptashnik et al. also showed that ~90 % of dimer absorption occurs over the 1200-8000 cm^{-1} region. This means that the shortwave absorption shown at 5 degrees south can be roughly compared to values of Ptashnik et al. Both this work and Ptashnik et al. predict a similar upper value of around 7 Wm^{-2}. The best estimate of this work gives a value of 1.2 Wm^{-2} and the lower value an estimate of 0.3 Wm^{-2} , both values which are less than the lower value of 2 Wm^{-2} given by Ptashnik et al. The reason for this is because this work does not use Lorentzian bands and thus predicts far less absorption between the bands.

The upper estimate of this work does suggest that the upper value of the Ptashnik value could be correct. However, the spectral regions that contribute to this value differ greatly. This is shown in Figure 7.9, which compares the continuum coefficients (panel A) to the shortwave absorption (panel B) per wavenumber for an upper estimate of the water dimer (A(351K) = 0.015 atm^{-1}) with Lorentzian wings, MT_CKD, CKD and the best, upper and lower estimate of the self continuum derived in this for this work. This is performed for the 5 degree south March monthly averaged atmosphere. The cumulative shortwave absorption is also shown (panel C).

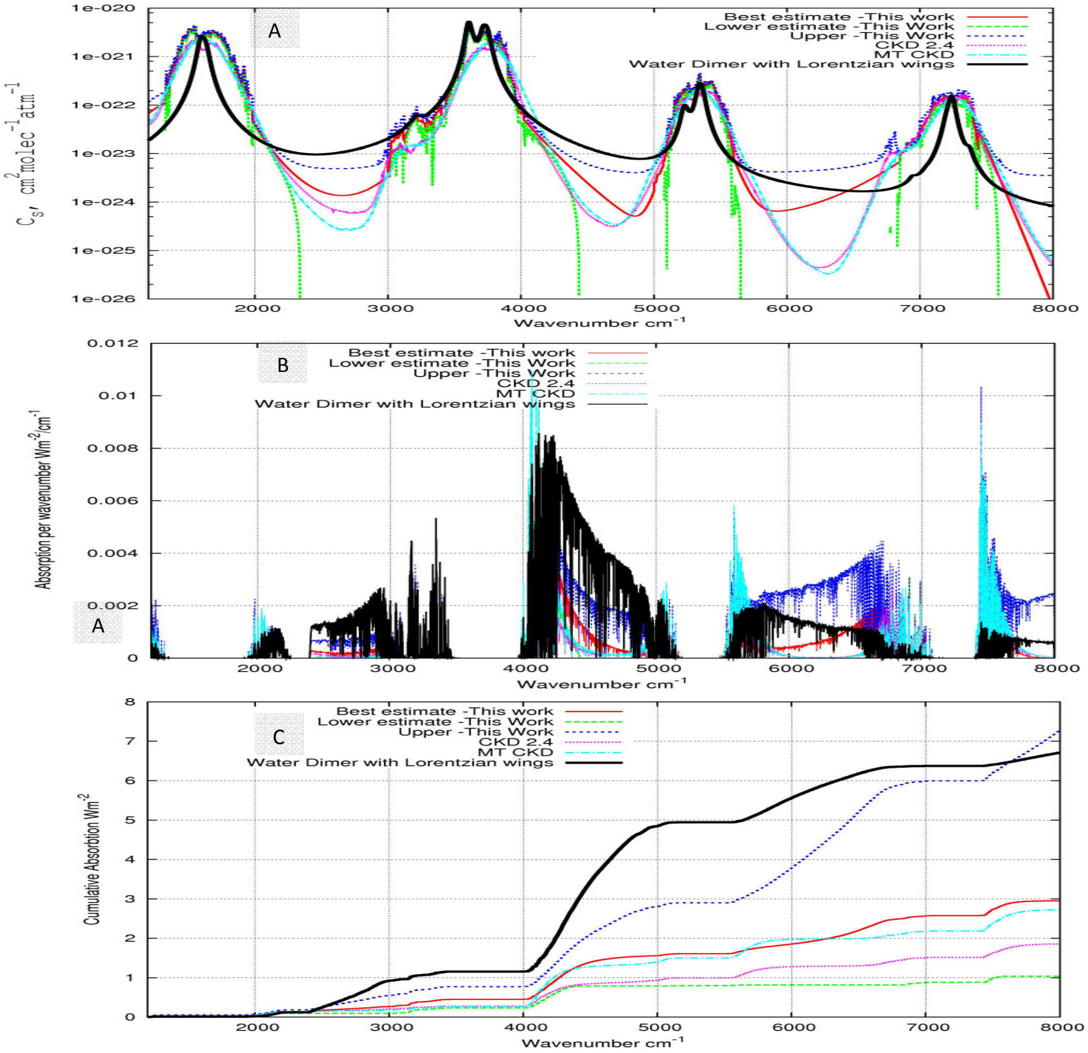

Figure 7.9 Panel A: The lower, best and upper estimate of the continuum derived in this work compared to CKD, MT_CKD and the theoretical predictions of S&K for the water dimer with a Lorentzian band shape. For the water dimer a band half-width of 30 cm^{-1} and value of A(351) =0.015 atm^{-1} is assumed (see section 4.7). For the continuum derived in this work and the water dimer, the water dimer temperature dependence as shown in Figure 7.2 is used. Panel B: The shortwave absorption per a wavenumber for the March atmosphere at 5^0 South assuming an overhead sun for each of the formulations of the continuum in Panel A and no albedo. Panel C: The cumulative absorption for panel B.

This clearly shows that, for the upper estimate of the water dimer, the majority of the absorption occurs between 4000 cm^{-1} and 5000 cm^{-1}. While, for the upper estimate of the continuum derived in this work most of absorption occurs between 5600 and 8000 cm^{-1}. This is because the upper limit of this work is based upon the estimate of the baseline error, which is constant with wavenumber. In the 5600-8000 cm^{-1} region this value is considerably greater, than even the upper dimer estimate. If one assumes that in fact the absorption in the 5600 and 8000 cm^{-1} region will be much less than the baseline error, then it is very likely that the upper value will be substantially less than 7.2 Wm^{-2}

This plot also provides a nice demonstration of how on the edge of bands (for example in the 7500-7800 cm^{-1} and 5600-5800 regions) that MT_CKD (light blue lines) suggests there should be considerably more continuum absorption than predicted by this work and other models.

7.7. Clear Sky Heating Rates

Calculating the heating rate tells us where in the atmosphere the predicted C_GWSA occurs. Figure 7.10 shows the daily shortwave heating rates for each season, calculated for all absorbers between 1200 and 8000 cm^{-1}, excluding the continuum and plotted as a function of latitude and atmospheric pressure. In general it can be seen that at around 200 mb the heating increases rapidly to a maximum at 400 mb. Below 400 mb the heating then slowly falls off towards the surface. This heating pattern can be explained by the fact that between 200 mb and 400 mb there is a significant increase in the amount of water vapour. Whilst the amount of water vapour does increase nearer the surface, because the bands are saturated there is actually a decrease in heating.

In March and September there is very little heating near the poles compared to the equator. This is because there is less water vapour in these regions, coupled with a smaller top of the atmosphere flux and shorter day length. However, in the respective summers at higher latitudes there is as much heating as at equator. Here, a mixture of a longer day length, a stronger top of the atmosphere flux and a longer path length cancels out the effect of less water vapour.

The same heating rate calculations were performed, but with the different continuum formulations included. Figure 7.11 presents the difference between the annually averaged heating rates calculated with and without MT_CKD (panel A), Ma and Tipping (panel B) and this work (panel C). As the continuum effect is quite small, these figures are in units of milli-Kelvin per day. Panel D shows the self continuum of this work used in combination with the MT_CKD foreign continuum. These plots reveal two distinct areas of heating in the atmosphere. One area is in the upper troposphere between 200 mb and 600 mb and another one nearer the surface below 800 mb. It can be shown that in these upper areas the heating is due to the foreign continuum, whilst the lower area it is due to the self continuum.

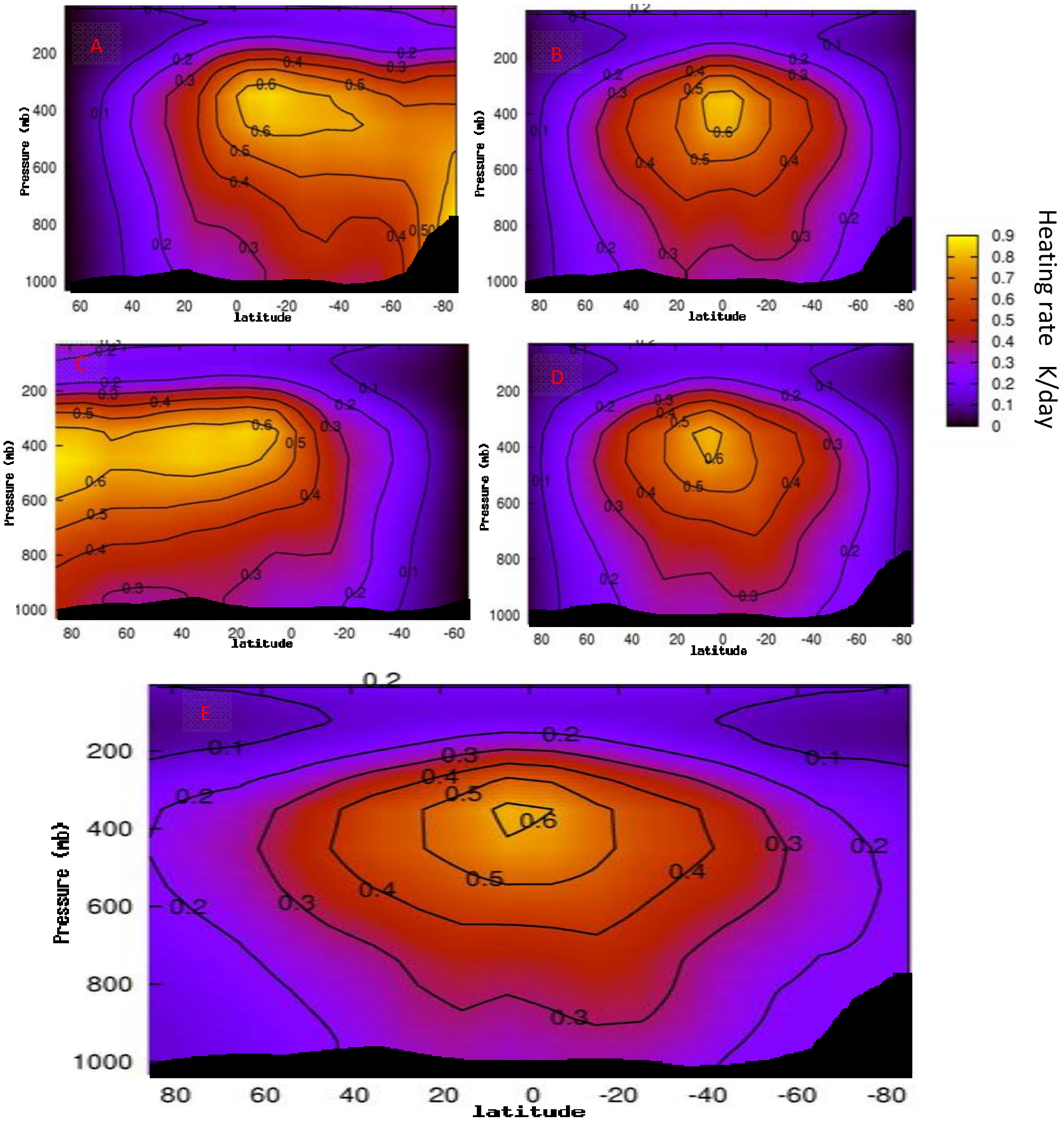

Figure 7.10 Panels A-D: The clear-sky zonal mean monthly averaged heating rate in Kelvin per day for the 1200-8000 cm^{-1} spectral region for the months of December, March, June and September respectively. Panel E : The annual average. No continuum included.

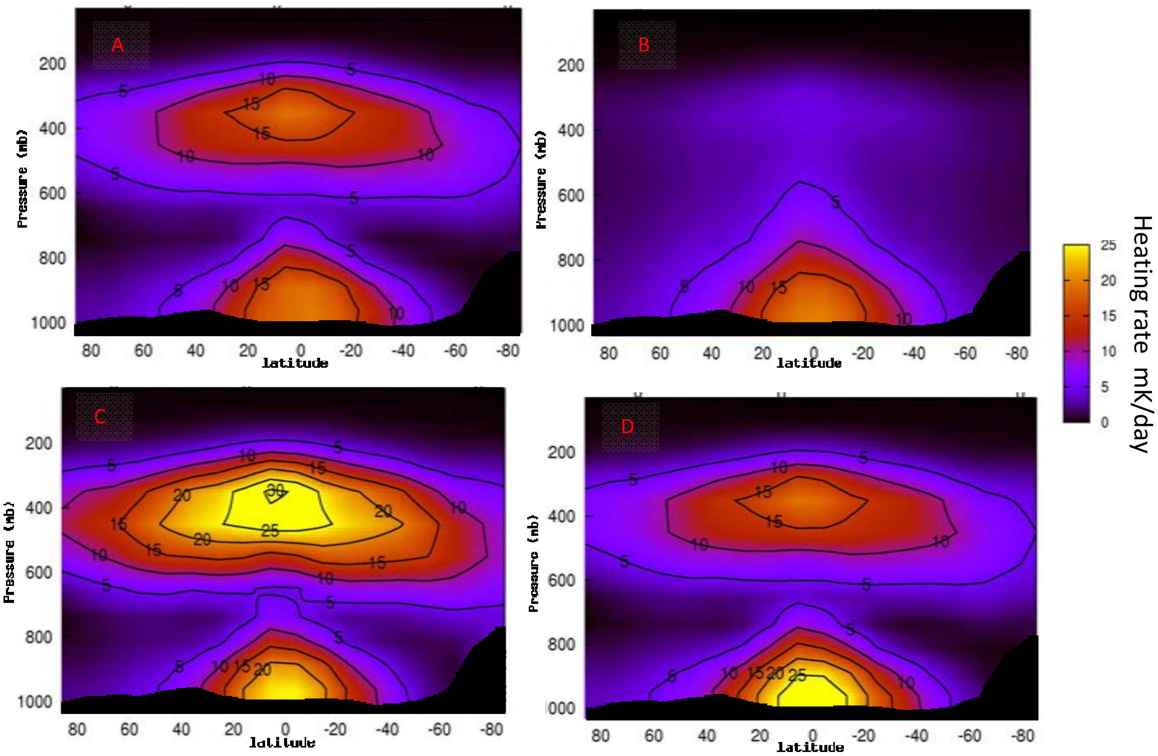

Figure 7.11 The zonal mean clear-sky annually averaged daily heating rate in mK per day for the 1200-8000 cm^{-1} spectral region of MT_CKD, the Ma and Tipping continuum and this work are shown in panel A, B and C respectively. Panel D shows the same result using this work self continuum and the MT_CKD foreign continuum.

The two separate heating features caused by the continuum can be explained by reference to Figure 7.12, which presents the optical depths and daily heating rate for the atmosphere at 5^0 south in March. Panel A shows the optical depth of all absorbers excluding the continuum for each layer and panel B shows the corresponding heating rate. Paying attention to the two bands beyond 5000 cm^{-1}, it can be seen that between 50 mb and 150 mb the optical depth in the band centres varies quite significantly over a small wavenumber region. This is because water vapour is a strong absorber; therefore the strongest lines become saturated even at very low pressures, but as the lines are very narrow this absorption does not occur over a very broad spectral region. This leads to heating occurring in these upper atmosphere regions even though there is very little water vapour.

As one moves lower in the atmosphere the amount of water vapour increases and thus, because of the saturation at the lines centres, absorption occurs further away from the line centres and the micro-windows start to become important. This can be seen to occur at pressures as low as 50 mb at the centre of the strongest fundamental bands and around 300 mb for the weaker bands above 5000 cm^{-1}. Below these levels whilst there is an increase in the optical depth there is no heating because these micro-windows are now completely saturated. This effect can be clearly observed in panel B, where there is a decrease in heating below the band centres. It should be noted that between 3400 and 3800 cm^{-1} the carbon dioxide present also leads to a great deal of saturation occurring and thus this nullifies the effect of water vapour in this region.

As the optical depth of the atmosphere between the bands is far lower, these regions start to become increasingly important for atmospheric heating nearer the surface, where there is more water vapour. Thus, it can be seen from panel B that at the surface, all of the heating results from the non-saturated wing regions away from the main band centres. Panel C shows the optical depth for each layer of the foreign continuum, while Panel D shows the corresponding heating rates per a wavenumber. Panel E and F show the same, but for the self continuum. These results show that the strongest foreign continuum absorption is in band centres beyond 5000 cm^{-1} and that while the self continuum contributes very little to heating in the band centres, it does contribute in the band wings at the surface.

Continuum absorption will be significant in regions where the water line spectrum is not already saturated. Within these regions the actual magnitude of either the foreign or self continuum contribution is controlled by its optical depth. For the self continuum the optical depth is proportional to the product of the self continuum coefficient and vapour pressure squared, whilst the foreign continuum is product of the foreign continuum coefficient, the atmospheric pressure and vapour pressure. It is this difference which explains why the two continua dominate in different regions.

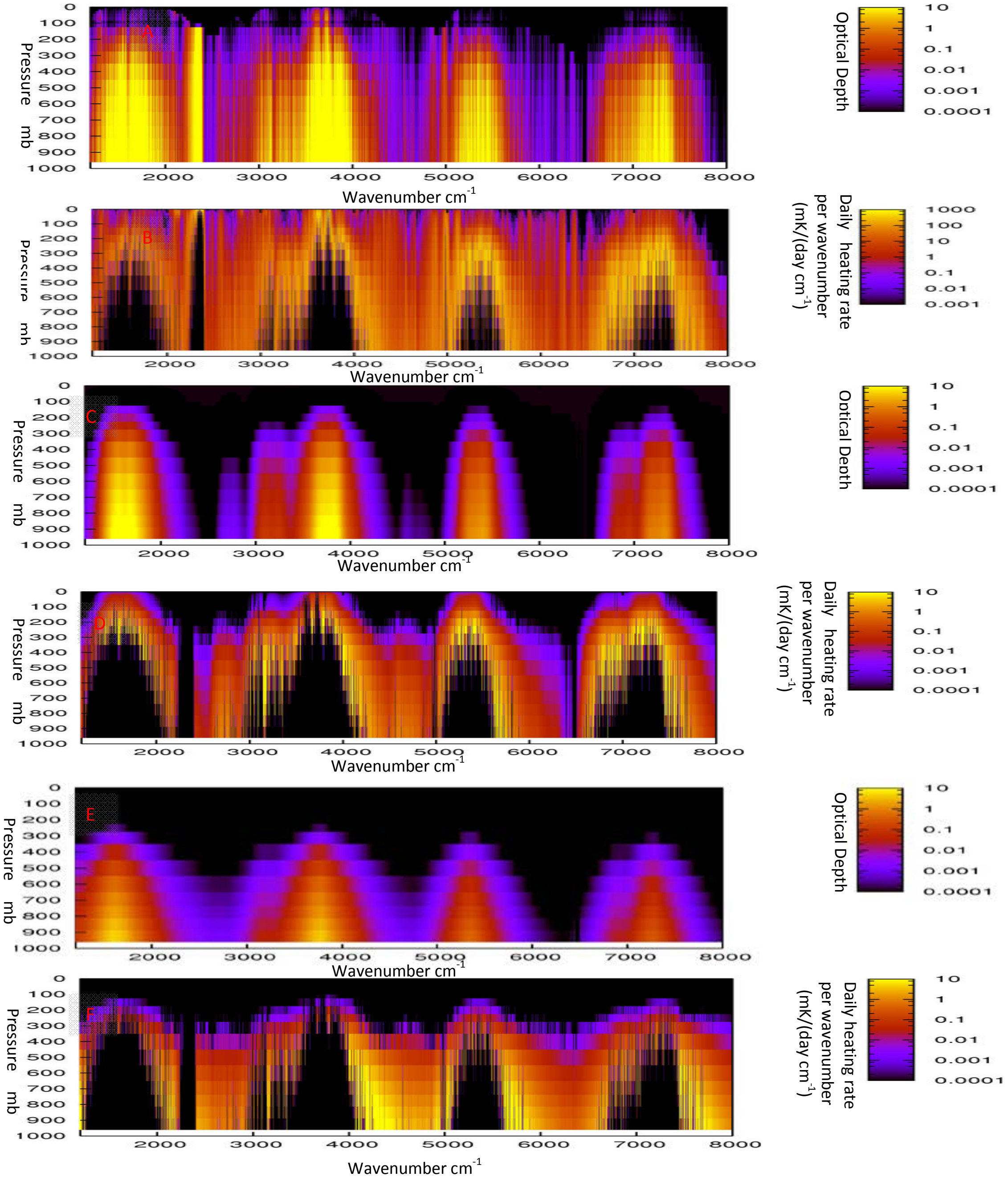

Figure 7.12 Panel A: The optical depth per wavenumber for 5^0 south in March of each layer in the atmosphere excluding the continuum. Panels B: The daily heating rate per wavenumber resulting from this atmosphere. Panel C: The predicted optical depth of the MT_CKD foreign continuum. Panel D The daily heating rate per wavenumber resulting from MT_CKD the foreign continuum. Panel E and F are the same as C and D but for the MT_CKD self continuum. All calculations for clear-sky conditions.

Consider the region of the atmosphere between 200 mb and 600 mb, here the amount of water vapour varies between about 2 mb and 0.01 mb. Because of the different scaling with optical depth of the two continua if there is 0.1 mb of water vapour and 100 mb of air then the optical depth of the foreign continuum will be still be 30 times greater, even taking into account that the foreign continuum coefficient is 30 times weaker. Hence, in these regions it is the foreign continuum in the micro-windows of bands that is dominant.

Moving further down in the atmosphere, as the water vapour increases the optical depth of the self continuum becomes significant. However, in this region the bands are already saturated and thus only between the bands can the self continuum can be effective. It can be seen that between the bands according to both MT_CKD and the Ma and Tipping continuum the self continuum coefficient is between 100 to 500 times stronger than the foreign continuum (see Figure 7.2.) Hence, consider that at an air pressure of 900 mb and vapour pressure of 20mb, if one assumes that the self continuum is 300 times the foreign, then the optical depth of the self continuum will be 10 times the foreign. This demonstrates why the self continuum is more important at the surface.

7.7.1. The differences between MT_CKD and CKD.

It was shown in section 7.6 that C_GSWA of the CKD continuum was 23% larger than that predicted by MT_CKD. When the continuum was broken into the S_GSWA and F_GSWA components it could be seen that the self component was 25% smaller in CKD than MT_CKD, but the foreign component was about 90% greater. Panel A of Figure 7.13 shows the annual mean heating rate calculated for CKD. Panel B shows the difference between CKD and MT_CKD. It can be seen that the heating rate reflects the trend in the GSWA. There is actually about 50% less heating due to the self continuum. However, it can be seen that foreign continuum is about 100% greater than MT_CKD.

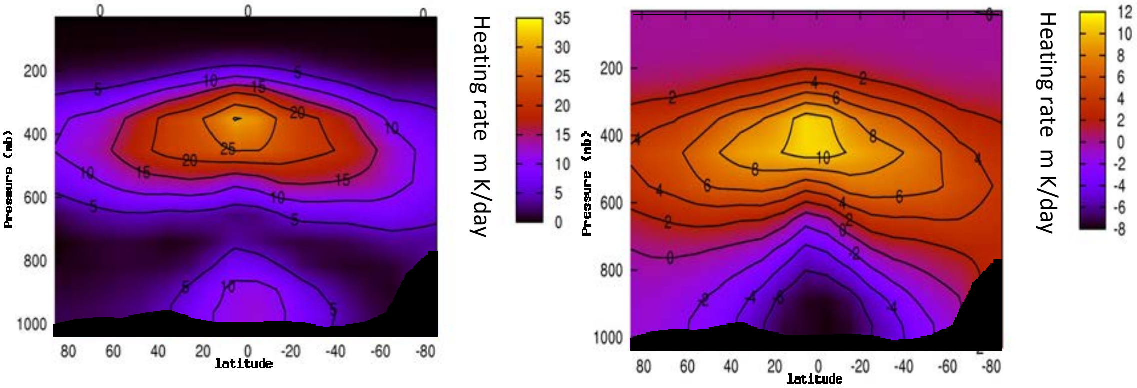

Figure 7.13 Panel A: The zonal mean clear-sky annually averaged daily heating rate in mK per day for the 1200-8000 cm^{-1} spectral region using the CKD 2.4 continuum. Panel B: As panel A, but the difference between CKD and MT_CKD (i.e. CKD – MT_CKD).

7.7.2. Seasonal variation in continuum heating rates

Figure 7.14 shows how the heating due to the continuum varies with different seasons when using the MT_CKD model. It can be seen that the foreign continuum very much mirrors the variation seen in the heating rate of water vapour. Given the arguments of the last sections this is somewhat expected, as to put it in general terms the foreign continuum absorption is important where water vapour absorption is.

The self continuum absorption does not increase as much at the poles in the respective summers as the foreign continuum. This can simply be explained by the self continuum vapour pressure squared dependence; the increase in day and path length seen at the poles not being strong enough to cancel out the decrease in absorption due to less water vapour in the atmosphere.

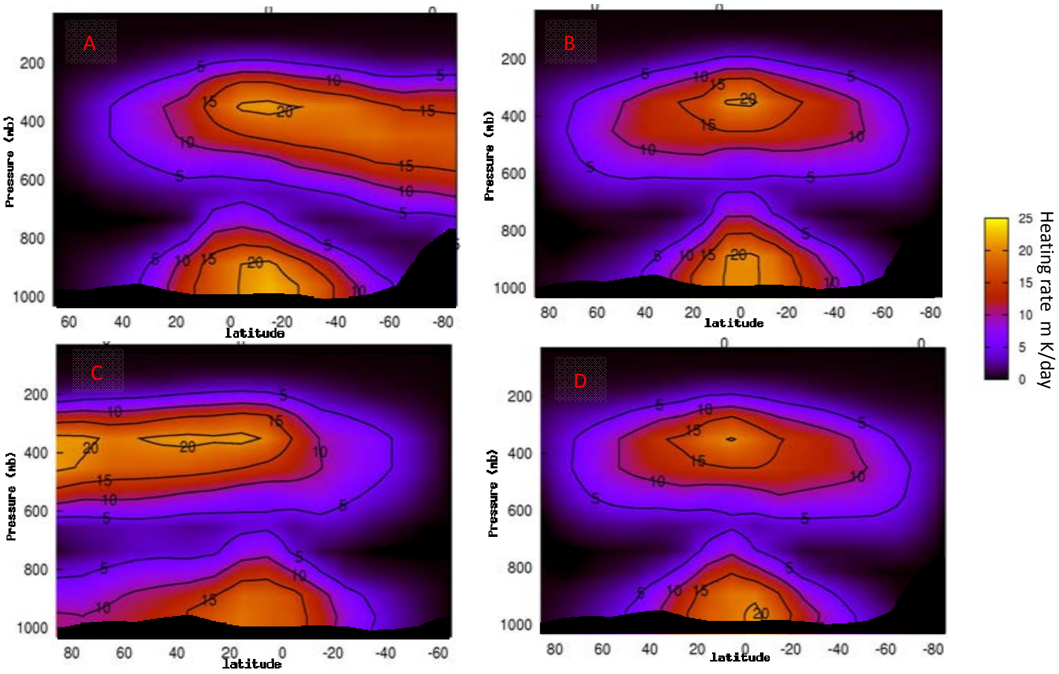

Figure 7.14 Panels A-D: The zonal mean clear-sky daily heating rate in mK per day for the 1200-8000 cm^{-1} region using the MT_CKD continuum for the months of December, March, June and September respectively.

Figure 7.15 reveals the difference between the daily heating rates calculated for this work and MT_CKD. Panel A considers the difference between the two when using both the foreign and self continua derived in this work for the month of March. Panel B has the same analysis but for June. This shows where in the atmosphere the extra C_GSWA predicted for the continuum derived from this work occurs. Panels C and D show differences using the MT_CKD foreign continuum and the self continuum derived in this work (i.e showing where the S_GSWA occurs). Likewise panels E and F show the effect of only including the foreign of this work and using the self continuum of MT_CKD (i.e showing where the F_GSWA occurs). In both cases it can be seen that while this work does predict extra absorption this generally does occurs in the same regions of the atmosphere as predicted by MT_CKD.

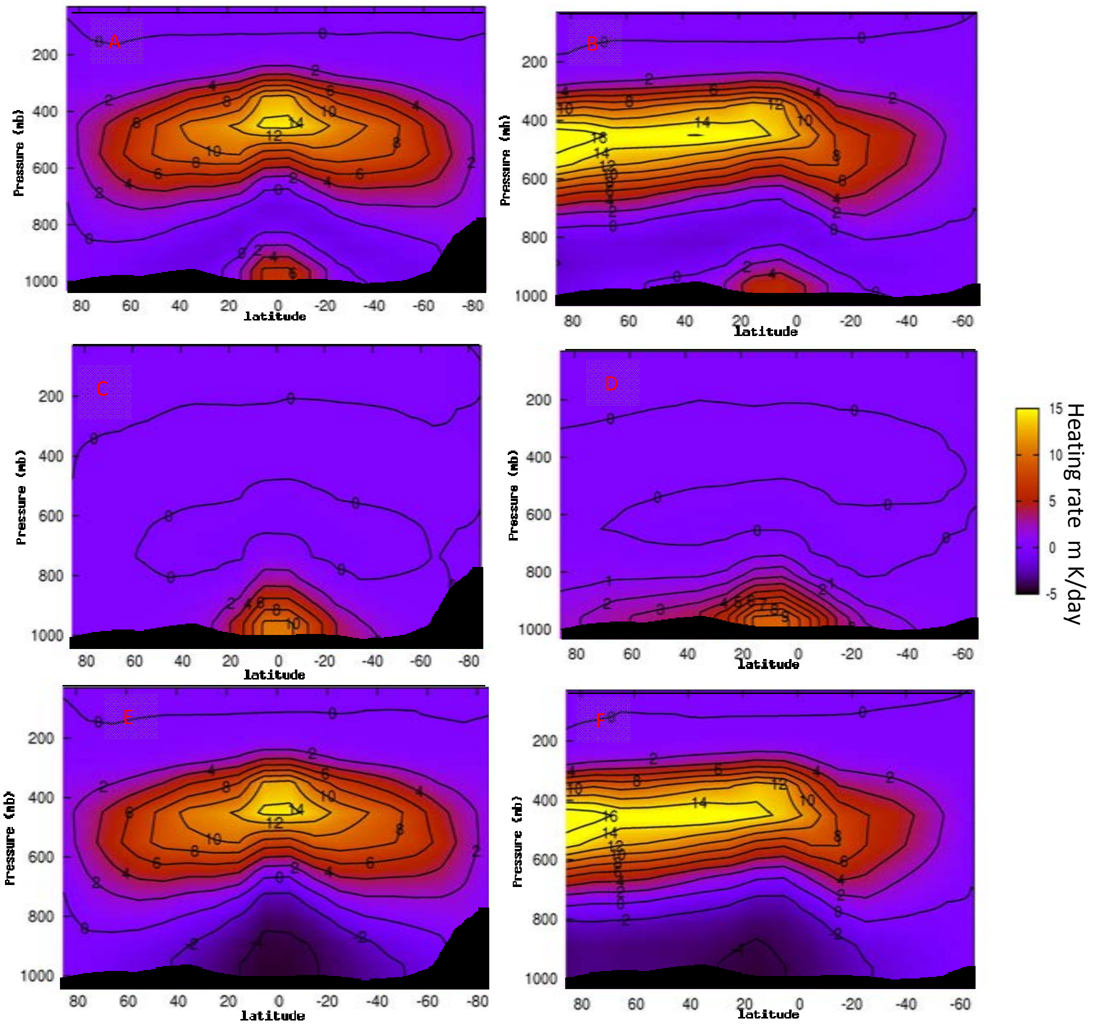

Figure 7.15 The seasonal differences in the zonal mean clear-sky daily heating rate in mK per day for the 1200-8000 cm^{-1} region zonal between this work and MT_CKD. Panels A and B show the difference between this work and MT_CKD for both the self and foreign continuum for the months of March and June respectively. Panel C and D show the same but for the self continuum only. Panels E and F show the same, but for the foreign continuum only. (note: Difference = This work – MT_CKD, i.e. positive values means this work predicts a larger value than MT_CKD.)

7.7.3. The effect of different spectral regions and errors

The derived continuum of this work predicted more heating caused by the foreign continuum than MT_CKD. As already discussed there was considerable uncertainty in F_GSWA obtained, as Table 7.3 demonstrates, the minimum value attached to this additional absorption is only very slightly greater than MT_CKD. The difference between the heating rate calculated using MT_CKD and the minimum estimate of this work assuming experimental error is presented in Figure 7.16 panel A. As expected this mirrors the F_GSWA, still showing an increase in heating. The difference though is about half of that between MT_CKD and CKD. This suggests that the slightly higher value of CKD may indeed be more realistic than MT_CKD, but more accurate measurements of the foreign continuum are required before any definite conclusions can be drawn. If anything this result can be seen as highlighting the importance of accurate measurements of the foreign continuum.

So far this analysis has focused upon the difference in the heating rates between the MT_CKD and this work over the whole spectral region between 1200 and 8000 cm^{-1}. However, as was seen in the calculations of C_GSWA, there is far more confidence in some spectral regions that others. Panel B shows for the self continuum if one looks at the difference between the heating rates predicted by MT_CKD and this work in the band centres, as defined in Figure 7.6. In these regions, where there is the most confidence in the continuum measurements, we can say very little about any corrections that need to be made to MT_CKD, as the difference in heating is very small.

Panels C and D show the difference in heating between this work and MT_CKD moving out either side of the 3700 cm^{-1} band. The reader will recall that between 3100 and 3400 cm^{-1} this work suggested that there is considerably more continuum absorption than that predicted by MT_CKD and was a feature detected that was consistent with the water dimer. Figure 7.6 tells us that in this region there was not a significant amount of S_GSWA. The magnitude of heating in Panel C reflects this result too. However, it is interesting to observe the extra absorption that results in more heating higher in the atmosphere and a slight cooling at the surface. This can be explained by considering that the dimer feature causes saturation at a higher point in the atmosphere than would otherwise be the case.

Between 3700 cm^{-1} and 4400 cm$_{-1}$ it was shown in Figure 7.6 that, despite the differences between this work and MT_CKD, when calculating the S_GSWA these cancel each other out. However, it is fascinating to see in Panel D, that the negative difference near the band centre causes less heating further up in the atmosphere, while the greater absorption further away from the band centre causes heating nearer the surface.

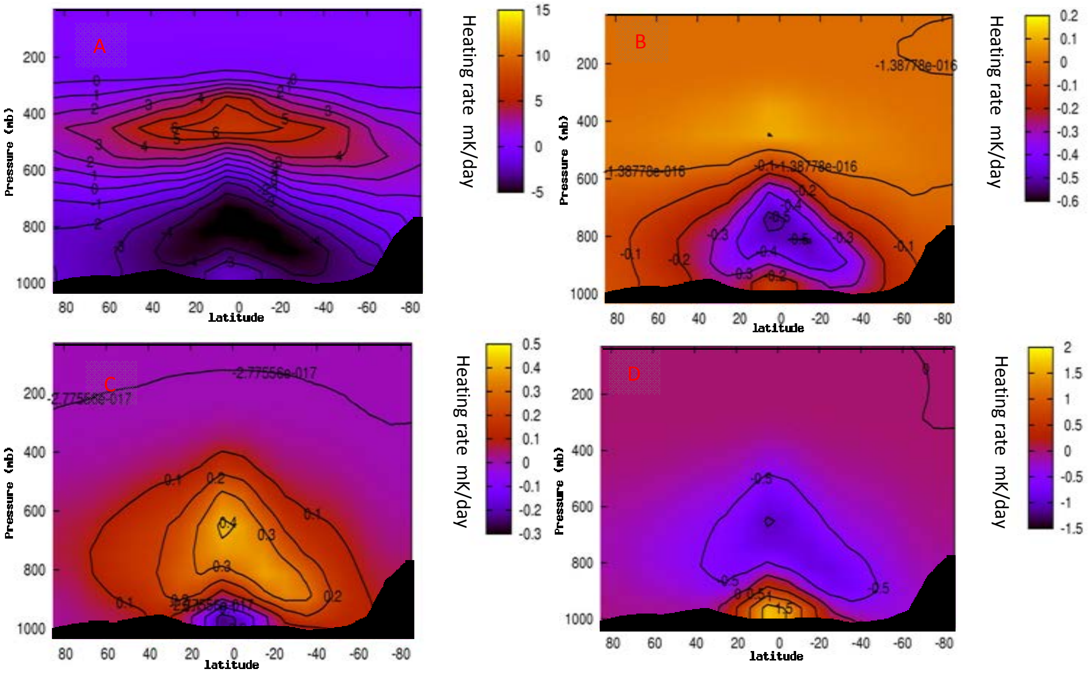

Figure 7.16. Panel A: The difference between MT_CKD and this work assuming the minimum estimated foreign continuum in the zonal mean clear-sky annually averaged daily heating rate in mK per day for the 1200-8000 cm^{-1} spectral region. Panel B: The difference between MT_CKD and this work for the self continuum in the band centres as defined in Figure 7.6. Panel C: The difference between this work and MT_CKD for the self continuum between 3100 and 3700 cm^{-1}. Panel D: The difference between this work and MT_CKD for the self continuum between 3700 and 4400 cm^{-1}. (note: Difference = This work – MT_CKD, i.e. positive values means this work predicts a larger value than MT_CKD.)

One way of seeing in detail in which spectral regions MT_CKD and this work differ is to plot the percentage difference in the heating as a function of wavenumber and height for a particular atmosphere. Figure 7.17 has this analysis for the zonal mean atmosphere at 5^{0} south in March. This reconfirms what has been observed for the GSWA; that the greatest difference is in the regions between the bands. In general it appears for the self continuum that MT_CKD seems to consistently over estimate the heating near the band centre and under estimate further away from the band. Panel B contains this analysis for the foreign continuum. This once again confirms that all of the additional heating observed in this work compared to MT_CKD is due to the two bands beyond 5000 cm^{-1}.

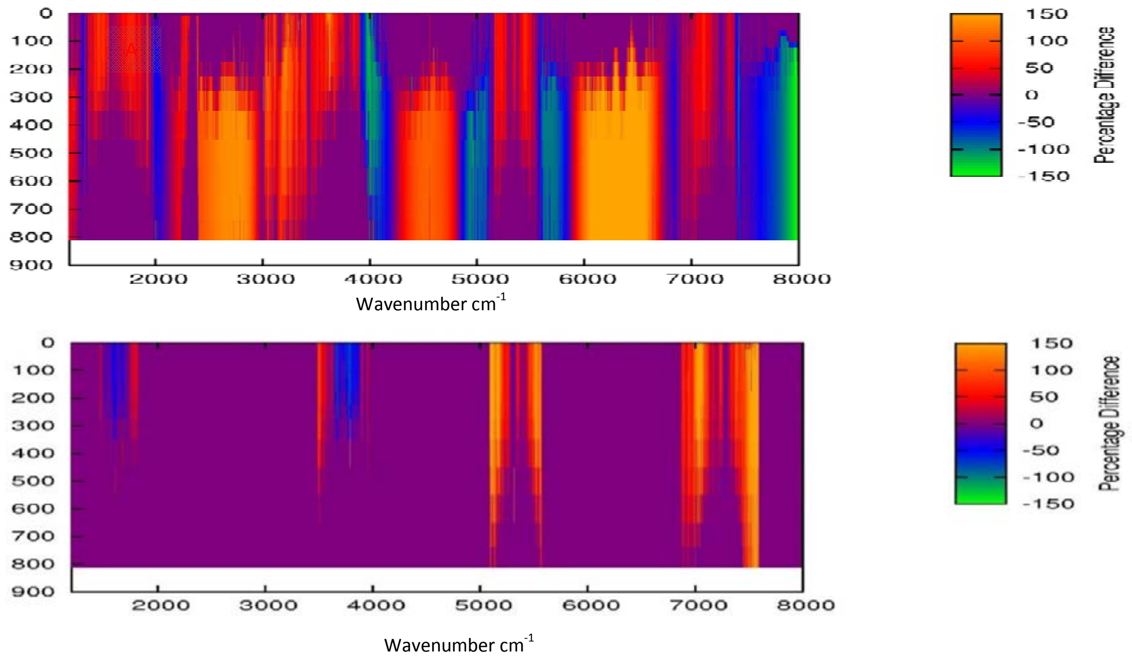

Figure 7.17 panel A The percentage difference in the clear-sky daily heating rates in a 5^0 south March atmosphere between the self continuum predicted by this work and that predicted by MT_CKD as a function of wavenumber and pressure (larger value means more heating predicted by this work). Panel B, The same as A but for the foreign continuum.

It was known that the greatest uncertainty in S_GWSA resulted from in between the bands. It was also shown that it was possible to estimate from this work an upper limit on the amount of absorption that can occur in-between the bands. Figure 7.18 Panel A shows the maximum difference between MT_CKD and this work assuming the maximum estimate for both the self and foreign continuum.

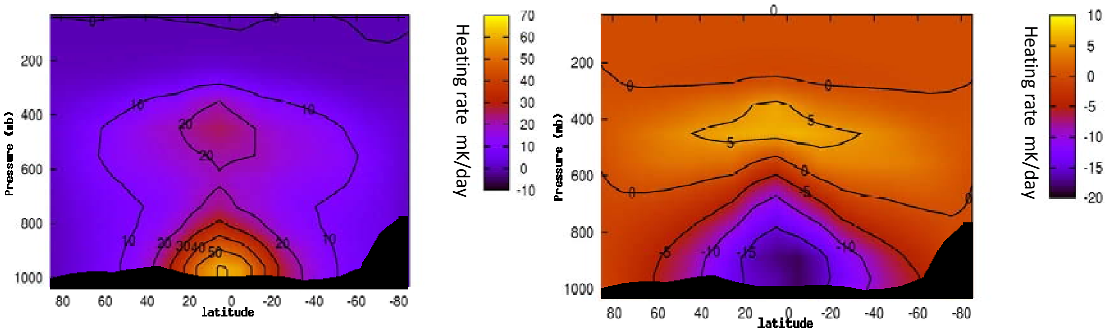

Figure 7.18. Panel A, The difference between the annually averaged daily clear-sky heating rates calculated using the maximum estimate of the continuum derived in this work and that calculated using MT_CKD. Panel B: The difference between the annually averaged daily clear-sky heating rate calculated using the minimum estimate of the continuum derived in this work and that calculated using MT_CKD. (note Difference = This work – MT_CKD, i.e. positive values means this work predicts a larger value than MT_CKD.)

This demonstrates that extra absorption will have the greatest effect in the equatorial regions where there is a large amount of water vapour. The fact that it leads to a triping of the heating predicted by MT_CKD shows how important good measurements of the continuum between the major absorption bands are.

7.7.4. The effect of different temperature dependence

It has been previously demonstrated that the temperature dependence does not have much of an effect upon the S_GSWA. Figure 7.19 shows the difference between the MT_CKD continuum used with the MT_CKD temperature dependence and with the dimer like temperature dependence. Thus, this result can be considered to show the effect of changing the temperature dependence. Whilst the change in heating is comparatively small, it is interesting to observe that, due to the stronger temperature dependence of the dimer model, there is an increase in absorption higher up in the atmosphere.

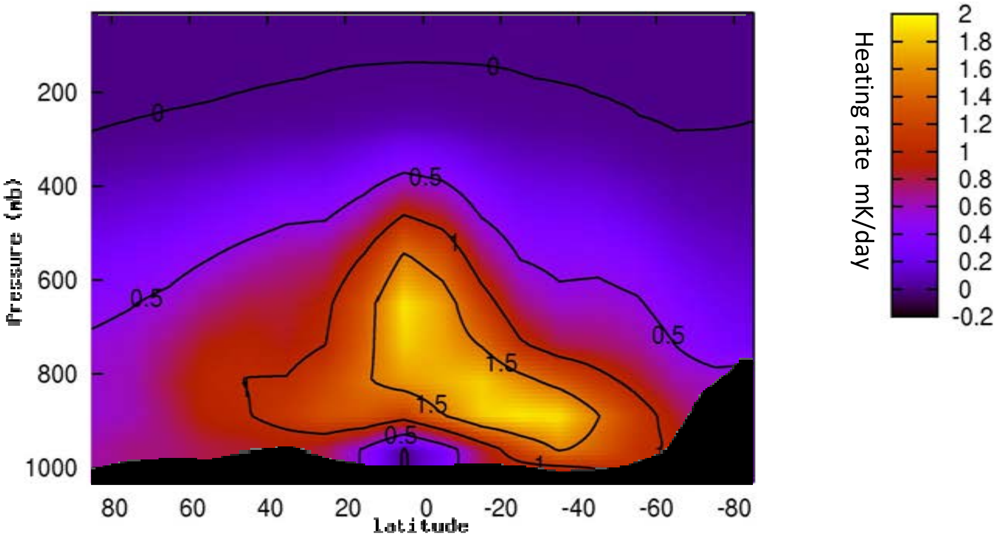

Figure 7.19. The difference between the zonal mean annually averaged clear sky heating rates calculated in 1200-8000 cm^{-1} spectral region for the MT_CKD continuum with the MT_CKD temperature dependence assumed and with the dimer like temperature dependence.

7.8. Conclusions

This chapter has investigated the magnitude of clear sky shortwave absorption and heating rates in the atmosphere within the spectral region in which the continuum has been derived. It was seen that the CKD continuum predicted that the continuum should contribute about 2.9% of the GSWA in the spectral region between 1200 and 8000 cm^{-1} compared to 2.2% for MT_CKD. This was the result of the CKD continuum predicting almost double the contribution from the foreign continuum compared to MT_CKD.

The continuum derived in this thesis suggests that the continuum should contribute 3.1% of the GSWA. However, there is a large uncertainty in this result with a minimum value of 1.3 % and a maximum value of 5.9%. This uncertainty was mainly due to not knowing the self continuum accurately between the bands. The baseline error was used for an upper estimate of the self continuum absorption. The greatest area of uncertainty resulted from the region between 5700 and 7000cm^{-1}. Here the baseline error was almost an order of magnitude greater than the expected value of absorption and thus contributed significantly. Thus, even though the upper value of the self continuum absorption was similar to that predicted by Ptashnik et al. (2004) for the water dimer with Lorentzian band shape, it was demonstrated that most of this absorption occurred in this region, rather than the 4000-5000 cm^{-1} region where Ptashnik et al. suggest. As was discussed in chapter 4 there is no evidence, apart from in the region between 3200 and 4000 cm^{-1}, that the absorption between the bands is Lorentzian in nature.

A lesser, but still significant contribution to this uncertainty is from the foreign continuum in the two bands between 5000-5600 cm^{-1} and 6900-7700 cm^{-1}. Here, due to lack of repeat measurements and the short path length at which these measurements were conducted, it was not possible to be very confident about the continuum.

When calculating the heating rates it was demonstrated that the foreign continuum contributes to heating high up in the troposphere between 200 and 800mb, whilst the self continuum was more important near the surface. The latitudinal variation in the continuum was also greater for the self continuum compared to the foreign. It was argued that both of effects are caused by the fact that the optical depth of the foreign continuum scales with the product of the pressure of water vapour and the broadening gas, while the self continuum scales with the vapour pressure squared.

8. Summary

This chapter will summarise the findings of this thesis. It aims to provide a brief summary of the results found in this work and then suggest future work that could be performed.

8.1. Conclusions

The continuum was derived by measuring the water vapour spectrum in laboratory conditions in the near infra-red at wavenumber between 1200 and 8000 cm^{-1}, with particular focus on the continuum near the centres of the absorption bands of the water molecule. A line by line code and the HITRAN 2004 database were used to calculate the line spectra for the measurement conditions. The continuum was initially derived by taking the difference between the measured and calculated spectra. However, as was shown in chapter 4, this resulted in a very noisy residual, which meant that the continuum had to be filtered. By filtering out regions near the line centres and those with an error above a certain value, a clear structured continuum was obtained in all bands.

In chapter 3, various errors affecting the continuum were discussed. It was shown that within the band centres the most significant errors were in the calculated spectra, because of uncertainties in the line half-widths and strengths as catalogued in HITRAN. Despite these errors, the continuum in many micro-windows within the bands was observed to be more than double the value of the errors. Therefore, while it can be stated that there is continuum absorption in all bands, because of these errors, it is still uncertain how much of the structure in the continuum is real and how much is the result of errors in catalogued lines.

The performance of the widely used CKD and MT_CKD models for describing the self continuum varied from band to band. In most regions the estimates of both models fell within the error bars of the derived continuum. In general it could be argued that the older CKD model actually captures the shape and magnitude of the continuum better. Within the bands perhaps the biggest failing was that neither model predicted the peaks observed at 3620 cm^{-1} and 3730 cm^{-1}.

In terms of the temperature dependence of the self continuum, over the temperature range for which the continuum was derived from measurements (296K-351K), it was shown that the form of the CKD/MT_CKD temperature dependence fitted very well to the derived continuum. The actual temperature dependence of MT_CKD (and CKD) was shown to predict the continuum derived from measurements at 296 K within the experimental errors. Once again the two notable exceptions were the peaks at 3620 cm^{-1} and 3730 cm^{-1} where a stronger temperature dependence was observed.

Overall, given that in the region between 2000 and 8000 cm^{-1} neither the CKD nor the MT_CKD model is based upon measurements the method by which they both derive the continuum (from the monomer absorption) can be seen to estimate the continuum to within a reasonable level of accuracy in most areas. It could be suggested that part of the reason for this is that by altering the water monomer absorption, albeit empirically; they are capturing something of the truth about the origins of the continuum. That is, some of the continuum may be caused by a mechanism or mechanisms related to the water monomer line absorption. Further supporting evidence for this was shown in chapter 5 where it was demonstrated that the wavenumber-integrated area under the self continuum in all of the bands was directly proportional to the integrated water monomer band strengths within experimental errors.

The possibility that the water dimer contributes to the continuum was analysed in chapter 4 and 5. The theoretical predictions of S&K were compared to the derived self continuum. The peak in the derived continuum around 3620 cm^{-1} agreed well with the predicted $|0\rangle_f|1\rangle_b|0\rangle$ transition and the 3730 cm^{-1} peak with the $|1\rangle_f|0\rangle_b|0\rangle)$ and $|01\rangle_-|0\rangle$ transitions. While, the latter peak was in a region of strong monomer absorption the former was found to be slightly red shifted away from the major monomer absorbing area, as one would expect for the dimer. In addition the peak around 5230 cm^{-1} agrees well with the $|0\rangle_f|1\rangle_b|1\rangle$ transition and that at 5330 cm^{-1} with the $1_f|0\rangle_b|1\rangle$ and $|10\rangle_-|1\rangle$ transitions.

The peak detected at 5330 cm^{-1} was about 20% smaller than that derived by Ptashnik et al. (2004). This was most likely due to a mixture of different versions of HITRAN used and the fact that in this region of the spectra, the water monomer absorption is very strong, making it highly susceptible to errors in pressure measurements. In this region a 2.5 times larger value of the A(T) scaling factor was required to fit the water dimer to the continuum than at 3620 cm^{-1}. The other significant feature detected was that at 3200 cm^{-1} which seemed consistent with the predicted $|00\rangle\ \ 2\rangle$ feature. In the 1200-2000 cm^{-1} and 6900-7500 cm^{-1} regions there was no detectable features that matched up with the S&K predictions. In addition the water dimer theory could not explain the continuum between 3800 and 4000 cm^{-1} or between 5400 and 5600cm^{-1}.

The temperature analysis was inconclusive in terms of suggesting what is the major contributing mechanism to the continuum. It can be said for certain that the temperature dependence of the continuum is far greater than the temperature dependence given for water vapour lines in HITRAN 2004. Both the dimer and the CKD form of temperature dependence were seen to fit to the derived continuum very well in all bands. As was shown in chapter 7, a difference between these two forms will only be detectable over a larger temperature range than was measured here.

It can also be said that there is a noticeable spectral dependence in this temperature dependence with, in general, there being a stronger negative temperature dependence where the continuum is strongest. However, due to large uncertainties in the spectra calculated using HITRAN, how much of this variation is real and how much is a product of errors in the lines in HITRAN remains to be seen.

It was suggested that if the continuum was the result of the water dimer, it would be expected that there would be a spectrally-independent component of the temperature dependence relating to the equilibrium constant and another spectrally-varying component that is the result of the lower state energy (and perhaps the line shape). If a value for the equilibrium constant was assumed, it was shown that this spectral variation was more significant than would be expected from the variation caused by the lower state energy of the dimer. That is, of course, assuming that the water dimer has a lower state energy which is similar to the monomer. Furthermore, in the 1200-2000 cm^{-1} region, the magnitude of the lower state energy term was twice as big as in the other regions.

Such a result does not mean that the water dimer is not a significant contributor to the continuum. This difference could be because the water dimer theory is more complex than has been suggested here. The reader should also recall that in the 1200-2000 cm^{-1}, 5000-5600 cm^{-1} and 6900-7500 cm^{-1} regions measurements have only been conducted at 3 temperatures. Therefore, measurements are required at more temperatures to investigate these trends further.

Presently, it can be said that the evidence suggests that the self continuum is not solely the result of the water dimer. The two clearest dimer features detected at 3200 cm^{-1} and 3620 cm^{-1} are those which were shifted away from the monomer absorption. As already mentioned the A(351 K) value used to fit these features was 0.008 atm^{-1} compared to 0.020 atm^{-1} required to get some agreement between continuum and dimer other regions. It appears then that the regions with the clearest water dimer signature require less water dimer abundance to explain the feature. One way of explaining this maybe to assume that there is some other, presently unknown, mechanism which is roughly proportional to the water monomer absorption also contributes to the continuum in addition to the dimer. Therefore, in the regions shifted away from the water monomer absorption we can assume that the dimer is the major contributor to the continuum and thus the abundances predicted in these regions are close to reality. However, in the some regions A(351 K) has an artificially large value caused by it being fitted to some of the continuum which is the result of this unknown monomer mechanism. Even when assuming a value of 0.008 atm^{-1} for A(351 K), at certain wavenumbers the dimer absorption will be still be detectable . Hence, the peaks observed at 3730 cm^{-1} 5250 cm^{-1} and 5330 cm^{-1} could be well dimer features observed in addition to this monomer mechanism. This might also explain why the temperature dependence around these peaks is slightly stronger than in other regions.

Of course this suggestion still leaves many questions which need to be answered. What is the cause of this mechanism related to the monomer absorption? Why are either the equilibrium constant or the dimer band strengths less than theory currently suggests? How does the influence of these dimer transitions decrease away from the band centre?

As was clearly demonstrated in chapter 7, it is the continuum between the bands that is most important for quantifying the effect of the continuum on atmospheric radiation. Even though it was not possible to measure accurately all of these regions certain conclusions can still be drawn. Firstly, the MT_CKD continuum overestimates the size of the continuum at the far edge of each absorption band between 3950 – 4150 cm^{-1}, 5500-5700 cm^{-1} and 7400-7600 cm^{-1}. This to a lesser extent was also seen to be case with the CKD and Ma and Tipping continua. Second, that all three continuum models considerably underestimate the absorption between 3100 cm^{-1} and 3700 cm^{-1}. Third, that the continuum 'wings' are not Lorenzian, and to assume a Lorentzian will overestimate the amount of shortwave absorption observed in the atmosphere by up to a factor of 2.

With less confidence it could be suggested that as one moves even further away from the bands that all three models underestimate the amount of continuum absorption. However, due to the weakness of the signal in these regions, this could just be an artefact of the baseline errors.

The foreign continuum was also derived in this work, although it was subject to much less attention. Due to the weaker foreign continuum signal, there was far less confidence especially in the two bands above 5000 cm^{-1}. In fact it was shown that the errors due to HITRAN were of a similar level to the derived continuum. However, a clear positive continuum was observed in all bands. In the 1200-2000 cm^{-1} and 3400-4000 cm^{-1} regions both CKD and MT_CKD appeared to overestimate the continuum by around 20%.

Rather unfortunately, it was not possible for this work to significantly improve our estimates of the shortwave continuum absorption. This was because between the bands, which is the most important region for continuum absorption, there is the least confidence in the continuum derived in this work.

8.2. Future work

Future work can be split into two sections. Firstly there is the question of what can be done to improve the quality of the measured continuum. Secondly there is the question of what theoretical steps need to be taken to improve our understanding of the mechanisms behind the continuum. Of course to some degree these two processes are related to each other. Better measurements of the continuum will aid the theoreticians in postulating various continuum processes, while better theoretical studies will help to improve some of the uncertainties in the measurements.

In terms of improving the measurements, it was very apparent from the results presented in this thesis that the experimental setup was not adequate to obtain properties of the continuum which are important firstly when calculating shortwave absorption and secondly when attempting to attribute a mechanism to the continuum. It could be argued that for both of these processes, that the continuum has to be accurately measured in the band centres and in-between the bands over the entire solar spectrum from 1200-16000 cm^{-1} where water vapour is a significant absorber. One also needs to obtain the temperature dependence of the continuum accurately over a wide range of temperatures.

If it is assumed that due to baseline errors there will always be an uncertainty in the measured optical depth of 0.01, then if the continuum is to be derived to a reasonable level of confidence a minimum optical depth of about 0.05 would be required. With the current experimental set up with a path length of 19.3 m at maximum pressure of 275 mb it was only possible to accurately measure the self continuum to a value of $2x10^{-23}$ $cm^2.molec^{-1}.atm^{-1}$. In the spectral region 1200-8000cm^{-1} MT_CKD and CKD suggests that the continuum is as small as 2x10^{-25} cm^2.molec^{-1}.atm^{-1}. In order to measure values this small there are two options; either increase the temperature enough to allow enough water vapour in the cell and/or increase the path length to increase the signal suitably.

To increase the optical depth 200 times would require a vapour pressure of around 3850 mb with the current path length. In order to obtain this pressure one would need a temperature of at least 425 K. However, one has to remember that the continuum will most likely be weaker at this temperature, so possibly even more water vapour will be needed. In this case a possible future measurement strategy would be to derive the continuum at numerous temperatures above 425 K and then attempt from this to extrapolate the continuum to lower temperatures, assuming that a function can be easily fit to the data.

A more ideal option would be to measure at lower temperatures, but to increase the path length. However, this may not be feasible. For instance at 296 K the maximum pressure in the cell is 20mb; at this pressure to achieve an optical depth of 0.05 for an area of the continuum with strength 1x10^{-24} cm^2.molec^{-1}.atm^{-1} a path length of about 40 km is required. This is much larger than the path lengths achievable with a laboratory based cell.

This suggests that in order to achieve measurements between the bands a more sensitive method such as cavity ring down spectroscopy is required to measure the continuum. Successful continuum measurements have been performed before in other regions using this technique (e.g. Cormier et al. 2005) Although this technique can not cover such a broad spectral range as FTS measurements, it has been shown that between the bands the continuum does decrease in a smooth manner. Therefore, measurements could be conducted at quite broad spectral intervals, say every 100 wavenumber and then a curve could be fitted between the derived values.

In terms of the foreign continuum, obtaining good continuum measurements is not quite as demanding. This firstly is because the foreign continuum is more important in the bands, and secondly because the amount of air in the cell is not limited by temperature. Still at 296 K to measure a continuum of strength 1x10^{-25} cm^2.molec^{-1}.atm^{-1} a path length of 6 km is required, assuming there is 20 mb of water vapour and 2000 mb of broadening gas. Due to these requirements, atmospheric measurements could be a good way of estimating both the self and foreign continuum in the regions of weaker absorption.

When deriving the continuum within the bands, the most significant errors are those from HITRAN. For the self continuum these do not affect the atmospheric effects of the continuum that much, because here the self continuum is most important away from the bands. However, in terms of trying to understand the mechanisms behind the continuum, these errors are quite significant. Even for the clearest dimer feature around 3620 cm^{-1}, the errors due to HITRAN caused considerable uncertainties. The biggest problem is for the features in the stronger areas of absorption at 3730 cm^{-1} and 5350 cm^{-1}. Here the errors in HITRAN can be seen to cause a 50% uncertainty in the result. There are numerous smaller deviations in the continuum which could well be water dimer features, but this cannot be said with any confidence until these uncertainties are resolved.

For the foreign continuum, due to its weaker nature, the errors due to HITRAN are even more significant. As in the bands the foreign continuum has a greater effect upon atmospheric calculations, this means that in these regions accurate information about the line absorption of the monomer is vital. Another area which has not been investigated in this thesis is the possibility of water complexes like H_2O-N_2. This was mainly because there exists very little in the literature about the possible contribution of these complexes.

Another area where improvement is needed is in understanding the water monomer line shape. While Ma and Tipping do model the far wings accurately beyond 25 cm^{-1} there has currently been no detailed theoretical assessment of the suitability of the Lorentzian to describe the water monomer absorption between 1 cm^{-1} and 25 cm^{-1} from the line centre. The magnitude of collision induced absorption in water vapour also needs to be investigated further.

For the water dimer, more theoretical work is also required. Perhaps the area of greatest uncertainty is the shape and temperature dependence of the bands, an area in which there is presently no published work. Another useful improvement would be more detailed ro-vibrational calculations of the spectrum of the water dimer. Whilst there has been a significant amount of work on the equilibrium constant, there is still considerable disagreement in as to the value. A repeat of the Curtiss et al. (1979) work would perhaps be a good starting point to further constrain the possible range of values.

In summary, by improving the accuracy of measurements and HITRAN the confidence in the continuum can be improved. If in parallel our understanding of the three main possible contributors (monomer line shape, CIA and water complexes) to the continuum also improves, it should be possible to be a lot more confident about what contributes to the continuum in different regions. The first steps towards these improvements are being taken by the newly formed NERC-EPSRC CAVIAR consortium. This will combine FTS measurements in the laboratory, from the surface and from an aircraft with laboratory cavity ring down measurements to derive the continuum from the far infrared to the visible spectral region over as wide a temperature range as possible. Ultimately the aim is to offer an alternative to the CKD continuum which is based on measurements in all regions. In addition theoretical work on the water monomer and dimer will be performed to achieve better understanding of the sources of the continuum.

Finally, the shortwave heating calculations presented in this thesis could be made more complete. Firstly they only investigated the effect of the continuum over a narrow wavenumber range (1200 – 8000 cm^{-1}). Secondly the range of climate conditions for which the continuum was studied for was limited, with only zonal-mean calculations performed for 4 months of the year for the current climate. The next logical step would be investigate how in a warmer climate the effect of the continuum changes. Since climate models indicate that relative humidity may stay constant as the climate warms, the continuum may play an increasingly important role in a warmer climate.

The model used here was also relatively simple; it would be interesting to see if the effect of the continuum was changed if the atmosphere was modelled in a more realistic manner. For example the effects of aerosol dust, scattering and clouds could be included into the calculations. Another area which was not covered in this work was to look at the effect that errors in HITRAN have on the shortwave absorption by the continuum. This work also only looked at the effect of static radiation phenomena like heating rates and fluxes, the impact on temperatures and circulations could also be investigated using GCMs.

-*-*-*THE END*-*-*-

Bibliography

Arking, A. (1996). "Absorption of Solar Energy in the Atmosphere: Discrepancy between Model and Observations." Science **273**(5276): 779-782

Arking, A. (1999). "Bringing Climate Models into Agreement with Observations of Atmospheric Absorption." Journal of Climate **12**(6): 1589-1600

Atkins, P. W. and R. S. Friedman (2005). Molecular Quantum Mechanics Oxford, Oxford University Press.

Bevington, P. R. (1969). Data Reduction and Error Analysis for the Physical Sciences, McGraw-Hill.

Bignell, K. J. (1970). "Water-Vapour Infra-Red Continuum." Quarterly Journal of the Royal Meteorological Society **96**(409): 390-&

Borysow, A. and L. Frommhold (1986). "Collision-Induced Rototranslational Absorption-Spectra of N_2-N_2 Pairs for Temperatures from 50 K to 300 K." Astrophysical Journal **311**(2): 1043-1057

Braly, L. B., K. Liu, M. G. Brown, F. N. Keutsch, R. S. Fellers and R. J. Saykally (2000). "Terahertz Laser Spectroscopy of the Water Dimer Intermolecular Vibrations. Ii. $(H_2o)_2$." Journal of Chemical Physics **112**(23): 10314-10326

Burch, D. E. (1982). "Continuum Absorbtion by H_2o." Tech. Rep. AFGL-TR-81-0300

Burch, D. E. (1984). "Continuum Absorption by H_2o in the 700 -1200cm^{-1} and 2400-2800 Cm^{-1} Windows " Tech. Rep. AFGL-TR-84-0128

Burch, D. E. (1985). "Absorption by H_2o in Narrow Windows between 3000-4200 Cm^{-1}." Tech. Rep. AFGL-TR-85-0036

Cess, R. D., M. H. Zhang, P. Minnis, L. Corsetti, E. G. Dutton, B. W. Forgan, D. P. Garber, W. L. Gates, J. J. Hack, E. F. Harrison, X. Jing, J. T. Kiehl, C. N. Long, J. J. Morcrette, G. L. Potter, V. Ramanathan, B. Subasilar, C. H. Whitlock, D. F. Young and Y. Zhou (1995). "Absorption of Solar-Radiation by Clouds - Observations Versus Models." Science **267**(5197): 496-499

Chylek, P., Q. Fu, H. C. W. Tso and D. J. W. Geldart (1999). "Contribution of Water Vapor Dimers to Clear Sky Absorption of Solar Radiation." Tellus Series a-Dynamic Meteorology and Oceanography **51**(2): 304-313

Clough, S. A., F. X. Kneizys and R. W. Davies (1989). "Line Shape and the Water Vapor Continuum." Atmos. Res **23**: 229–241

Collins, W. D., J. M. Lee-Taylor, D. P. Edwards and G. L. Francis (2006). "Effects of Increased near-Infrared Absorption by Water Vapor on the Climate System." Journal of Geophysical Research-Atmospheres **111**(D18).D18109

Artn d18109

Cormier, J. G., J. T. Hodges and J. R. Drummond (2005). "Infrared Water Vapor Continuum Absorption at Atmospheric Temperatures." Journal of Chemical Physics **122**(11).114309

Artn 114309

Coudert, L. H. and J. T. Hougen (1990). "Analysis of the Microwave and Far Infrared-Spectrum of the Water Dimer." Journal of Molecular Spectroscopy **139**(2): 259-277

Curtiss, L. A., D. J. Frurip and M. Blander (1979). "Studies of Molecular Association in H_2o and D_2o Vapors by Measurement of Thermal-Conductivity." Journal of Chemical Physics **71**(6): 2703-2711

Daniel, J. S., S. Solomon, H. G. Kjaergaard and D. P. Schofield (2004). "Atmospheric Water Vapor Complexes and the Continuum." Geophysical Research Letters **31**(6).L06118

Artn l06118

Daniel, J. S., S. Solomon, R. W. Sanders, R. W. Portmann, D. C. Miller and W. Madsen (1999). "Implications for Water Monomer and Dimer Solar Absorption from Observations at Boulder, Colorado." Journal of Geophysical Research-Atmospheres **104**(D14): 16785-16791

Denbigh, K. G. (1981). The Principles of Chemical Equilibrium. Cambridge, Cambridge University Press.

Dianovklokov, V. I., V. M. Ivanov, V. N. Arefev and N. I. Sizov (1981). "Water-Vapor Continuum Absorption at 8-13 Um." Journal of Quantitative Spectroscopy & Radiative Transfer **25**(1): 83-92

Drayson, S. R. (1976). "Rapid Computation of Voigt Profile." Journal of Quantitative Spectroscopy & Radiative Transfer **16**(7): 611-614

Dudhia, A. (2005). "Reference Forward Model Version 4: Software User Manual, Http://Www.Atm.Ox.Ac.Uk/Rfm."

Elsasser, W. M. (1938). "Far Infrared Absorption of Atmospheric Water Vapor." *APJ* **87**: 497-507

Fraser, G. T., R. D. Suenram and L. H. Coudert (1989). "Microwave Electric-Resonance Optothermal Spectroscopy of $(H_2o)_2$." Journal of Chemical Physics **90**(11): 6077-6085

Frommhold, L. (1993). Collision Induced Absorption in Gas. Cambridge, Cambridge University.

Gamache, R. R. and J. Fischer (2003). "Half-Widths of (H2o)-O-16, (H2o)-O-18, (H2o)-O-17, (Hdo)-O-16, and (D2o)-O-16: I. Comparison between Isotopomers." Journal of Quantitative Spectroscopy & Radiative Transfer **78**(3-4): 289-304

Gamache, R. R. and J.-M. Hartmann (2004). "Collisional Parameters of H_2o Lines: Effects of Vibration." Journal of Quantitative Spectroscopy and Radiative Transfer **83**(2): 119-147

Gamache, R. R. and J. M. Hartmann (2004). "An Intercomparison of Measured Pressure-Broadening and Pressure-Shifting Parameters of Water Vapor." Canadian Journal of Chemistry-Revue Canadienne De Chimie **82**(6): 1013-1027

Goody, R. M. and Y. L. Yung (1989). Atmospheric Radiation: Theoretical Basis Oxford, Oxford University Press.

Gordon, I. E., L. S. Rothman, R. R. Gamache, D. Jacquemart, C. Boone, P. F. Bernath, M. W. Shephard, J. S. Delamere and S. A. Clough (2007). "Current Updates of the Water-Vapor Line List in Hitran: A New "Diet" For Air-Broadened Half-Widths." Journal of Quantitative Spectroscopy & Radiative Transfer **108**(3): 389-402

Griffiths, P. R., De Haseth, J.A. (1986). Fourier Transform Infrared Spectrometry. London, Wiley.

Harvey, A. H. and E. W. Lemmon (2004). "Correlation for the Second Virial Coefficient of Water." Journal of Physical and Chemical Reference Data **33**(1): 369-376

Held, I. M. and B. J. Soden (2000). "Water Vapor Feedback and Global Warming." Annual Review of Energy and the Environment **25**: 441-475

Herbert, F. (1974). "Spectrum Line-Profiles - Generalized Voigt Function Including Collisional Narrowing." Journal of Quantitative Spectroscopy & Radiative Transfer **14**(9): 943-951

Hettner, G. (1918). "The Ultra Violet Absorption Spectrum of Water Vapour." ANNALEN DER PHYSIK **55**: 476

Hill, C. and R. L. Jones (2000). "Absorption of Solar Radiation by Water Vapor in Clear and Cloudy Skies: Implications for Anomalous Absorption." Journal of Geophysical Research-Atmospheres **105**(D7): 9421-9428

Huang, Z. S. and R. E. Miller (1989). "High-Resolution near-Infrared Spectroscopy of Water Dimer." Journal of Chemical Physics **91**(11): 6613-6631

Huisken, F., M. Kaloudis and A. Kulcke (1996). "Infrared Spectroscopy of Small Size-Selected Water Clusters." Journal of Chemical Physics **104**(1): 17-25

Jacquemart, D., R. Gamache and L. S. Rothman (2005). "Semi-Empirical Calculation of Air-Broadened Half-Widths and Air Pressure-Induced Frequency Shifts of Water-Vapor Absorption Lines." Journal of Quantitative Spectroscopy & Radiative Transfer **96**(2): 205-239

Jacquinet-Husson, N., N. A. Scott, A. Chedin, K. Garceran, R. Armante, A. A. Chursin, A. Barbe, M. Birk, L. R. Brown, C. Camy-Peyret, C. Claveau, C. Clerbaux, P. F. Coheur, V. Dana, L. Daumont, M. R. Debacker-Barilly, J. M. Flaud, A. Goldman, A. Hamdouni, M. Hess, D. Jacquemart, P. Kopke, J. Y. Mandin, S. Massie, S. Mikhailenko, V. Nemtchinov, A. Nikitin, D. Newnham, A. Perrin, V. I. Perevalov, L. Regalia-Jarlot, A. Rublev, F. Schreier, I. Schult, K. M. Smith, S. A. Tashkun, J. L. Teffo, R. A. Toth, V. G. Tyuterev, J. V. Auwera, P. Varanasi and G. Wagner (2005). "The 2003 Edition of the Geisa/Iasi Spectroscopic Database." Journal of Quantitative Spectroscopy & Radiative Transfer **95**(4): 429-467

Keutsch, F. N., L. B. Braly, M. G. Brown, H. A. Harker, P. B. Petersen, C. Leforestier and R. J. Saykally (2003). "Water Dimer Hydrogen Bond Stretch, Donor Torsion Overtone, And "In-Plane Bend" Vibrations." Journal of Chemical Physics **119**(17): 8927-8937

Keutsch, F. N., N. Goldman, H. A. Harker, C. Leforestier and R. J. Saykally (2003). "Complete Characterization of the Water Dimer Vibrational Ground State and Testing the Vrt(Asp-W)Iii, Sapt-5st, and Vrt(Mcy-5f) Surfaces." Molecular Physics **101**(23-24): 3477-3492

Kiehl, J. T. and K. E. Trenberth (1997). "Earth's Annual Global Mean Energy Budget." Bulletin of the American Meteorological Society **78**(2): 197-208

Kjaergaard, H. G., T. W. Robinson, D. L. Howard, J. S. Daniel, J. E. Headrick and V. Vaida (2003). "Complexes of Importance to the Absorption of Solar Radiation." Journal of Physical Chemistry A **107**(49): 10680-10686

Kuma, S., M. N. Slipchenko, K. E. Kuyanov, T. Momose and A. F. Vilesov (2006). "Infrared Spectra and Intensities of the H2o and N-2 Complexes in the Range of the V(1)- and V(3)-Bands of Water." Journal of Physical Chemistry A **110**(33): 10046-10052

Kuma, S., M. N. Slipchenko, T. Momose and A. F. Vilesov (2007). "Study of Complexes of Water and Ammonia Molecules in He Droplets." Chemical Physics Letters **439**(4-6): 265-269

Kurucz, R. L. (1994). Synthetic Infrared-Spectra. Infrared Solar Physics**:** 523-531.

Li, Z. Q., L. Moreau and A. Arking (1997). "On Solar Energy Disposition: A Perspective from Observation and Modeling." Bulletin of the American Meteorological Society **78**(1): 53-70

Lotter, K. A. (2006). Field Measurements of Water Continuum and Water Dimer Absorption by Active Long Path Differential Optical Absorption Spectroscopy. Heidelberg Germany,, University of Heidelberg. **PhD**.

Low, G. R. and H. G. Kjaergaard (1999). "Calculation of Oh-Stretching Band Intensities of the Water Dimer and Trimer." Journal of Chemical Physics **110**(18): 9104-9115

Ma, Q. and R. H. Tipping (1999). "The Averaged Density Matrix in the Coordinate Representation: Application to the Calculation of the Far-Wing Line Shapes for H2o." Journal of Chemical Physics **111**(13): 5909-5921

Ma, Q. and R. H. Tipping (2002). "The Frequency Detuning Correction and the Asymmetry of Line Shapes: The Far Wings of H2o-H2o." Journal of Chemical Physics **116**(10): 4102-4115

Mandin, J. Y., C. Camypeyret, J. M. Flaud and G. Guelachvili (1982). "Measurements and Calculations of Self-Broadening Coefficients of Lines Belonging to the 2-Nu-2,Nu-1, and Nu-3 Bands of (H_2o)." Canadian Journal of Physics **60**(1): 94-101

Marcus, V. and J. Tennyson (2000). "Accurate Partition Function and Thermodynamic Data for Water." The Journal of Chemical Physics **113**(21): 9766-9771

Mertz, L. (1976). "Field Compensation for High-Dispersion Spectrographs." Optics Communications **17**(3): 313-314

Mlawer, E. J., S. A. Clough, P. D. Brown and D. C. Tobin (1999). Recent Developments in the Water Vapor Continuum. Ninth ARM Science Team Meeting Proceedings. San Antonio, TX.

Mlawer, E. J., D. C. Tobin and S. A. Clough In Preparation.

Montgomery, G. P. (1978). "Temperature-Dependence of Infrared-Absorption by Water-Vapor Continuum near 1200 Cm^{-1}." Applied Optics **17**(15): 2299-2303

Morse, P. M. (1929). "Diatomic Molecules According to the Wave Mechanics. Ii. Vibrational Levels." Physical Review **34**(1): 57

MunozCaro, C. and A. Nino (1997). "Effect of Anharmonicities on the Thermodynamic Properties of the Water Dimer." Journal of Physical Chemistry A **101**(22): 4128-4135

Nizkorodov, S. A., M. Ziemkiewicz, D. J. Nesbitt and A. E. W. Knight (2005). "Overtone Spectroscopy of H2o Clusters in the V(Oh)=2 Manifold: Infrared-Ultraviolet Vibrationally Mediated Dissociation Studies." Journal of Chemical Physics **122**(19).194316

Artn 194316

Norton, R. H. and R. Beer (1976). "New Apodizing Functions for Fourier Spectrometry." Journal of the Optical Society of America **66**(3): 259-264

Paul, J. B., C. P. Collier, R. J. Saykally, J. J. Scherer and A. Okeefe (1997). "Direct Measurement of Water Cluster Concentrations by Infrared Cavity Ringdown Laser Absorption Spectroscopy." Journal of Physical Chemistry A **101**(29): 5211-5214

Paul, J. B., R. A. Provencal, C. Chapo, K. Roth, R. Casaes and R. J. Saykally (1999). "Infrared Cavity Ringdown Spectroscopy of the Water Cluster Bending Vibrations." Journal of Physical Chemistry A **103**(16): 2972-2974

Penner, S. S. and P. Varanasi (1967). "Spectral Absorption Coefficient in the Pure Rotational Spectrum of Water Vapour." *J. Quant. Spectrosc. Ra* **7**(4): 687-690

Perchard, J. P. (2001). "Anharmonicity and Hydrogen Bonding Ii - a near Infrared Study of Water Trapped in Nitrogen Matrix." Chemical Physics **266**(1): 109-124

Perchard, J. P. (2001). "Anharmonicity and Hydrogen Bonding. Iii. Analysis of the near Infrared Spectrum of Water Trapped in Argon Matrix." Chemical Physics **273**(2-3): 217-233

Petty, G. W. (2004). A First Course in Atmoshpereic Radiation Madison, Sundog Publishing.

Pfeilsticker, K., A. Lotter, C. Peters and H. Bosch (2003). "Atmospheric Detection of Water Dimers Via near-Infrared Absorption." Science **300**(5628): 2078-2080

Phillips, A. C. (2003). Introduction to Quantum Mechanics. London, Wiley.

Pierluissi, J. H., P. C. Vanderwood and R. B. Gomez (1977). "Fast Calculational Algorithm for Voigt Profile." Journal of Quantitative Spectroscopy & Radiative Transfer **18**(5): 555-558

Ptashnik, I. V. (2008). "Evidence for the Contribution of Water Dimers to the near-Ir Water Vapour Self-Continuum." Journal of Quantitative Spectroscopy & Radiative Transfer **109**(5): 831-852

Ptashnik, I. V., K. M. Smith and K. P. Shine (2005). "Self-Broadened Line Parameters for Water Vapour in the Spectral Region 5000-5600 Cm-1." Journal of Molecular Spectroscopy **232**(2): 186-201

Ptashnik, I. V., K. M. Smith, K. P. Shine and D. A. Newnham (2004). "Laboratory Measurements of Water Vapour Continuum Absorption in Spectral Region 5000-5600 Cm^{-1}: Evidence for Water Dimers." Quarterly Journal of the Royal Meteorological Society **130**(602): 2391-2408

Ramanathan, V., B. Subasilar, G. J. Zhang, W. Conant, R. D. Cess, J. T. Kiehl, H. Grassl and L. Shi (1995). "Warm Pool Heat-Budget and Shortwave Cloud Forcing - a Missing Physics." Science **267**(5197): 499-503

Ramanathan, V. and A. M. Vogelmann (1997). "Greenhouse Effect, Atmospheric Solar Absorption and the Earth's Radiation Budget: From the Arrhenius-Langley Era to the 1990s." Ambio **26**(1): 38-46

Remedios, J. J. (1990). Spectroscopy for Remote Sounding of the Atmosphere. Oxford, University of Oxford **PHd**.

Roberts, R. E., J. E. A. Selby and L. M. Biberman (1976). "Infrared Continuum Absorption by Atmospheric Water-Vapor in 8-12um Window." Applied Optics **15**(9): 2085-2090

Rothman, L. S., A. Barbe, D. C. Benner, L. R. Brown, C. Camy-Peyret, M. R. Carleer, K. Chance, C. Clerbaux, V. Dana, V. M. Devi, A. Fayt, J. M. Flaud, R. R. Gamache, A. Goldman, D. Jacquemart, K. W. Jucks, W. J. Lafferty, J. Y. Mandin, S. T. Massie, V. Nemtchinov, D. A. Newnham, A. Perrin, C. P. Rinsland, J. Schroeder, K. M. Smith, M. A. H. Smith, K. Tang, R. A. Toth, J. Vander Auwera, P. Varanasi and K. Yoshino (2003). "The Hitran Molecular Spectroscopic Database: Edition of 2000 Including Updates through 2001." Journal of Quantitative Spectroscopy & Radiative Transfer **82**(1-4): 5-44.10.1016/s0022-4073(03)00146-8|issn 0022-4073

Rothman, L. S., R. R. Gamache, A. Goldman, L. R. Brown, R. A. Toth, H. M. Pickett, R. L. Poynter, J. M. Flaud, C. Camypeyret, A. Barbe, N. Husson, C. P. Rinsland and M. A. H. Smith (1987). "The Hitran Database - 1986 Edition." Applied Optics **26**(19): 4058-4097

Rothman, L. S., R. R. Gamache, R. H. Tipping, C. P. Rinsland, M. A. H. Smith, D. C. Benner, V. M. Devi, J. M. Flaud, C. Camypeyret, A. Perrin, A. Goldman, S. T. Massie, L. R. Brown and R. A. Toth (1992). "The Hitran Molecular Database - Editions of 1991 and 1992." Journal of Quantitative Spectroscopy & Radiative Transfer **48**(5-6): 469-507

Rothman, L. S., D. Jacquemart, A. Barbe, D. C. Benner, M. Birk, L. R. Brown, M. R. Carleer, C. Chackerian, K. Chance, L. H. Coudert, V. Dana, V. M. Devi, J. M. Flaud, R. R. Gamache, A. Goldman, J. M. Hartmann, K. W. Jucks, A. G. Maki, J. Y. Mandin, S. T. Massie, J. Orphal, A. Perrin, C. P. Rinsland, M. A. H. Smith, J. Tennyson, R. N. Tolchenov, R. A. Toth, J. Vander Auwera, P. Varanasi and G. Wagner (2005). "The Hitran 2004 Molecular Spectroscopic Database." Journal of Quantitative Spectroscopy & Radiative Transfer **96**(2): 139-204

Rothman, L. S., C. P. Rinsland, A. Goldman, S. T. Massie, D. P. Edwards, J. M. Flaud, A. Perrin, C. Camy-Peyret, V. Dana, J. Y. Mandin, J. Schroeder, A. McCann, R. R. Gamache, R. B. Wattson, K. Yoshino, K. V. Chance, K. W.

Jucks, L. R. Brown, V. Nemtchinov and P. Varanasi (1998). "The Hitran Molecular Spectroscopic Database and Hawks (Hitran Atmospheric Workstation): 1996 Edition." Journal of Quantitative Spectroscopy & Radiative Transfer **60**(5): 665-710

Schofield, D. P. and H. G. Kjaergaard (2003). "Calculated Oh-Stretching and Hoh-Bending Vibrational Transitions in the Water Dimer." Physical Chemistry Chemical Physics **5**(15): 3100-3105

Schofield, D. P., J. R. Lane and H. G. Kjaergaard (2007). "Hydrogen Bonded Oh-Stretching Vibration in the Water Dimer." Journal of Physical Chemistry A **111**(4): 567-572

Scribano, Y., N. Goldman, R. J. Saykally and C. Leforestier (2006). "Water Dimers in the Atmosphere Iii: Equilibrium Constant from a Flexible Potential." Journal of Physical Chemistry A **110**(16): 5411-5419

Slanina, Z. and J. F. Crifo (1992). "A Refined Evaluation of the Gas-Phase Water-Dimerization Equilibrium-Constant within Nonrigid Bjh-Type and Mcy-Type Potentials." International Journal of Thermophysics **13**(3): 465-476

Theocharous, E., G. Hawkins and N. P. Fox (2005). "Reversible Ageing Effects in Cryogenically Cooled Infrared Filter Radiometers." Infrared Physics & Technology **46**(4): 339-349

Thorne, P., U. Litzen and S. Johansson (1999). Spectrophysics: Principles and Applications, Springer.

Tobin, D. C., L. L. Strow, W. J. Lafferty and W. B. Olson (1996). "Experimental Investigation of the Self- and N-2-Broadened Continuum within the Nu(2) Band of Water Vapor." Applied Optics **35**(24): 4724-4734

Toth, R. A. (1993). "Nu(1)-Nu(2), Nu(3)-Nu(2), Nu(1), and Nu(3) Bands of (H2o)-O-16 - Line Positions and Strengths." Journal of the Optical Society of America B-Optical Physics **10**(11): 2006-2030

Toth, R. A. (2005). "Measurements and Analysis (Using Empirical Functions for Widths) of Air- and Self-Broadening Parameters of H2o." Journal of Quantitative Spectroscopy & Radiative Transfer **94**(1): 1-50.10.1016/j.jqsrt.2004.08.041|ISSN 0022-4073

Toth, R. A. (2005). "Measurements of Positions, Strengths and Self-Broadened Widths of H2o from 2900 to 8000cm(-1): Line Strength Analysis of the 2nd Triad Bands." Journal of Quantitative Spectroscopy & Radiative Transfer **94**(1): 51-107.10.1016/j.jqsrt.2004.08.042|ISSN 0022-4073

Tso, H. C. W., D. J. W. Geldart and P. Chylek (1998). "Anharmonicity and Cross Section for Absorption of Radiation by Water Dimer." Journal of Chemical Physics **108**(13): 5319-5329

Vaida, V., J. S. Daniel, H. G. Kjaergaard, L. M. Goss and A. F. Tuck (2001). "Atmospheric Absorption of near Infrared and Visible Solar Radiation by the Hydrogen Bonded Water Dimer." Quarterly Journal of the Royal Meteorological Society **127**(575): 1627-1643

Vigasin, A. A. (2000). "Water Vapor Continuous Absorption in Various Mixtures: Possible Role of Weakly Bound Complexes." Journal of Quantitative Spectroscopy & Radiative Transfer **64**(1): 25-40

Wild, M. (2005). "Solar Radiation Budgets in Atmospheric Model Intercomparisons from a Surface Perspective." Geophysical Research Letters **32**(7).L07704

Artn l07704

Zou, Q. and P. Varanasi (2003). "Laboratory Measurement of the Spectroscopic Line Parameters of Water Vapor in the 610-2100 and 3000-4050 Cm^{-1} Regions at Lower-Tropospheric Temperatures." Journal of Quantitative Spectroscopy and Radiative Transfer **82**(1-4): 45-98